Argonne
NATIONAL LABORATORY

ANL-09/10

Melt Spreading Code Assessment, Modifications, and Applications to the EPR Core Catcher Design

Nuclear Engineering Division

About Argonne National Laboratory

Argonne is a U.S. Department of Energy laboratory managed by UChicago Argonne, LLC under contract DE-AC02-06CH11357. The Laboratory's main facility is outside Chicago, at 9700 South Cass Avenue, Argonne, Illinois 60439. For information about Argonne, see www.anl.gov.

Availability of This Report

This report is available, at no cost, at http://www.osti.gov/bridge. It is also available on paper to the U.S. Department of Energy and its contractors, for a processing fee, from:

U.S. Department of Energy
Office of Scientific and Technical Information
P.O. Box 62
Oak Ridge, TN 37831-0062
phone (865) 576-8401
fax (865) 576-5728
reports@adonis.osti.gov

ANL-09/10

Melt Spreading Code Assessment, Modifications, and Applications to the EPR Core Catcher Design

by
M.T. Farmer
Nuclear Engineering Division, Argonne National Laboratory

March 2009

Table of Contents

List of Figures

List of Figures (Cond.)

Figure **Page**

List of Figures (Cond.)

List of Figures (Cond.)

List of Figures (Cond.)

List of Figures (Cond.)

List of Tables

List of Tables (Contd.)

1.0 INTRODUCTION

1.1 Background

The Evolutionary Power Reactor (EPR) is under consideration by various utilities in the United States to provide base load electrical production, and as a result the design is undergoing a certification review by the U.S. Nuclear Regulatory Commission (NRC). The severe accident design philosophy for this reactor is based upon the fact that the projected power rating results in a narrow margin for in-vessel melt retention by external cooling of the reactor vessel. As a result, the design addresses ex-vessel core melt stabilization using a mitigation strategy that includes: i) an external core melt retention system to temporarily hold core melt released from the vessel; ii) a layer of "sacrificial" material that is admixed with the melt while in the core melt retention system; iii) a melt plug in the lower part of the retention system that, when failed, provides a pathway for the mixture to spread to a large core spreading chamber; and finally, iv) cooling and stabilization of the spread melt by controlled top and bottom flooding. The overall concept[1] is illustrated in Figure 1.1. The melt spreading process relies heavily on inertial flow of a low-viscosity admixed melt to a segmented spreading chamber, and assumes that the melt mass will be distributed to a uniform height in the chamber. The spreading phenomenon thus needs to be modeled properly in order to adequately assess the EPR design. The MELTSPREAD code, developed at Argonne National Laboratory, can model segmented, and both uniform and non-uniform spreading. The NRC is thus utilizing MELTSPREAD to evaluate melt spreading in the EPR design.

MELTSPREAD was originally developed to support resolution of the Mark I containment shell vulnerability issue.[2-5] Following closure of this issue, development of MELTSPREAD ceased in the early 1990's,[6-7] at which time the melt spreading database upon which the code had been validated was rather limited. In particular, the database that was utilized for initial validation consisted of: i) comparison to an analytical solution for the dam break problem,[8] iii) water spreading tests in a 1/10 linear scale model of the Mark I containment by Theofanous et al.,[2] and iii) steel spreading tests by Suzuki et al.[9] that were also conducted in a geometry similar to the Mark I.

Following MELTSREAD utilization in the U.S., there was a vast amount of research carried out principally in the European Union (EU) to support the development and licensing of the EPR concept. This work consisted of both experimental and analytical programs. In terms of experiments, large isothermal spreading tests were carried out at the Commissariat á l'Énergie Atomique (CEA) in France with water and glycerol by Veteau et al.[10] in the Corine test facility. This test series was subsequently expanded to investigate the effects of bottom gas injection on spreading behavior, as well as freezing effects using low temperature eutectic metal melt mixtures.[10] Spreading tests with high temperature simulant oxide (calcia – boria eutectic) under both wet and dry cavity conditions were also conducted by Dinh et al.[11] at the Royal Institute of Technology (RIT) in Sweden. In addition, several series of spreading tests with both high temperature steel and oxide simulants were performed at Forschungszentrum Karlsruhe (FZK) by Engel et al.[12] and Eppinger et al.[13] in the KATS test facility, and by Foit[14] and Alsmeyer et al.[15] using a slightly modified oxide simulant in the ECOKATS facility.

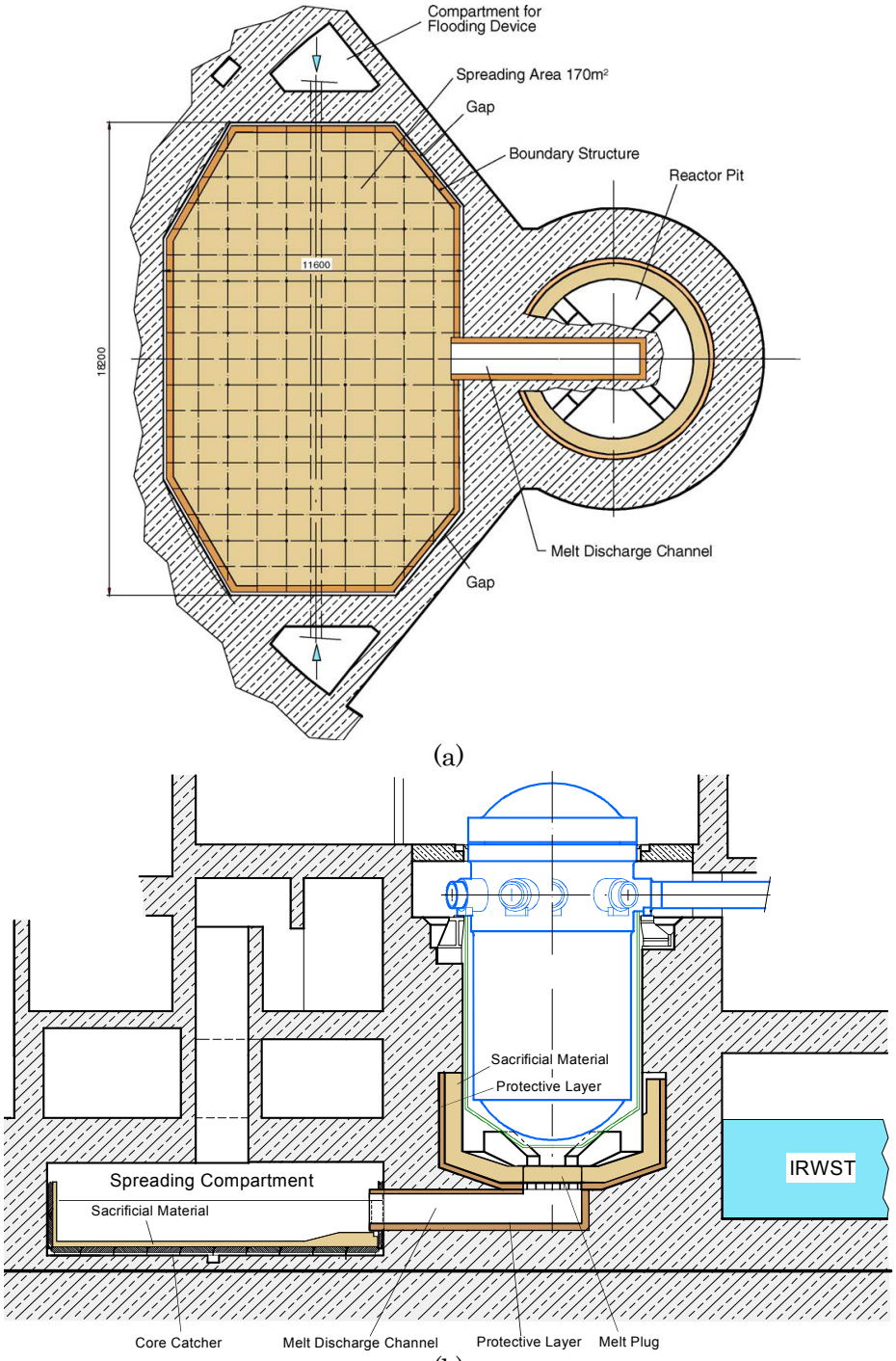

Figure 1.1. (a) Plan and (b) elevation views of the EPR core catcher design.[1]

Aside from simulant tests, several reactor material melt spreading programs were performed in the EU to provide prototypic melt spreading data. As reported by Cognet et al.[16] and Journeau et al.,[17-18] several corium melt spreading tests were carried out at CEA with varying melt compositions and substrate materials in the VULCANO facility. Two corium tests were also conducted by Magallon and Tromm[19] as part of the FARO program, one of them under wet cavity conditions. Finally, several large scale spreading tests at up to 2 metric ton melt mass

were conducted at Siempelkamp Nuklear in Germany on various types of surface materials (Sappok and Steinwarz[20] and Steinwarz et al.[21]).

As previously noted, experiment data from these various simulant and reactor material experiment programs was not available during MELTSPREAD development, and so one key element of the current workscope was to assess the code against this database.

Aside from experiments, extensive model and code development activities were also carried out as part of the EU program to address spreading issues associated with the EPR. At CEA, the THEMA code was developed[22-24] to simulate spreading while accounting for the effects of heat transfer and solidification, in addition to ablation of the underlying spreading surface. THEMA uses conservation equations that are locally averaged over the melt depth. This same approach is used in MELTSPEAD,[6-7] but THEMA has the advantage that it is able to calculate two dimensional spreading, whereas MELTSPREAD is 1-D. Other three dimensional codes were developed as part of the EU effort that included axial meshing over the melt depth. These codes include CROCO[25] developed at IRSN in France, LAVA[26] developed at GRS in Germany, and CORFLOW[27] developed by Areva in Germany. The drawback of these codes is that they are computationally intensive, with associated long run times that do not lend themselves to the type of parametric analysis that has been adopted for the current study. Aside from code development, other modeling activities[28] have been performed to provide approximate closed form solutions for spreading of high temperature melts, in addition to studies to develop models[29] that better correlate corium viscosity, which is one of the key variables affecting melt spreading.

These analysis and code development activities were also predominately completed and documented after MELTSPREAD development had ceased. Thus, another key element of the current workscope is to incorporate lessons learned from these activities.

1.2 Objectives and Approach

With this background, the objectives of the current work are to:

1) assess MELTSPREAD against the available world-wide melt spreading database,
2) make necessary improvements and upgrades to the code that are required to adequately model these tests, and
3) carry out confirmatory plant calculations with the updated code.

To this end, the code assessment against the database, as well as upgrades to the code that were made to better model the tests, are summarized in Section 2. This is followed by presentation of the EPR confirmatory plant calculations in Section 3. Principal findings from this work are then summarized in Section 4. For the interested reader, detailed descriptions of the code validation calculations performed for all tests are provided in Appendix A, while the array of code verification calculations that were carried out are described in Appendix B.

2.0 CODE ASSESSMENT

2.1 Assessment Database

The first step in the code assessment process was to assemble a set of test cases against which the code could be compared to check the accuracy of the numerical algorithms and to determine the extent to which the model could reproduce actual spreading behavior. This validation matrix is shown in Table 2.1. A determining factor in the decision to include a given test in the matrix was that sufficient information was available through open literature sources to assemble a model that included details of the spreading geometry, materials employed, and test operating conditions. Note that this table does not include every test that was reported in the literature. Rather, the matrix was selected to cover the full range of programs for which information was available (e.g., addition tests were conducted as part of the KATS and VULCANO spreading programs), and to provide diversity in the validation database. As shown in the table, a total of 35 different cases were calculated as part of the code verification and validation exercise. The matrix includes tests from all data sources that were described in Section 1 as part of the literature review. The information can be broken down as follows:

1. Analytical solution to dam break problem (*1 case*[8])
2. Isothermal tests (*6 cases*[2,10])
3. Flow and freezing tests (*28 cases*); i.e., core oxides (*7 tests*[16-21]), core oxide – steel mixtures (*4 tests*[20-21]), simulant oxides (*12 tests*[11-15]), and steel alone (*5 tests*[9,12-13])

The category of flow and freezing tests include five cases in which water was present in the cavity. Spreading on concrete, ceramic, and steel substrates has been investigated. The database includes information on spreading velocity, total melt penetration, posttest debris profile, substrate heatup/ablation profiles, and local melt temperatures. The data available from each of these experiments is shown in Table 2.2. The MELTSPREAD validation calculations include comparisons to all available information for each test in order to evaluate the overall predictive capability of the code.

The code was first compared with the isothermal spreading data to verify proper behavior before moving on to the tests involving freezing effects that are described later in this section. The code was found to reproduce the analytical solutions for leading edge depth and velocity for the dam break problem[8] (see Appendix B). For the water spreading tests of Theofanous et al.,[2] the code was also found to reasonably replicate fluid arrival times and subsequent depth profiles at various locations within a scaled mockup of a Mark I containment. Code predictions were also compared with Corine spreading data; [10] the comparison for a low flowrate water test is provided in Figure 2.1, while the comparison for a high flowrate glycerol (HEC) test is shown in Figure 2.2. Depth profiles at various times are also shown in these figures to illustrate the effect of viscosity on wave form. In general, the leading edge penetration vs. time for both cases is reasonably reproduced. Calculations for both wetted and non-wetted surface conditions are shown to illustrate the effect of surface tension on leading edge propagation. Further comparisons of code predictions with other Corine spreading tests, as well as the Theofanous water spreading tests, are provided in Appendix A to this report. This appendix provides details of all validation calculations carried out as part of this work.

Table 2.1. MELTSPREAD-2 Validation Test Matrix (35 cases in total).

Program	Test or Case	Fluid	Substrate	Flow Geometry	Cavity Condition
N/A	1-D dam break solution	Water	Inert	1-D channel	N/A
Theofanous	Run no. 1	Water	″	1/10 linear scale model of Mark-I containment	″
	Run no. 2	″	″	″	″
Corine	WAT_Q1.5_G0	Water	″	Feedbox with 24 cm weir → 17º sector	″
	WAT_Q0.5_G0	″	″	″	″
	HEC_3_G0_0.1[a]	HEC[a]	″	″	″
	HEC_3_G0_2[a]	″	″	″	″
RIT	3MDC-Ox-1	Oxide simulant[b]	Concrete	Feedbox → 1-D channel	Dry
	3MDS-Ox-1	″	Steel	″	″
	3MDS-Ox-2	″	″	″	″
	2MWS-Ox-1	″	″	″	12 cm H_2O
	2MWS-Ox-2	″	″	″	″
	2MWS-Ox-3	″	″	″	″
Kats	KATS-12	Iron	Ceramic	Feedbox → 1-D channel	Dry
		Oxide simulant[c]	″	″	″
	KATS-13	Iron	Concrete	″	
		Oxide simulant[c]	″	″	″
	KATS-14	Iron	Ceramic	″	″
		Oxide simulant[c]	″	″	
ECOKATS	V1	Oxide simulant[d]	Ceramic	″	″
	1	″	Concrete	Feedbox → 1-D channel → 2-D floor	″
	2	″	″	″	″
SPREAD	Test 15	Stainless steel	″	Cylindrical cavity with door →180º sector	″
	Test 21	″	″	″	7 cm H_2O
COMAS	COMAS-5a	Core oxides + iron	Concrete	Feedbox with 5 cm weir → 1-D channel	Dry
		″	Ceramic	″	″
		″	Steel	″	″
	EU-2b	Core oxides	Concrete	″	″
		″	Ceramic	″	″
		″	Steel	″	″
	EU-4	Core oxides + iron	″	Feedbox with 5 cm weir → 1-D channel → 45º sector	″
Faro	L-26S	″	″	Cylindrical cavity with 4 cm weir → 17º sector	″
	L-32S	″	″	″	1 cm H_2O
Vulcano	VE-U7	″	Concrete	Feedbox box with 0.5 cm weir → 9.5º sector	Dry
		″	Ceramic	″	″

[a]Hydroxyl ethyl cellulose; [b]30/70 wt% CaO/B_2O_3; [c]83/8.5/6/1.5/1 wt% Al_2O_3/ SiO_2/FeO/MgO/MnO; [d]41/24/19/16 wt% Al_2O_3/FeO/CaO/SiO_2

Table 2.2. Open Literature Validation Test Matrix Data Availability.

Program	Case	Available Information						
		Leading Edge vs. Time	**Spreading Distance**	**Posttest Debris Profile**	**Substrate Ablation Profile**	**Substrate Thermal Response**	**Local Melt Temp. vs. Time.**	**Local Melt Height vs. Time**
N/A	Dam break solution	X	N/A	N/A	N/A	N/A	N/A	X
Theofanous	Run no. 1	X	N/A	N/A	N/A	N/A	N/A	X
	Run no. 2	X	N/A	N/A	N/A	N/A	N/A	X
Corine	WAT_Q1.5_G0	X	N/A	N/A	N/A	N/A	N/A	
	WAT_Q0.5_G0	X	N/A	N/A	N/A	N/A	N/A	
	HEC_3_G0_0.1[a]	X	N/A	N/A	N/A	N/A	N/A	
	HEC_3_G0_2[a]	X	N/A	N/A	N/A	N/A	N/A	
RIT	3MDC-Ox-1	X	X	X		X		
	3MDS-Ox-1	X	X	X				
	3MDS-Ox-2	X	X	X				
	2MWS-Ox-1		X					
	2MWS-Ox-2		X					
	2MWS-Ox-3		X					
Kats	KATS-12	X	X	X			X	
		X	X	X			X	
	KATS-13	X	X	X			X	
		X	X	X			X	
	KATS-14	X	X	X	X		X	
		X	X	X			X	
ECOKATS	V1	X	X	X				
	1	X	X			X		
	2	X				X	X	
SPREAD	Test 15		X	X				
	Test 21		X	X				
COMAS	COMAS-5a	X	X					
		X	X					
		X	X			X		
	EU-2b	X	X					
		X	X					
		X	X					
	EU-7	X	X					
Faro	L-26S	X	X	X				
	L-32S	X	X	X				
Vulcano	VE-U7	X	X	X		X		
		X	X	X		X		

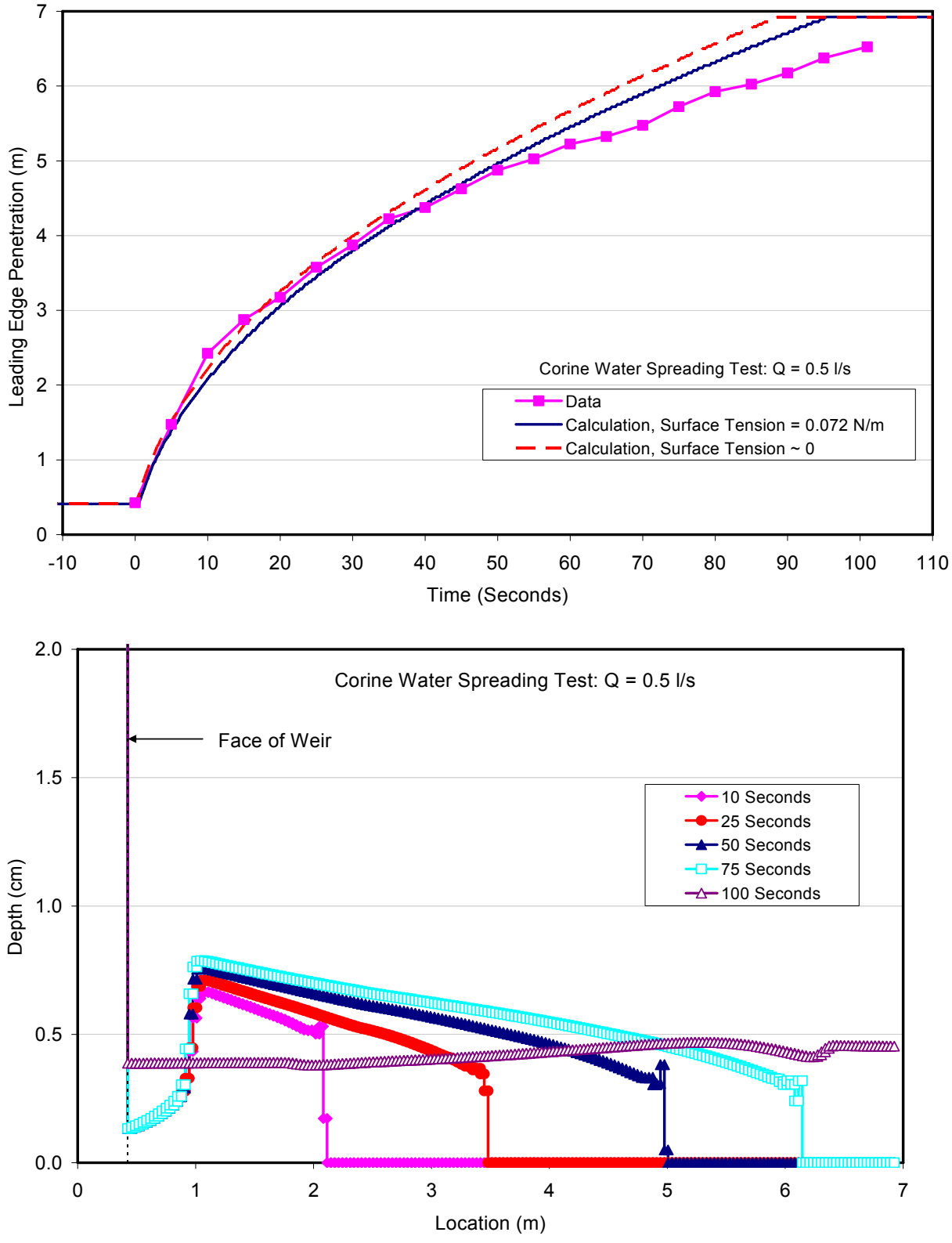

Figure 2.1. Leading edge penetration (top) and depth profiles (bottom) for Corine[10] water spreading test WAT_Q0.5_G0.

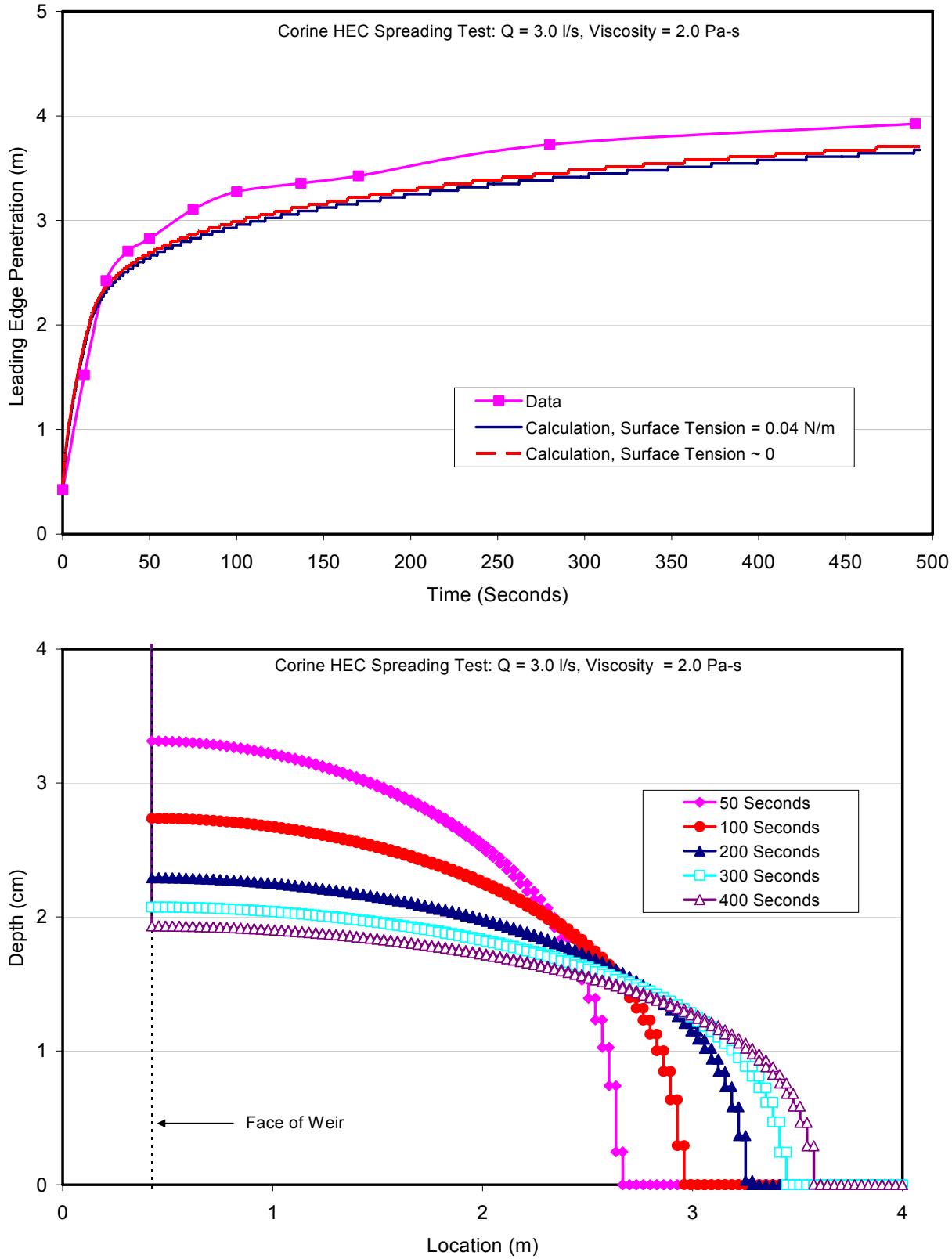

Figure 2.2. Leading edge penetration (top) and depth profiles (bottom) for Corine[10] glycerol spreading test HEC_3_G0_2.

2.2 Code Improvements

Base on the literature review, it was clear that several improvements to the code would be needed in order to make comparisons with the full range of melt spreading data involving heat transfer and solidification. In particular, the melt property subroutines in the original code were only capable of treating mixtures of core and cladding metals and their corresponding oxides, and only substrates composed of concrete, steel, or an arbitrary combination thereof. Thus, the code was incapable of calculating tests that utilized a corium simulant and/or a ceramic substrate. As a result, one of the first improvements was to provide the user the ability to input simulant melt and/or substrate material properties (density, thermal conductivity, solid/liquid phase specific heats, heat of fusion, emissivity). This allowed all 'simulant oxide' tests shown in Table 2.1 to be calculated, as well as tests with ceramic substrate, using property data that was in almost all cases provided by the institutions who carried out the experiments. The ability to overwrite selected melt material properties was also added for sensitivity analysis. Another key improvement in the area of material properties was providing the ability to input a tabular function for the oxide phase solid fraction variation between the liquidus and solidus temperatures. The original version of the code assumed that the solid fraction varied linearly in this range, but research since then has shown that the functional dependence is highly non-linear for multi-component oxide melts (e.g., see Journeau et al.[18]). Since solid fraction has an important effect on viscosity which, in turn, strongly affects spreading behavior, this was one of the key modeling improvements in the area of material properties evaluation.

Several other improvements were also made. The capability to carry out inviscid and/or adiabatic spreading analysis was added, so that the dam break case shown in Table 2.1, as well as the Theofanous and Corine isothermal spreading tests, could be calculated by appropriate selection of input data. (This option was used for the cases presented in Section 2.1). The ability to model a heat transfer resistance at the melt-substrate interface was also added. This is important in terms of calculating spreading behavior for metallic melts, for which shrinkage at the melt – substrate interface can have a marked effect on local heat transfer rate.[18,30-32]

Finally, of the thermo-physical properties affecting spreading, viscosity is the most important.[17] The initial code version used the Ishii-Zuber[33] correlation to account for the effects of solids buildup in the melt on increasing corium viscosity. However, early applications to the expanded database indicated that spreading behavior was much better reproduced using the correlation developed by Ramacciotti et al.[29] In this model, the apparent melt viscosity in the freezing range is correlated as:

$$\mu_{app} = \mu_o e^{2.5 C_R \alpha_{sol}} \tag{2.1}$$

where μ_o is the viscosity at the melt liquidus, α_{sol} is the melt solid fraction, and C_R is an empirical constant that depends upon experiment conditions and varies between 4 and 8.[29] This model was added as a user option, with the constant C_R left as a user-specified input parameter.

As is evident from Eq. (1), accurate knowledge of the melt solid-fraction variation between the liquidus-solidus is important when using this viscosity correlation. The assumed solid fraction functions for the various melt compositions that were considered as part of this study are shown in Figure 2.3. For several programs, these functions were provided as part of

the test results; i.e., the KATS,[13] ECOKATS,[34] and Vulcano[18] programs. However, for the balance of the tests, these functions were either evaluated from other sources or simply estimated. In particular, for the FARO[19] and COMAS[20-21] core melt compositions, the functions were evaluated using property subroutines embedded in the CORQUENCH ex-vessel debris coolability code.[35] These subroutines are, in turn, based on early thermophysical property calculations carried out with the OXY5-GEMINI2 code by Chevalier.[36] Finally, for the calcia-boria melt composition used in the RIT melt spreading tests,[11] as well as the KATS[13] and SPREAD[9] steel melt spreading tests, a simple linear function was assumed in lieu of other information or data sources.

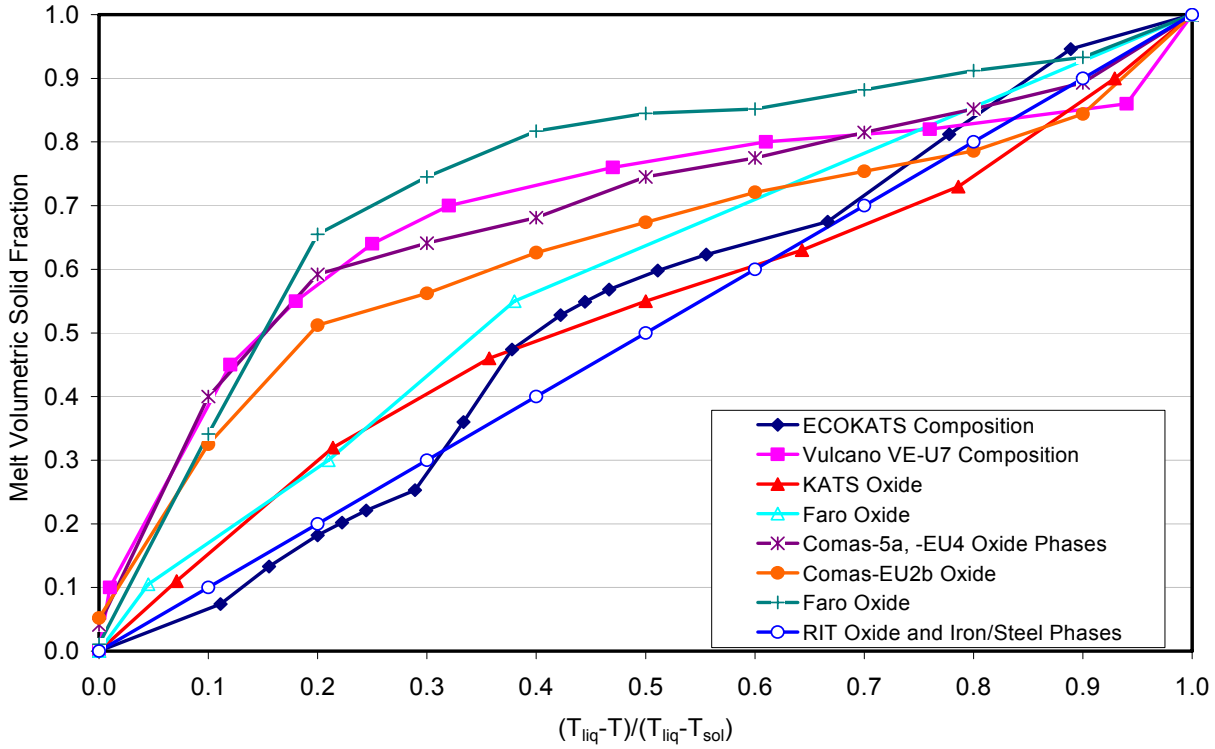

Figure 2.3. Oxide and metal phase solid fraction functions assumed for the various melt compositions addressed in this study.

2.3 Validation Approach and Results for Freezing Tests

One of the key questions to address in the assessment exercise was how to translate uncertainties in the spreading analysis to the EPR plant calculations. A modeling sensitivity study was performed by Journeau et al.[17] with the THEMA code.[22-24] The results of this study[17] indicate that the exponential parameter C_R in the Ramacciotti[29] correlation, Eq. (1), is one of the primary factors influencing melt spreading length. Melt spreading length is also the key computed result for the EPR analysis, since the primary question to be addressed in that case is the extent of spreading within the core catcher. On this basis, the decision was made to carry out a set of parametric calculations for each test shown in Table 2.1 to find the value of C_R which reproduced (matched) the experimentally observed spreading length for the test. With this information, a simple statistical analysis would then be performed to find the average C_R that best fits the test data, as well as the standard deviation in the fit. This statistical data would then be used to characterize modeling uncertainties based on test results in the EPR plant calculations.

The results of the parametric analysis for the best-fit values of C_R are summarized graphically in Figure 2.4, while the detailed results along with the statistics are provided in Tables 2.3 through 2.5. The data in the graph and tables have been divided into four different categories, depending upon melt composition. The average C_R for the reactor material oxide and oxide plus metal tests was 7.26 with a standard deviation of 0.95. As noted earlier, the value of C_R in the Ramacciotti correlation generally falls in the range of 4 to 8,[29] although the technical basis for this statement is not provided in the reference. In any case, the value for the reactor material tests falls near the upper end of the reported range. Conversely, the average C_R for the RIT calcia-boria spreading tests is 4.75 (standard deviation is 1.03), which is near the middle of this range. Note that the data for this test series is correlated about as well for both wet and dry cavity conditions.

Table 2.3. C_R Fits for Kats and ECOKATS Oxide Simulant Melt Spreading Tests.

Test	**Fluid**	**Substrate**	**Best Fit C_R**	$\overline{C_R}$	σ_{C_R}
KATS-12	Oxide simulant[a]	Ceramic	1.83	2.34 (Omits Kats-13)	1.04 (Omits Kats-13)
KATS-13	″	Concrete	10.28		
KATS-14	″	Ceramic	1.56		
ECOKATS V1	Oxide simulant[b]	″	1.83		
ECOKATS 1	″	Concrete	4.13		

[a]83/8.5/6/1.5/1 wt% Al_2O_3/ SiO_2/FeO/MgO/MnO; [b]41/24/19/16 wt% Al_2O_3/FeO/CaO/SiO_2

Table 2.4. Best Fit C_R Constants for RIT Tests CaO - B_2O_3 Melt Spreading Tests.

Test	**Cavity Condition**	**Substrate**	**Best Fit C_R**	$\overline{C_R}$	σ_{C_R}
3MDC-1	Dry	Concrete	5.03	4.75	1.03
3MDS-1	″	Steel	3.03		
3MDS-2	″	″	6.55		
2MWS-1	Wet	″	4.40		
2MWS-2	″	″	4.80		
2MWS-3	″	″	4.66		

Table 2.5. C_R Fits for Dry Cavity Reactor Material Melt Spreading Tests.

Test	**Fluid**	**Substrate**	**Best Fit C_R**	$\overline{C_R}$	σ_{C_R}
COMAS-5a	Core oxides + iron	Concrete	7.23	7.26	0.95
	″	Ceramic	7.80		
	″	Steel	7.93		
COMAS EU-4	″	″	8.17		
COMAS EU-2b	Core oxides	Concrete	5.33		
	″	Ceramic	8.40		
	″	Steel	6.89		
Faro L-26S	″	″	5.77		
Vulcano VE-U7	″	Concrete	7.58		
	″	Ceramic	7.48		

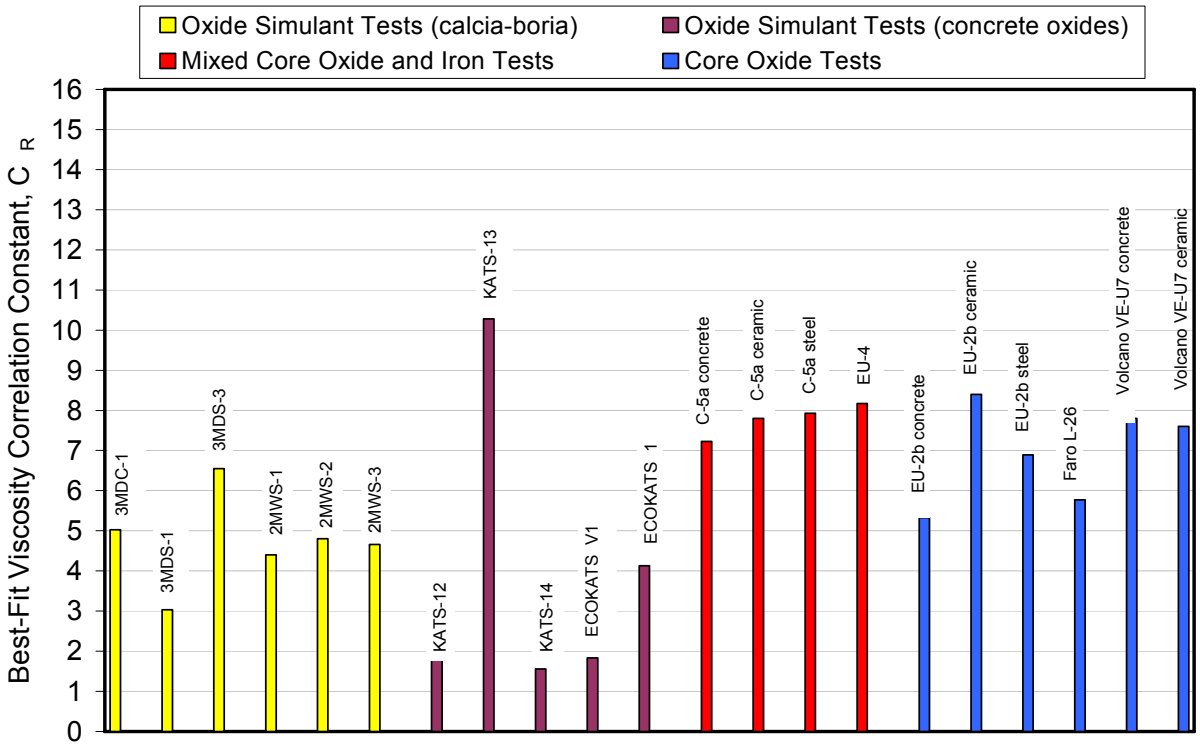

Figure 2.4. Bar graph showing best fit values of C_R for each oxide spreading test.

Finally, as shown in Table 2.3, the KATS and ECOKATS tests conducted with Al_2O_3 - SiO_2 rich melts seem to group together at a somewhat lower average C_R of 2.34, with a standard deviation of 1.04. One test, KATS-13, required a significantly higher C_R of 10.28 to match the actual spreading length. This discrepancy indicates that: i) the initial conditions for the experiment are not well defined, and/or ii) the model is not capturing some physical aspect(s) of the experiment. In any event, this particular test has been omitted in the statistical analysis so that the results are not skewed. Further note that the ECOKATS-2 test was not included in the evaluation of C_R since the melt in this experiment covered the entire spreading surface, and so the ultimate spreading length was not determined.

Given the C_R range calculated for the various experiment categories, it is of interest to evaluate the effective viscosity enhancement, defined as μ_{app}/μ_o from Eq. 2-1, for a particular case to provide the reader with a feeling for the extent of enhancement due to solids buildup in the melt, and also to illustrate the model sensitivity to the choice of C_R. Since the primary focus of this study is melt spreading in the EPR core catcher, the enhancement factor is plotted in Figure 2.5 as a function of solid fraction for C_R and $C_R \pm 2\sigma_{C_R}$ based on the reactor material melt spreading database. For the average value of C_R, significant enhancement begins at a solid fraction of $\alpha_{sol} \sim 0.35$, and reaches a level of 10^5 at $\alpha_{sol} \sim 0.64$. Conversely, for the $+2\sigma_{C_R}$ case, enhancement begins at $\alpha_{sol} \sim 0.28$, and reaches a level of 10^5 at $\alpha_{sol} \sim 0.50$. Finally, for the $-2\sigma_{C_R}$ case, significant enhancement does not begin until $\alpha_{sol} \sim 0.45$, and finally reaches a level of 10^5 at $\alpha_{sol} \sim 0.86$.

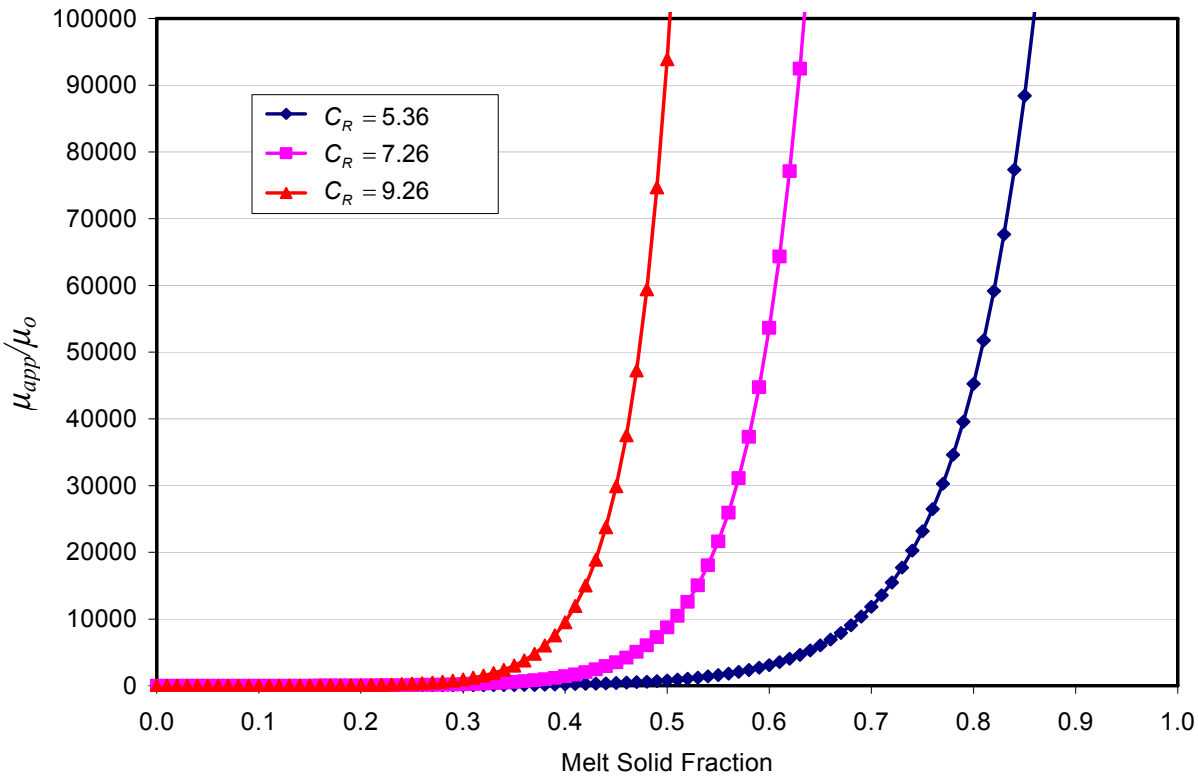

Figure 2.5. Viscosity enhancement vs. solid fraction evaluated from the Ramacciotti correlation for C_R and $C_R \pm 2\sigma_{C_R}$ based on the reactor material melt spreading database.

To illustrate the overall results, two cases are briefly presented. The first case is the KATS-12 oxide simulant melt spreading test on a ceramic substrate. The calculated leading edge penetration vs. time is compared to the test data in Figure 2.6, while local melt temperature and post-spreading material profile predictions are compared with data in Figure 2.7. This was a high pour rate test in which the spreading rate was initially dominated by inertial effects. As a result, viscous forces that retard the spreading rate do not show up until late in the spreading transient (see Figure 2.6). Results for C_R and $C_R \pm 2\sigma_{C_R}$ (Table 2.3) are shown in the figure of melt penetration vs. time. As is evident from Figure 2.7, despite discrepancies in melt arrival times, peak melt temperatures are predicted to within ~ 30 K near the melt injection point, but the discrepancy grows to ~ 70 K near the channel midpoint. As shown in the lower figure, the debris profile is reasonably predicted (code data are for the average C_R case). The large structure to the left in this figure is the melt feedbox that was located at an elevation of +7 cm relative to the spreading surface. As is evident, the feedbox was modeled in the calculation. Given this design and high melt injection rate, the possibility exists that the melt jetted out of feedbox, causing overshoot of some (unknown) distance of the spreading surface and an initial spreading velocity that would exceed what the code would calculate based on gravity-driven spreading alone. This may explain the discrepancy in initial spreading rate seen early in the transient, as the code assumes continuous flow through the mesh with no possibility of bypass.

The second case that is presented is the VULCANO VE-U7 core oxide melt spreading test on a concrete surface. The calculated leading edge penetration vs. time is compared to the test data in Figure 2.8, while substrate heatup and post-spreading material profile predictions are compared with data in Figure 2.9. In contrast to the previous case, this was a low pour rate experiment in which the spreading rate was initially dominated by viscous effects. Thus, the calculated range in final melt penetration distance is much more sensitive to the statistical variation in C_R. Temperatures in the concrete substrate 30 cm from the injection box are under-estimated by about 250 K near the concrete surface (i.e. 2 mm recessment), but the discrepancy decreases as depth into the substrate increases. Finally, the overall shape in the posttest debris profile is reasonably reproduced, but the depth is consistently less than reported. This is due to the fact that the oxide material freezes with porosity due to gas sparging, but porosity during solidification is not modeled by the code.

The balance of the code validation calculations for tests involving flow and freezing effects (see Table 2.2) are provided in Appendix A to this report.

As noted earlier, initial scoping calculations for the metal tests consistently under-predicted actual spreading lengths (as well as over-predicting substrate ablation), even for relatively low input values for C_R. The underlying reason was the large calculated convective heat transfer losses to the substrate due to the low Prandtl number for these metallic fluids. Based on findings from earlier work,[18,30-32] this shortcoming was addressed by adding the ability to model an interfacial heat transfer resistance between melt and substrate, with the heat transfer resistance is left as a user-defined input constant.

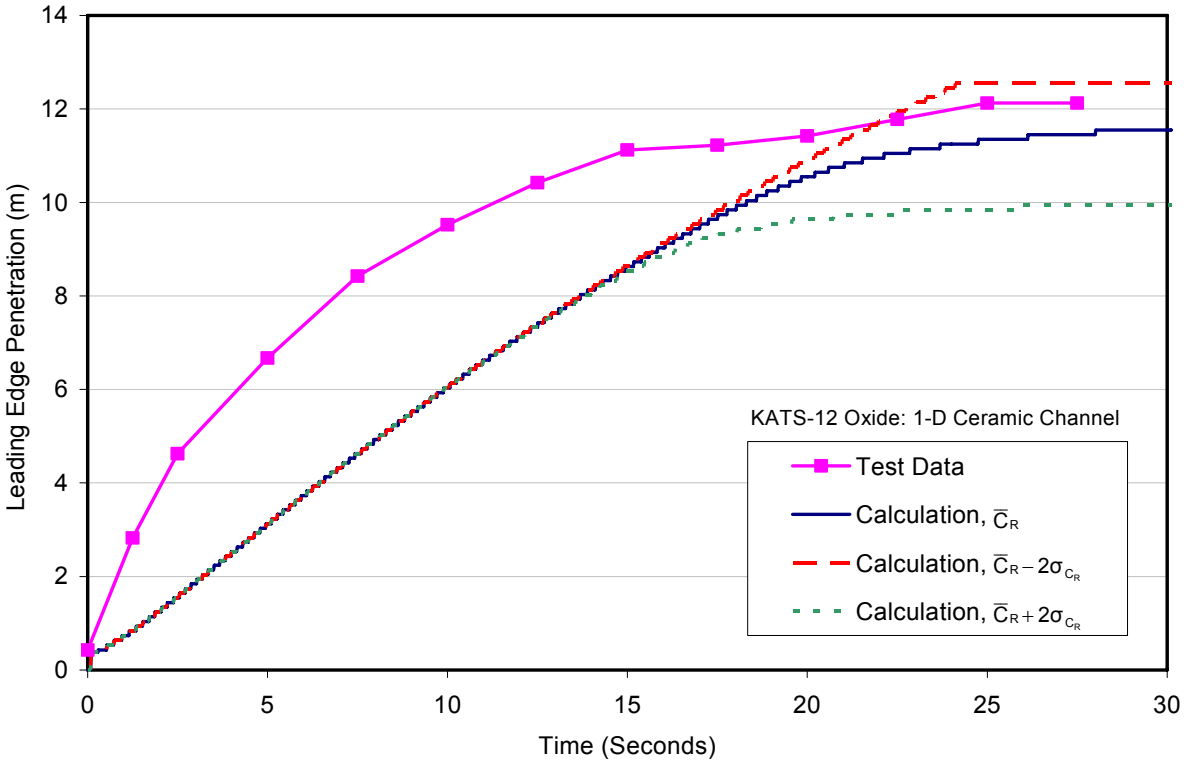

Figure 2.6. Comparison of code predictions of melt leading edge penetration vs. time to the KATS-12[13] oxide simulant spreading test on a ceramic surface for various values of the empirical constant in the Ramacciotti melt viscosity correlation.

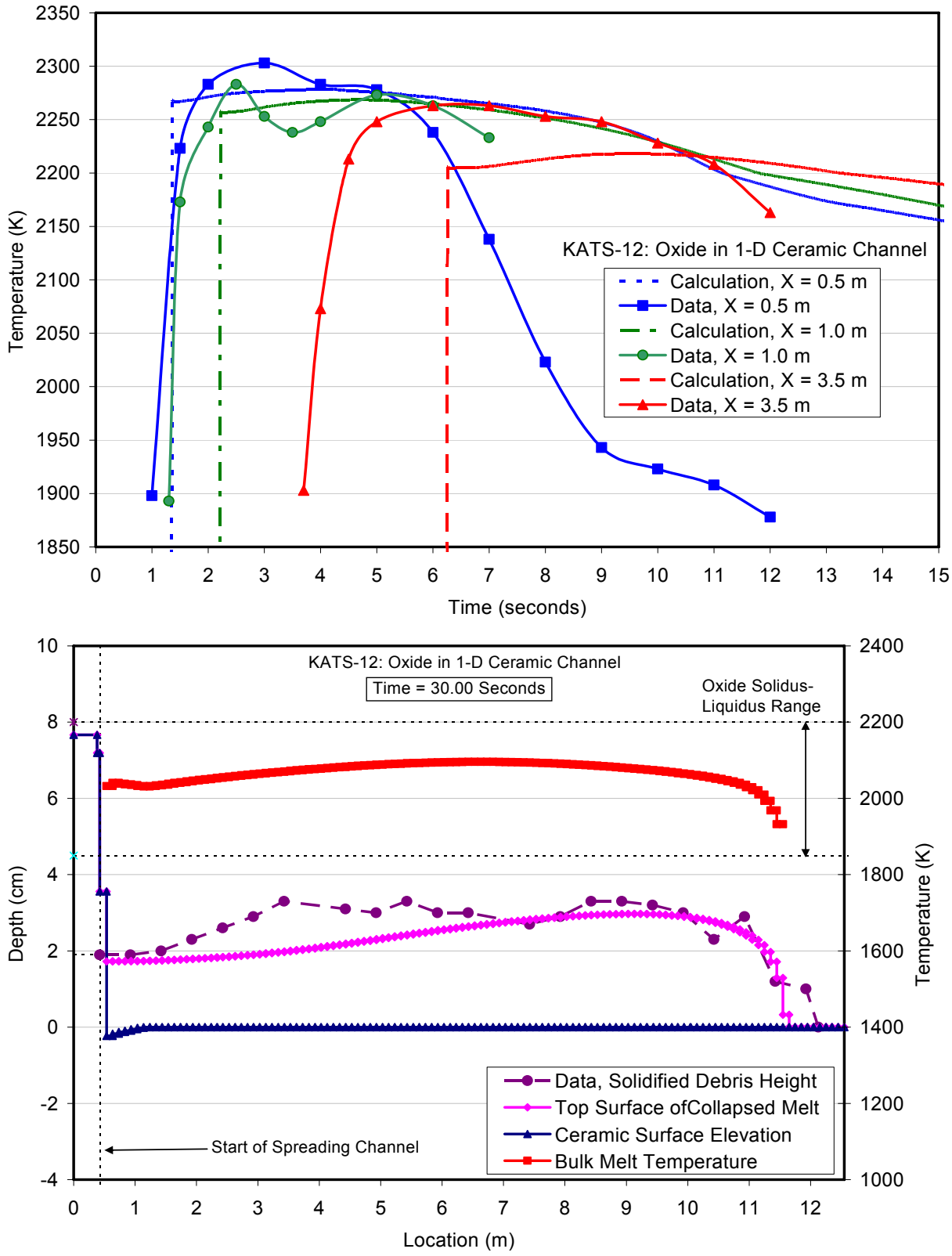

Figure 2.7. Comparisons of local melt temperature and posttest debris profile with test data from the KATS-12[13] oxide simulant spreading test on a ceramic surface.

With this change, the new problem was how to best fit the model to the dataset given the fact that the interfacial heat transfer resistance, h_R, constituted a second independent variable to adjust in the analysis. One significant observation is that steel is a common melt constituent calculated for many LWR accident sequences involving core melting. On this basis, the approach for fitting the model to the steel spreading tests was to fix the value of C_R at the average value for the reactor material tests; i.e., C_R = 7.26. With this assumption, another set of parametric calculations were performed to find the best-fit h_R to match the spreading lengths for the four dry metal spreading tests shown in Table 2.1. The results are shown in Table 2.6. As is evident, three of the four metal spreading tests indicated a best-fit h_R near 5000 W/m^2-K. However, the KATS-13 test was again found to be an outlier, with a much higher h_R of 12,000 W/m^2-K required to match the spreading length for this test. On this basis, KATS-13 was again omitted in the statistical analysis for the heat transfer resistance so that the results are not skewed. With this assumption, the best-fit interface heat transfer resistance is found to be h_R = 4800 W/m^2-K, with a standard deviation of 1020 W/m^2-K. For the reader's information, the best fit h_R with the KATS-13 result included is 6600 W/m^2-K, with a standard deviation of 3240 W/m^2-K.

With these results, the question then arose as to what effect the inclusion of an interface heat transfer resistance would have on the results for the oxide spreading tests. To answer this question, all oxide tests were recalculated with the heat transfer resistance set at the average value of 4800 W/m^2-K to assess the impact on the predicted spreading lengths. For these calculations, C_R in the Ramacciotti correlation was set to the best estimate value for each test (see Tables 2.3 through 2.5). The results are shown in Table 2.7. As is evident, the changes in predicted spreading lengths was not that large; i.e., lengths increased on average by 3.6 %, with the high being 8.6 %. The reason is that the oxides generally have much lower convective heat

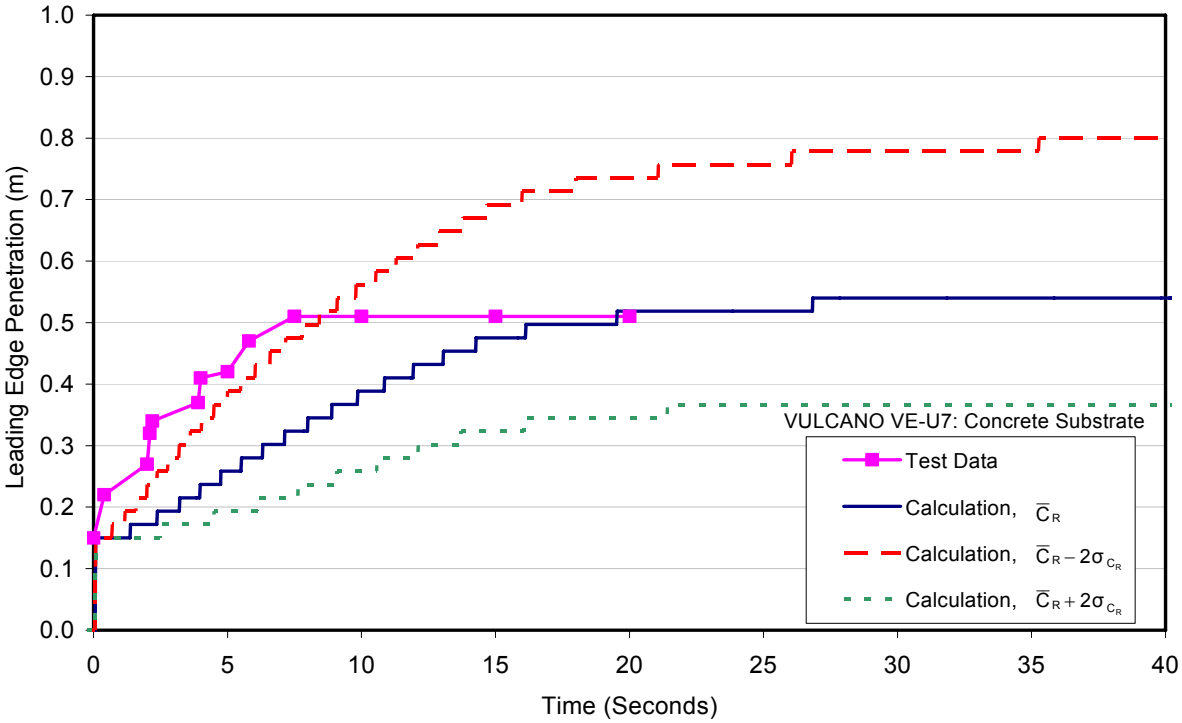

Figure 2.8. Comparison of code predictions of melt leading edge penetration vs. time to the VULCANO VE-U7[17] core oxide spreading test on a concrete surface for various values of the empirical constant in the Ramacciotti melt viscosity correlation.

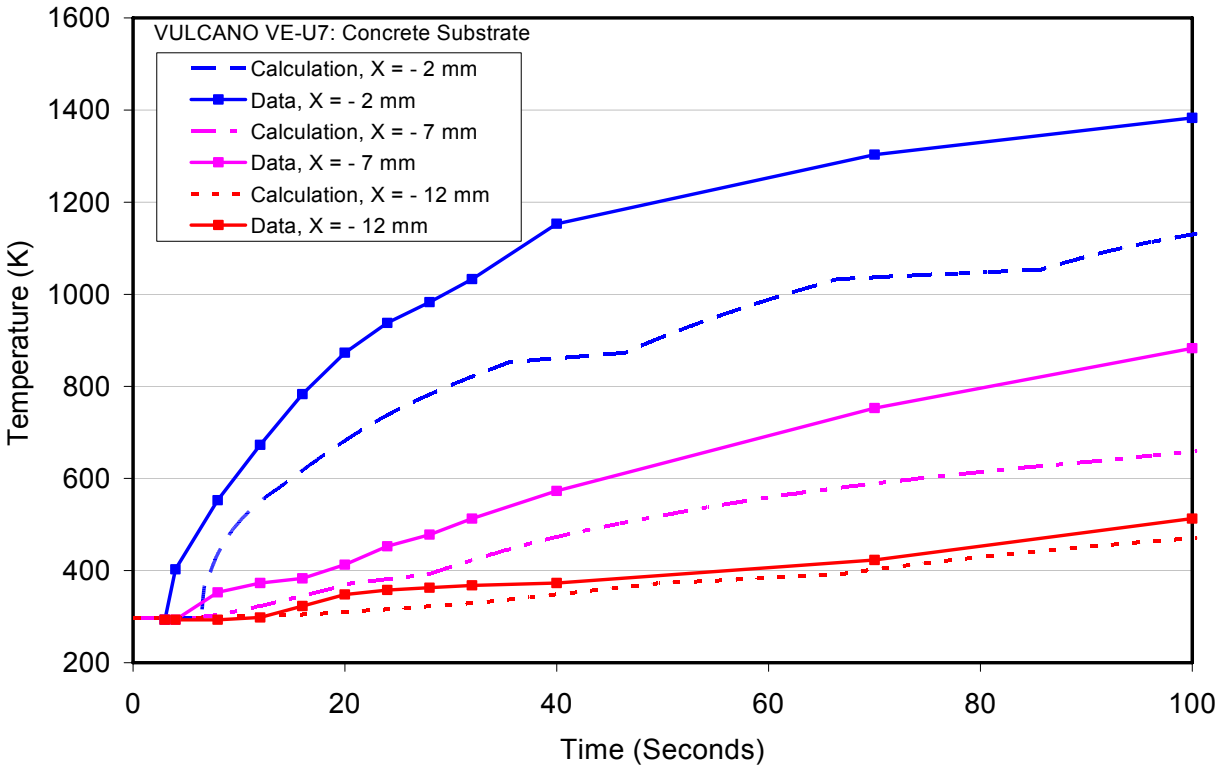

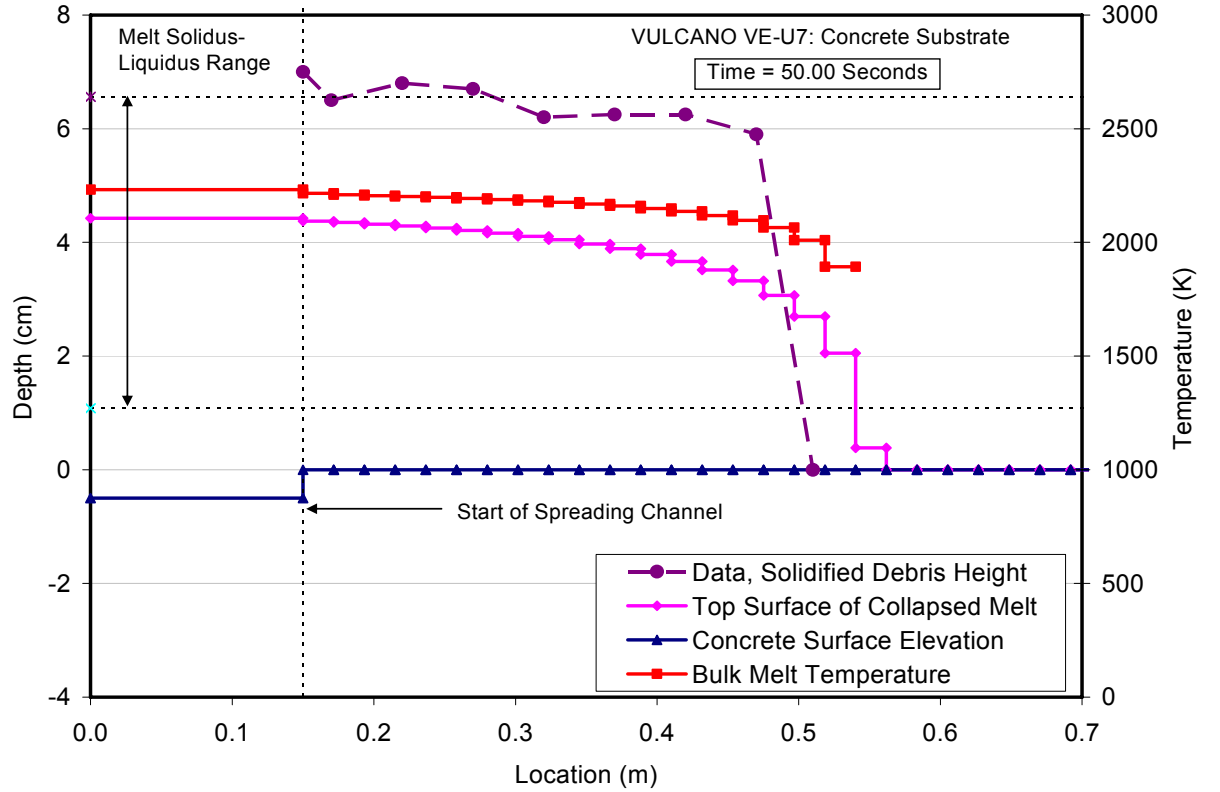

Figure 2.9. Comparisons of substrate temperatures (top) and posttest debris profile (bottom) with test data from the VULCANO VE-U7[17] core oxide spreading test on a concrete surface.

Table 2.6. Average and Standard Deviation Interfacial Heat Transfer Resistances Required to Match Spreading Lengths for Metal Melt Tests with C_R = 7.26.

Test	Melt	Substrate	Best Fit h_c (W/m^2-K)	$\bar{h}_c$ for test class (W/m^2-K)	$\sigma_{\bar{h}_c}$ (W/m^2-K)
KATS-12	Iron	Ceramic	3470	4800 (Omits Kats-13)	1020 (Omits Kats-13)
KATS-13	″	Concrete	12000		
KATS-14	″	Ceramic	5950		
Test 15	SS	″	4980		

Table 2.7. Increase in Spreading Length for Oxide Melt Tests when a Melt-Substrate Interfacial Heat Transfer Resistance of 4800 W/m^2-K is Included in the Analysis.

Test Series	Test	Fluid	Substrate	Cavity Condition	% Increase in Spreading Distance
RIT	3MDC-Ox-1	Oxide simulant	Concrete	Ambient	1.6
	3MDS-Ox-1	″	Steel	″	3.2
	3MDS-Ox-2	″	″	″	2.6
	2MWS-Ox-1	″	″	12 cm H_2O	~ 0[a]
	2MWS-Ox-2	″	″	″	3.3
	2MWS-Ox-3	″	″	″	2.3
KATS	KATS-12	Oxide simulant	Ceramic	Ambient	8.6
	KATS-13	″	Concrete	″	7.5
	KATS-14	″	Ceramic		0.6
ECOKATS	V1	Oxide simulant	Ceramic	″	~ 0[a]
	1	″	Concrete	″	~ 0
COMAS	COMAS-5a	Core oxides + iron	Concrete	″	2.9
		″	Ceramic	″	2.9
		″	Steel	″	2.6
	EU-2b	Core oxides	Concrete	″	6.1
		″	Ceramic	″	5.1
		″	Steel	″	8.1
	EU-4	Core oxides + iron	″	″	6.4
Faro	L-26S	Core oxides	″	″	~ 0
	L-32S	″	″	1 cm H_2O	14.9
Vulcano	EU-7	Core oxides	Concrete	Ambient	~ 0
		″	Ceramic	″	~ 0

[a]When change is ~ 0, this means that differences in spreading distance could not be resolved to within the mesh size.

transfer coefficients (principally due to low thermal conductivity) in comparison to the metals, and so the net change in the combined (convection plus interfacial resistance) heat transfer coefficient is not that much for oxides compared to metals. In any event, with the model fit in this manner, the code should provide reasonable estimates of spreading behavior across the range of potential metal-oxide core melt compositions.

Finally, aside from these various assessment exercises, several code verification studies were also performed to confirm that the numerical methods produced convergent solutions in terms of timestep and spreading domain nodalization. Details of these verification exercises are provided in Appendix B.

3.0 EPR MELT SPREADING ANALYSIS

Given the code assessment results, the final step in the analysis program was to exercise the code to evaluate the extent of spreading in the EPR core catcher design. These results are described in this section. The modeling assumptions for the base case spreading scenario are described first, followed by a presentation of the results for this case. A sensitivity study is then performed to check the assumption of uniform spreading over a wider range of conditions.

3.1 Base Case Modeling Assumptions and Results

The high level modeling assumptions for the EPR base case spreading analysis are summarized in Table 3.1, while a detailed description of the model input is provided in Table 3-2. The model was constructed based on information principally provided by Fischer and Henning[1] and Fischer.[37] In terms of geometry, the meshing mocks up the configuration shown in Figure 1.1 to the greatest extent possible. The spreading domain consists of a one-dimensional spreading channel that is 7.25 m long, issuing into a spreading room that is modeled as a 180º sector with an area of ~ 170 m^2. There appears to be discrepancies between References 1 and 37 as to whether or not the spreading channel has any inclination. In Reference 37, the channel is shown with an incline that is estimated to be 1.75º with respect to the horizontal, whereas in Reference 1 the channel is shown as essentially horizontal. Thus, for the base case, the channel is treated as inclined at 1.75º and the case of a horizontal channel is addressed in the sensitivity study provided in the next section. The step down between the 1-D channel and spreading room shown in Figure 1.1 is also modeled. The substrate in the channel is specified to be refractory ceramic, while the substrate in the spreading room is modeled as sacrificial concrete.

Table 3.1. Summary of Base Case Modeling Assumptions for Melt Pour Scenario.

Model Input	Base Case	Note(s)
Melt pour mass	400 MT	Full core mass
Melt composition	65.9 % oxide, 34.1 % steel	-
Melt pour duration	6.67 MT/sec	"Low flow" case
Pour condition	Homogeneous	Homogeneous metal - oxide mixture
Melt pour temperature	2270 K	100 K below oxide phase liquidus
Cavity condition	Dry	-
C_R in viscosity correlation	7.26	Based on curve fit to reactor material melt spreading database
Spreading Channel Angle	1.75º	-

In terms of pour conditions, the case considered here assumes essentially a whole core release of 400 MT melt mass through the melt gate at a steady pour rate over a time period of 1.0 minute. This is reported to be a 'low flow' case, corresponding to the opening of only ~ 1/8 of the melt gate surface area,[37] and therefore conservative in terms of assessing ultimate melt penetration in the spreading room. The melt composition is assumed to consist of 66 wt% oxide and 34 wt% metal phases that are uniformly mixed for the base case. The initial melt temperature is conservatively set at 100 K below the reported oxide liquidus of ~ 2370 K. The decay heat level in the debris is taken as 412 W/kg fuel.

Table 3.2. Input File Summary for the EPR Base Case Melt Spreading Scenario.

Parameter	Value
Melt composition (wt %)	32.0 UO_2, 7.5 ZrO_2, 24.7 Fe, 5.8 Cr, 3.6 Ni, 26.4 concrete slag
Melt delivery	Steady pour of 400,000 melt mass at 6667 kg/sec through the gate for a period of 60 seconds.
Melt temperature	2270 K
Total pour mass	400,000 kg
Decay heat level	412 W/kg fuel
Substrate material	Spreading channel: zirconia. Spreading room: sacrificial concrete
Spreading geometry	The system consists of a 7.25 m long spreading channel (including the gate area) at an inclination of 1.75º. The channel discharges into the spreading room that is 18.2 m wide by 11.6 m long, and area of 170 m^2. The spreading room floor is 1.01 m below the channel exit. A step is present just outside the channel exit, and is 67 cm below the exit.

Code input parameter(s)	Value(s)
Melt composition (wt %)	32.0 UO_2, 7.5 ZrO_2, 24.7 Fe, 5.8 Cr, 3.6 Ni, 26.4 concrete slag
Melt pour temperature	2270 K
Melt oxide phase solidus – liquidus	1270 K – 2370 K
Melt metal phase solidus – liquidus	1671 K – 1727 K
Melt pour rate and duration	The melt is discharged through a gate located at the bottom of the reactor pit into a single node cell that has a surface area equal to that of the gate; i.e., 2.4 m^2. The cell width is set equal to the channel width of 1.2 m. The length is thus set to 2.0 m to conserve the gate area. The 400 MT melt mass is assumed to drain at a steady rate of 6667 kg/sec through the gate for a period of 60 seconds.
Decay heat level	412 W/kg fuel
Melt material property evaluation	Code subroutines
Substrate composition	Spreading channel: zirconia Spreading room sacrificial concrete: 2.42 CO_2, 5.02 H_2O, 71.7 SiO_2, 13.96 CaO, 0.33 MgO, 4.87 Al_2O_3, 1.7 Fe_2O_3
Substrate initial temperature	300 K
Substrate material properties evaluation[a]	Zirconia: user-specified material properties evaluation; i.e., $c_s = c_l =$ 575 J/kg-K, $\Delta h_f =$ 0.706 MJ/kg, $\rho_s = \rho_l =$ 5300 kg/m^3, $k_s = k_l =$ 4.7 W/m-K, and $\varepsilon = 0.3$ Sacrificial concrete: Code subroutines
Substrate solidus - liquidus temperatures	Zirconia: 1780 K – 2900 K Sacrificial concrete: 1353 – 1703 K
Substrate nodalization	At each substrate nodal location: six 5 mm cells, then five 10 mm cells, and then six 20 mm cells. All nodes cell-centered.
Spreading cavity nodalization	Spreading channel gate: modeled with a single 1.2 m wide by 2.0 m long cell. Balance of spreading channel: modeled using 100 cells; each was 5.25 cm long and 1.2 wide. The channel was inclined at an angle of 1.75º. Spreading room: modeled as a 180º sector with 100 cells; each had a radial length of 9.9 cm (total floor area is 170 m^2). Step in the spreading room also modeled; the elevation was 67 cm below the channel exit, and tapered down to the spreading room floor which was at 1.01 m below the exit. All nodes cell-centered.
Cavity condition	Dry
Upper atmosphere temperature	300 K
Upper atmosphere emissivity	0.3
Ambient pressure	0.1 MPa
Melt/substrate heat transfer coefficient model	Dittus - Boelter
Melt/substrate interfacial heat transfer resistance	Not modeled
Constant in Ramacciotti correlation	7.26
Solid-fraction variation between liquidus/solidus	Same as COMAS melt composition; see Figure 2.3.
Timestep	0.02 seconds

[a]Here, c denotes specific heat, Δh_f is latent heat of fusion, ρ is density, k is thermal conductivity, ε is emissivity, and subscripts s and l denote solid and liquid phases, respectively.

As discussed in Section 2.0, one of the key aspects of the code assessment was to adjust the empirical constant C_R in the Ramacciotti viscosity correlation (Eq. 2.1) so that the code best fit the data in terms of matching melt spreading length. This included a simple statistical analysis to determine the standard deviation in the fit based on the data comparisons For the base case scenario, C_R is set at the average value of 7.26 which is based on the curve fit to the reactor material melt spreading database; see Table 2.3. The statistical variation (range) in the curve fit for C_R is addressed as part of the sensitivity study. Of equal importance to the selection of C_R is the choice of the solid fraction function within the freezing range. In this analysis, the function is set equal to that used for the COMAS[20-21] spreading test cases (see Figure 2.3), since this composition is similar to that expected for the EPR under ex-vessel accident conditions.

Aside from viscosity modeling, the melt-substrate heat transfer coefficient was modeled with the classical Dittus-Boelter correlation. For the base case, additional interfacial heat transfer resistance at the substrate surface was not modeled. Heat transfer upwards was modeled assuming radiation to overlying structure. As is evident from Figure 1.1, this structure is predominately concrete, and on this basis, the structure emissivity was set at 0.3. The boundary temperature was maintained at 300 K over the calculation which is unrealistic, but also conservative in terms of predicting minimum melt penetration within the core catcher.

Before proceeding with the analysis, a few verification calculations were performed with the input file to verify that the meshing and timestep choices were adequate to achieve a converged solution. The results are shown in Figure 3.1, which provides the predicted melt leading edge location in the system versus time. This data indicates that a 20 ms timestep is sufficient to achieve temporal convergence, and that the 200 node meshing scheme is adequate

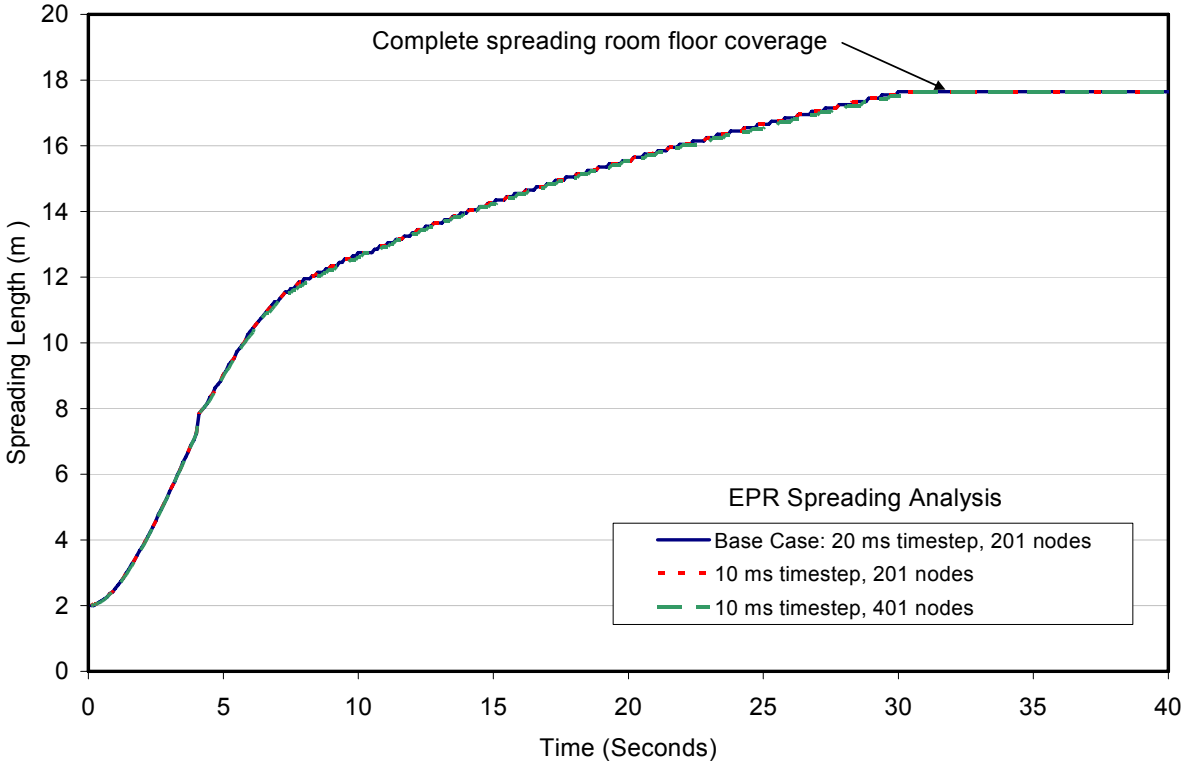

Figure 3.1. Verification calculations for EPR base case spreading calculation.

to achieve spatial convergence. For the case in which the number of mesh cells was doubled (i.e., cell sizes reduced by a factor of two), the timestep had to be reduced to 10 ms in order to satisfy the Courant condition due to the high predicted spreading velocities in the channel.

With this background, the calculated melt depth and temperature profiles for the base case are shown in Figure 3.2 at 10, 30, 60, and 240 seconds after pour initiation. The calculated behavior is a steady melt progression down the 1-D spreading channel and accumulation in the spreading chamber. After 30 seconds, the melt front has reached the back of the spreading chamber. After four minutes, the melt has essentially spread to a uniform depth of ~ 50 cm in the spreading room, with a thin (~ 10 cm) layer of cooler, viscous corium remaining in the channel that continues to slowly drain towards the room. In terms of substrate heatup and attack by the spreading corium, a few millimeters of sacrificial concrete are calculated to be eroded from the surface of the step-down just outside the spreading channel exit to the spreading room. However, substrate erosion during the spreading transient is limited to this particular area.

3.2 Sensitivity Study

Given the base case results, a sensitivity study was then performed to check the assumption of uniform spreading over a wider range of conditions. These parametric variations are summarized in Table 3.3. The variations that are addressed include melt pour mass, composition, temperature, and duration (viz. pour rate). In addition, a calculation was performed to examine the assumption of a well-mixed metal-oxide system (base case), versus a stratified system in which the metal is beneath the oxide at the time of gate opening and thus the metal phase drains first into the channel, followed by the oxide phase.

Table 3.3. Parametric Variations for Sensitivity Study.

Parameter	Base Case	Parametric(s)
Melt pour mass	400 MT (full core)	1) 300 MT 2) 200 MT 3) 100 MT
Melt composition	65.9 % oxide, 34.1 % steel	1) 84 % oxide, 17 % steel; 2) 100 % oxide
Melt pour duration	60 sec	1) 120 sec 2) 240 sec 3) 360 sec
Pour condition	Uniform metal – oxide mixture	Metal phase drains first, followed by oxide
Melt pour temperature	2270 K (100 K below liquidus)	1) Inviscid, adiabatic 2) 2370 K (at liquidus) 3) 2170 K (200 K below liquidus)
Cavity condition	Dry	Wet
Spreading channel angle	1.75º	Spreading angle = 0º (horizontal)
C_R in viscosity correlation	Best estimate	1) C_R plus two sigma 2) C_R minus two sigma

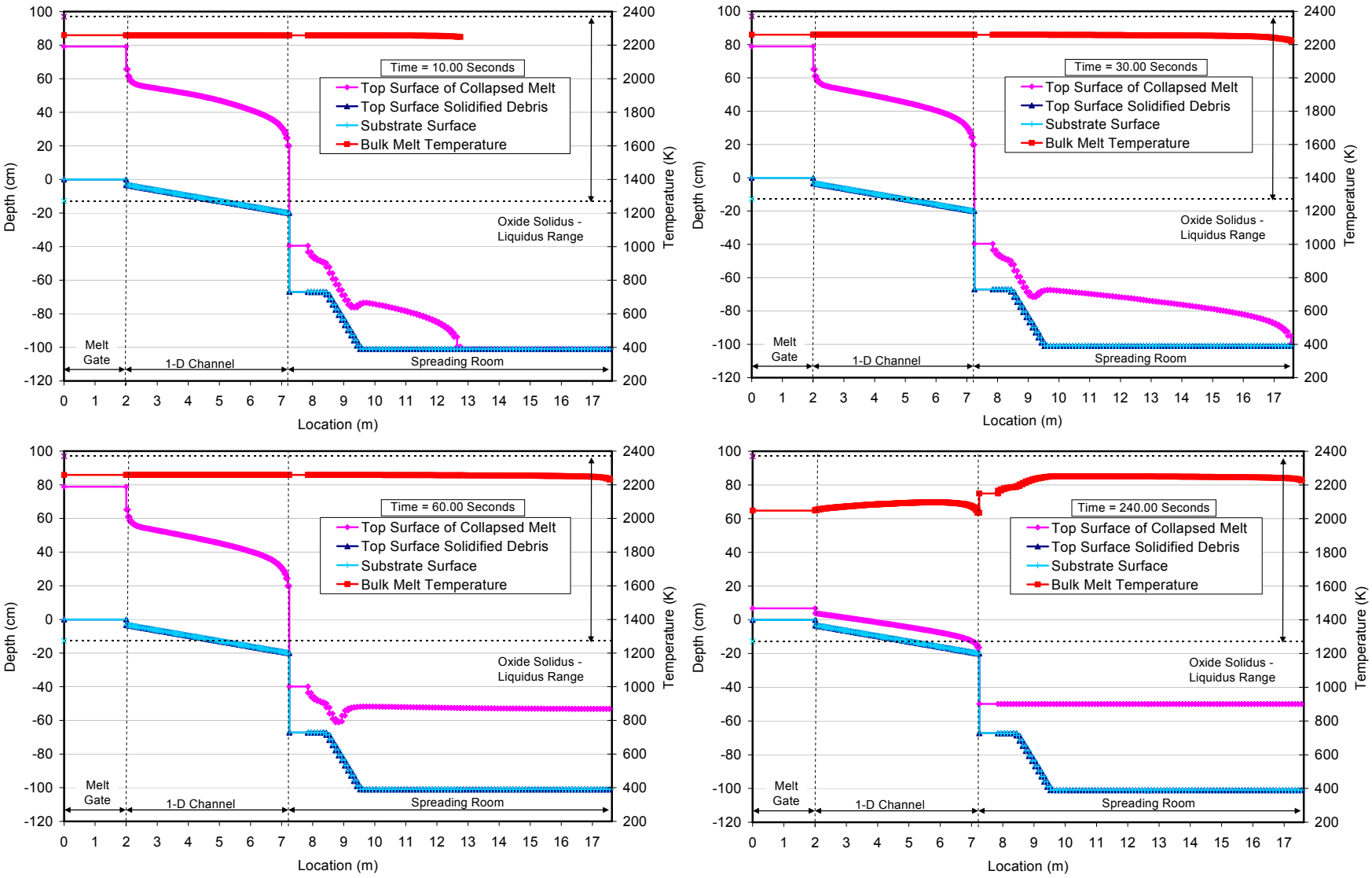

Figure 3.2. Melt depth and temperature profiles at 10, 30, 60, and 240 seconds for EPR base case melt spreading scenario.

Aside from melt pour characteristics, one calculation was performed to examine the influence of water present in the cavity as a pre-existing condition during the spreading transient. Also, it is not clear what the spreading channel inclination angle will be in the final plant design, and so a calculation was performed assuming a horizontal channel geometry to evaluate the affect of channel inclination on spreading behavior.

The final set of parametric calculations considers statistical variations in the constant C_R in the Ramacciotti viscosity correlation (Eq. 2.1). In particular, relying on the results of the reactor material melt spreading test analyses (see Table 2.3), a 2σ uncertainty band translates into a range of 7.26 ± 1.90 on C_R which, in theory, captures uncertainties related to code predictions of maximum melt penetration for the reactor material database to within a 95% confidence level.

The results of the sensitivity study are presented in the order they are described in Table 3.3. The first case considers the effect of melt pour mass on the rate of leading edge propagation in the core catcher. The results are shown in Figure 3.3. In order to isolate the effect of pour mass on the spreading characteristics, the melt pour rate was fixed at the base case value of 6667 kg/sec (see Table 3.2) for all these cases. Thus, the duration of the melt pour decreases linearly from 60 seconds for the base case down to 15 seconds for the lowest pour mass case of 100 MT. As is evident, leading edge penetration is not influenced by pour mass except for the lowest mass case of 100 MT. This is due to the fact that the time for the melt to completely cover the floor in the spreading room is nominally 30 seconds, and only for the 100 MT case does the pour duration fall below this time. Thus, in this case the upstream hydraulics begin to influence the

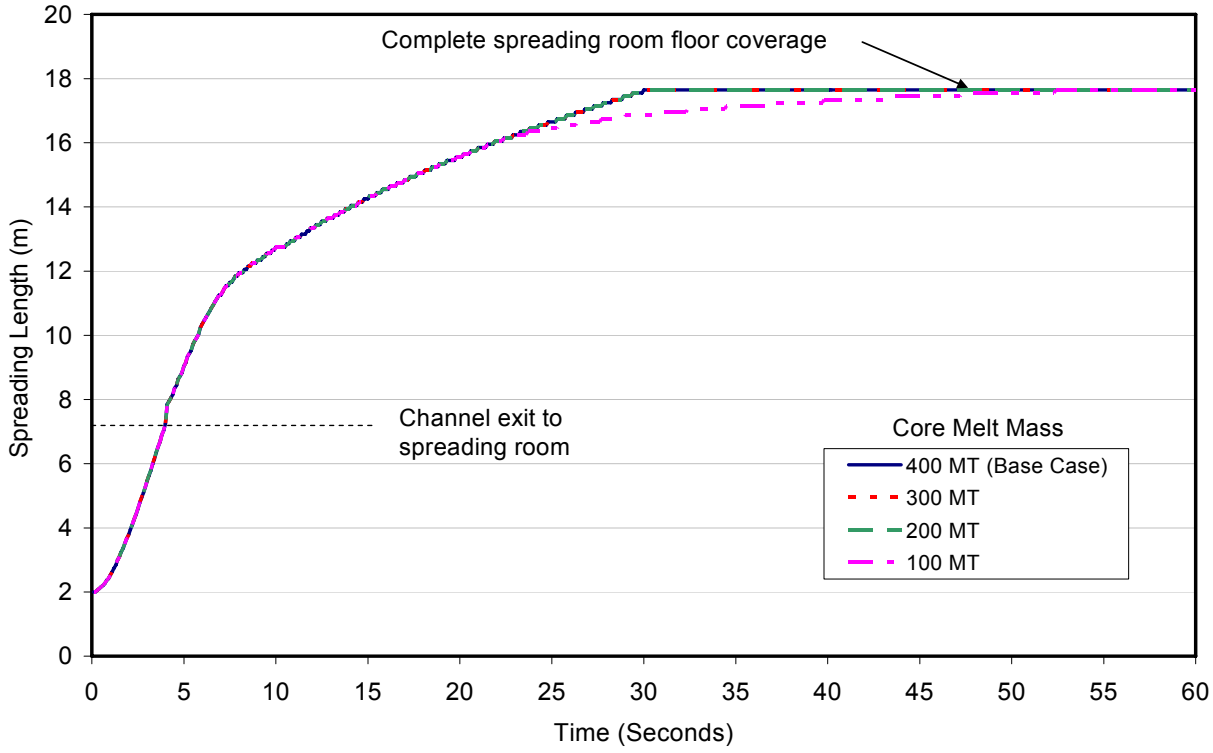

Figure 3.3. The influence of melt pour mass on spreading behavior in the EPR core catcher.

leading edge propagation, resulting in a reduced spreading velocity late in the transient. However, in all four cases the melt eventually spread to a uniform depth in the spreading room. In addition, substrate erosion for all cases was consistent with that calculated for the base case (i.e., a few millimeters are eroded from the step down just outside the channel exit). Thus, it is concluded that melt pour mass has a weak influence on spreading behavior in the core catcher.

The second parametric case considers the influence of metal content (structural steel) on spreading behavior. The results are shown in Figure 3.4. In order to isolate the effect of composition, the melt pour mass, pour rate, and compositions of the oxide and metal phases were fixed at the base case values (see Table 3.2), while the metal and oxide fractions were varied within the range shown on the graph. In reality, as the metal oxidizes, the overall melt mass would increase slightly as additional oxygen is brought into the system, and the composition of the oxide phase would change as steel oxidation byproducts are incorporated. However, the compositions shown in Figure 3.4 could just as easily be achieved by varying fractions of core and structural steel melting and relocating into the reactor pit during the in-vessel stage of the accident sequence, and so it is not clear that more detailed evaluation is warranted as part of this parametric study.

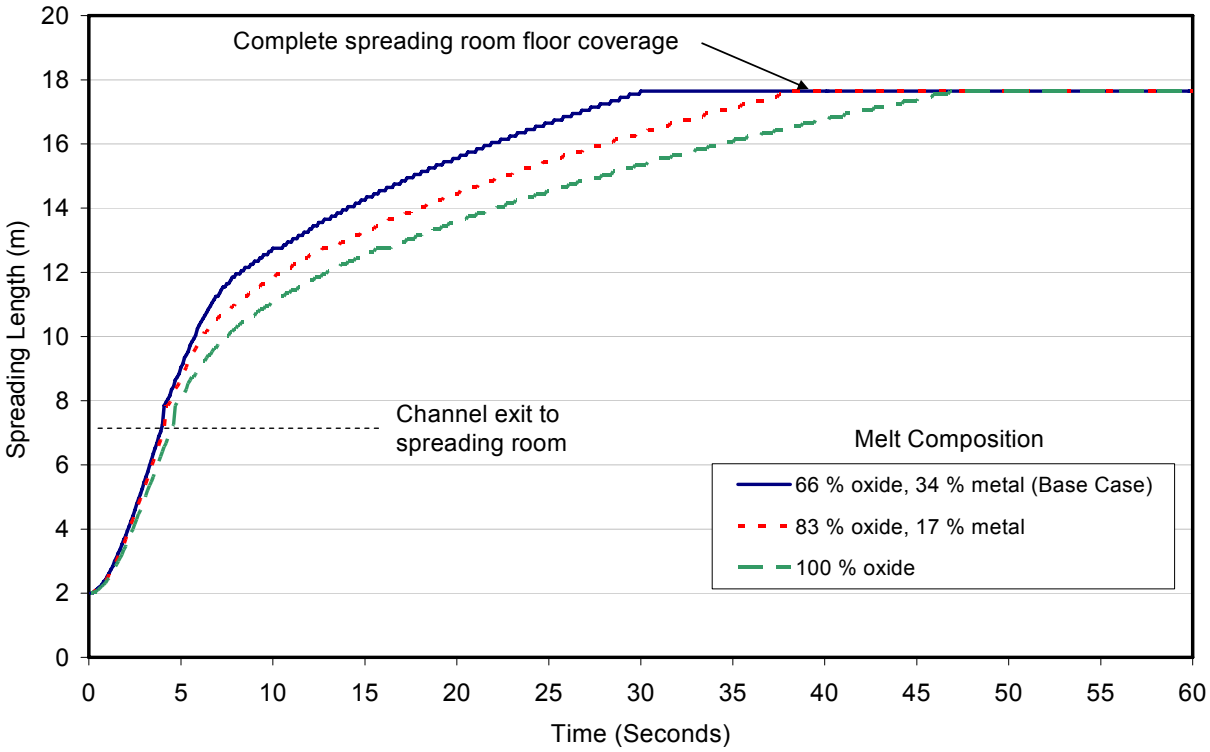

Figure 3.4. The influence of melt composition (metal-oxide fraction) on spreading behavior in the EPR core catcher.

With these assumptions, the data in Figure 3.4 indicate that the melt spreading rate increases with the amount of metal present in the melt, but in the range of compositions considered a uniform melt distribution in the spreading room is still achieved. The spreading velocity decreases as metal content is reduced due to the fact that the metal phase is highly superheated (by ~ 540 K) at the melt pour temperature of 2270 K (stainless steel liquidus

temperature is 1727 K). Thus, overall melt fluidity decreases (i.e., viscosity increases) as metal content is reduced for a well mixed system. In addition, no substrate ablation was calculated to occur for the 83 and 100 % oxide cases, which is again attributable to the fact that the melt becomes more viscous as metal content is decreased. Thus, it is concluded that reduction in metal content reduces spreading velocity, but does not alter the fact that the melt eventually spreads to a uniform thickness in the core catcher.

The third parametric case considers the influence of melt pour rate on spreading behavior. The results are shown in Figure 3.5. In order to isolate the effect of pour rate, the melt composition and pour mass were fixed at the base case values (see Table 3.2), but the pour rates were linearly reduced over the increased pour durations shown in Figure 3.5. As is evident, the spreading velocity systematically decreases with pour rate, but in all cases uniform spreading is achieved in the spreading room at the end of the transients. A small amount of erosion of the step just outside the channel exit was calculated for all three cases. At three minutes after the pour ends, the peak erosion depth systematically increased from 1.8 mm for the base case to 6.6 mm for the 6 minute pour case. However, the floor area that undergoes erosion decreases with increasing pour duration. Note here that the increase in erosion depth with decreasing pour rate is due to the fact that these depths are all reported at 3 minutes after pour termination, which means that the larger erosion depths occur over longer times. With the reduction in pour rate, local erosion velocities decrease due to local reductions in the calculated convective heat transfer coefficients. Based on these results, it is concluded that reduction in pour rate reduces spreading velocity, but this does not change the fact that the melt eventually spreads to a uniform thickness in the core catcher over the range of pour rates considered.

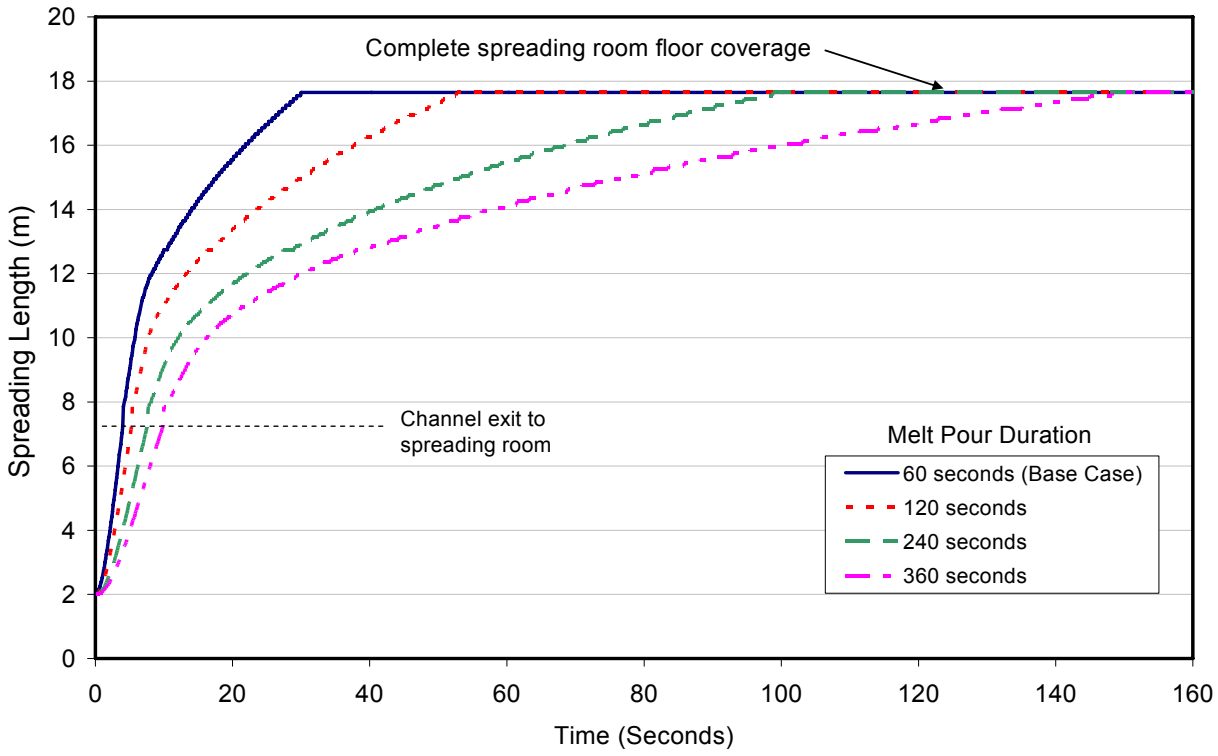

Figure 3.5. The influence of melt pour duration (pour rate) on spreading behavior in the EPR core catcher.

The fourth parametric case examines the assumption of a well-mixed metal-oxide pour condition on the spreading behavior. In particular, the stainless steel phase is more dense in comparison to the oxide (i.e., the liquid densities are calculated as 6940 and 3990 kg/m^3 for these two phases, respectively), and is also not miscible in the oxide. Thus, for low gas sparging rates in the reactor pit during core-concrete interaction, the two phases could easily stratify into a system with the metal on the bottom and the oxide on top. This in turn would lead to two distinct pour streams at the time of gate failure; i.e., the first stream would consist of core structural steel, and the second would be the core oxides mixed with oxides of structural steel and concrete oxides.

A case was constructed to investigate this scenario. In particular, the overall melt pour composition, temperature, and volumetric flowrate were kept the same as the base case (see Table 3.2). However, the code input was set up so that the 136.4 metric tones of structural steel present in the melt drained first, followed by the 263.6 metric tones of oxide. The flows were partitioned to conserve the volumetric flowrate over the 1 minute pour duration. Thus, the metal (22.9 vol %) was assumed to discharge at a rate of 9927 kg/sec over a period of 13.74 seconds, with the oxide (77.1 vol %) following at a rate of 5698 kg/sec over a period of 46.26 seconds. The temperature of both melt pour streams was taken equal to the base case value of 2270 K. This may be the most questionable assumption in this part of the analysis. In particular, when a stratified system develops, it is not clear that the temperature of these two zones will remain the same. However, evaluating these temperatures in a stratified configuration to determine the correct initial conditions for the spreading analysis requires application of a sophisticated core-concrete interaction tool such as the CORCON module within MELCOR. This analysis is beyond the current scope of work, and in lieu of better data, the temperatures of both the metal and oxide phases are set at 2270 K, with the caveat that the metal phase temperature may well be unrealistically high.

The final note regarding modeling for this case is that since a distinct metal spreading transient occurs first, the user-option of applying a melt-substrate interfacial heat transfer resistance is invoked. Recall from Section 2 that a heat transfer resistance had to be added in order to adequately fit the model to the metal melt spreading tests. For the current application, the heat transfer resistance is set to the value that best-fit the test data; i.e., h_r = 4800 W/m^2-K. As further noted in Section 2, inclusion of this resistance had little effect on the predicted spreading behavior for oxide melts since the low convective heat transfer coefficients that are typically calculated for these materials controls heat losses to the underlying substrate. Thus, with the model applied in this manner, reasonable estimates of the spreading behavior for both metal and oxide phase pour streams is expected.

With these assumptions, the data in Figure 3.6 indicates that the initial spreading rate for the superheated metal phase is very rapid, nearly matching the inviscid and adiabatic solution that has also been calculated for this case. It is noteworthy that in the ECOKATS-2 experiment[15] that involved a similar stratified pour configuration, an early very rapid metal (iron) melt spreading transient was observed, followed by a slower progression of the oxide phase. To further illustrate the results, the calculated melt depth and temperature profiles are shown in Figure 3.7 at 10, 20, 30, and 120 seconds after pour initiation. During the metal pour phase, the calculated behavior somewhat resembles a tidal wave effect in which the fluid accelerates down the 1-D channel, and then forms a blunt leading edge as the material expands out into the

spreading room. Subsequently, the oxide pour begins and the calculated mixing distribution of the two phases can be seen in the figure. These plots reveal a computational strength of the code, as well as a weakness. The strength is that complicated flow configurations can be addressed in which distinct metal and oxide pours occur. However, as illustrated by the plot at 120 seconds that is shown in Figure 3.7, the weakness is that the code does not properly handle the fluid mechanics later in the spreading transient when the stratified melt layers, behaving as two interacting gravity currents, would gradually relocate into a well defined oxide-over metal pool configuration. This is due to the fact that the two phases are assumed to be intermixed during spreading and so they relocate with the same velocity through the mesh. A more thorough analysis would treat the two distinct gravity currents with heat and mass transfer between them. However, this would be a major modeling change to the code which lies beyond the current scope of work.

Aside from the flow analysis, the code calculates substantially more substrate ablation for this stratified situation relative to the base case. In particular, roughly 3 mm of the refractory liner in the 1-D spreading channel is calculated to be eroded, while approximately 10 mm of sacrificial concrete is eroded in the spreading room, with the amount of erosion tapering off as the outer wall is approached.

Given these overall results, it is concluded that if a stratified melt configuration exists at the time of gate failure, this will not prevent the melt from spreading to a uniform thickness in the core catcher.

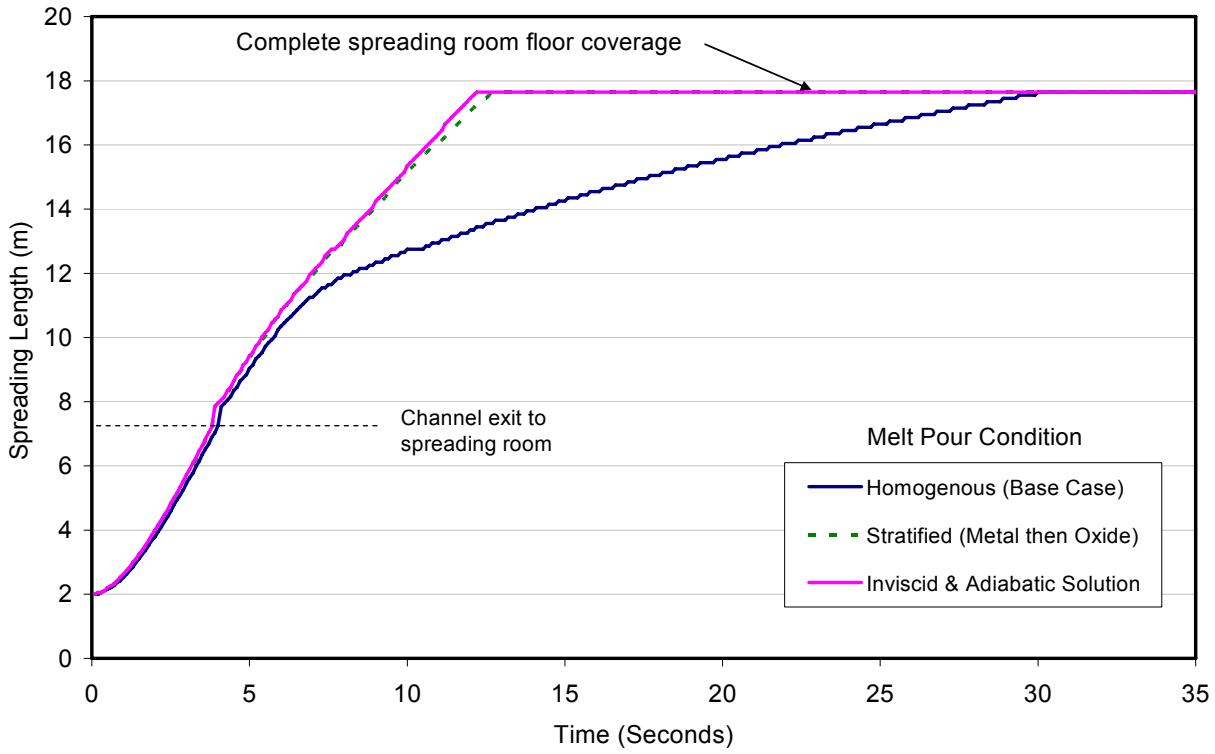

Figure 3.6. The influence of melt stratification (oxide over metal vs. homogeneous mixture) on spreading behavior in the EPR core catcher.

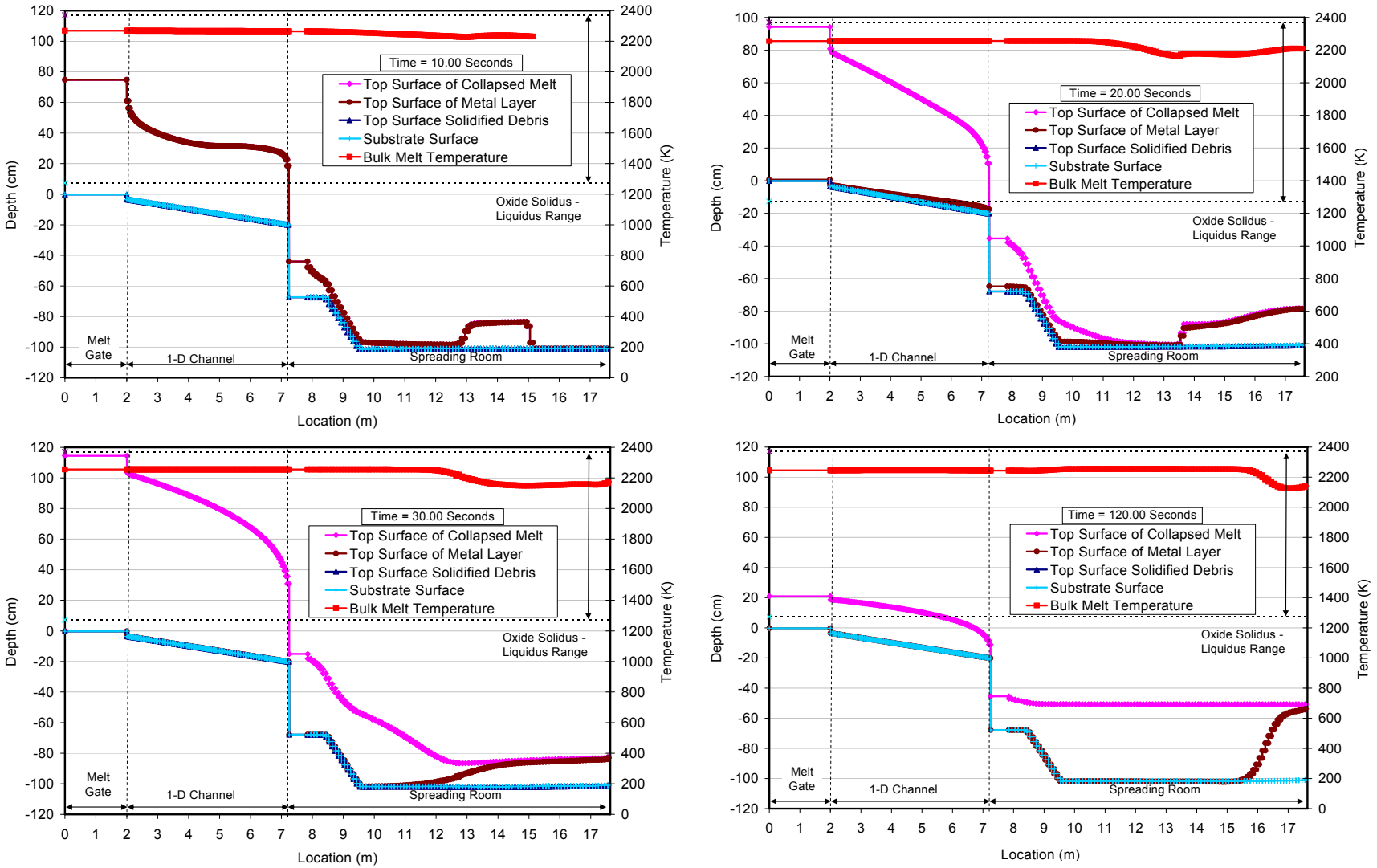

Figure 3.7. Melt depth and temperature profiles at 10, 20, 30, and 120 seconds for the case in which the metal phase is discharged first into the spreading chamber, followed by the oxide phase.

The fifth parametric case considers the influence of melt pour temperature on spreading behavior. The results are shown in Figure 3.8. For this situation, melt composition and pour rate were fixed at the base case values (see Table 3.2), and the pour temperatures were simply changed to the values shown in the figure. As is evident, the spreading velocity systematically decreases with melt temperature, but in all cases a uniform melt depth was eventually achieved in the spreading room at the end of the transients. As one may expect, the case in which the initial melt temperature is at the oxide phase liquidus approaches the inviscid, adiabatic solution.

For this case, calculated substrate erosion was found to be a strong function of melt temperature. For the 2170 K temperature case (viz. 200 K below the oxide liquidus), no substrate ablation is predicted after four minutes. However, for the 2370 K case, substantial erosion occurs; i.e., up to 9 mm of the refractory ceramic in the spreading channel is eroded (peaking just at the channel exit), while up to 5 cm of sacrificial concrete is eroded in the first ½ of the spreading chamber. No erosion occurs in the back ½ of the chamber near the back wall.

Based on these results, it is concluded that the melt will uniformly spread in the core catcher for melt temperatures as low as 200 K below the oxide phase liquidus, which is the range that has been addressed in this study.

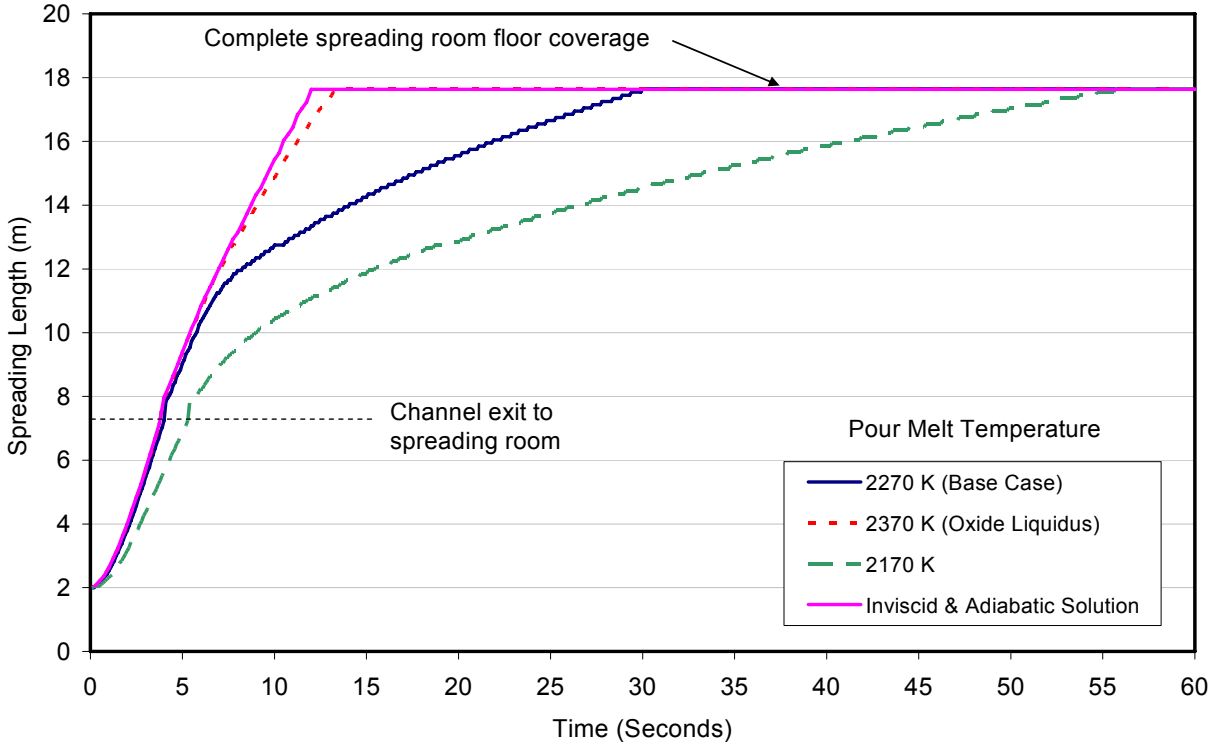

Figure 3.8. The influence of melt temperature on spreading behavior in the EPR core catcher.

The sixth case addresses the situation in which water is present in the core catcher as an initial condition. Here, the containment pressure is taken as 4 Bar, and the water temperature is assumed to be at saturation (viz. 417 K at 4 Bar). The leading edge penetration is compared to the base case solution in Figure 3.9. As is evident, the presence of water reduces the spreading rate, but only slightly. The reduction is due to the increased heat transfer rate to overlying water,

which in turn causes melt viscosity to increase, but the change is minimal due to the large mass pour rate (and corresponding energy transfer rate) for the scenario under consideration. Thus, the increase in upwards heat transfer only has a modest effect on spreading velocity.

The seventh parametric case addresses the affect of spreading channel inclination angle on the spreading behavior. As discussed earlier, there are discrepancies in the literature as to whether the spreading channel is inclined, and the base case assumes an inclination angle of 1.75º. The parametric case treats the channel as horizontal. The two results are compared in Figure 3.10. As is evident, inclination angle has a very weak effect on the spreading behavior, at least in the range of 0 - 1.75º. In addition, calculated substrate erosion between the two cases is virtually indistinguishable.

The eighth and final parametric case considers the statistics that were developed for the empirical constant C_R in the Ramacciotti viscosity correlation (Eq. 2.1) so that the code best fit the reactor material melt spreading database in terms of matching spreading length. The leading edge penetration for the best estimate value of C_R = 7.26, along with the ±2σ cases, are plotted in Figure 3.11, along with the inviscid flow solution for comparison. (Refer to Figure 2.5 for an indication of the relative effect of the ±2σ variation in C_R on the viscosity enhancement during spreading). In all three cases, the melt is predicted to cover the entire spreading room floor area, the only question is the rate at which spreading occurs. The - 2σ case is very similar to the invisicid case, except for the last few meters of the initial spreading transient. Conversely, melt viscosity plays an important role in determining the spreading rate over the entire transient for

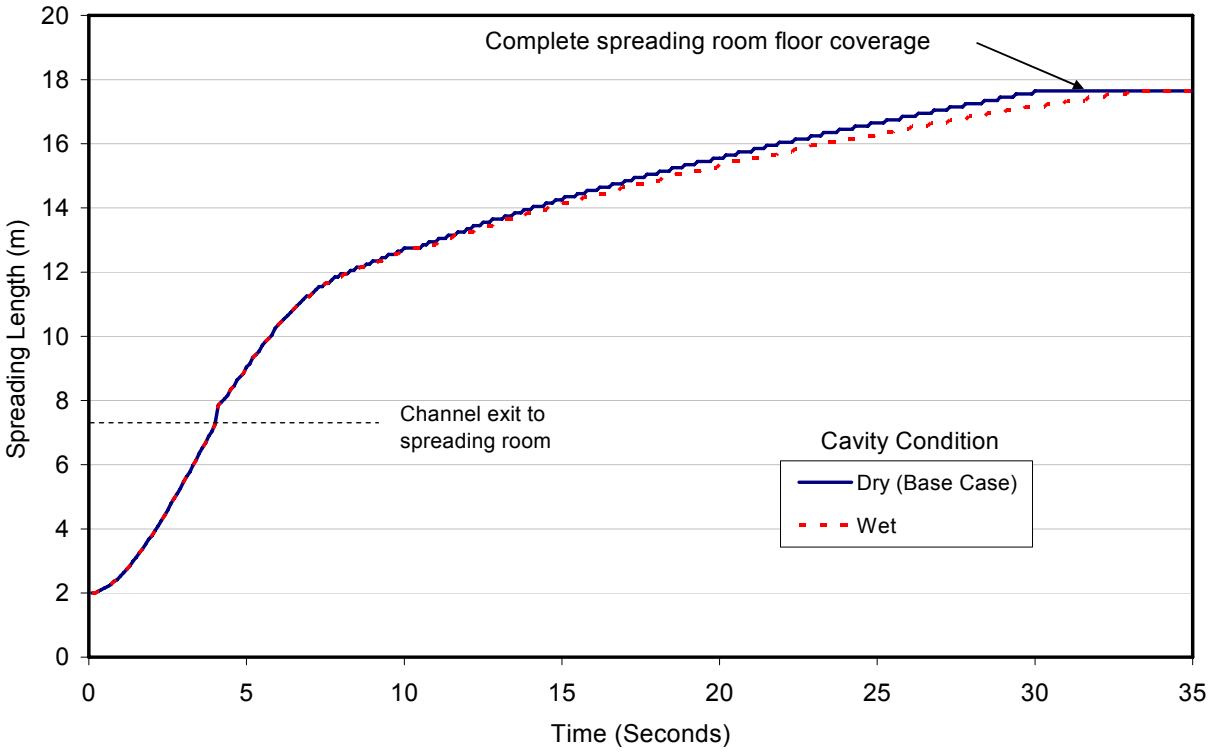

Figure 3.9. The influence of cavity condition (flooded vs. dry) at the time of gate failure on spreading behavior in the EPR core catcher.

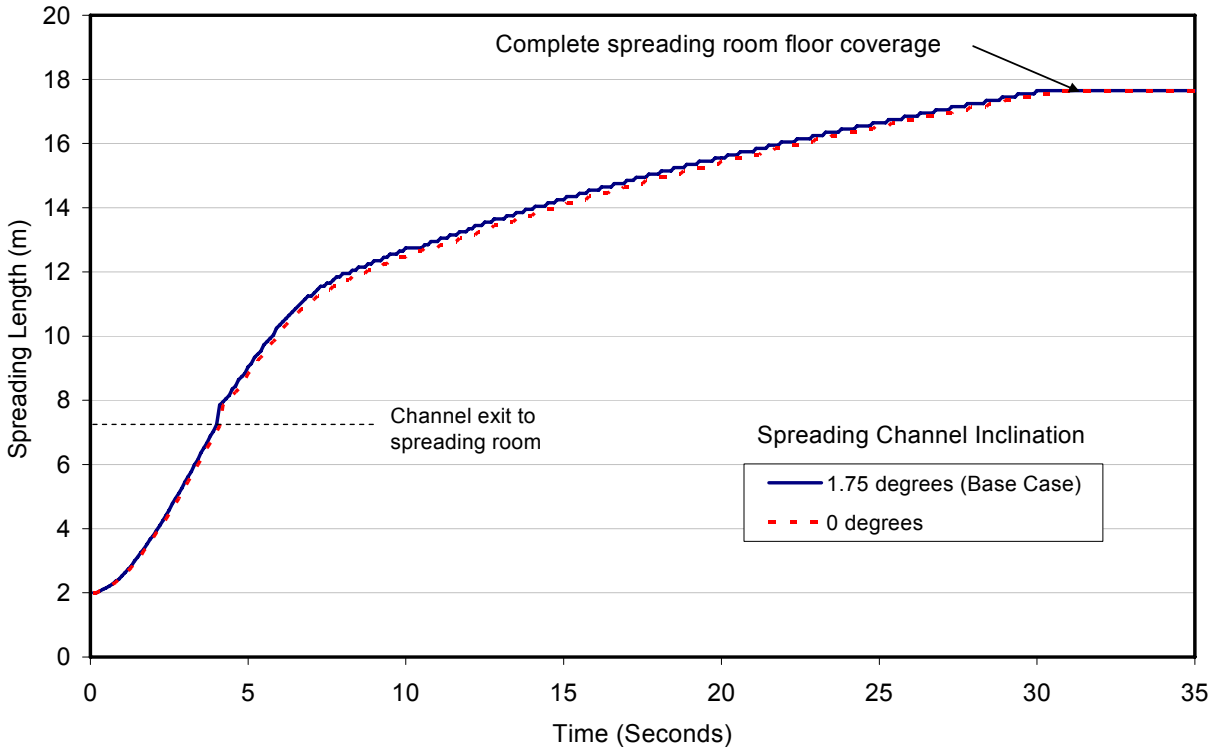

Figure 3.10. The influence of spreading channel angle of inclination on spreading behavior in the EPR core catcher.

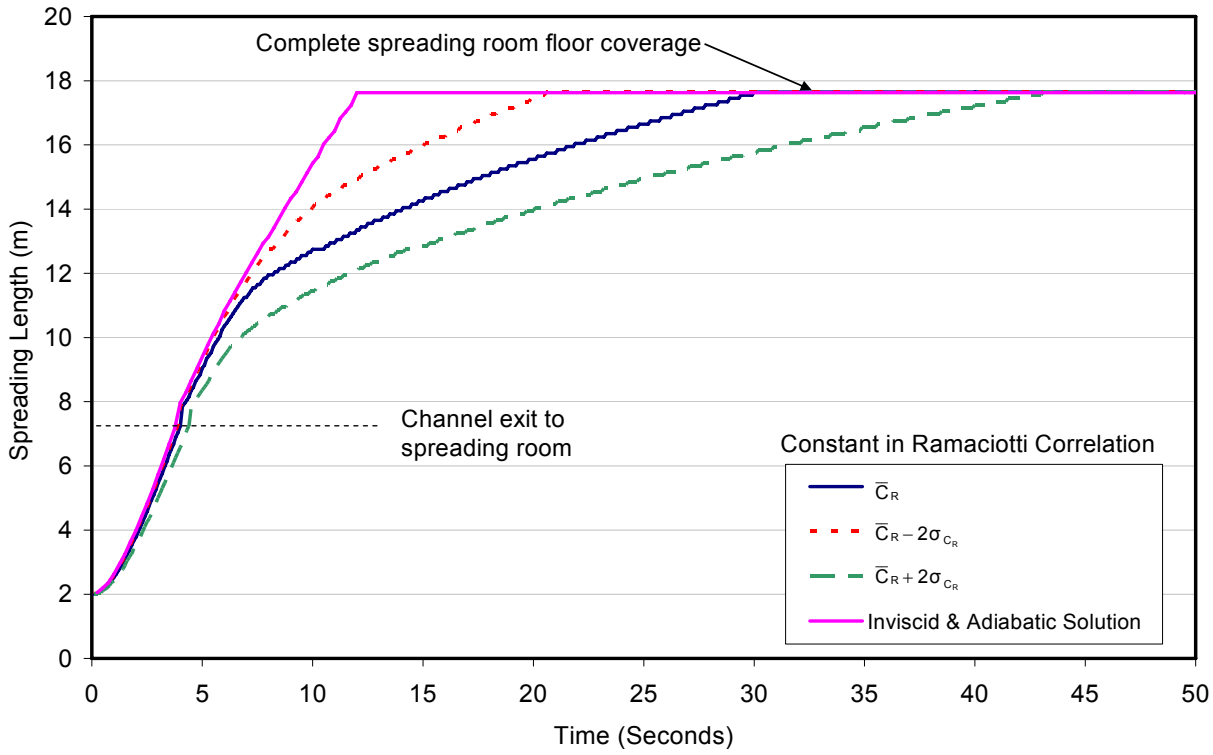

Figure 3.11. The influence of the value of the constant C_R in the Ramacciotti melt viscosity correlation on spreading behavior in the EPR core catcher.

the +2σ case. In addition, no attack of the ceramic or sacrificial concrete surfaces is predicted for the +2σ case. Conversely, up to 10 mm of erosion is calculated near the channel exit in the spreading room after four minutes for the -2σ case, but the rest of the floor remains intact. Thus, factoring in the uncertainties in the melt viscosity correlation that are based on comparisons with the reactor material melt spreading database, the current study indicates that uniform spreading in the core catcher will be achieved.

In summary, this sensitivity study has addressed parametric variations in: i) melt pour mass, ii) melt composition, iii) melt pour rate, iv) pour configuration (i.e., homogeneous vs. stratified metal-oxide phases), v) melt temperature, vi) cavity condition (wet vs. dry), vii) spreading channel inclination angle, and finally viii) uncertainties in the melt viscosity correlation that are based on comparisons with the reactor material melt spreading database. Although differences are found in the rate of spreading and the degree to which the sacrificial concrete is ablated during the transients, in all cases the melt eventually (over a period of minutes) spreads to a uniform depth in the spreading chamber.

4.0 SUMMARY AND CONCLUSIONS

The objective of this work was to utilize the MELTSPREAD code to check the assumption of uniform melt spreading in the EPR core catcher design. As a starting point for the project, the code was validated against the worldwide melt spreading database that emerged after the code was originally written in the very early 1990's. As part of this exercise, the code was extensively modified and upgraded to incorporate findings from these various analytical and experiment programs. In terms of expanding the ability of the code to analyze various melt simulant experiments, the options to input user-specified melt and/or substrate material properties was added. The ability to perform invisicid and/or adiabatic spreading analysis was also added so that comparisons with analytical solutions and isothermal spreading tests could be carried out. In terms of refining the capability to carry out reactor material melt spreading analyses, the code was upgraded with a new melt viscosity model; the capability was added to treat situations in which solid fraction buildup between the liquidus-solidus is non-linear; and finally, the ability to treat an interfacial heat transfer resistance between the melt and substrate was incorporated. This last set of changes substantially improved the predictive capability of the code in terms of addressing reactor material melt spreading tests.

Aside from improvements and upgrades, a method was developed to fit the model to the various melt spreading tests in a manner that allowed uncertainties in the model predictions to be statistically characterized. With these results, a sensitivity study was performed to investigate the assumption of uniform spreading in the EPR core catcher that addressed parametric variations in: i) melt pour mass, ii) melt composition, iii) melt pour rate, iv) pour configuration (i.e., homogeneous vs. stratified metal-oxide phases), v) melt temperature, vi) cavity condition (wet vs. dry), vii) spreading channel inclination angle, and finally viii) uncertainties in the melt viscosity correlation that are based on comparisons with the reactor material melt spreading database. Although differences were found in the rate of spreading and the degree to which the sacrificial concrete in the spreading room is ablated during the transients, in all cases the melt eventually (over a period of minutes) spreads to a uniform depth in the system.

5.0 REFERENCES

1. M. Fischer and H. Henning, "EPR™ Engineered Features for the Mitigation of Severe Accidents," Proceedings of ICAPP '09, Tokyo, Japan, May 10-14, 2009.

2. T. G. Theofanous, W. H. Amarasooriya, H. Yan, and U. Ratnam, "The Probability of Liner Failure in a Mark I Containment," NUREG/CR-5423, 1991.

3. T. G. Theofanous, H. Yan, M. Z. Podowski, C.S. Cho, D. A. Powers, T. J. Heames, J. J. Sienicki, C. C. Chu, B. W. Spencer, J. C. Castro, Y. R. Rashid, R. A. Dameron, and J. S. Maxwell, "The Probability of Mark-I Containment Failure by Melt-Attack of the Liner," NUREG/CR-6025, 1993.

4. J. J. Sienicki, M. T. Farmer and B. W. Spencer, "Spreading of Molten Corium in Mark I Geometry Following Vessel Meltthrough," Fourth Proceedings Nuclear Thermal Hydraulics, Washington, DC, October 30-November 4, 1988.

5. J. J. Sienicki, C. C. Chu and M. T. Farmer, "Analyses of Corium Spreading in Mark I Containment Geometry," 19th Water Reactor Safety Meeting, Bethesda, MD, October 28-30, 1991

6. M. T. Farmer, J. J. Sienicki and B. W. Spencer, "The MELTSPREAD-1 Computer Code for the Analysis of Transient Spreading in Containments," ANS Winter Meeting Session on Thermal Hydraulics of Severe Accidents, Washington, DC, November 11-15, 1990.

7. M. T. Farmer, J. J. Sienicki, B. W. Spencer and C. C. Chu, "Status of the MELTSPREAD-1 Computer Code for the Analysis of Transient Spreading of Core Debris Melts," 2nd CSNI Specialist Meeting on Core Debris-Concrete Interactions, Karlsruhe, Germany, April 1-3, 1992.

8. T. Brooke Benjamin, "Gravity Currents and Related Phenomena," J. Fluid Mechanics, Vol. 31, pp. 208-248, 1968.

9. H. Suzuki, et al., "Fundamental Experiments and Analysis for Melt Spreading on a Concrete Floor," 2nd International Conference on Nuclear Engineering (ICONE-2), San Francisco, CA, March 21-25, 1993.

10. J M. Veteau, B. Spindler, and G. Daum, "Modelling of Two-Phase Friction from Isothermal Spreading Experiments with Gas Fed from the Bottom and Application to Spreading Accompanied by Solidification," 10th International Topical Meeting on Nuclear Reactor Thermal Hydraulics (NURETH-10), Seoul, Korea, 2003.

11. T. N. Dinh, M. Konovalikhin, and B. R. Sehgal, "Core Melt Spreading on a Reactor Containment Floor," Progress in Nuclear Energy, Vol. 36, pp. 405–468, 2000.

12. G. Engel, G. Fieg, H. Massier, U. Stegmaier, and W. Schütz, “KATS Experiments to Simulate Corium Spreading in the EPR Core Catcher Concept,” OECD Workshop on Ex-Vessel Debris Coolability, Karlsruhe, Germany, November 15-18, 1999.

13. B. Eppinger, G. Fieg, H. Massier, W. Schütz, and U. Stegmaier, and G. Stern, "SternSimulationsexperimente zum Ausbreitungsverhalten von Kernschmelzen: KATS-8 bis KATS-17," FZKA 6589, March 2001.

14. J. Foit, "Large-Scale ECOKATS Experiments: Spreading of Oxide Melt on Ceramic and Concrete Surfaces,” Nuclear Engineering and Design, Vol. 236, pp. 2567-2573, 2006.

15. H. Alsmeyer, T. Cron, J. J. Foit, G. Messemer, S. Schmidt-Stiefel, W. Hafner, and H. Kriscio, “Experiment ECOKATS-2 on Melt Spreading and Subsequent Top Flooding,” FZKA 7084, January 2005.

16. G. Cognet, H. Alsmeyer, W. Tromm, D. Magallon, R. Wittmaack, B. R. Sehgal, W. Widmann, L. DeCecco, R. Ocelli, G. Azaria, D. Pineau, B. Spindler, G. Fieg, H. Werle, C. Journeau, M. Cranga, and G. Laffont, “Corium Spreading and Coolability CSC Project,” Nuclear Engineering and Design, Vol. 209, pp. 127-138, 2001

17. C. Journeau, E. Boccaccio, C. Brayer, G. Cognet, J .F. Haquet, C. Jégou, P. Piluso, and J. Monerris, “Ex-Vessel Corium Spreading: Results from the VULCANO Spreading Tests,” Nuclear Engineering and Design, Vol. 223, pp. 75-102, 2003.

18. C. Journeau, J.-F. Haquet, B. Spindler, C. Spengler, and J. Foit, “The VULCANO VE-U7 Corium Spreading Benchmark,” Progress in Nuclear Energy, Vol. 48, pp. 215–234, 2006.

19. D. Magallon and W. Tromm, “Dry and Wet Spreading Experiments with Prototypic Material at the FARO Facility,” OECD Workshop on Ex-Vessel Debris Coolability, Karlsruhe, Germany, November 15-18, 1999.

20. M. Sappok and W. Steinwarz, “COMAS Experiments as Contribution to the Validation of the EPR Mitigation Concept for Core Melt Accidents,” 6th International Conference on Nuclear Engineering (ICONE-6), San Diego, California, May 10-15, 1998.

21. W. Steinwarz, A. Alemberti, W. Häfner, Z. Alkan, and M. Fischer, “Investigations on the Phenomenology of Ex-Vessel Core Melt Behavior (COMAS),” Nuclear Engineering and Design, Vol. 209, pp. 139-146, 2001.

22. B. Spindler, J. M. Veteau, C. Brayer, M. Cranga, L. De Cecco, P. Montanelli, and D. Pineau, “Assessment of THEMA Code Against Spreading Experiments,” OECD Workshop on Ex-Vessel Debris Coolability, Karlsruhe, Germany, November 15-18, 1999.

23. B. Spindler and J.M. Veteau, “The Simulation of Melt Spreading with THEMA Code Part 1: Model, Assessment Strategy and Assessment Against Analytical and Numerical Solutions,” Nuclear Engineering and Design, Vol. 236, pp. 415–424, 2006.

24. B. Spindler and J.M. Veteau, "The Simulation of Melt Spreading with THEMA Code Part 2: Model, Assessment Against Spreading Experiments," Nuclear Engineering and Design, Vol. 236, pp. 425–441, 2006.

25. B. Piar, B. D. Michel, F. Babik, J. C. Latché, G. Guillard, and J. M. Ruggiéri, "CROCO: a Computer Code for Corium Spreading," 9th International Topical Meeting on Nuclear Reactor Thermal Hydraulics (NURETH-9), San Francisco, California, October 3-8, 1999.

26. H. J. Allelein, A. Breest, and C. Spengler, "Simulation of Core Melt Spreading with LAVA: Theoretical Background and Status of Validation," OECD Workshop on Ex-Vessel Debris Coolability, Karlsruhe, Germany, November 15-18, 1999.

27. R. Wittmaack, "Numerical Simulation of Corium Spreading in the EPR with CORFLOW," OECD Workshop on Ex-Vessel Debris Coolability, Karlsruhe, Germany, November 15-18, 1999.

28. J. J. Foit, "Spreading under Variable Viscosity and Time-Dependent Boundary Conditions: Estimate of Viscosity from Spreading Experiment," Nuclear Engineering and Design, Vol. 227, pp. 239-253, 2004.

29. M. Ramacciotti, C. Journeau, F. Sudreau, and G. Cognet, "Viscosity Models for Corium Melts," Nuclear Engineering and Design, Vol. 204, pp. 377-389, 2001.

30. T. Loulou, E. A. Artyukhin, and J. P. Bardon, "Estimation of Thermal Contract Resistance During the First Stages of Metal Solidification Process: I – Experiment Principle and Modelisation," International J. of Heat and Mass Transfer, Vol. 42, pp. 2119-2127, 1999.

31. T. Loulou, E. A. Artyukhin, and J. P. Bardon, "Estimation of Thermal Contract Resistance During the First Stages of Metal Solidification Process: II – Experimental Setup and Results," International J. of Heat and Mass Transfer, Vol. 42, pp. 2129-2142, 1999.

32. W. Wang and H.–H. Qiu, "Interfacial Thermal Conductance in Rapid Contact Solidification Process," International J. of Heat and Mass Transfer, Vol. 45, pp. 2043-2053, 2002.

33. M. Ishii and N. Zuber, "Drag Coefficient and Relative Velocity in Bubbly, Droplet or Particulate Flows," AlChE Journal, Vol. 25, pp. 843-855, 1979.

34. C. Spengler, J. J. Foit, and W. Häfner, "Dataset for the Blind Benchmark Calculation of the ECOKATS-V1 Spreading Experiment," SAM-ECOSTAR-P09/01, July, 2003.

35. M. T. Farmer, "Modeling of Ex-Vessel Corium Coolability with the CORQUENCH Code," Proceedings 9th Int. Conf. on Nucl. Eng., ICONE-9696, April 8-12, 2001.

36. P. Y. Chevalier, "Presentation of the OXY5-GEMINI2 Code," Advanced Containment Experiments (ACE) Technical Advisory Committee Meeting, EPRI Headquarters, Palo Alto, CA, 4-8 November, 1991.

37. M. Fischer, "The Severe Accident Mitigation Concept and the Design Measures for Core Melt Retention of the European Pressurized Reactor (EPR)," Nuclear Engineering and Design, Vol. 230, pp. 169-180, 2004.

38. T. N. Dinh, M. Konovalikhin, D. Paladino, J. A. Green, A. Gubaidulin, and B. R. Sehgal, "Experimental Simulation of Core Melt Spreading on a LWR Containment Floor in a Severe Accident," 6th International Conference on Nuclear Engineering (ICONE-6), San Diego, California, May 10-15, 1998.

APPENDIX A
Compilation of MELTSPREAD Validation Calculations

The purpose of this appendix is to present the results of the various code validation calculations that were carried out as part of this study using a summary format. As discussed in Section 2 and shown in Table 2.1, the validation database can be broken down into the following categories: i) isothermal spreading tests with simulant fluids, ii) high temperature flow and freezing tests with simulant oxide melts, iii) high temperature flow and freezing tests using metallic melts, and iv) reactor material melt spreading tests. The results are presented in this appendix under the same generalized headings.

A.1 Isothermal Spreading Tests with Simulant Fluids

The code was first benchmarked against the isothermal spreading data to verify proper behavior before moving on to tests that involved heat transfer and freezing effects. Tests that were considered in this area include the water spreading tests of Theofanous et al.,[2] in addition to the Corine program[10] water and glycerol spreading tests.

A.1.1 Theofanous Water Spreading Tests

Theofanous et al.[2] conducted water spreading tests in a 1/10 linear scale model of the Mark I BWR containment. Local depth versus time profiles were reported at four different positions within the apparatus: i) Position A, just inside the pedestal doorway to the drywell, ii) Position C, adjacent to the annulus directly across from the doorway, iii) Position D, in the annulus 90º from the doorway, and Position E, in the annulus 180º from the doorway. Two tests were conducted; Run 1 was considered to be a 'high flowrate' case simulating the flow at reactor scale of a 10 m^3 pour volume at a flowrate of 6.5 m^3/minute. Based on a scaling analysis in which the flow characteristics were preserved on the basis of conserving the Froude number, the corresponding flowrate at test scale was deduced to be 0.325 liters/second. The test characteristics, as well as code input information that was compiled to simulate Run No. 1, are described in Table A.1. A comparison of the predicted water leading edge penetration through the apparatus as a function of time is provided in Figure A.1, while local responses at Positions A, C, D, and E are compared with the data in Figures A.2 - A.5, respectively. Finally, local depth profiles throughout the apparatus at several different times are shown in Figure A.6. As is evident from these figures, calculations were carried out for two cases; i.e., both non-wetted and wetted (surface tension ~ 0) surfaces. Examination of the figures indicates that the wetted surface solution provides a better overall fit to the test data. The code seems to provide a reasonable estimate of arrival times (viz. leading edge penetration rate) and subsequent depth profiles at the positions where data were reported in the apparatus.

Run No. 2 also simulated a 10 m^3 pour volume but at ½ the flowrate (i.e., 3.25 m^3/minute). Test characteristics and the corresponding code input are summarized in Table A.2, while analogous plots of leading edge penetration, local depth responses, and depth profiles at several times are shown in Figures A.6 through A.12. Again, the wetted surface calculation seems to provide a better agreement, and overall predictions of arrival times and depth profiles seem to reasonably replicate the behavior observed in the experiments.

Table A.1. Input File Data Sheet for Theofanous Water Spreading Test No. 1.

Test parameter	Value
Test name	Theofanous Test No. 1
Fluid composition (wt %)	100 H_2O
Melt delivery technique	Water poured into a 28.3 cm radius cylindrical cavity that simulated the pedestal of a Mark I containment.
Total pour mass	10.2 kg
Spreading geometry	1/10 linear scale model of a Mark I containment: A 28.3 cm inner radius cylindrical cavity with a 9.5 cm wide doorway leading to an annular spreading region with a radius of 56.5 cm. The wall thickness of the pedestal was 3.2 cm.
Code input parameter(s)	**Value(s)**
Fluid composition (wt %)	100 H_2O
Fluid pour rate and duration	Flowrate constant at 0.325 kg/sec for 31.5 seconds.
Melt material property evaluation[a]	User-specified property data: $\rho = 997$ kg/m^3, $\mu_o = 0.826$ mPa-s, and $\sigma = 0.073$ N-m
Heat transfer modeling assumption	Flow is "adiabatic"
Spreading cavity nodalization	Automated Mark I shell meshing option used: melt assumed pour into the sump which was taken to have a radius of 19.9 cm and was flush with the concrete surface; balance of pedestal interior meshed with 2 nodes that were 4.2 cm long. The 9.5 cm wide doorway was meshed with 2 cells that were 1.6 cm long. The water was assumed to spread outside the doorway with a spreading angle of 90º. The distance from the doorway to the shell was meshed with 7 cells that were 3.57 cm long. The balance of the annulus was meshed using 25 cells. All nodes cell-centered.
Timestep	0.05 seconds

[a]As applicable, ρ is density, μ_o is viscosity at the liquidus, and σ is surface tension.

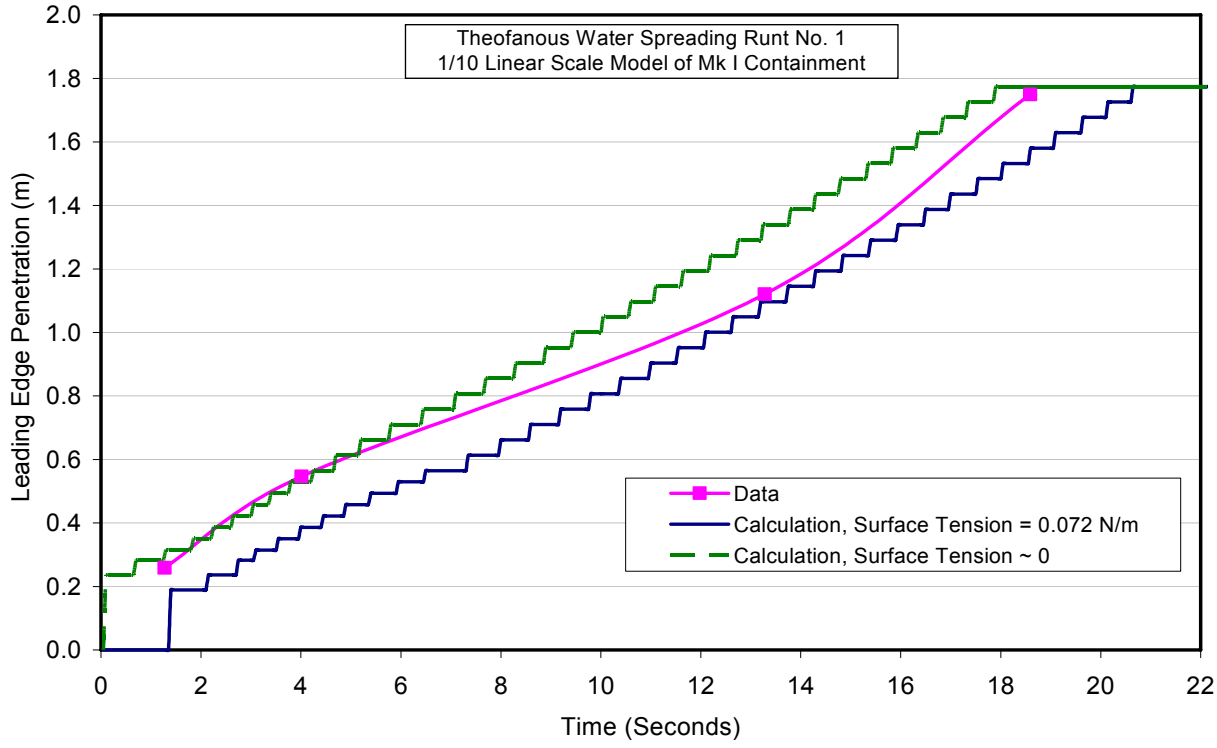

Figure A.1. Leading edge penetration comparison for Theofanous et al. Run No. 1.

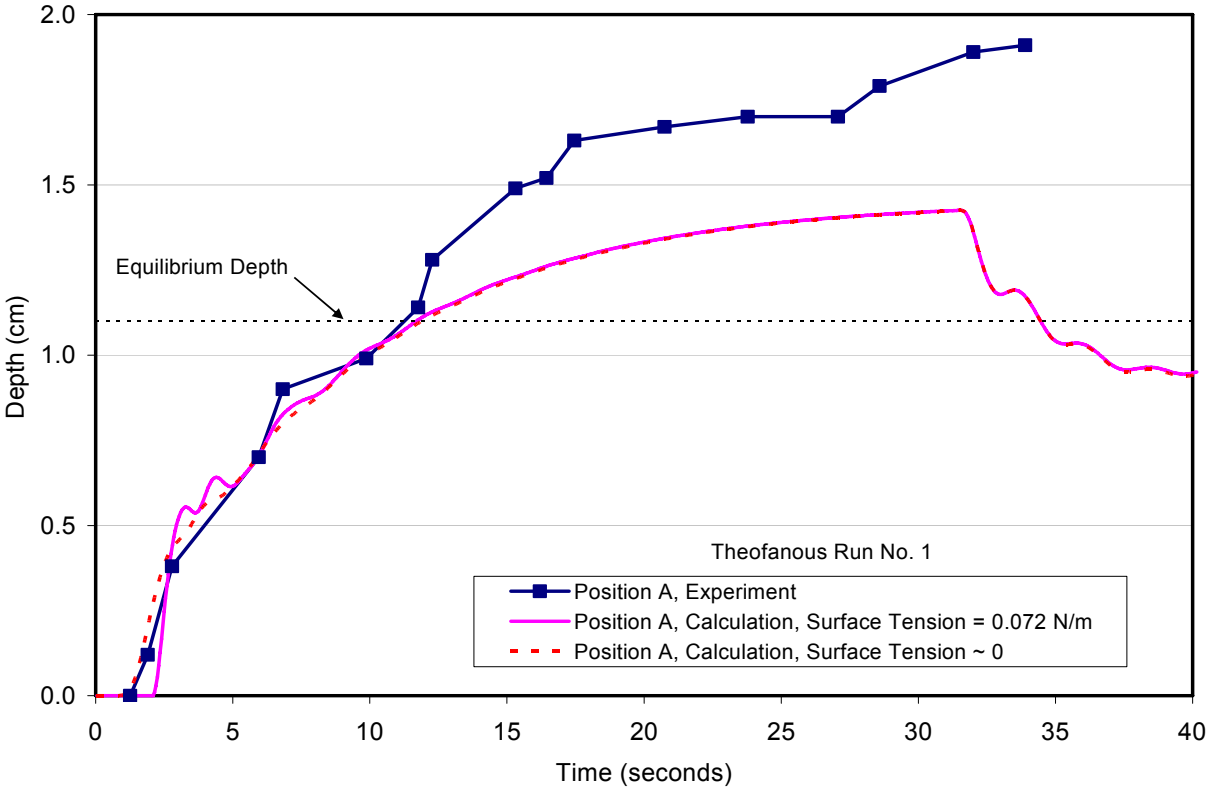

Figure A.2. Comparison of local depth response at Position A for Theofanous Run No. 1.

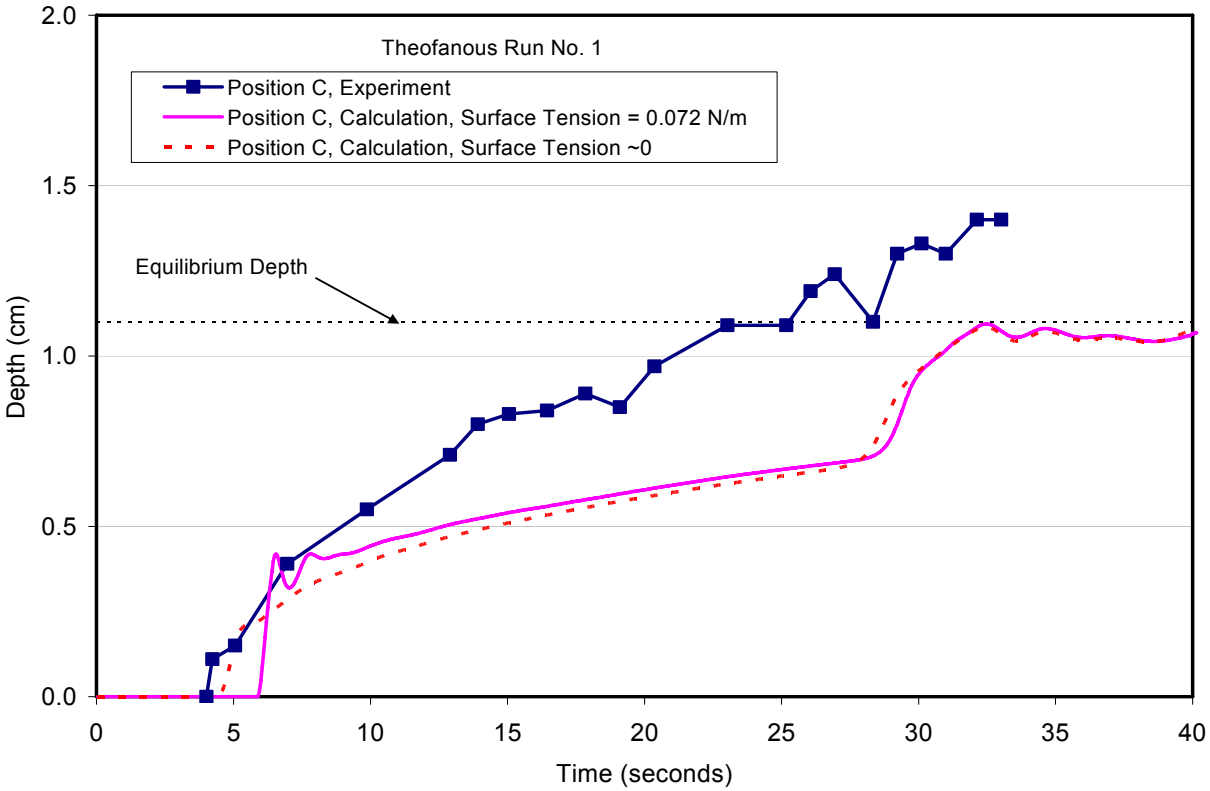

Figure A.3. Comparison of local depth response at Position C for Theofanous Run No. 1.

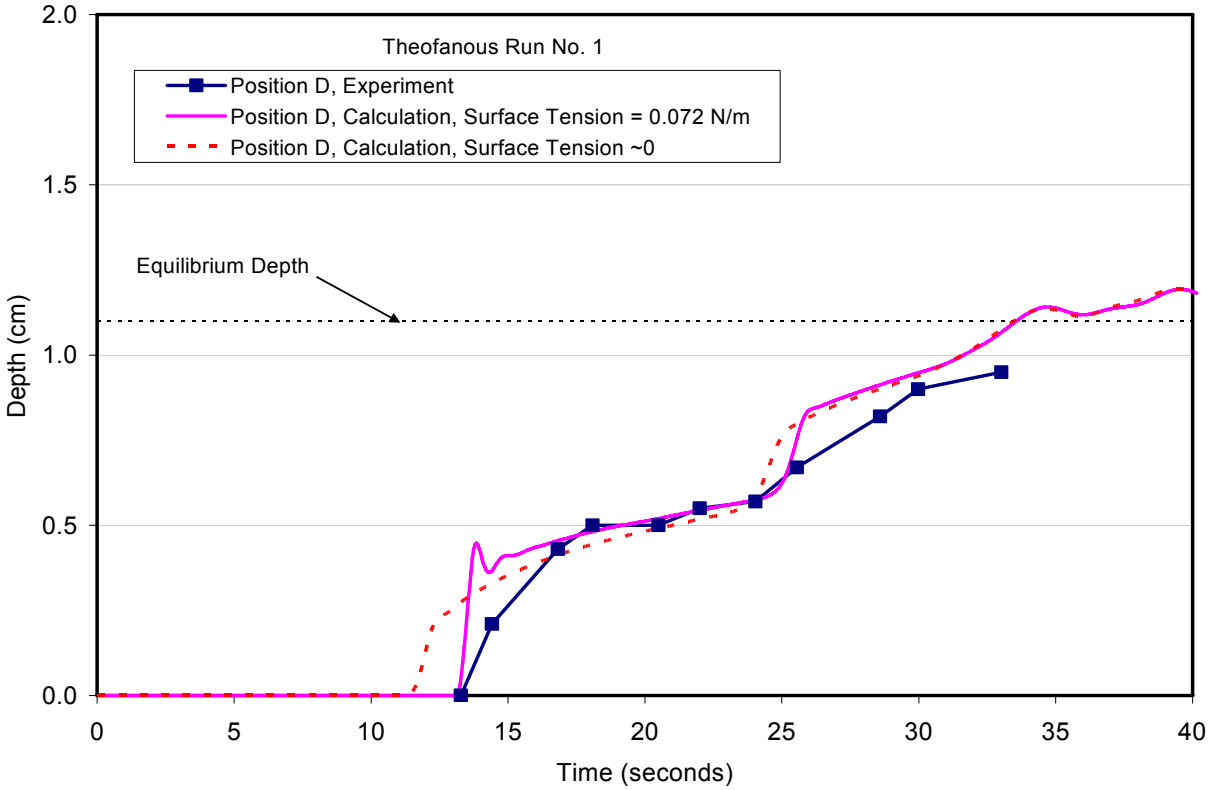

Figure A.4. Comparison of local depth response at Position D for Theofanous Run No. 1.

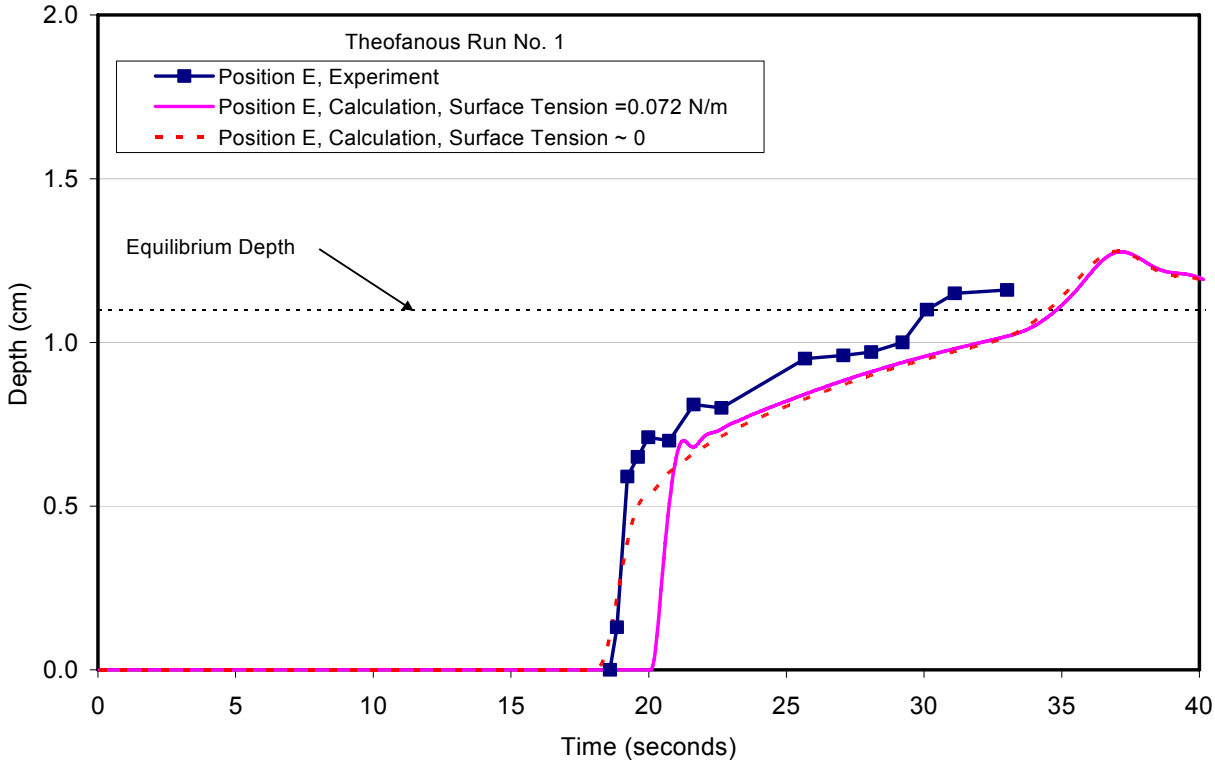

Figure A.5. Comparison of local depth response at Position E for Theofanous Run No. 1.

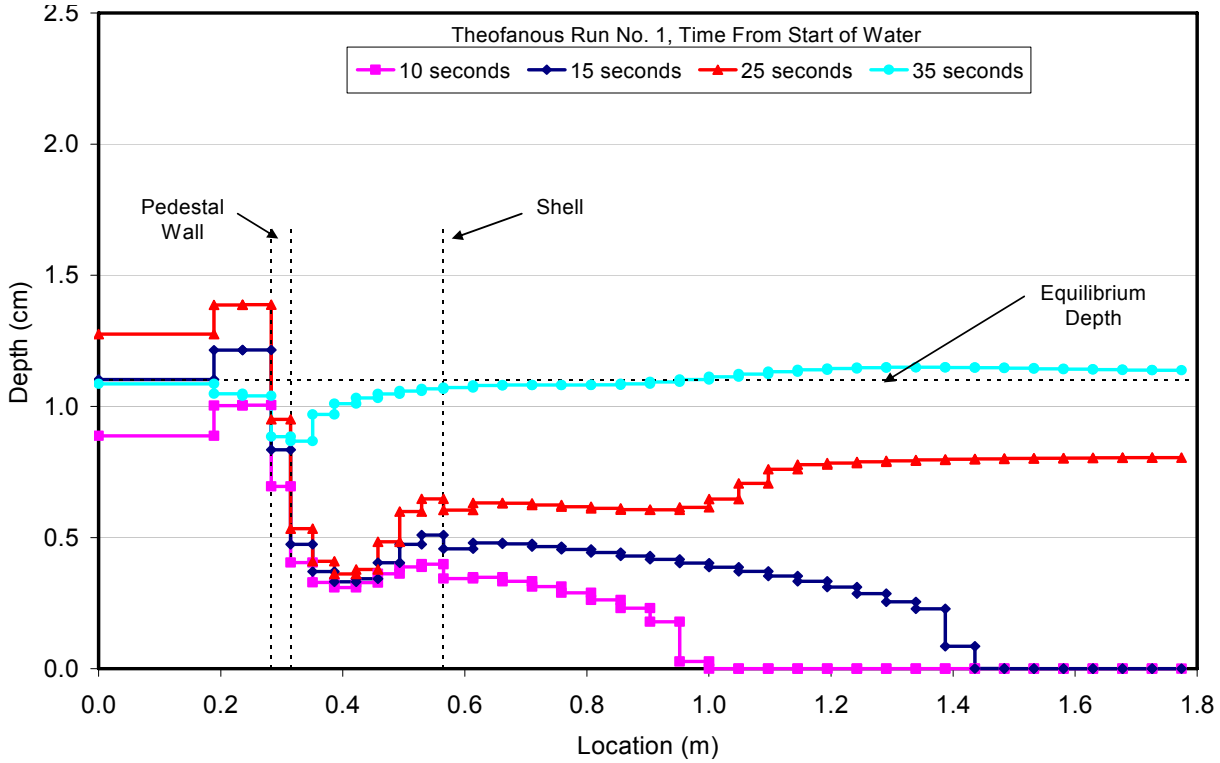

Figure A.6. Predicted local depth profiles at various times for Theofanous Run No. 1.

Table A.2. Input File Data Sheet for Theofanous Water Spreading Test No. 2.

Test parameter	**Value**
Test name	Theofanous Test No. 2
Fluid composition (wt %)	100 H_2O
Melt delivery technique	Water poured into a 28.3 cm radius cylindrical cavity that simulated the pedestal of a Mark I containment.
Total pour mass	10.2 kg
Spreading geometry	1/10 linear scale model of a Mark I containment: A 28.3 cm inner radius cylindrical cavity with a 9.5 cm wide doorway leading to an annular spreading region with a radius of 56.5 cm. The wall thickness of the pedestal was 3.2 cm.
Code input parameter(s)	**Value(s)**
Fluid composition (wt %)	100 H_2O
Fluid pour rate and duration	Flowrate constant at 0.1625 kg/sec for 63.0 seconds.
Melt material property evaluation[a]	User-specified property data: $\rho = 997$ kg/m^3, $\mu_o = 0.826$ mPa-s, and $\sigma = 0.073$ N-m
Heat transfer modeling assumption	Flow is "adiabatic"
Spreading cavity nodalization	Automated Mark I shell meshing option used: melt assumed pour into the sump which was taken to have a radius of 19.9 cm and was flush with the concrete surface; balance of pedestal interior meshed with 2 nodes that were 4.2 cm long. The 9.5 cm wide doorway was meshed with 2 cells that were 1.6 cm long. The water was assumed to spread outside the doorway with a spreading angle of 90º. The distance from the doorway to the shell was meshed with 7 cells that were 3.57 cm long. The balance of the annulus was meshed using 25 cells. All nodes cell-centered.
Timestep	0.05 seconds

[a]As applicable, ρ is density, μ_o is viscosity at the liquidus, and σ is surface tension.

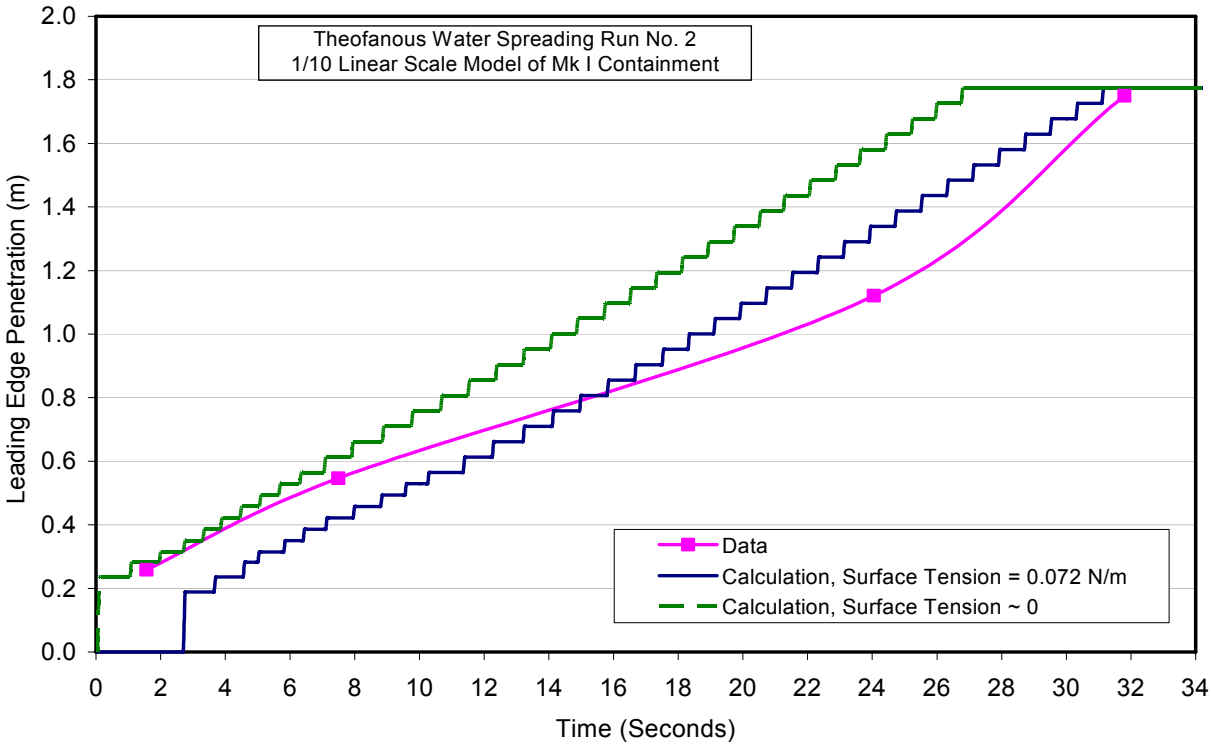

Figure A.7. Leading edge penetration comparison for Theofanous et al. Run No. 2.

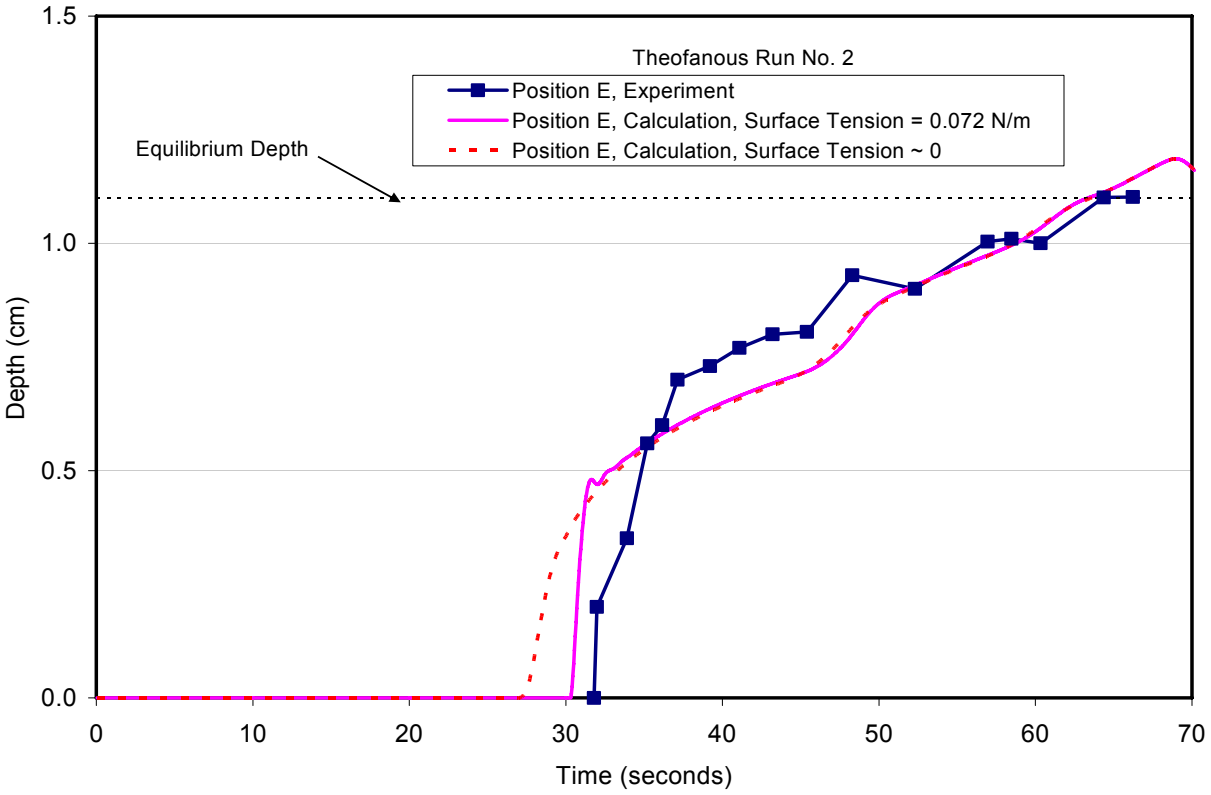

Figure A.8. Comparison of local depth response at Position A for Theofanous Run No. 2.

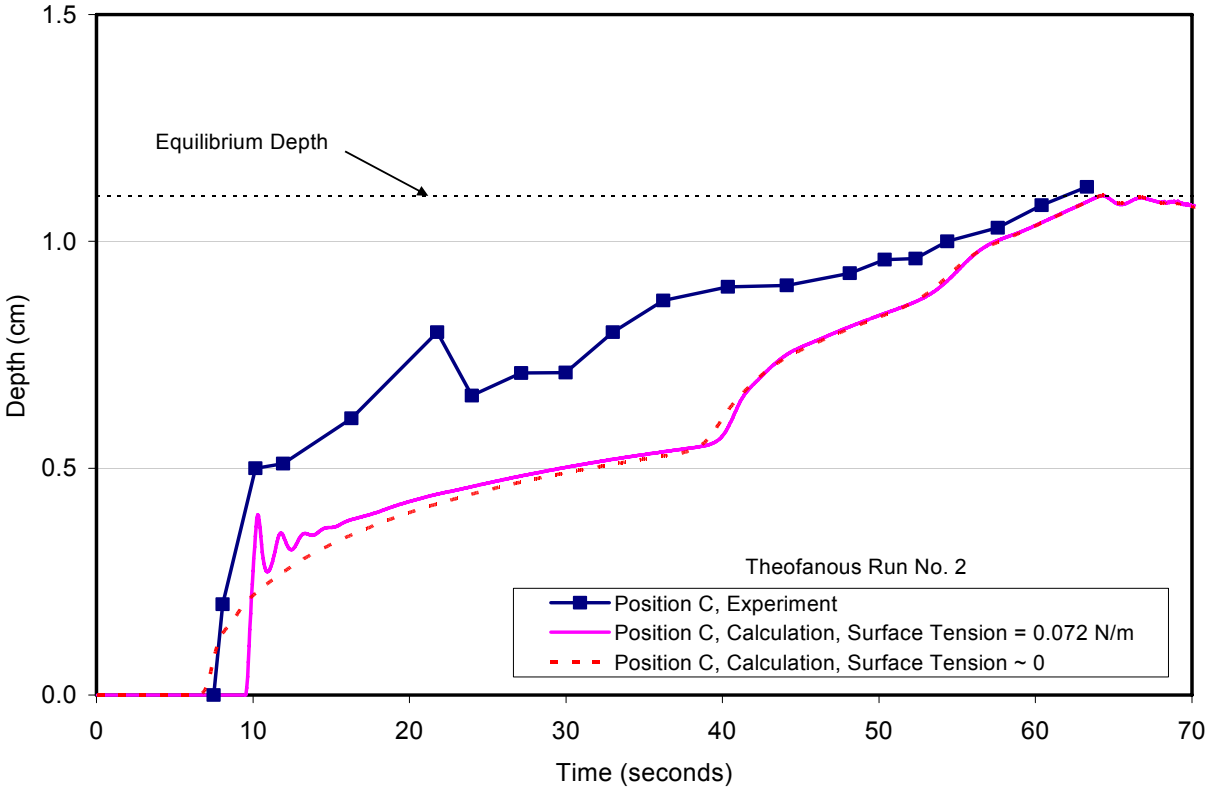

Figure A.9. Comparison of local depth response at Position C for Theofanous Run No. 2.

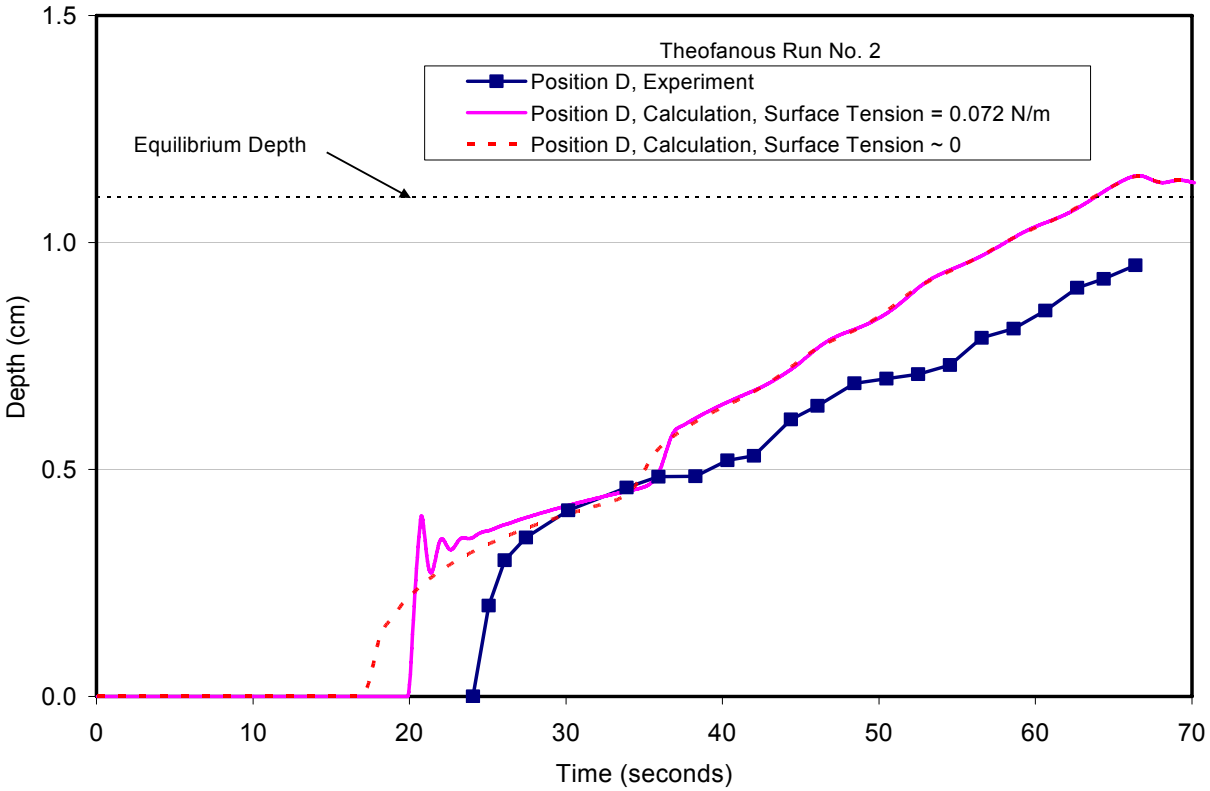

Figure A.10. Comparison of local depth response at Position D for Theofanous Run No. 2.

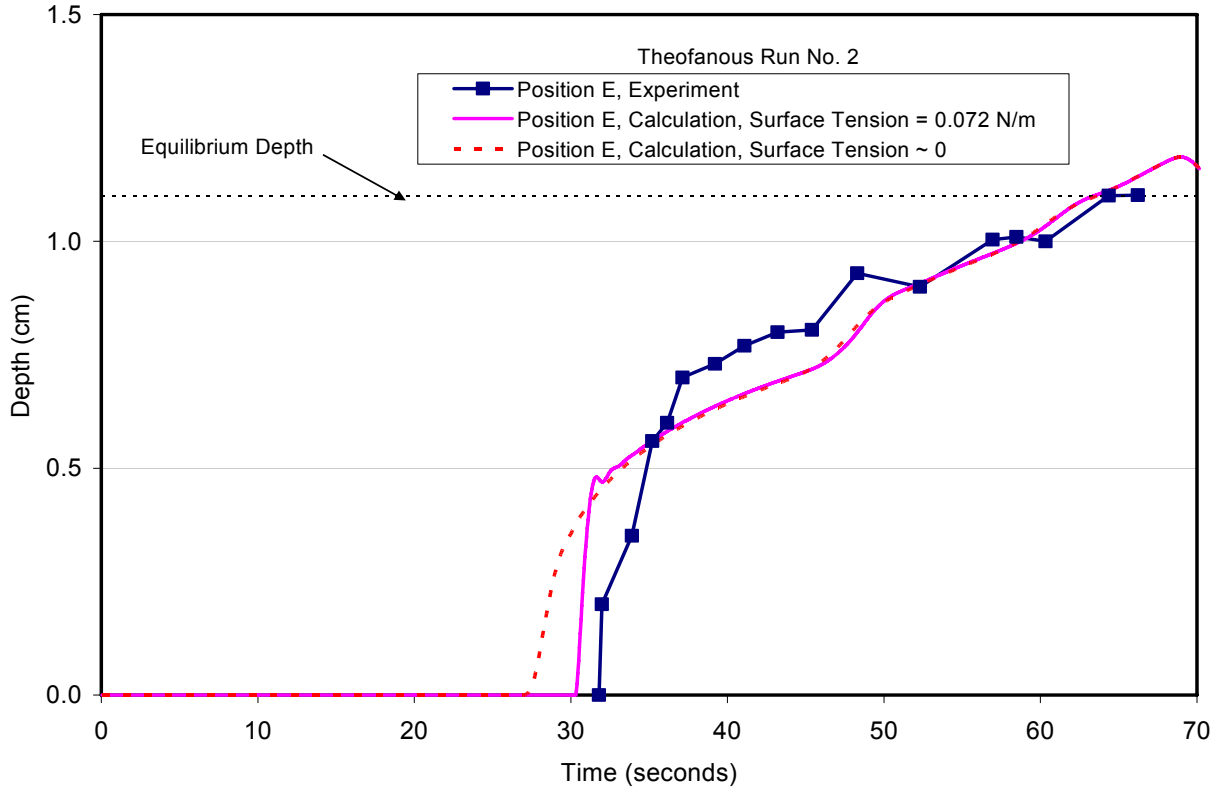

Figure A.11. Comparison of local depth response at Position E for Theofanous Run No. 2.

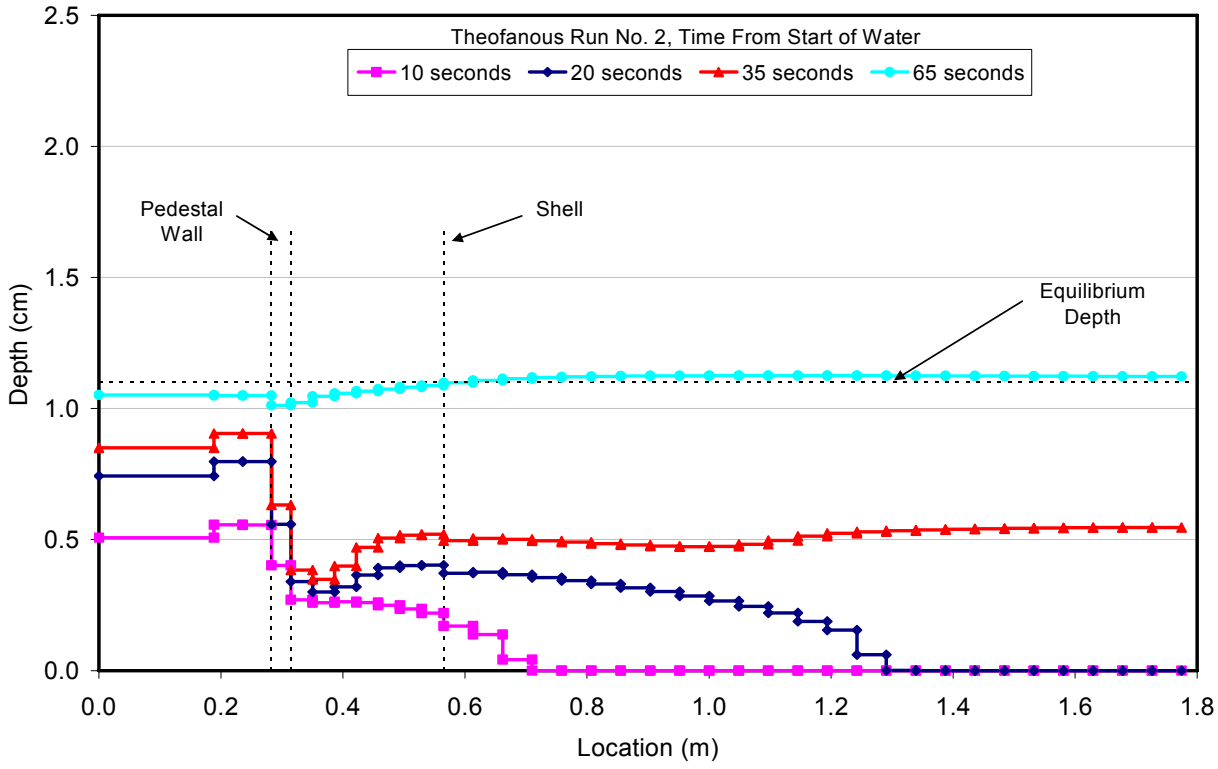

Figure A.12 Predicted local depth profiles at various times for Theofanous Run No. 2.

A.1.2 Corine Water and HEC Spreading Tests

The second validation exercise involving spreading under isothermal conditions consisted of comparing code predictions with water and glycerol spreading data obtained as part of the Corine[10] program. These were large-scale simulant experiments involving the spreading of ~ 40 liters of fluid within an instrumented 19º sector. The principal parameters that were varied in the test matrix included pour rate and fluid viscosity. As shown in Table 2.1, four tests were selected from this experiment series for analysis: two water tests at different flowrates (i.e., 0.5 and 1.5 liters/second), and two glycerol tests at the same flowrate but with different fluid viscosities (i.e., 0.1 and 2.0 Pa-sec). Test characteristics and the corresponding code input for the low water flowrate test WAT_Q0.5_GO are described in Table A.3. A comparison of the predicted water leading edge penetration rate with the test data is provided in Figure A.13, while local depth profiles at several times are shown in Figure A.14. In Figure A.13, results are again provided for both wetted and non-wetted surface conditions. For this case, the non-wetted surface solution seems to provide slightly better agreement, although the difference is not dramatic. In general, the code seems to reasonably estimate leading edge penetration rate for this experiment.

Test characteristics and the corresponding code input for the high water flowrate test WAT_Q1.5_GO are summarized in Table A.4, while the analogous plots of leading edge penetration and depth profiles at several times are shown in Figures A.15 and A.16. For this test, the non-wetted surface solution provides a slightly better fit to the leading edge penetration data, and the solution seems to reasonably replicate the overall trends observed in the experiment.

Table A.3. Input File Data Sheet for Corine Test WAT_Q0.5_GO (water in a 19º sector).

Test parameter	**Value**
Test name	WAT_Q0.5_GO
Fluid composition (wt %)	100 H_2O
Fluid delivery technique	Water pumped from below into a fluid delivery reservoir that was circular with a cross-sectional area of 0.1064 m^2. The reservoir was separated from the spreading channel by a weir that was 24.0 cm high and had a wall thickness of 1.4 cm.
Total pour mass	65 (25 kg to fill the reservoir, 40 kg spread)
Spreading geometry	6.5 m long, 19º angular sector
Code input parameter(s)	**Value(s)**
Fluid composition (wt %)	100 H_2O
Fluid pour rate and duration	Injection flowrate into the reservoir constant at 0.5 kg/sec over a time interval of 130 seconds.
Fluid material property evaluation[a]	User-specified property data: ρ = 1000 kg/m^3, μ_o = 0.826 mPa-s, and σ = 0.073 N-m
Heat transfer modeling assumption	Flow is "adiabatic"
Spreading cavity nodalization	Reservoir modeled as a single cell with area 0.1064 m^2, spreading arc length of 19.05 cm, node length of 41.1 cm, and elevation flush with the spreading surface. The weir was modeled with a single cell that was 24.0 cm above the spreading surface and had a thickness (length) of 1.4 cm. The spreading channel was modeled as a 19º angular sector; the 6.5 m radial length was subdivided into 200 nodes of equal radial length of 3.25 cm.
Timestep	0.05 seconds

[a]As applicable, ρ is density, μ_o is viscosity at the liquidus, and σ is surface tension.

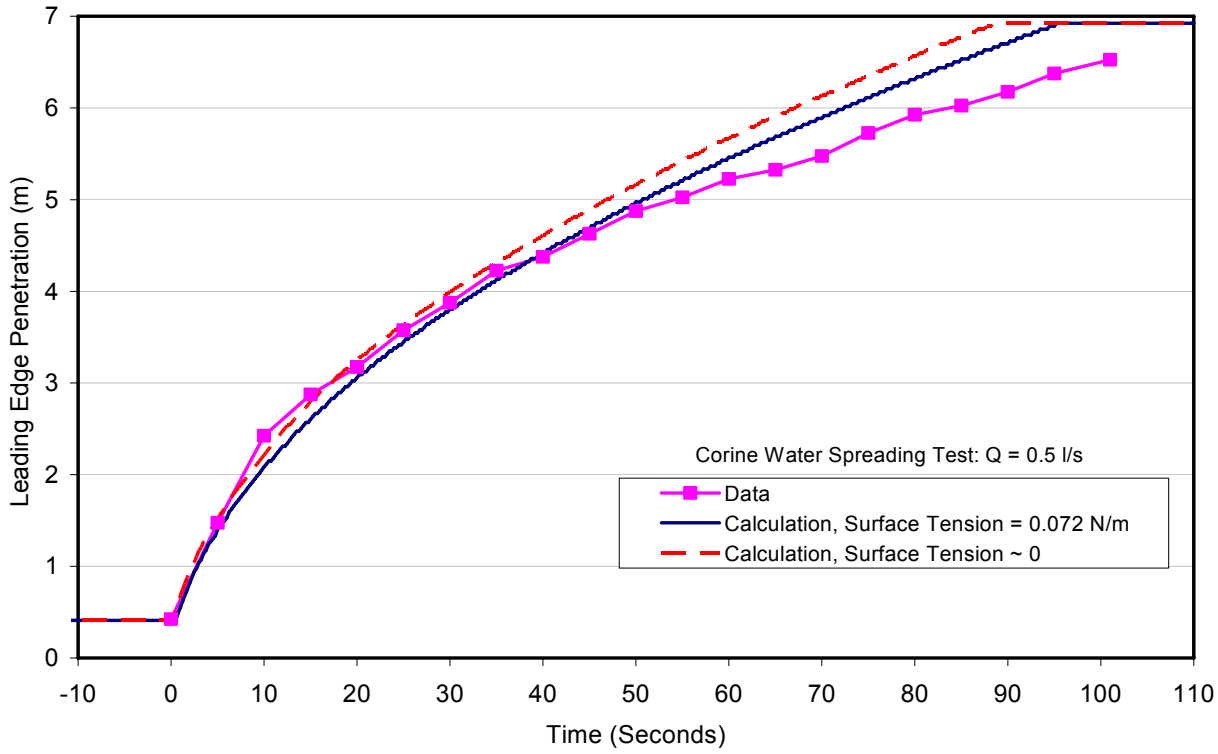

Figure A.13. Leading edge penetration comparison for Corine Test WAT_Q0.5_GO.

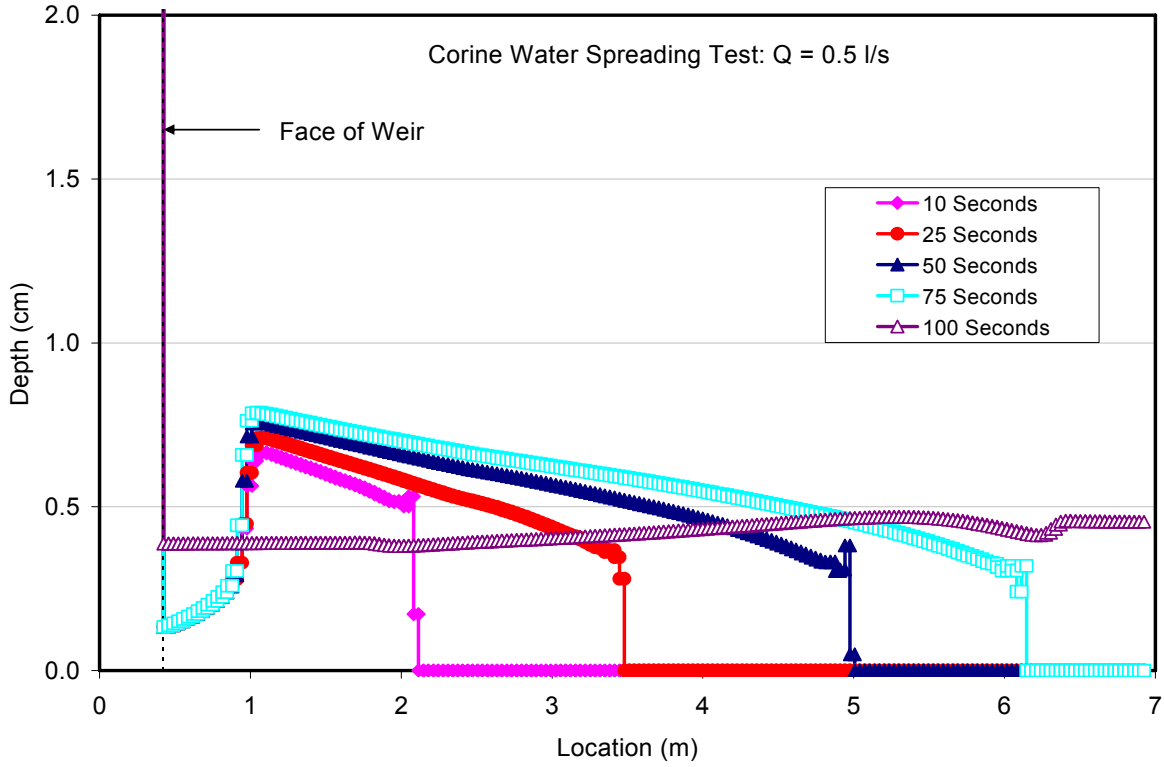

Figure A.14. Predicted local depth profiles at various times for Corine Test WAT_Q0.5_GO.

Table A.4. Input File Data Sheet for Corine Test WAT_Q1.5_GO (water in a 19º sector).

Test parameter	Value
Test name	WAT_Q1.5_GO
Fluid composition (wt %)	100 H_2O
Fluid delivery technique	Water pumped from below into a fluid delivery reservoir that was circular with a cross-sectional area of 0.1064 m^2. The reservoir was separated from the spreading channel by a weir that was 24.0 cm high and had a wall thickness of 1.4 cm.
Total pour mass	65 (25 kg to fill the reservoir, 40 kg spread)
Spreading geometry	6.5 m long, 19º angular sector
Code input parameter(s)	**Value(s)**
Fluid composition (wt %)	100 H_2O
Fluid pour rate and duration	Injection flowrate into the reservoir constant at 1.5 kg/sec over a time interval of 43.3 seconds.
Fluid material property evaluation[a]	User-specified property data: $\rho = 1000$ kg/m^3, $\mu_o = 0.826$ mPa-s, and $\sigma = 0.073$ N-m
Heat transfer modeling assumption	Flow is "adiabatic"
Spreading cavity nodalization	Reservoir modeled as a single cell with area 0.1064 m^2, spreading arc length of 19.05 cm, node length of 41.1 cm, and elevation flush with the spreading surface. The weir was modeled with a single cell that was 24.0 cm above the spreading surface and had a thickness (length) of 1.4 cm. The spreading channel was modeled as a 19º angular sector; the 6.5 m radial length was subdivided into 200 nodes of equal radial length of 3.25 cm.
Timestep	0.05 seconds

[a]As applicable, ρ is density, μ_o is viscosity at the liquidus, and σ is surface tension.

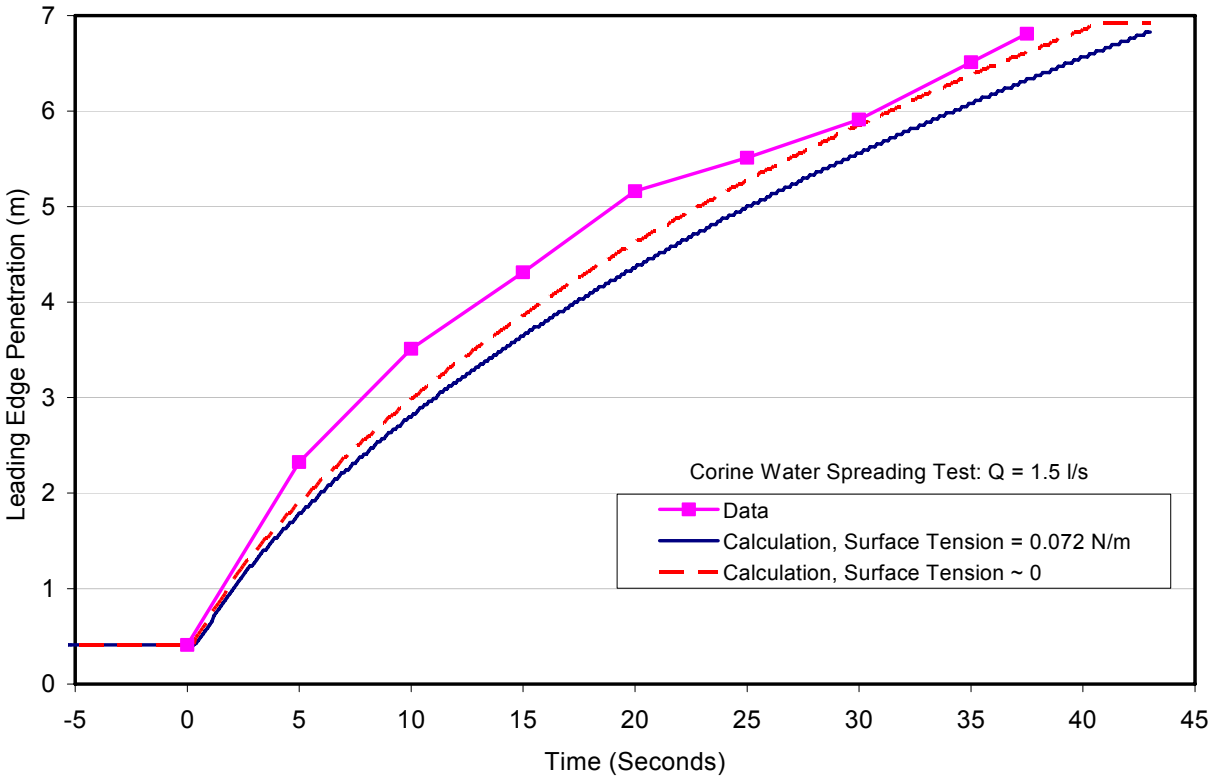

Figure A.15. Leading edge penetration comparison for Corine Test WAT_Q1.5_GO.

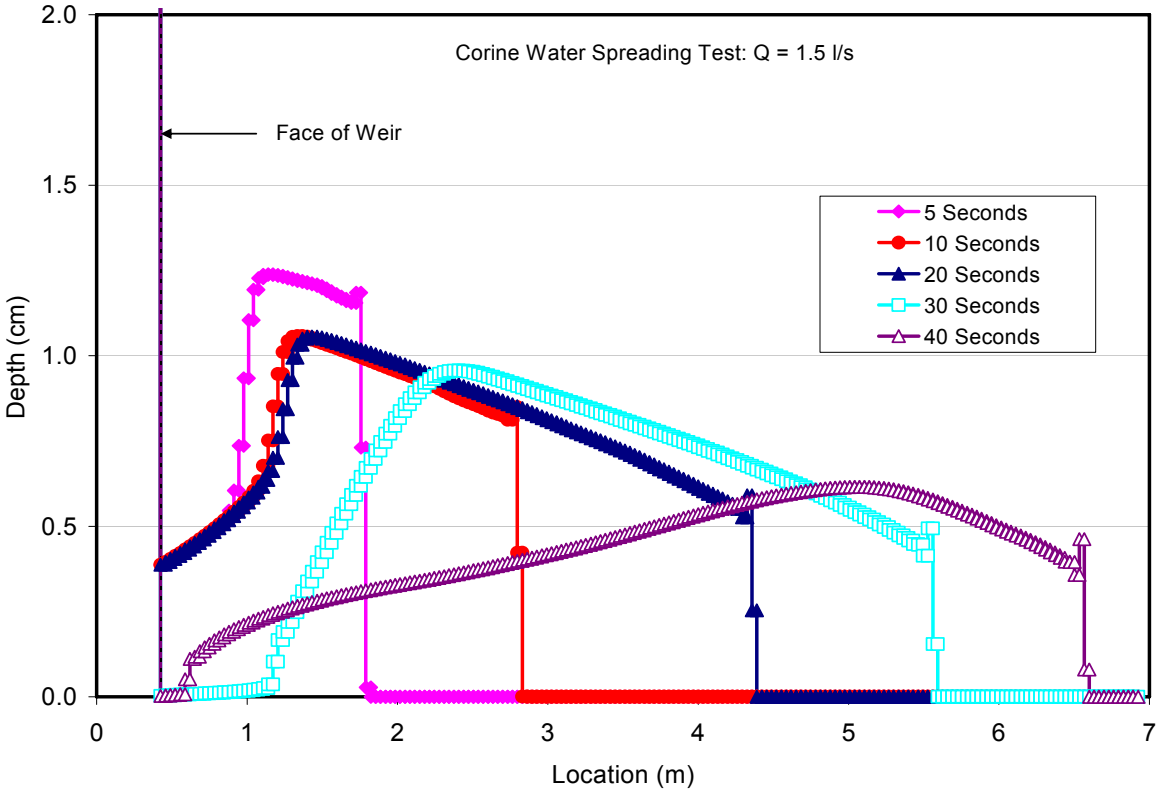

Figure A.16. Predicted local depth profiles at various times for Corine Test WAT_Q1.5_GO.

Aside from the water spreading experiments, test characteristics and corresponding code input for the Corine low viscosity (0.1 Pa-sec) glycerol spreading test HEC_3_GO_0.1 are summarized in Table A.5, while plots of leading edge penetration and depth profiles at several different times are shown in Figures A.17 and A.18. For this test, the non-wetted surface solution provides a slightly better fit to the leading edge penetration data, and the overall shape of the position vs. time curve is reasonably reproduced. However, the code systematically under-predicts the leading edge penetration distance by about 30 cm for all times past approximately 20 seconds into the experiment sequence. The reason for the discrepancy is not clear, but one possibility is offered; i.e., edge effects may play an important role in these higher viscosity tests, and so penetration at the centerline (where progression was measured) was systematically greater than at the edges, and so the average penetration distance was less than reported at any given time. Recall that MELTSREAD is a one-dimensional code, and so edge effects cannot be accurately modeled with this code.

Test information and modeling details for the Corine high viscosity (2.0 Pa-sec) spreading test HEC_3_GO_0.1 are summarized in Table A.6. Conversely, plots of leading edge penetration and depth profiles at several different times are shown in Figures A.19 and A.20. As for the previous case, the non-wetted surface solution provides a slightly better fit to the leading edge penetration data, and the overall shape of the position vs. time curve is reasonably reproduced. However, as for the previous case, the code systematically under-predicts the leading edge penetration distance by ~ 30 cm for all times past ~ 20 seconds into the experiment sequence. A possible explanation for the discrepancy was provided above.

Table A.5. Input File Data Sheet for Corine Test HEC_3_GO_0.1 (glycol in a 19º sector).

Test parameter	Value
Test name	HEC_3_GO_0.1
Fluid composition (wt %)	100 Hydroxyl ethyl cellulose (HEC)
Melt delivery technique	Fluid pumped from below into a delivery reservoir that was circular with a cross-sectional area of 0.1064 m^2. The reservoir was separated from the spreading channel by a weir that was 24.0 cm high and had a wall thickness of 1.4 cm.
Total pour mass	65 (25 kg to fill the reservoir, 40 kg spread)
Spreading geometry	6.5 m long, 19º angular sector
Code input parameter(s)	**Value(s)**
Fluid composition (wt %)	100 Hydroxyl ethyl cellulose (HEC)
Fluid pour rate and duration	Injection flowrate into the reservoir constant at 3.0 kg/sec over a time interval of 21.67 seconds.
Melt material property evaluation[a]	User-specified property data: $\rho = 1000$ kg/m^3, $\mu_o = 0.1$ Pa-s, and $\sigma = 0.04$ N-m
Heat transfer modeling assumption	Flow is "adiabatic"
Spreading cavity nodalization	Reservoir modeled as a single cell with area 0.1064 m^2, spreading arc length of 19.05 cm, node length of 41.1 cm, and elevation flush with the spreading surface. The weir was modeled with a single cell that was 24.0 cm above the spreading surface and had a thickness (length) of 1.4 cm. The spreading channel was modeled as a 19º angular sector; the 6.5 m radial length was subdivided into 200 nodes of equal radial length of 3.25 cm.
Timestep	0.05 seconds

[a]As applicable, ρ is density, μ_o is viscosity at the liquidus, and σ is surface tension.

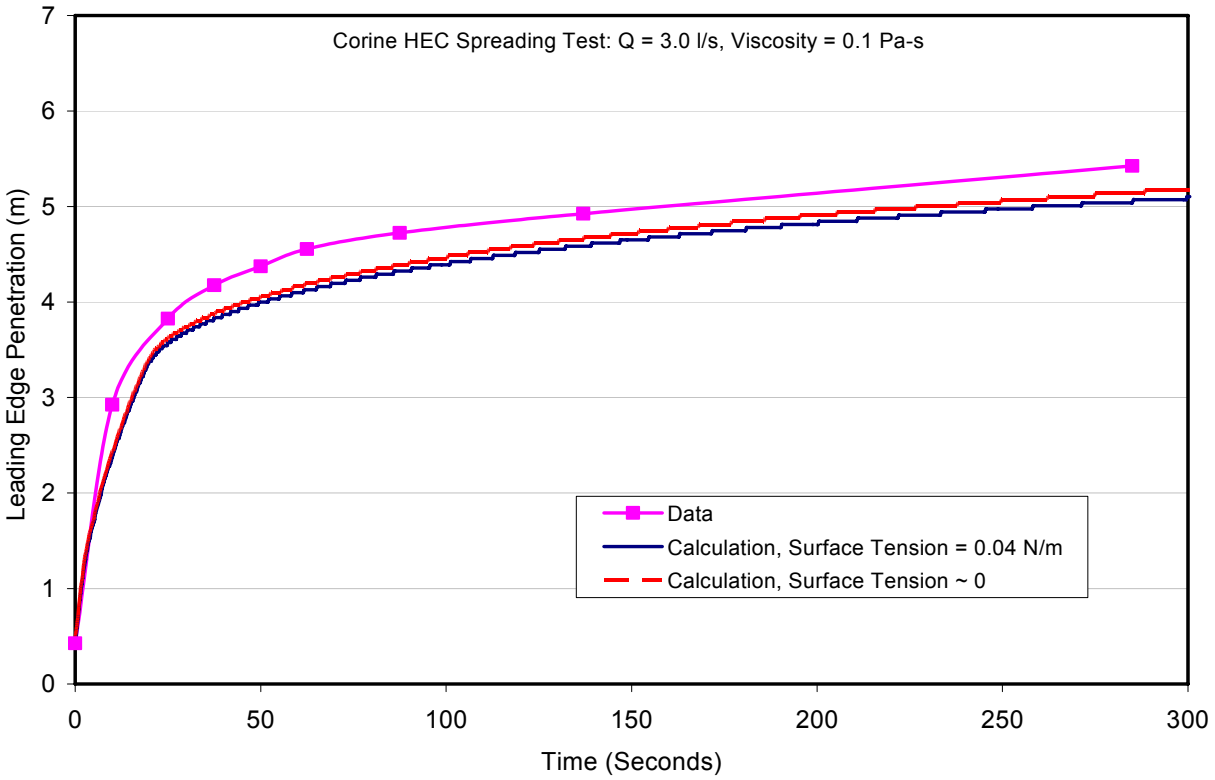

Figure A.17. Leading edge penetration comparison for Corine Test HEC_3_GO_0.1.

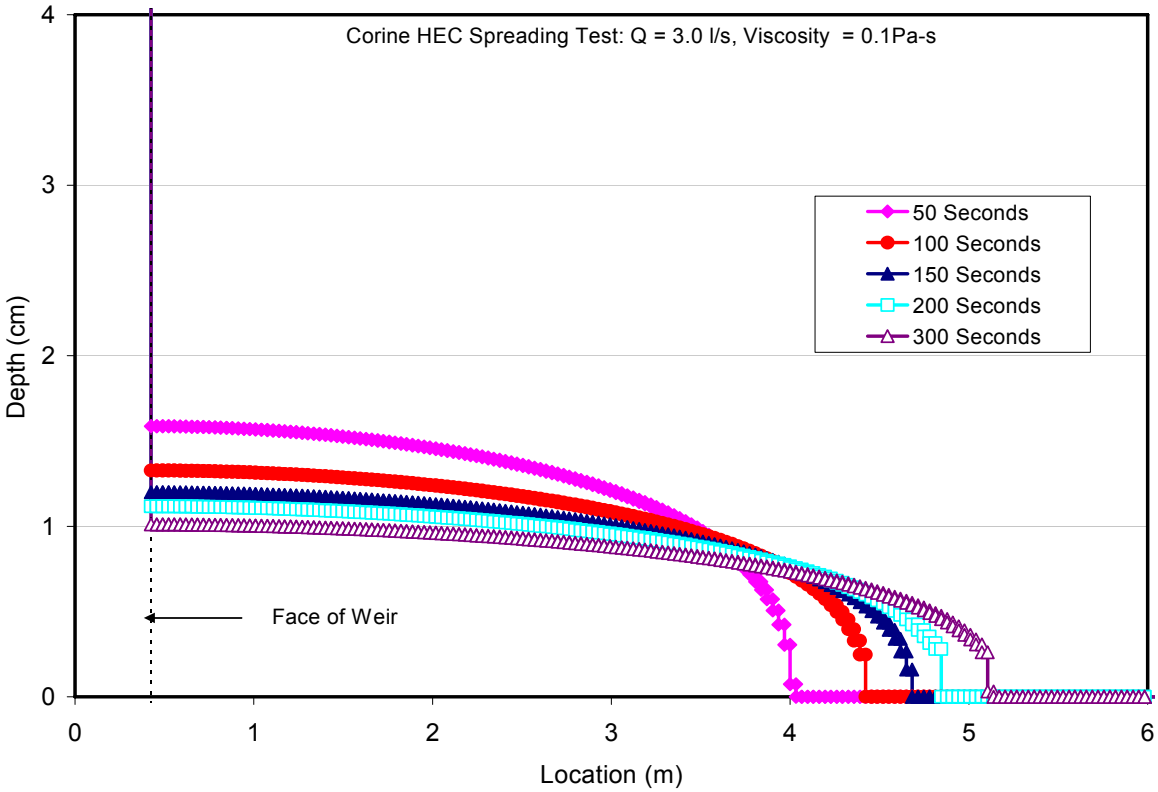

Figure A.18. Predicted local depth profiles at various times for Corine Test HEC_3_GO_0.1.

Table A.6. Input File Data Sheet for Corine Test HEC_3_GO_2.0 (glycol in a 19º sector).

Test parameter	**Value**
Test name	HEC_3_GO_2.0
Fluid composition (wt %)	100 Hydroxyl ethyl cellulose (HEC)
Fluid delivery technique	Fluid pumped from below into a delivery reservoir that was circular with a cross-sectional area of 0.1064 m^2. The reservoir was separated from the spreading channel by a weir that was 24.0 cm high and had a wall thickness of 1.4 cm.
Total pour mass	65 (25 kg to fill the reservoir, 40 kg spread)
Spreading geometry	6.5 m long, 19º angular sector
Code input parameter(s)	**Value(s)**
Fluid composition (wt %)	100 Hydroxyl ethyl cellulose (HEC)
Fluid pour rate and duration	Injection flowrate into the reservoir constant at 3.0 kg/sec over a time interval of 21.67 seconds.
Fluid material property evaluation[a]	User-specified property data: $\rho = 1000$ kg/m^3, $\mu_o = 2.0$ Pa-s, and $\sigma = 0.04$ N-m
Heat transfer modeling assumption	Flow is "adiabatic"
Spreading cavity nodalization	Reservoir modeled as a single cell with area 0.1064 m^2, spreading arc length of 19.05 cm, node length of 41.1 cm, and elevation flush with the spreading surface. The weir was modeled with a single cell that was 24.0 cm above the spreading surface and had a thickness (length) of 1.4 cm. The spreading channel was modeled as a 19º angular sector; the 6.5 m radial length was subdivided into 200 nodes of equal radial length of 3.25 cm.
Timestep	0.05 seconds

[a]As applicable, ρ is density, μ_o is viscosity at the liquidus, and σ is surface tension.

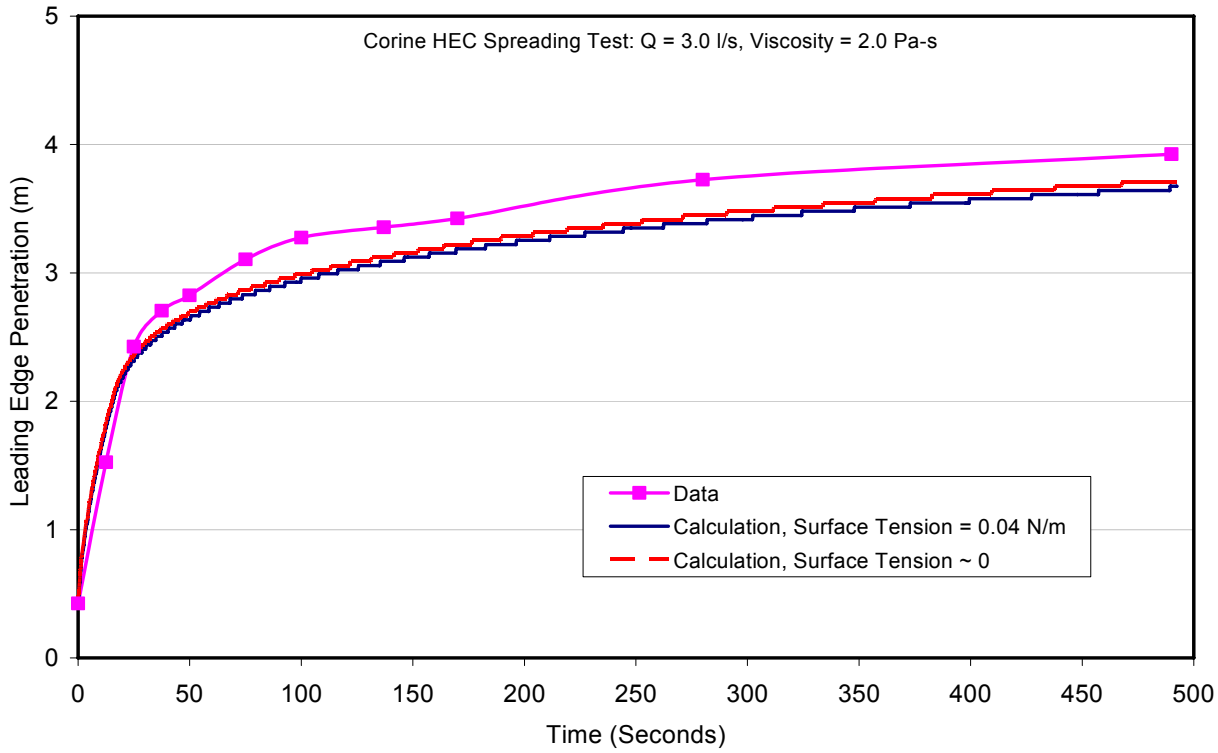

Figure A.19. Leading edge penetration comparison for Corine Test HEC_3_GO_2.0.

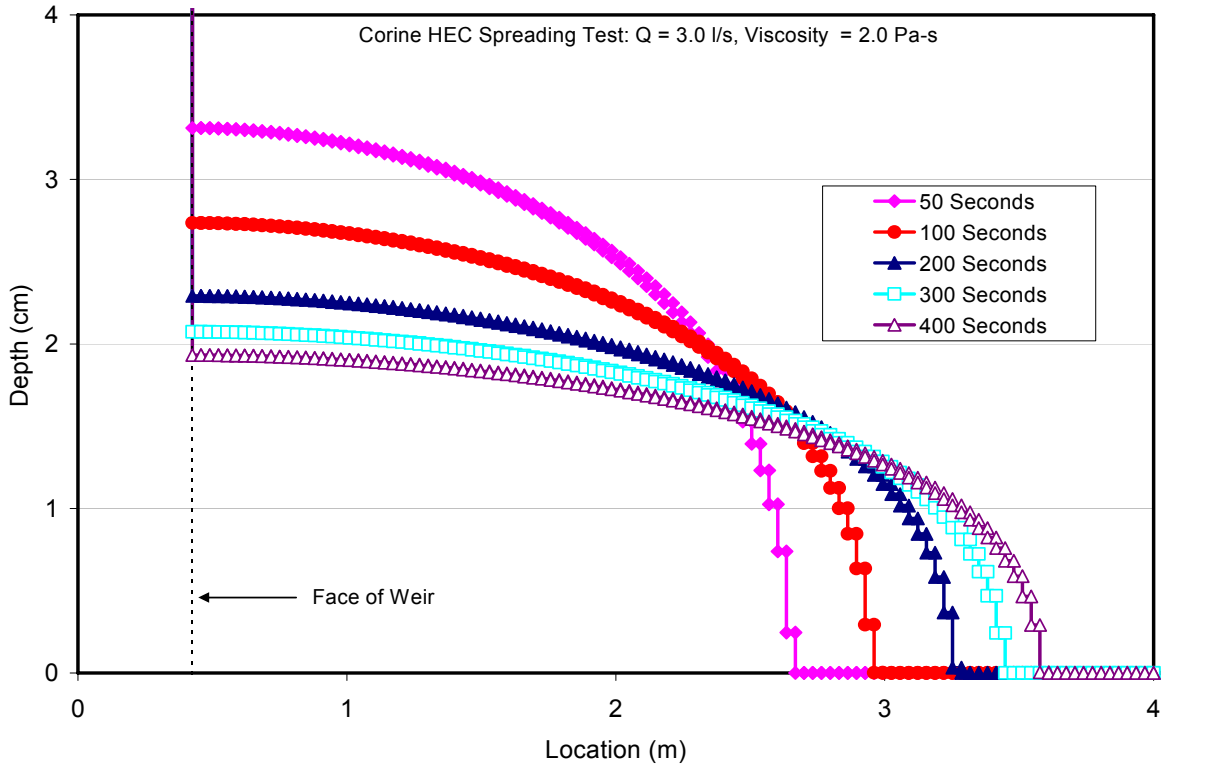

Figure A.20. Predicted local depth profiles at various times for Corine Test HEC_3_GO_2.0.

A.2 High Temperature Tests with Simulant Oxide Melts

Following the benchmarking exercise against isothermal spreading test results, the code was then applied to experiments involving heat transfer and freezing effects. The first class of tests considered were those that utilized simulant oxide materials. Tests that fall into this category include those by Engel et al.[12] and Eppinger et al.[13] in the KATS test facility, and those by Foit[14] and Alsmeyer et al.[15] in the ECOKATS facility. In addition, high temperature calcia – boria eutectic spreading experiments were carried out under both wet and dry cavity conditions by Dinh et al.[11,38] at the Royal Institute of Technology (RIT) in Sweden. Comparisons with these various tests are provided in this section.

A.2.1 KATS Oxide Simulant Spreading Tests

These tests involved spreading of high temperature oxide melts that principally contained concrete decomposition byproducts, but with a small amount of FeO (i.e., 83.0/8.5/6.0/1.5/1.0 wt % $Al_2O_3/SiO_2/FeO/MgO/MnO$). These melts were generated using a modified iron-alumina thermite reaction. The reaction byproduct consisted of a superheated iron metal phase that was segregated from the oxide, thereby allowing both the metal and oxide phases to be spread in separate one dimensional channels. The counterpart metal tests are analyzed later in this section.

For the oxide test series, the KATS-12, -13, and -14 experiments were selected for analysis (see Table 2.1). KATS-12 and -13 parameterized on substrate composition, with KATS-12 utilizing ceramic (Corderite), and KATS-13 utilizing concrete. KATS-14 was also conducted with a ceramic substrate, but the melt pour rate was reduced relative to KATS-12.

The accumulator design in these tests was somewhat novel, with a base that was slightly elevated relative to the spreading surface. The general characteristics are shown in Figure A.21, while the corresponding dimensions for each test are summarized in Table A.7. As is evident, a small incline connected the accumulator to the spreading channel.

Test characteristics and the code input that was developed for the KATS-12 test are summarized in Table A.8. As is evident, an effort was made with the meshing scheme to physically mock up the details of the melt accumulator, gate, and incline leading to the spreading channel. The experimenters[13] provided detailed specifications of melt pour rate vs. time as well as the material properties of the melt and ceramic substrate. This information was all used as part of the calculation.

The calculated leading edge penetration vs. time is compared to the test data in Figure A.22, while local melt temperature and post-spreading material profile predictions are compared with data in Figures A.23 and A.24, respectively. The pour rate in this test was relatively high and so the spreading rate was initially dominated by inertial effects. As a result, viscous forces that retard the spreading rate do not show up until late in the spreading transient (see Figure A.22). Results for C_R and $C_R \pm 2\sigma_{C_R}$ (Table 2.3) are shown in the figure of melt penetration vs. time. As is evident from Figure A.22, despite discrepancies in melt arrival times, peak melt temperatures are predicted to within ~ 30 K near the melt injection point, but the discrepancy grows to ~ 70 K near the channel midpoint. As shown in Figure A.23, the debris profile is

reasonably predicted (code data are for the average C_R case). The large structure to the left in this figure is the melt accumulator. Given this design and high melt injection rate, the possibility exists that the melt jetted out of feedbox, causing overshoot of some (unknown) distance of the spreading surface and an initial spreading velocity that would exceed what the code would calculate based on gravity-driven spreading alone. This may explain at least part of the discrepancy in initial spreading rate seen early in the sequence, as the code assumes continuous flow through the mesh with no possibility of bypass.

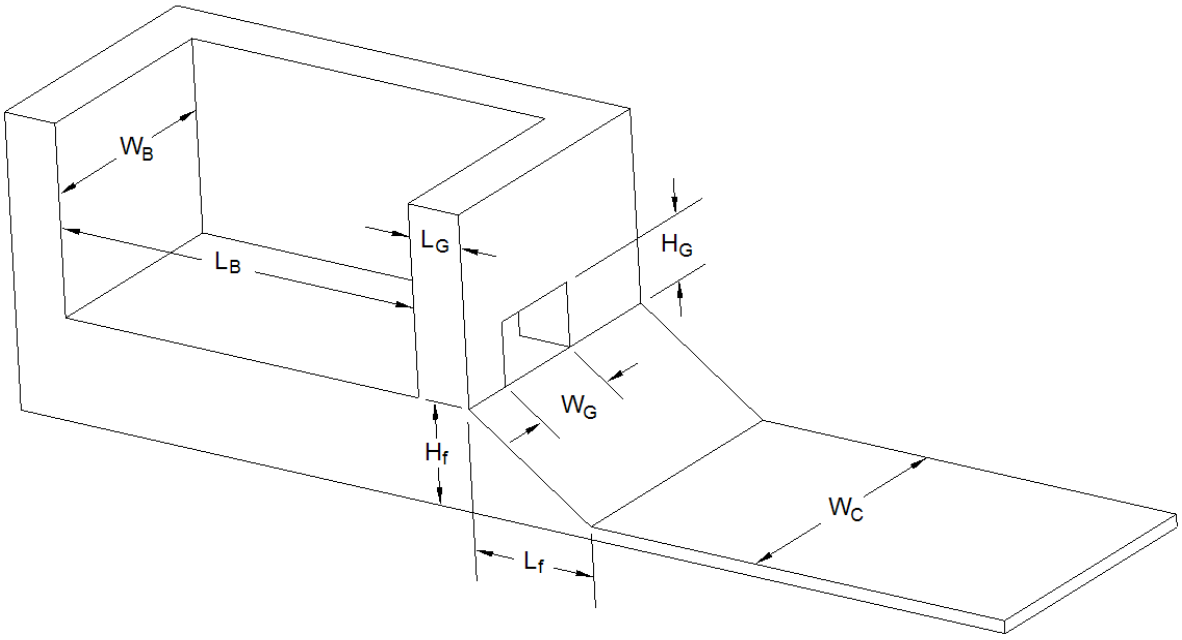

Figure A.21. Melt accumulator characteristics for the KATS tests.

Table A.7. Melt Accumulator Dimensions for KATS Tests (see Figure A.21 for nomenclature).

Test	Spreading Device Dimension (mm):						
	L_B	W_B	L_G	W_G	H_G	L_f	H_f
KATS-12 Metal	302	170	43	80	50	100	70
KATS-12 Oxide	382	367	43	140	50	110	70
KATS-13 Metal	302	170	43	80	50	100	90
KATS-13 Oxide	382	367	43	140	50	110	90
KATS-14 Metal	200	180	43	140	30	30	50
KATS-14 Oxide	300	300	43	240	40	80	100

Table A.8. Input File Data Sheet for the KATS-12 Oxide Melt Test with Ceramic Channel.

Test parameter	Value
Test name	KATS-12 oxide, ceramic channel
Melt composition (wt %)	83.0 Al_2O_3, 8.5 SiO_2, 6.0 FeO, 1.5 MgO, 1.0 MnO
Melt delivery technique	Melt poured into an accumulator box that was 36.7 cm wide, 38.2 cm long, and 7.0 cm above the spreading surface. Pour initiated by opening a gate to the spreading channel.
Melt temperature	2300 K
Total pour mass	186 kg
Substrate material	Cordierite
Spreading geometry	1-D channel, 12 m long by 25 cm wide
Code input parameter(s)	**Value(s)**
Melt composition (wt %)	83.0 Al_2O_3, 8.5 SiO_2, 6.0 FeO, 1.5 MgO, 1.0 MnO
Melt pour temperature	2300 K
Melt oxide phase solidus – liquidus	1850 K – 2200 K
Melt metal phase solidus – liquidus	1810 K – 1820 K
Melt pour rate and duration	Linear decrease in pour rate from 37.1 kg/sec to zero over 10 second interval
Melt material property evaluation[a]	User-specified property data used: c_s = 1280 J/kg-K, c_l = 1423 J/kg-K, Δh_f= 802 kJ/kg, $\rho_s = \rho_l$ = 2800 kg/m^3, $k_s = k_l$ = 5.4 W/m-K, μ_o = 0.05 Pa-s, σ = 0.5 N-m, M = 91.7 g/mole, and ε = 0.8
Substrate composition	Corderite (modeled using user-specified material input properties)
Substrate initial temperature	298 K
Substrate material properties evaluation[a]	$c_s = c_l$ = 840 J/kg-K, Δh_f= 1.0 MJ/kg, $\rho_s = \rho_l$ = 2200 kg/m^3, $k_s = k_l$ = 3.8 W/m-K, and ε = 0.3
Substrate solidus - liquidus temperatures	1893 K – 1923 K
Substrate nodalization	At each substrate nodal location, twelve 6.0 mm cells are used; all nodes are cell-centered.
Spreading cavity nodalization	Accumulator: modeled as a single cell that is 36.7 cm wide, 38.2 cm long, and 7.0 cm above the channel surface. Gate: modeled as a single cell that is 14 cm wide, 4.3 cm long, and 7.0 cm above the channel. Incline down to channel: modeled as a single cell that is 11 cm long, 25 cm wide, and 3.5 cm above the channel. Channel: modeled using 120 cells; each is 25 cm wide and 10 cm long. All nodes cell-centered.
Cavity condition	Dry
Upper atmosphere temperature	300 K
Upper atmosphere emissivity	0.7
Ambient pressure	0.1 MPa
Melt/substrate heat transfer coefficient model	Dittus - Boelter
Melt/substrate interfacial heat transfer resistance	Not modeled
Best-fit constant in Ramacciotti correlation	1.83
Solid-fraction variation between liquidus/solidus	See Figure 2.3
Timestep	0.02 seconds

[a]As applicable, c denotes specific heat, Δh_f is latent heat of fusion, ρ is density, k is thermal conductivity, μ_o is viscosity at the liquidus, σ is surface tension, M is molecular weight, ε is emissivity, and subscripts s and l denote solid and liquid phases, respectively.

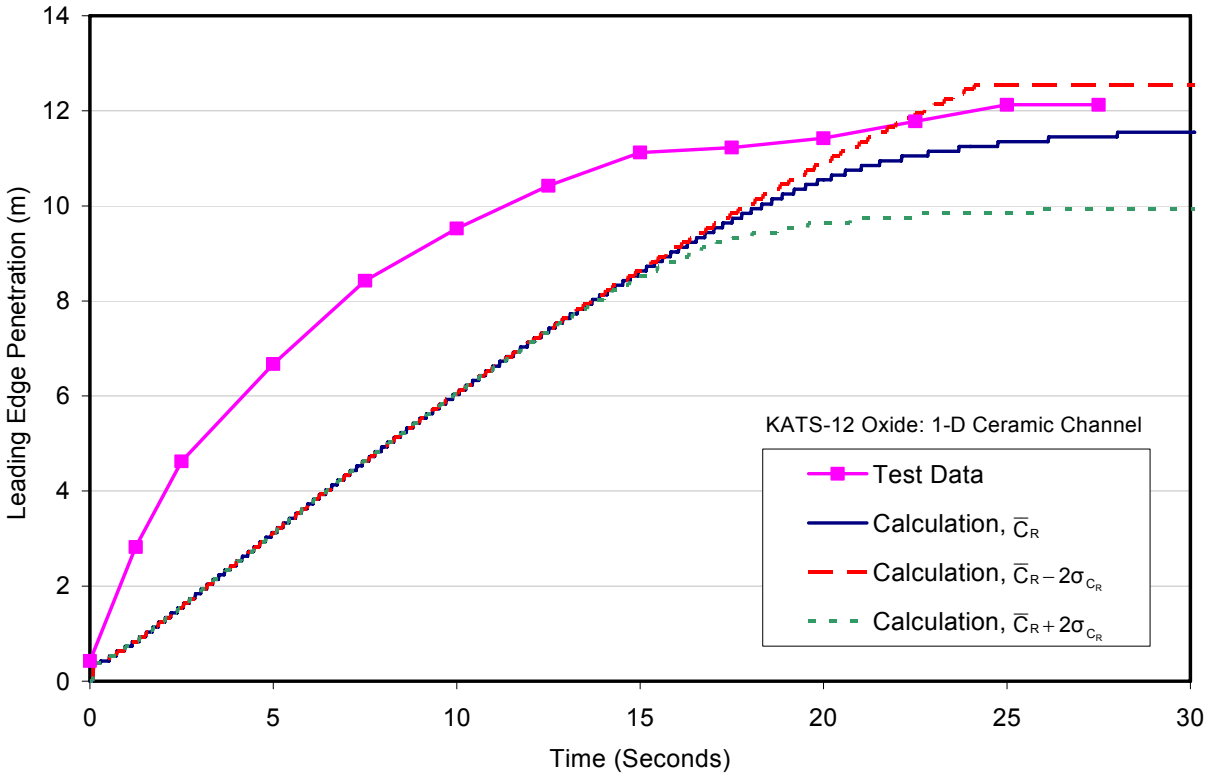

Figure A.22. Leading edge penetration comparison for the KATS-12 oxide spreading test.

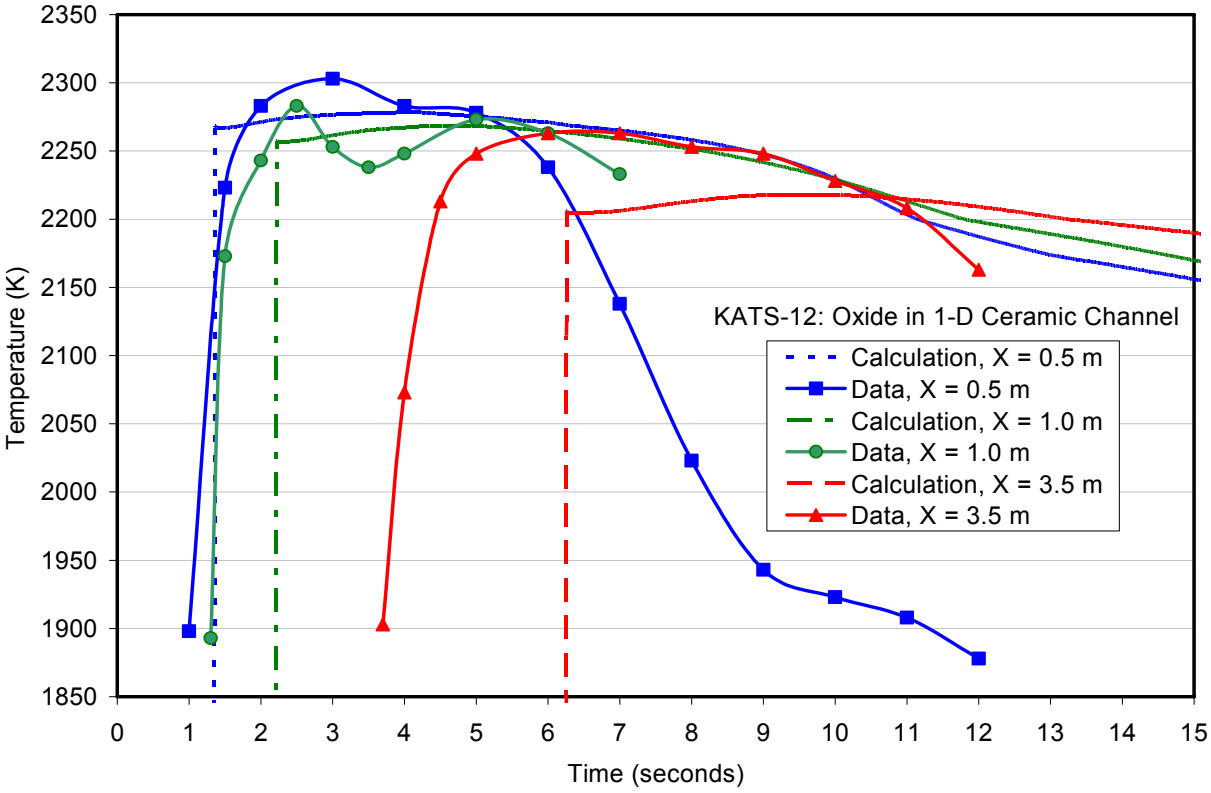

Figure A.23. Comparison of local melt temperature predictions with KATS-12 oxide data.

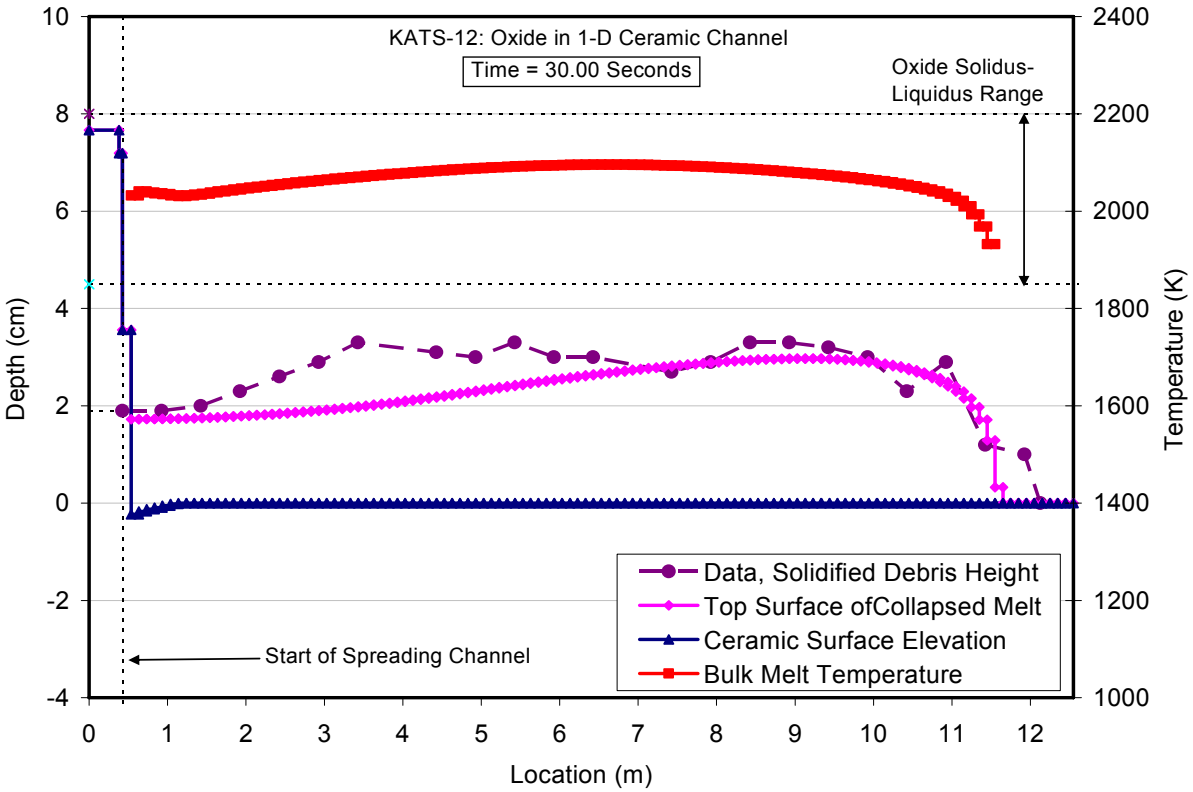

Figure A.24. Comparison of posttest debris profile prediction with KATS-12 oxide data.

Test characteristics and modeling input for the KATS-13 test are summarized in Table A.9. As for the KATS-12 simulation, the experimental specifications[13] for melt pour rate vs. time and the melt thermo-physical properties were used, but the code default composition for siliceous concrete was assumed since the data report did not provide this information. As discussed in Section 2, this test was an outlier in terms of the viscosity correlation constant C_R that was required to match the maximum melt penetration distance predicted by the code with the experiment (see Table 2.3). The calculated leading edge penetration vs. time is compared to the test data in Figure A.25, while local melt temperature and post-spreading material profile predictions are compared with the data in Figures A.26 and A.27, respectively. These results were obtained using the best fit C_R value of 10.28.

As for KATS-12, this was a high flowrate test and so the spreading rate was initially dominated by inertial effects. As noted previously, given the accumulator design and high melt flowate, the possibility exists that the melt overshot some distance of the spreading surface near the accumulator, leading to an apparent spreading velocity that was initially larger than the code prediction.

As is evident from Figure A.26, despite discrepancies in melt arrival times, peak melt temperatures are predicted to within ~ 40 K over the first 3.5 m of the spreading channel, but at the 6.5 m location, the code overpredicts the temperature by ~ 100 K. As shown in Figure A.27, local depths in the solidified debris are underpredicted, but the code calculates solidification assuming a fully dense melt condition, whereas the debris most likely solidified with porosity present from gas sparging due to concrete decomposition.

Table A.9. Input File Data Sheet for the KATS-13 Oxide Melt Test with Concrete Channel.

Test parameter	Value
Test name	KATS-13 oxide, concrete channel
Melt composition (wt %)	83.0 Al_2O_3, 8.5 SiO_2, 6.0 FeO, 1.5 MgO, 1.0 MnO
Melt delivery technique	Melt poured into an accumulator box that was 36.7 cm wide, 38.2 cm long, and 9.0 cm above the spreading surface. Pour initiated by opening a gate to the spreading channel.
Melt temperature	2320 K
Total pour mass	186 kg
Substrate material	Siliceous concrete
Spreading geometry	1-D channel, 12 m long by 25 cm wide
Code input parameter(s)	**Value(s)**
Melt composition (wt %)	83.0 Al_2O_3, 8.5 SiO_2, 6.0 FeO, 1.5 MgO, 1.0 MnO
Melt pour temperature	2320 K
Melt oxide phase solidus – liquidus	1850 K – 2200 K
Melt metal phase solidus – liquidus	1810 K – 1820 K
Melt pour rate and duration	Linear decrease in pour rate from 37.1 kg/sec to zero over 10 second interval
Melt material property evaluation[a]	User-specified property data used: c_s = 1280 J/kg-K, c_l = 1423 J/kg-K, Δh_f= 802 kJ/kg, $\rho_s = \rho_l$ = 2800 kg/m^3, $k_s = k_l$ = 5.4 W/m-K, μ_o = 0.05 Pa-s, σ = 0.5 N-m, M = 91.7 g/mole, and ε = 0.8
Substrate composition	Default siliceous concrete
Substrate initial temperature	298 K
Substrate material properties evaluation[a]	Code subroutines
Substrate solidus - liquidus temperatures	1403 – 1523 K (Code default values)
Substrate nodalization	At each substrate nodal location, twelve 6.0 mm cells are used; all nodes cell-centered.
Spreading cavity nodalization	Accumulator: modeled as a single cell that is 36.7 cm wide, 38.2 cm long, and 9.0 cm above the channel surface. Gate: modeled as a single cell that is 14 cm wide, 4.3 cm long, and 9.0 cm above the channel. Incline down to channel: modeled as a single cell that is 11 cm long, 25 cm wide, and 4.5 cm above the channel. Channel: modeled using 120 cells; each is 25 cm wide and 10 cm long. All nodes cell-centered.
Cavity condition	Dry
Upper atmosphere temperature	300 K
Upper atmosphere emissivity	0.7
Ambient pressure	0.1 MPa
Melt/substrate heat transfer coefficient model	Locally, largest of Dittus – Boelter and Bradley slag film heat transfer coefficients
Melt/substrate interfacial heat transfer resistance	Not modeled
Best-fit constant in Ramacciotti correlation	10.28
Solid-fraction variation between liquidus/solidus	See Figure 2.3
Timestep	0.02 seconds

[a]As applicable, c denotes specific heat, Δh_f is latent heat of fusion, ρ is density, k is thermal conductivity, μ_o is viscosity at the liquidus, σ is surface tension, M is molecular weight, ε is emissivity, and subscripts s and l denote solid and liquid phases, respectively.

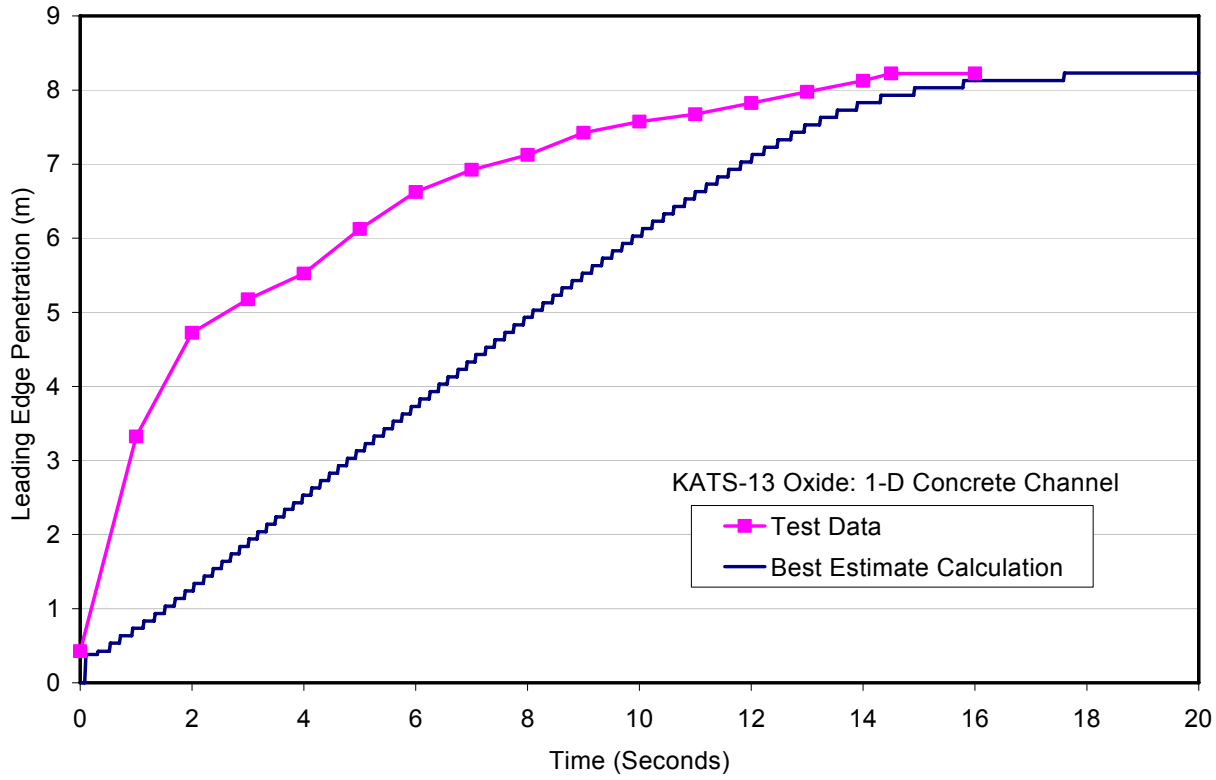

Figure A.25. Leading edge penetration comparison for the KATS-13 oxide spreading test.

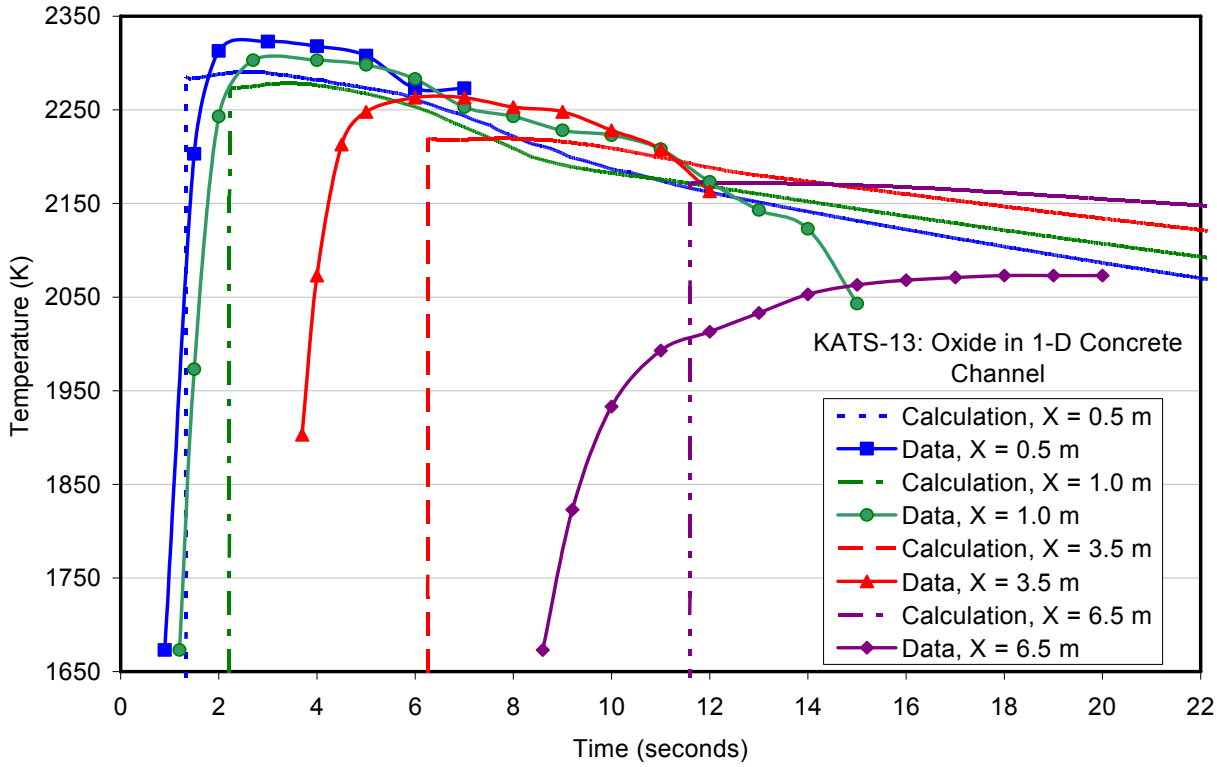

Figure A.26. Comparison of local melt temperature predictions with KATS-13 oxide data.

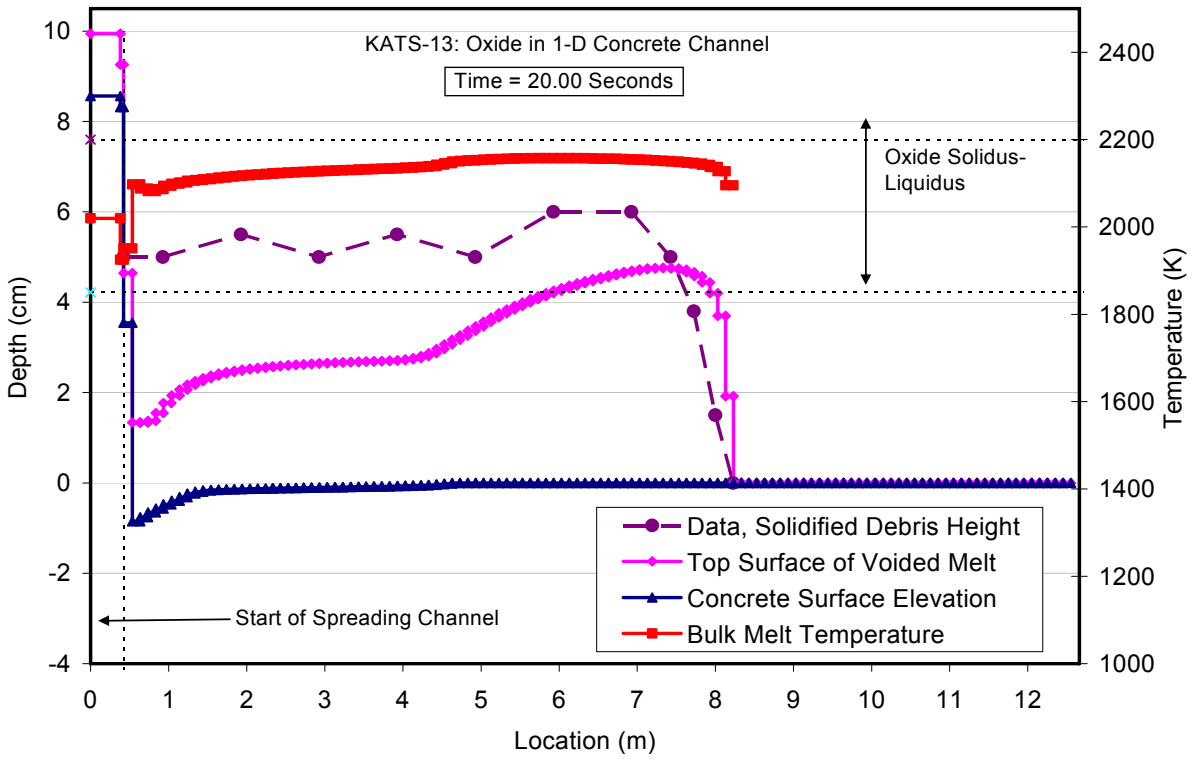

Figure A.27. Comparison of posttest debris profile prediction with KATS-13 oxide data.

Test characteristics and the corresponding code input that was developed for KATS-14 are summarized in Table A.10. As for KATS-12, the experimenter's specifications[13] for melt pour rate, as well as the melt and substrate thermo-physical properties, were used. The calculated leading edge penetration versus time is compared to the test data in Figure A.28, while local melt temperature and post-spreading material profile predictions are compared with the data in Figures A.29 and A.30, respectively. The pour rate in this test was lower compared to the the counterpart test KATS-12, and so the time interval over which the spreading characteristics were governed by viscous effects was larger. Results for leading edge penetration in Figure A.28 are shown for the average value of C_R, as well as $C_R \pm 2\sigma_{C_R}$ (Table 2.3). Due to the increased effect of viscosity, the spread in the maximum melt penetration for the various cases is correspondingly larger relative to KATS-12 (see Figure A.22). In general, the code does a much better job capturing the initial rate of melt spreading from the accumulator box in comparison to KATS-12.

Examination of the melt temperature data in Figure A.28 indicates that despite discrepancies in melt arrival times, peak melt temperatures are predicted to within ~ 50 K at the 1 meter location, and to within ~ 10 K at the 3 m location. The code under-predicts the melt temperature by ~ 150 K at the 5 m location, but note that the recorded peak here exceeds that at 3 m by ~ 30 K, which does not seem physically plausible. As shown in Figure A.30, the debris thickness after spreading is slightly underpredicted, but this is again due to the fact that the code assumes a fully dense condition upon solidification, whereas experience has shown that melts always solidify with some porosity present.

Table A.10. Input File Data Sheet for the KATS-14 Oxide Melt Test with Ceramic Channel.

Test parameter	Value
Test name	KATS-14 oxide, ceramic channel
Melt composition (wt %)	83.0 Al_2O_3, 8.5 SiO_2, 6.0 FeO, 1.5 MgO, 1.0 MnO
Melt delivery technique	Melt poured into an accumulator box that was 30.0 cm wide, 30.0 cm long, and 10.0 cm above the spreading surface. Pour initiated by opening a gate to the spreading channel.
Melt temperature	2245 K
Total pour mass	176 kg
Substrate material	Cordierite
Spreading geometry	1-D channel, 12 m long by 25 cm wide
Code input parameter(s)	**Value(s)**
Melt composition (wt %)	83.0 Al_2O_3, 8.5 SiO_2, 6.0 FeO, 1.5 MgO, 1.0 MnO
Melt pour temperature	2245 K
Melt oxide phase solidus – liquidus	1850 K – 2200 K
Melt metal phase solidus – liquidus	1810 K – 1820 K
Melt pour rate and duration	Linear decrease in pour rate from 5.95 kg/sec to 3.57 kg/sec over a 37 second interval
Melt material property evaluation[a]	User-specified property data used: c_s = 1280 J/kg-K, c_l = 1423 J/kg-K, Δh_f= 802 kJ/kg, $\rho_s = \rho_l$ = 2800 kg/m^3, $k_s = k_l$ = 5.4 W/m-K, μ_o = 0.05 Pa-s, σ = 0.5 N-m, M = 91.7 g/mole, and ε = 0.8
Substrate composition	Corderite (modeled using user-specified material input properties)
Substrate initial temperature	298 K
Substrate material properties evaluation[a]	$c_s = c_l$ = 840 J/kg-K, Δh_f= 1.0 MJ/kg, $\rho_s = \rho_l$ = 2200 kg/m^3, $k_s = k_l$ = 3.8 W/m-K, and ε = 0.3
Substrate solidus - liquidus temperatures	1893 K – 1923 K
Substrate nodalization	At each substrate nodal location, twelve 6.0 mm cells are used; all nodes are cell-centered.
Spreading cavity nodalization	Accumulator: modeled as a single cell that is 30.0 cm wide, 30.0 cm long, and 10.0 cm above the channel surface. Gate: modeled as a single cell that is 24 cm wide, 4.3 cm long, and 10.0 cm above the channel. Incline down to channel: modeled as a single cell that is 8 cm long, 25 cm wide, and 5.0 cm above the channel. Channel: modeled using 120 cells; each is 25 cm wide and 10 cm long. All nodes cell-centered.
Cavity condition	Dry
Upper atmosphere temperature	300 K
Upper atmosphere emissivity	0.7
Ambient pressure	0.1 MPa
Melt/substrate heat transfer coefficient model	Dittus – Boelter
Melt/substrate interfacial heat transfer resistance	Not modeled
Best-fit constant in Ramacciotti correlation	1.56
Solid-fraction variation between liquidus/solidus	See Figure 2.3
Timestep	0.02 seconds

[a]As applicable, c denotes specific heat, Δh_f is latent heat of fusion, ρ is density, k is thermal conductivity, μ_o is viscosity at the liquidus, σ is surface tension, M is molecular weight, ε is emissivity, and subscripts s and l denote solid and liquid phases, respectively.

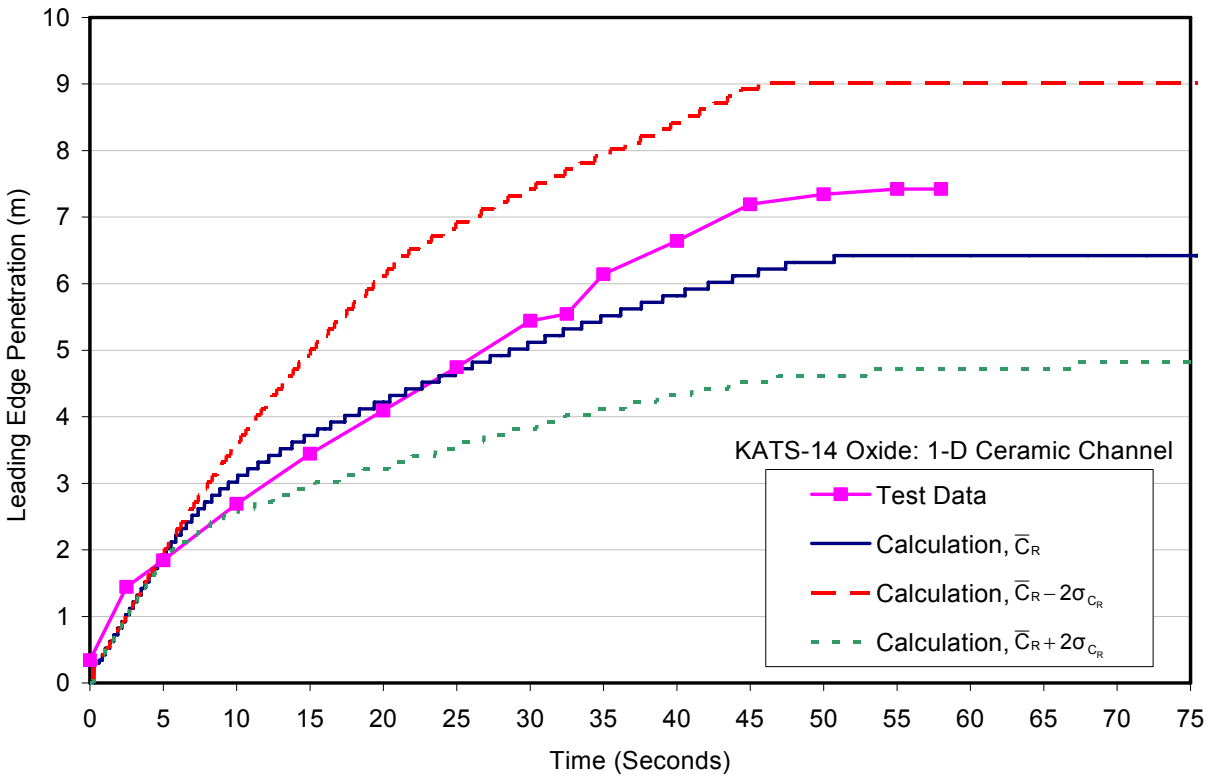

Figure A.28. Leading edge penetration comparison for the KATS-14 oxide spreading test.

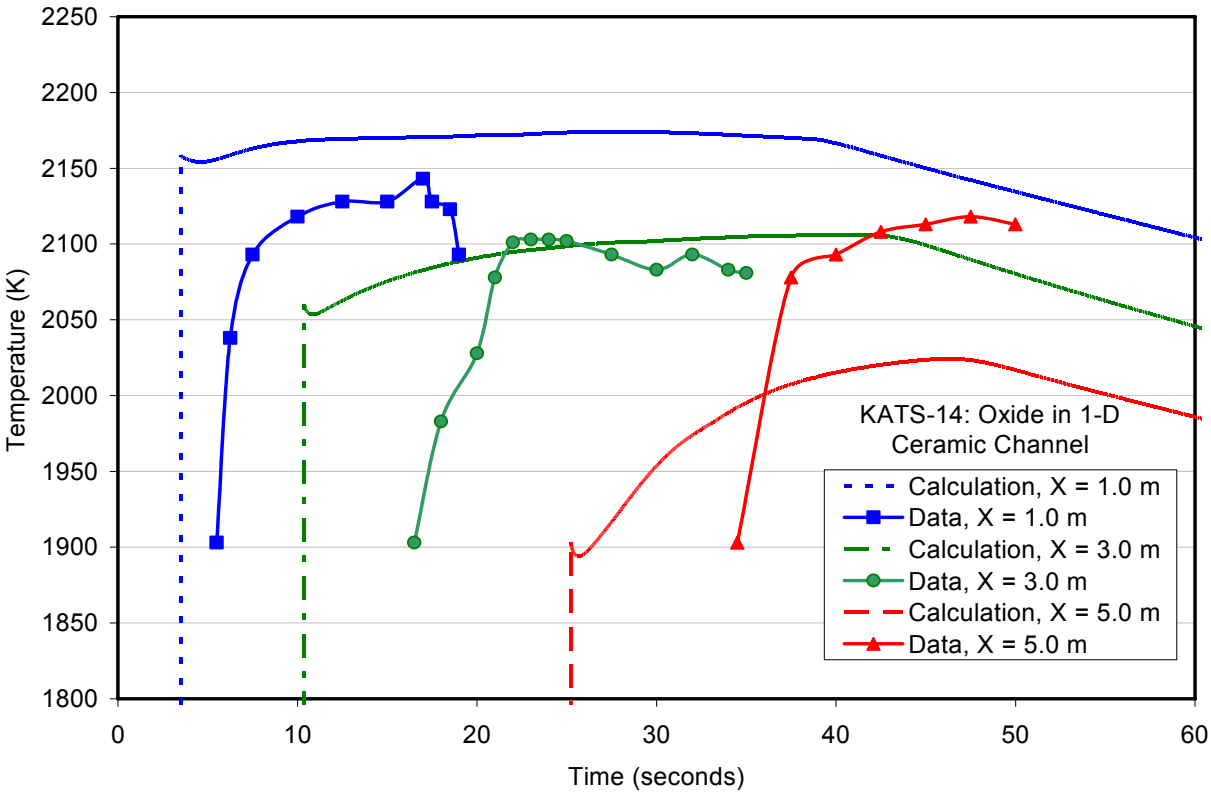

Figure A.29. Comparison of local melt temperature predictions with KATS-14 oxide data.

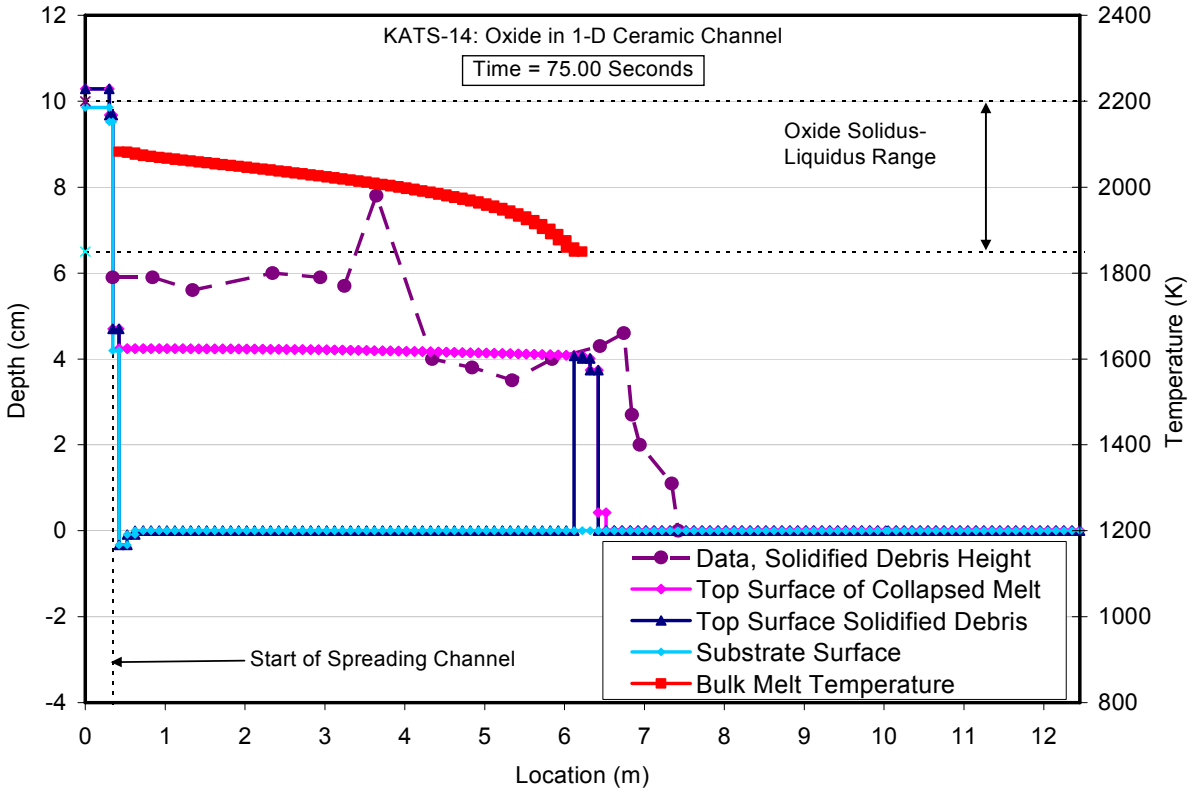

Figure A.30. Comparison of posttest debris profile prediction with KATS-14 oxide data.

A.2.2 ECOKATS Oxide Simulant Spreading Tests

These tests followed the KATS spreading tests described in the previous section, but the experiments were increased in scale and flow complexity to provide a more diverse database, and to examine some additional phenomenology (i.e. coolability) that was not considered in KATS. The experimenters again used a modified thermite reaction to generate the melts, but the resultant oxide was slightly different compared to KATS (i.e., 41.0/24.0/19.0/16.0 wt % Al_2O_3/FeO/CaO/SiO_2 for ECOKATS vs. 83.0/8.5/6.0/1.5/1.0 wt % Al_2O_3/SiO_2/FeO/MgO/MnO for KATS). As shown in Table 2.1, ECOKATS-V1 was a 1-D spreading test with a ceramic substrate, whereas ECOKATS-1 and -2 were 2-D tests using concrete substrates. ECOKATS-2 had the added dimension of a multi-component melt pour in which the iron phase was spread first, followed by the oxide.

Test characteristics and code input for the ECOKATS-V1 test are summarized in Table A.11, while leading edge penetration and the post-spreading material profile predictions are compared with the data in Figures A.31 and A.32, respectively. The experimentally specified melt pour rate, as well as the material properties of the melt and ceramic substrate, were input as part of the calculation.

Examination of these figures indicates that the overall rate of melt propagation during the spreading transient is captured reasonably well by the code. In addition, the shape of depth profile after spreading is reasonably predicted, but overall thickness of the layer is again somewhat underpredicted due to the fact the code does not include porosity during solidification.

Table A.11. Input File Data Sheet for the ECOKATS-V1 Test.

Test parameter	Value
Test name	ECOKATS-V1
Melt composition (wt %)	41.0 Al_2O_3, 24.0 FeO, 19.0 CaO, and 16.0 SiO_2
Melt delivery technique	Melt poured into an accumulator box that was modeled as a 29.3 cm wide, 22.5 cm long, and flush with the spreading surface. Pour initiated by melt injection into the accumulator box.
Melt temperature	1893 K
Total pour mass	193 kg
Substrate material	Cordierite
Spreading geometry	1-D channel, 8 m long by 29.3 cm wide
Code input parameter(s)	**Value(s)**
Melt composition (wt %)	41.0 Al_2O_3, 24.0 FeO, 19.0 CaO, and 16.0 SiO_2
Melt pour temperature	1893 K
Melt oxide phase solidus – liquidus	1373 K – 1822 K
Melt metal phase solidus – liquidus	1810 K – 1820 K
Melt pour rate and duration	For 0 – 13.7 sec, 4.238 kg/sec pour rate; for 13.7 – 40.5 sec, 3.463 kg/sec; for 40.5 – 47.6 sec, 3.291 kg/sec; for 47.6 – 54.7, 2.61 kg/sec; for t > 54.7 sec, pour rate is zero.
Melt material property evaluation[a]	User-specified property data used: c_s = 1055 J/kg-K, c_l = 1220 J/kg-K, Δh_f= 1162 kJ/kg, $\rho_s = \rho_l$ = 3263 kg/m^3, $k_s = k_l$ = 5.4 W/m-K, μ_o = 0.2 Pa-s, σ = 0.5 N-m, M = 74.6 g/mole, and ε = 0.95
Substrate composition	Corderite (modeled using user-specified material input properties)
Substrate initial temperature	276 K
Substrate material properties evaluation[a]	$c_s = c_l$ = 840 J/kg-K, Δh_f= 1.0 MJ/kg, $\rho_s = \rho_l$ = 2200 kg/m^3, $k_s = k_l$ = 3.8 W/m-K, and ε = 0.3
Substrate solidus - liquidus temperatures	1893 K – 1923 K
Substrate nodalization	At each substrate nodal location, three 2.0 mm cells, one 4.0 mm cell, and eight 6.0 mm cells are used; all nodes are cell-centered.
Spreading cavity nodalization	Accumulator: modeled as a single cell that is a 29.3 cm wide, 22.5 cm long, and flush with the spreading channel. Channel: modeled using 80 cells; each is 29.3 cm wide and 10 cm long. All nodes cell-centered.
Cavity condition	Dry
Upper atmosphere temperature	300 K
Upper atmosphere emissivity	0.7
Ambient pressure	0.1 MPa
Melt/substrate heat transfer coefficient model	Dittus - Boelter
Melt/substrate interfacial heat transfer resistance	Not modeled
Best-fit constant in Ramacciotti correlation	1.83
Solid-fraction variation between liquidus/solidus	See Figure 2.3
Timestep	0.02 seconds

[a]As applicable, c denotes specific heat, Δh_f is latent heat of fusion, ρ is density, k is thermal conductivity, μ_o is viscosity at the liquidus, σ is surface tension, M is molecular weight, ε is emissivity, and subscripts s and l denote solid and liquid phases, respectively.

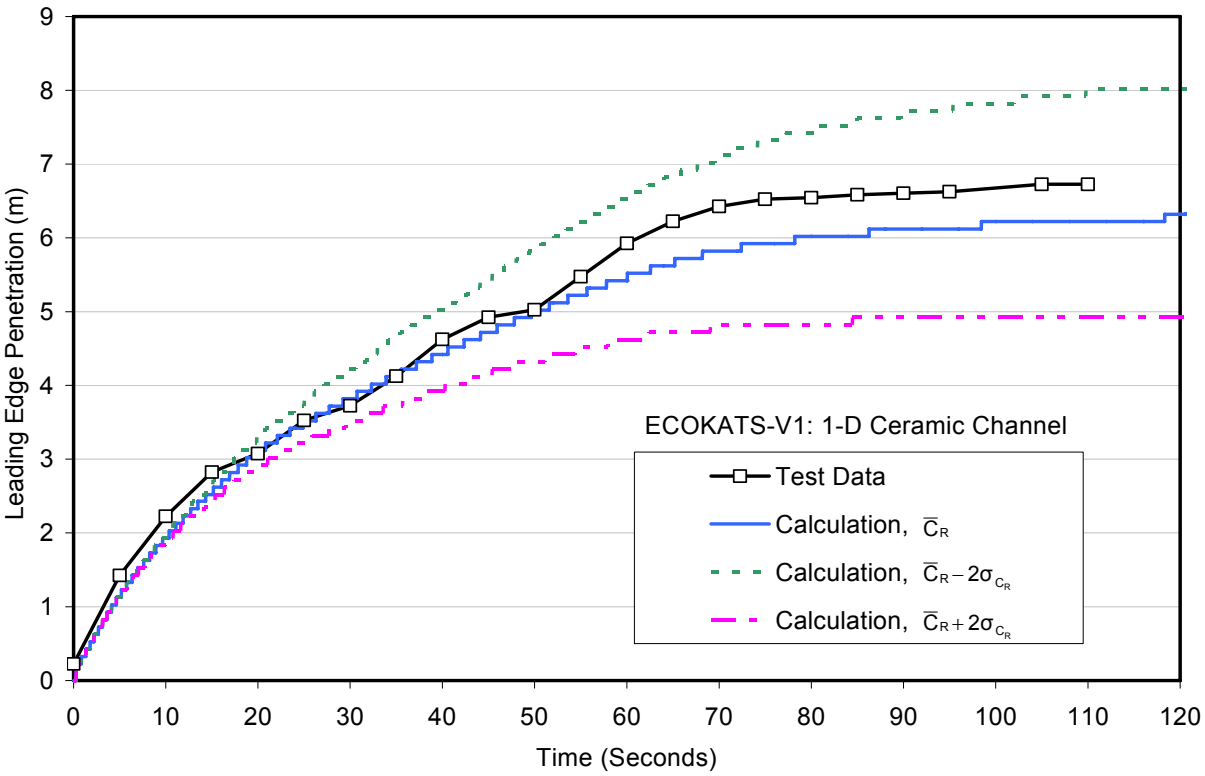

Figure A.31. Leading edge penetration comparison for the ECOKATS-V1 spreading test.

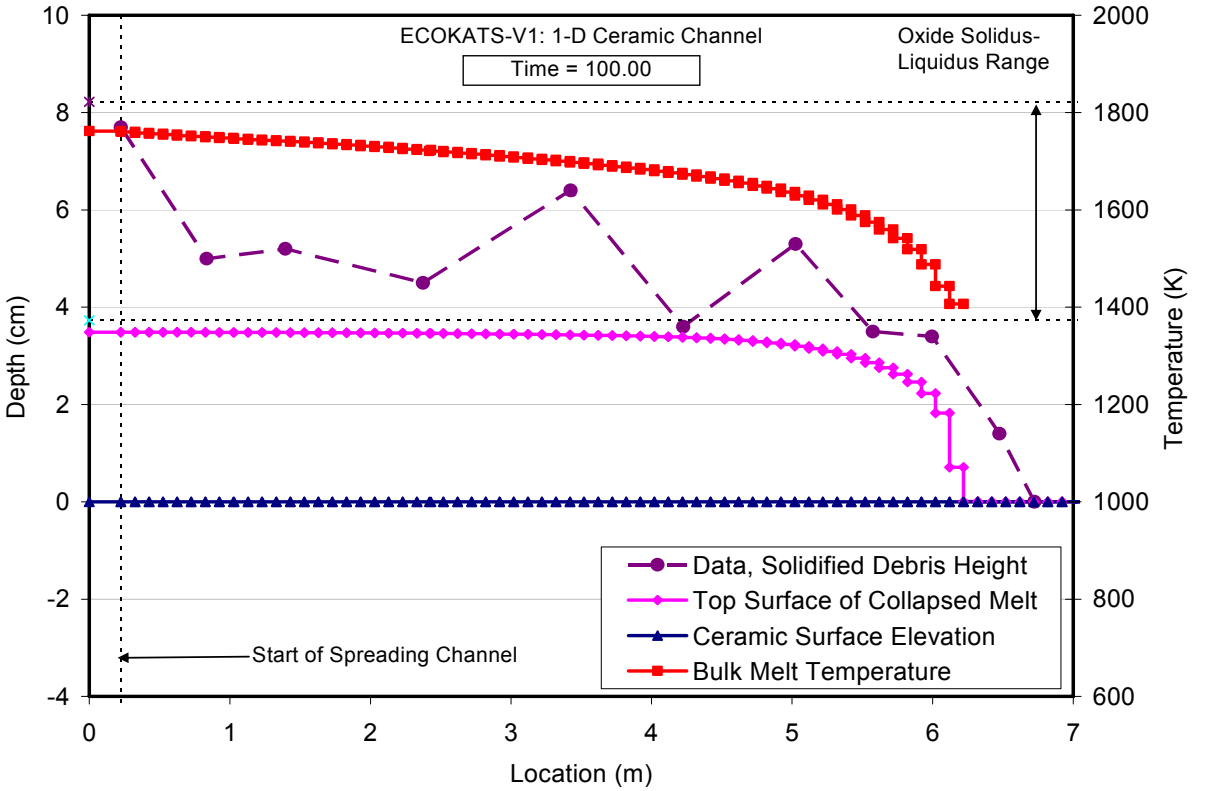

Figure A.32. Comparison of posttest debris profile prediction with ECOKATS-V1 data.

Test characteristics and code input for ECOKATS-1 are summarized in Table A.12. As for the ECOKATS-V1 simulation, the experimental specifications[13] for melt pour rate vs. time and the melt thermo-physical properties were used, but the code default composition for siliceous concrete was assumed since the data report did not provide this information. This test featured a melt accumulator box and a 2.6 m long 1-D spreading channel that entered into a 4 m long by 3 m wide rectilinear box on the centerline of one of the 3 m wide sides. The test data indicates that the melt roughly spread as a 180º sector, stopping just short of the outer wall of the box. On this basis, the system was modeled assuming flow into a 180º sector outside of the 1-D channel.

The calculated leading edge penetration versus time in the 1-D channel section is compared to the test data in Figure A.33, while the floor area coverage versus time in the balance of the system is compared in Figure A.34. In addition, predictions of the basemat thermal response 20 cm outside the channel exit are compared to the data in Figure A.35. Finally, the debris profile following spreading is shown in Figure A.36. Results for leading edge penetration indicate that the overall spreading velocity is reasonably predicted, and that the experiment result is bounded by the calculation using the statistical data for C_R (see Table 2.3). Examination of Figure A.35 indicates that, despite the offset in melt arrival time, the code does a reasonable job predicting the overall shape of the thermal response in the basemat, but temperatures are over-predicted by 50 to 80 K depending upon depth into the concrete. As shown in Figure A.36, the code predicts a few millimeters of concrete ablation in the last meter of the 1-D spreading channel. It is not known if this is physically reasonable since no mention is made of it in the documentation.

Test characteristics and code input for ECOKATS-2 are summarized in Table A.13. Similar to ECOKATS-1, this test featured a 2.7 m long, 1-D channel that issued into a 2 m long by 2 m wide spreading area. The substrate material was also siliceous concrete. However, for this test the channel entered adjacent to one of the spreading area walls and so, with the symmetry boundary condition, the experiment simulated a larger 2 m long by 4 m wide spreading surface. A second difference between the two tests was that the metal (iron) reaction byproduct from the thermite reaction was spread first, followed by the oxide, which offered the opportunity to examine a more complicated melt pour sequence. A third difference was that the melt was also flooded following spreading in this test to investigate the coolability of the spread melt. On this basis, a substantial pour mass (i.e., 3200 kg) was used so that a non-trivial post-spreading melt depth of ~ 15 cm was obtained in the apparatus. Since the melt covered the entire surface, this test could not be used to assess ultimate melt penetration distance with the code. The data also indicated that the melt spread roughly in a 45º sector after exiting the 1-D channel, and on that basis, the spreading geometry was modeled assuming a 45º sector flow outside the channel opening up until the melt reached the opposite side of the spreading box. Past this point, the material was assumed two relocate into two large nodes simulating the balance of the surface. Data for leading edge penetration was only provided up to the point when the melt contacted the opposite wall of the spreading box, and so a more detailed meshing beyond this point was not warranted.

The final note regarding modeling for this test is that since a distinct metal spreading transient occurred first, the user-option of applying a melt-substrate interfacial heat transfer resistance was invoked. As discussed in Section 2, a heat transfer resistance had to be added in

Table A.12 Input File Data Sheet for the ECOKATS-1 Test.

Test parameter	Value
Test name	ECOKATS-1
Melt composition (wt %)	41.0 Al_2O_3, 24.0 FeO, 19.0 CaO, and 16.0 SiO_2
Melt delivery technique	Melt poured into an accumulator box that was modeled as a 28.8 cm wide, 32.5 cm long, and flush with the spreading surface. Pour initiated by melt injection into the accumulator box.
Melt temperature	1873 K
Total pour mass	547 kg
Substrate material	Siliceous concrete
Spreading geometry	1-D channel, 2.6 m long, followed by a 4 m long by 3 m wide rectilinear spreading surface
Code input parameter(s)	**Value(s)**
Melt composition (wt %)	41.0 Al_2O_3, 24.0 FeO, 19.0 CaO, and 16.0 SiO_2
Melt pour temperature	1873 K
Melt oxide phase solidus – liquidus	1373 K – 1822 K
Melt metal phase solidus – liquidus	1810 K – 1820 K
Melt pour rate and duration	For 0 – 16.0 sec, 7.84 kg/sec pour rate; for 16.0 – 69.9 sec, 6.66 kg/sec; for 69.9 – 79.5 sec, 4.78 kg/sec; for 79.5 – 84.8 sec, 3.08 kg/sec; for t > 84.8 sec, pour rate is zero.
Melt material property evaluation[a]	User-specified property data used: c_s = 1055 J/kg-K, c_l = 1220 J/kg-K, Δh_f= 1162 kJ/kg, $\rho_s = \rho_l$ = 3263 kg/m^3, $k_s = k_l$ = 5.4 W/m-K, μ_o = 0.2 Pa-s, σ = 0.5 N-m, M = 74.6 g/mole, and ε = 0.95
Substrate composition	Default siliceous concrete
Substrate initial temperature	298 K
Substrate material properties evaluation[a]	Code subroutines
Substrate solidus - liquidus temperatures	1403 – 1523 K (Code default values)
Substrate nodalization	At each substrate nodal location, three 2.0 mm cells, one 4.0 mm cell, and eight 6.0 mm cells are used; all nodes are cell-centered.
Spreading cavity nodalization	Accumulator: modeled as a single cell that is a 28.8 cm wide, 32.5 cm long, and flush with the spreading channel. Channel: modeled using 52 cells; each is 28.8 cm wide and 5 cm long. 2-D spreading surface: modeled as a 180º sector using 30 nodes; nodes uniformly divided into 5.19 cm radial increments. All nodes cell-centered.
Cavity condition	Dry
Upper atmosphere temperature	300 K
Upper atmosphere emissivity	1.0
Ambient pressure	0.1 MPa
Melt/substrate heat transfer coefficient model	Locally, largest of Dittus – Boelter and Bradley slag film heat transfer coefficients
Melt/substrate interfacial heat transfer resistance	Not modeled
Best-fit constant in Ramacciotti correlation	4.13
Solid-fraction variation between liquidus/solidus	See Figure 2.3
Timestep	0.02 seconds

[a]As applicable, c denotes specific heat, Δh_f is latent heat of fusion, ρ is density, k is thermal conductivity, μ_o is viscosity at the liquidus, σ is surface tension, M is molecular weight, ε is emissivity, and subscripts s and l denote solid and liquid phases, respectively.

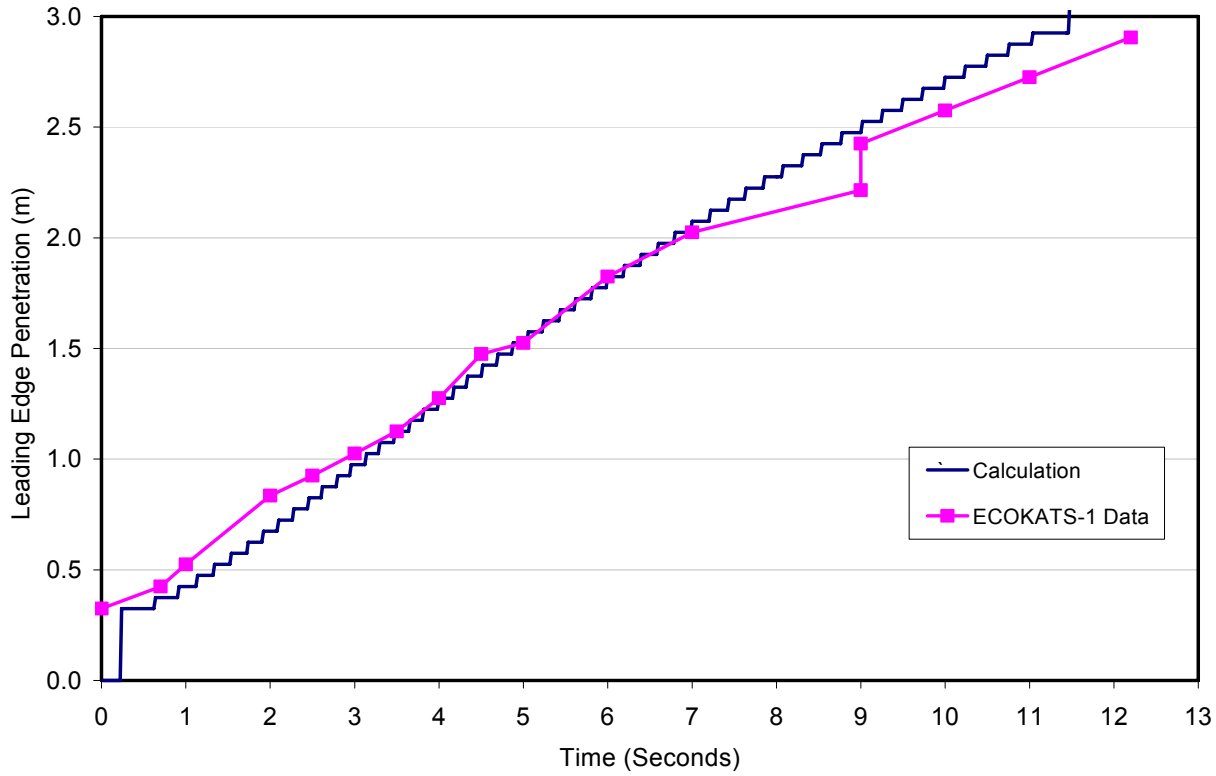

Figure A.33. Leading edge comparison (1-D channel section) for the ECOKATS-1 spreading test.

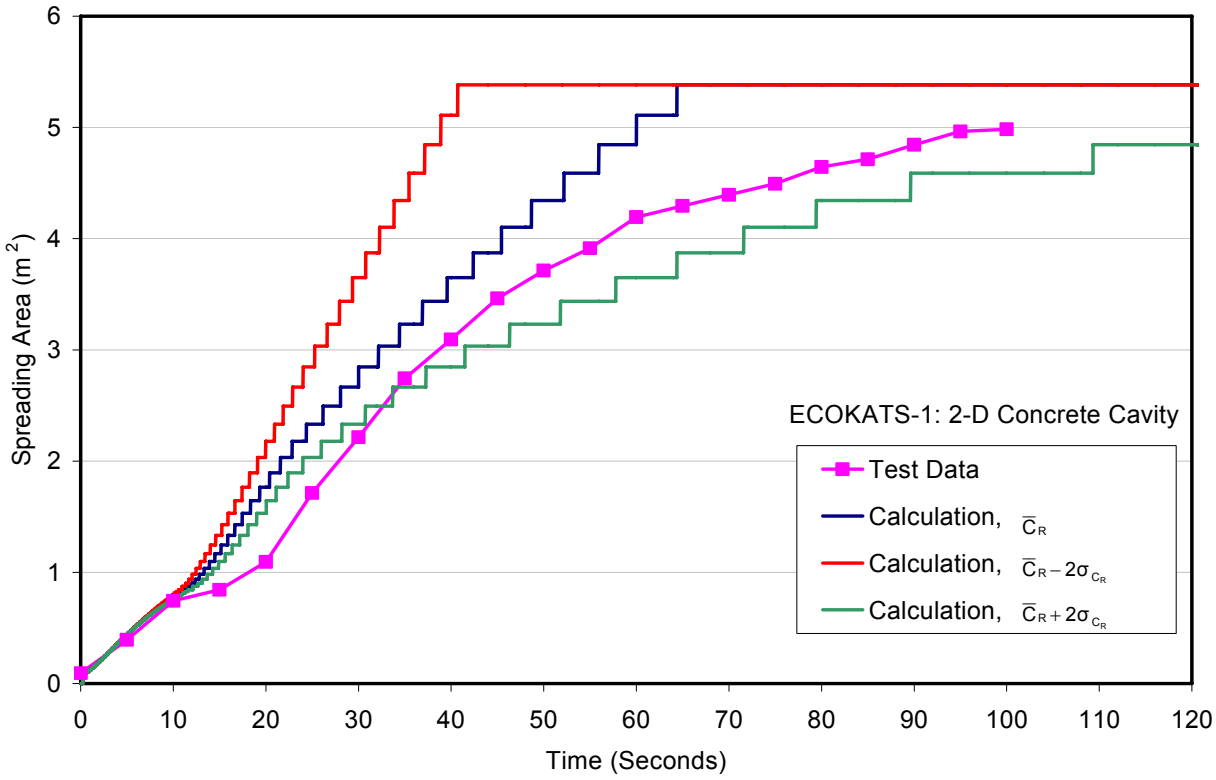

Figure A.34. Floor area coverage vs. time comparison for ECOKATS-1 spreading test.

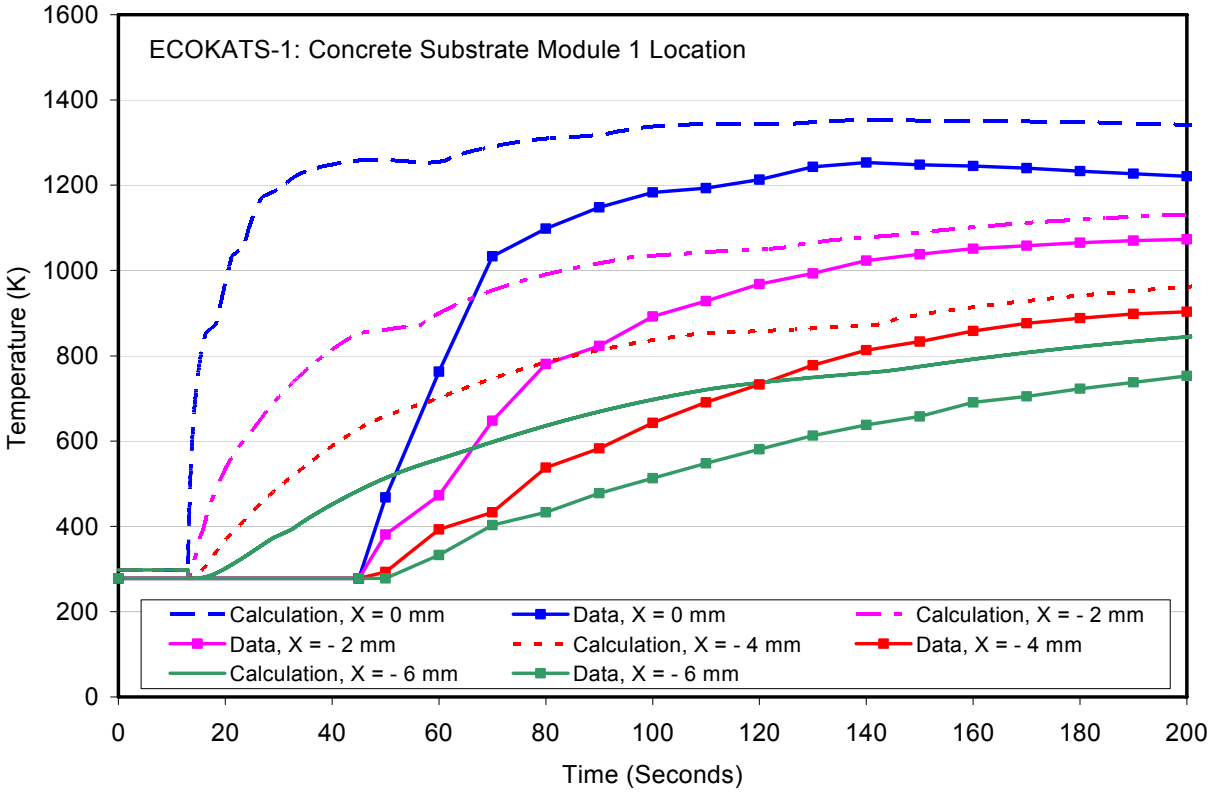

Figure A.35. Comparison of substrate thermal response predictions with ECOKATS-1 data 20 cm outside of the 1-D channel exit.

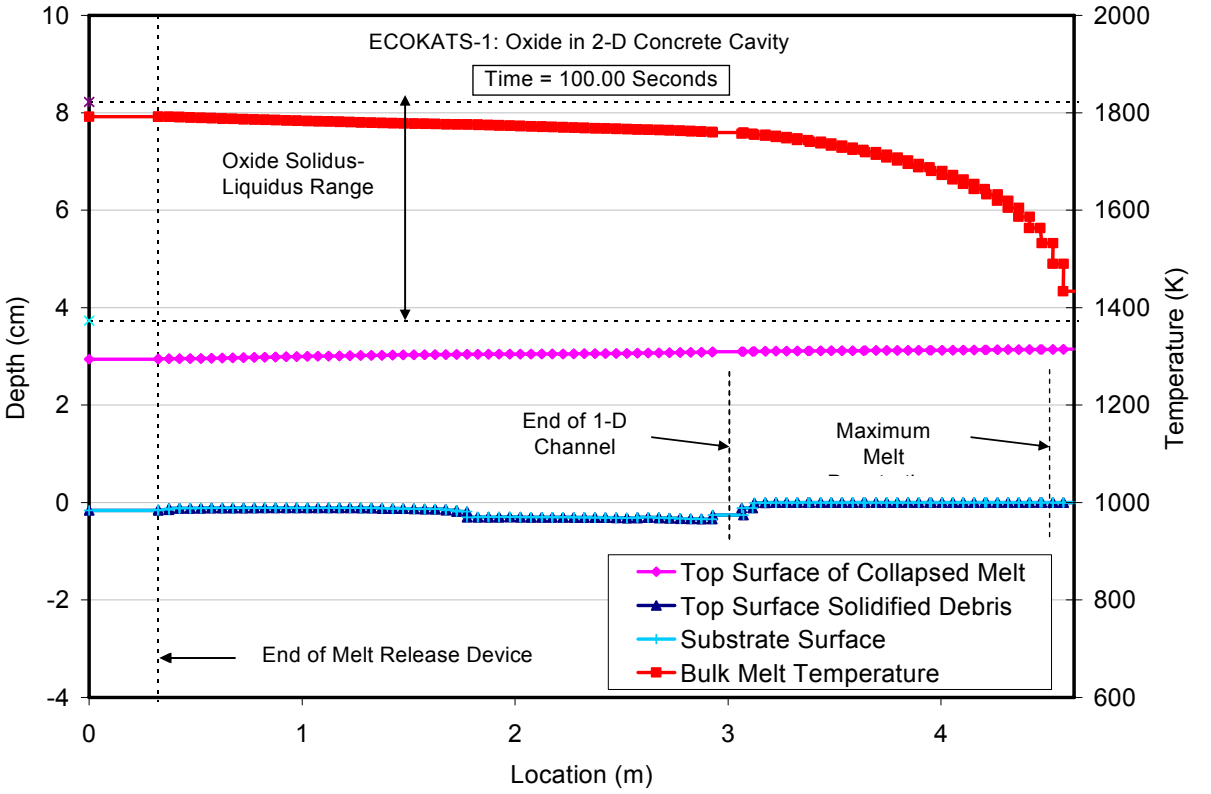

Figure A.36. Debris profile prediction for ECOKATS-1.

Table A.13. Input File Data Sheet for the ECOKATS-2 Test.

Test parameter	Value
Test name	ECOKATS-2
Melt composition (wt %)	Two-phases, initial is 100 Fe metal, and the second is oxide: 41.0 Al_2O_3, 24.0 FeO, 19.0 CaO, and 16.0 SiO_2
Melt delivery technique	Melt poured into an accumulator box that was modeled as 25 cm long by 25 cm wide, and flush with the spreading surface. Pour initiated by melt injection into the accumulator box.
Melt temperature	2103 K
Total pour mass	3200 kg (2305 kg oxide, 895 kg metal)
Substrate material	Siliceous concrete
Spreading geometry	1-D channel, 2.7 m long, followed by a 2 m long by 2 m wide rectilinear spreading surface.
Code input parameter(s)	**Value(s)**
Melt composition (wt %)	Metal phase: 100 Fe, oxide phase: 41.0 Al_2O_3, 24.0 FeO, 19.0 CaO, and 16.0 SiO_2
Melt pour temperature	2103 K
Melt oxide phase solidus – liquidus	1273 K – 1823 K
Melt metal phase solidus – liquidus	1810 K – 1820 K
Melt pour rate and duration	For 0 – 7.1 sec, 126.06 kg/sec Fe metal; for 7.1 – 33.2 sec, 88.3 kg/sec oxide; for t > 88.3 sec, pour rate is zero.
Melt material property evaluation[a]	For iron phase, code subroutines are used; for oxide phase, user-specified property data used: c_s = 1055 J/kg-K, c_l = 1220 J/kg-K, Δh_f= 1162 kJ/kg, $\rho_s = \rho_l$ = 3263 kg/m^3, $k_s = k_l$ = 5.4 W/m-K, μ_o = 0.2 Pa-s, σ = 0.5 N-m, M = 74.6 g/mole, and ε = 0.95
Substrate composition	Default siliceous concrete
Substrate initial temperature	298 K
Substrate material properties evaluation[a]	Code subroutines
Substrate solidus - liquidus temperatures	1403 – 1523 K (Code default values)
Substrate nodalization	At each substrate nodal location, seven 2.0 mm cells and five 4.0 mm cells are used; all nodes are cell-centered.
Spreading cavity nodalization	Accumulator: modeled as a single cell that is 25 cm long by 25 cm wide, and flush with the spreading surface. Channel: modeled using 54 cells; each is 30 cm wide and 5 cm long. 2-D spreading surface: from channel outlet to opposing wall, modeled as a 45º sector using 40 nodes uniformly divided into 4.69 cm radial increments. Outside of sector, the balance of the 2-D spreading surface modeled using 2 large notes to catch melt deflected from wall. All nodes cell-centered.
Cavity condition	Dry
Upper atmosphere temperature	300 K
Upper atmosphere emissivity	1.0
Ambient pressure	0.1 MPa
Melt/substrate heat transfer coefficient model	Locally, largest of Dittus – Boelter and Bradley slag film heat transfer coefficients
Melt/substrate interfacial heat transfer resistance	4800 W/m^2-K
Best-fit constant in Ramacciotti correlation	4.13
Solid-fraction variation between liquidus/solidus	See Figure 2.3
Timestep	0.01 seconds

[a]As applicable, c denotes specific heat, Δh_f is latent heat of fusion, ρ is density, k is thermal conductivity, μ_o is viscosity at the liquidus, σ is surface tension, M is molecular weight, ε is emissivity, and subscripts s and l denote solid and liquid phases, respectively

order to adequately fit the model to the metal melt spreading tests. As shown in Table A.13, the heat transfer resistance was set to the average value that best-fit the melt spreading test data; i.e., h_r = 4800 W/m^2-K. As further noted in Section 2, inclusion of this resistance had little effect on the predicted spreading behavior for oxide melts since the low convective heat transfer coefficients from the bulk melt to the interface that are typically calculated for these materials controls heat losses to the underlying substrate. Thus, with the model applied in this manner, the code should provide reasonable estimates of the spreading behavior for both metal and oxide phase pour streams.

The calculated leading edge penetration versus time is compared with the test data in Figure A.37. Conversely, predictions of the basemat thermal response at four different locations within the 2-D spreading area are compared with data in Figures A.38 through A.41. Finally, predicted melt depth and temperature profiles at four different times are provided in Figure A.42. Examination of Figure A.37 indicates that the code somewhat under-predicts the leading edge penetration rate for this test, particularly in the latter half of the 1-D channel that ends at 3 m (length includes that of the accumulator also). Examination of Figures A.38 through A.39 indicates mixed results. The overall shape of the thermal response curves seems to be captured in most cases. In addition, the code predicts onset and progression of basemat ablation as observed in the test. However, temperatures seem to be somewhat over-predicted, particularly near the channel exit. Finally, Figure A.42 reveals a computational strength of the code, as well as a weakness. The strength is that complicated flow configurations can be addressed in which distinct metal and oxide pours occur. However, as illustrated by the plot at 25 seconds, the weakness is that the code does not properly handle the fluid mechanics later in the spreading

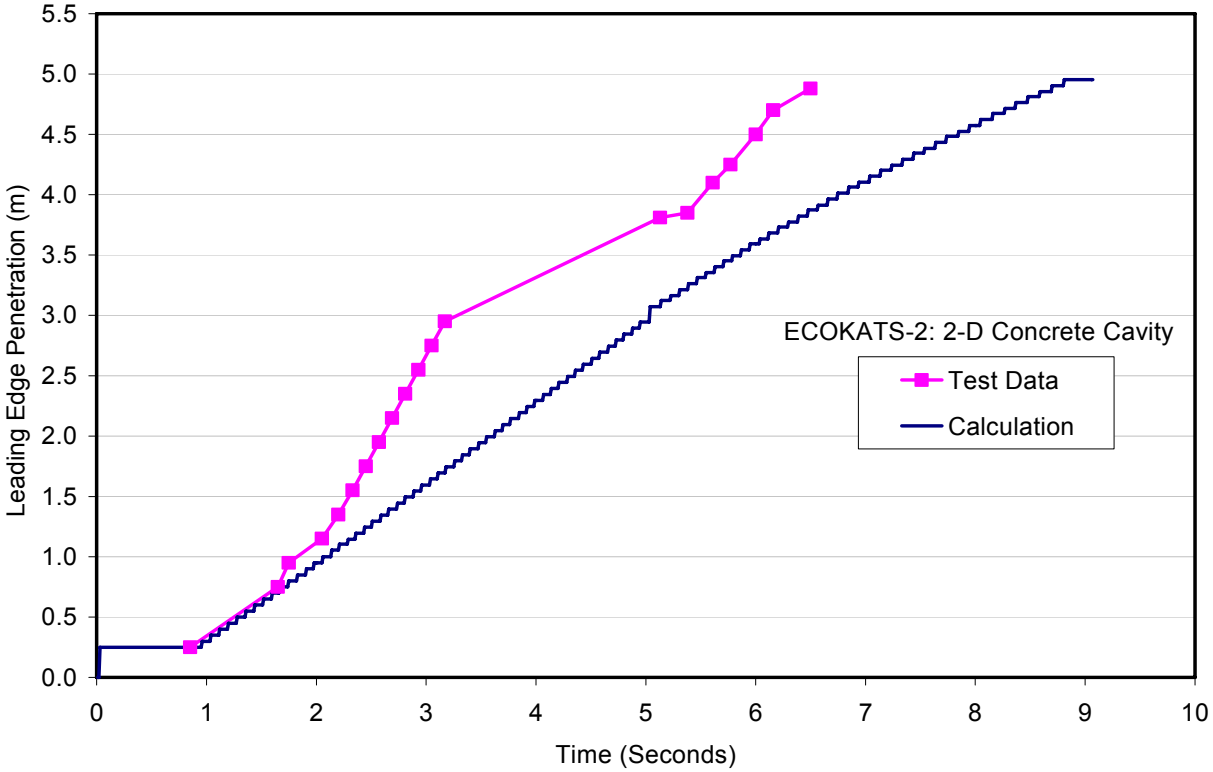

Figure A.37. Leading edge comparison for the ECOKATS-2 spreading test.

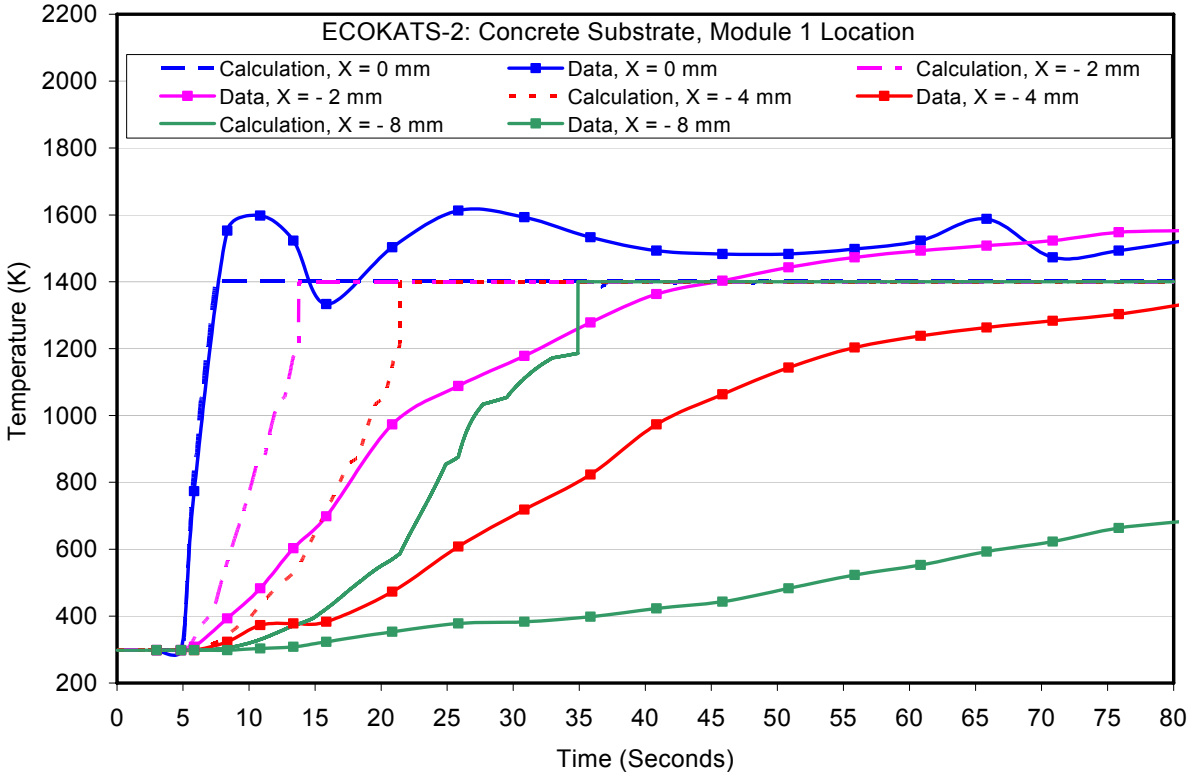

Figure A.38. Comparison of substrate thermal response predictions with ECOKATS-2 data 20 cm from channel exit.

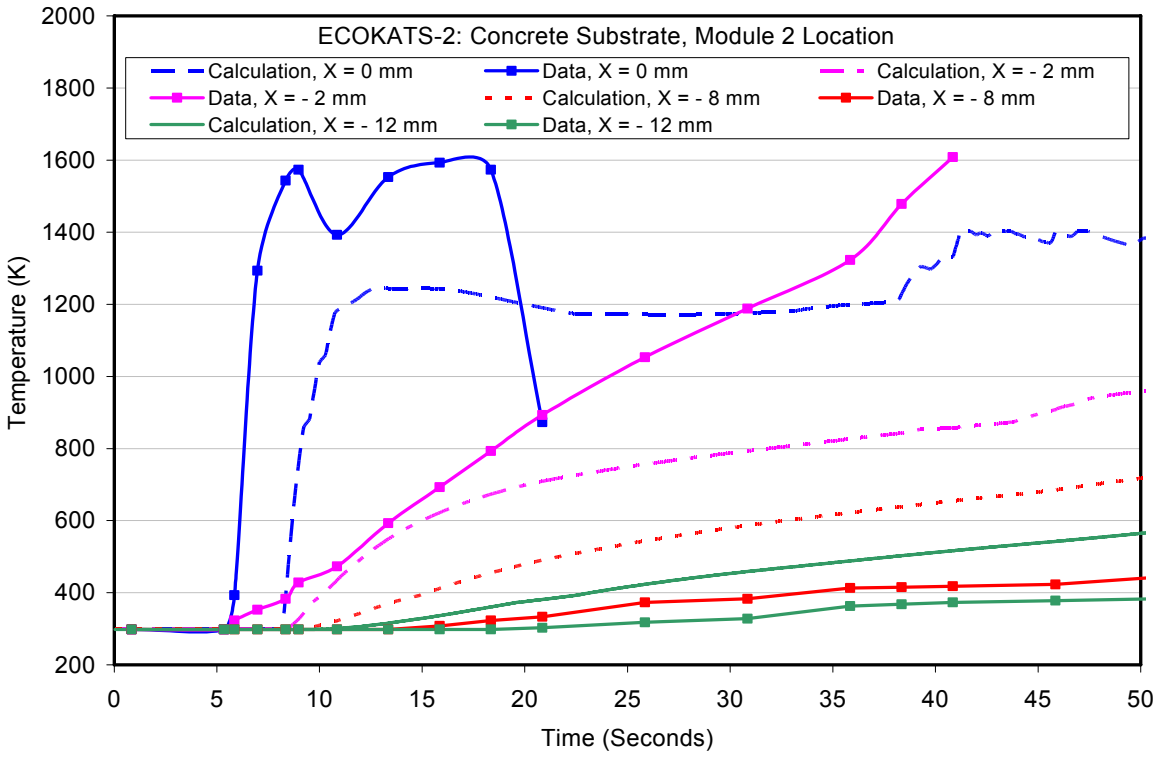

Figure A.39. Comparison of substrate thermal response predictions with ECOKATS-2 data 1.8 m directly across from channel exit.

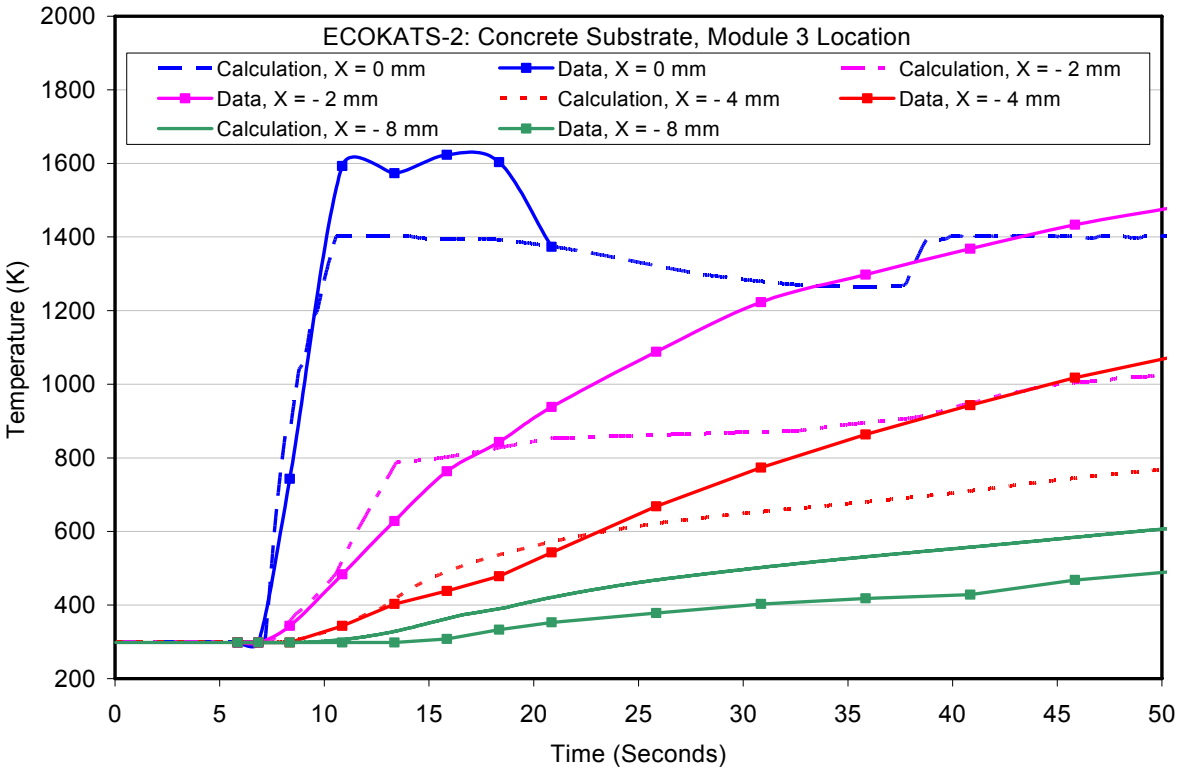

Figure A.40. Comparison of substrate thermal response predictions with ECOKATS-2 data at the centerline of rectilinear spreading box.

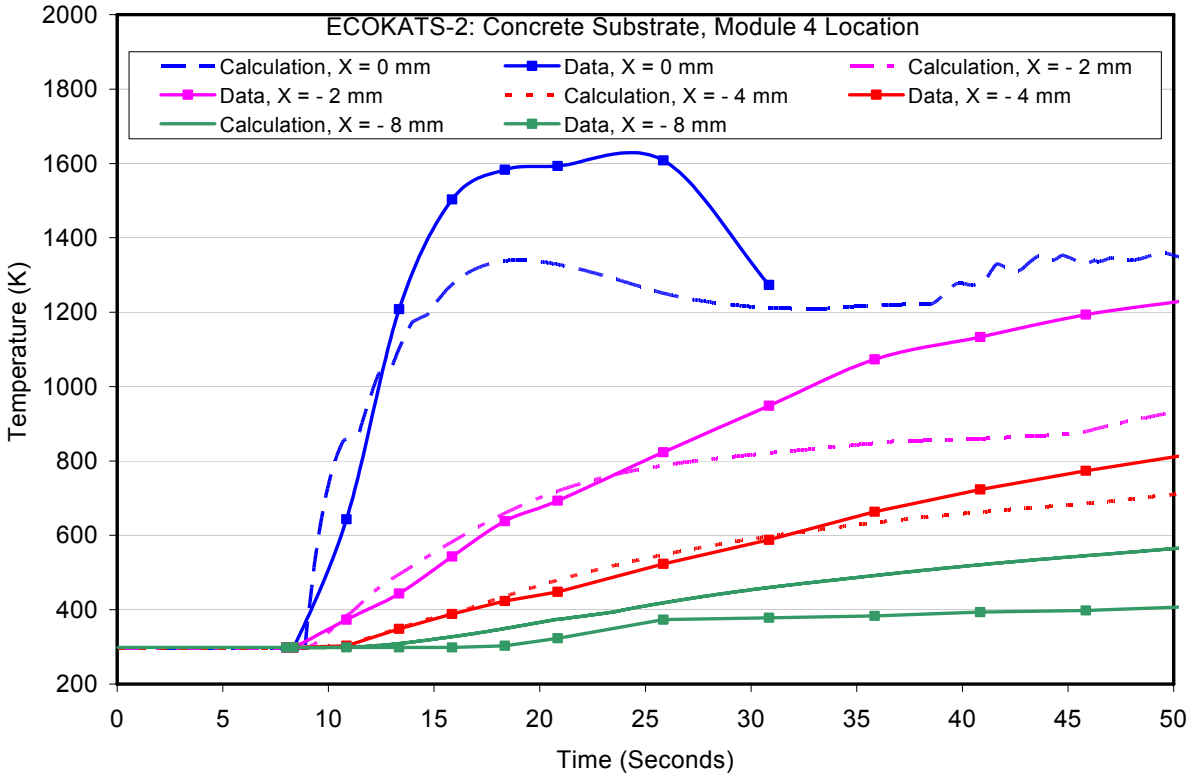

Figure A.41. Comparison of substrate thermal response predictions with ECOKATS-2 data diametrically across from channel exit.

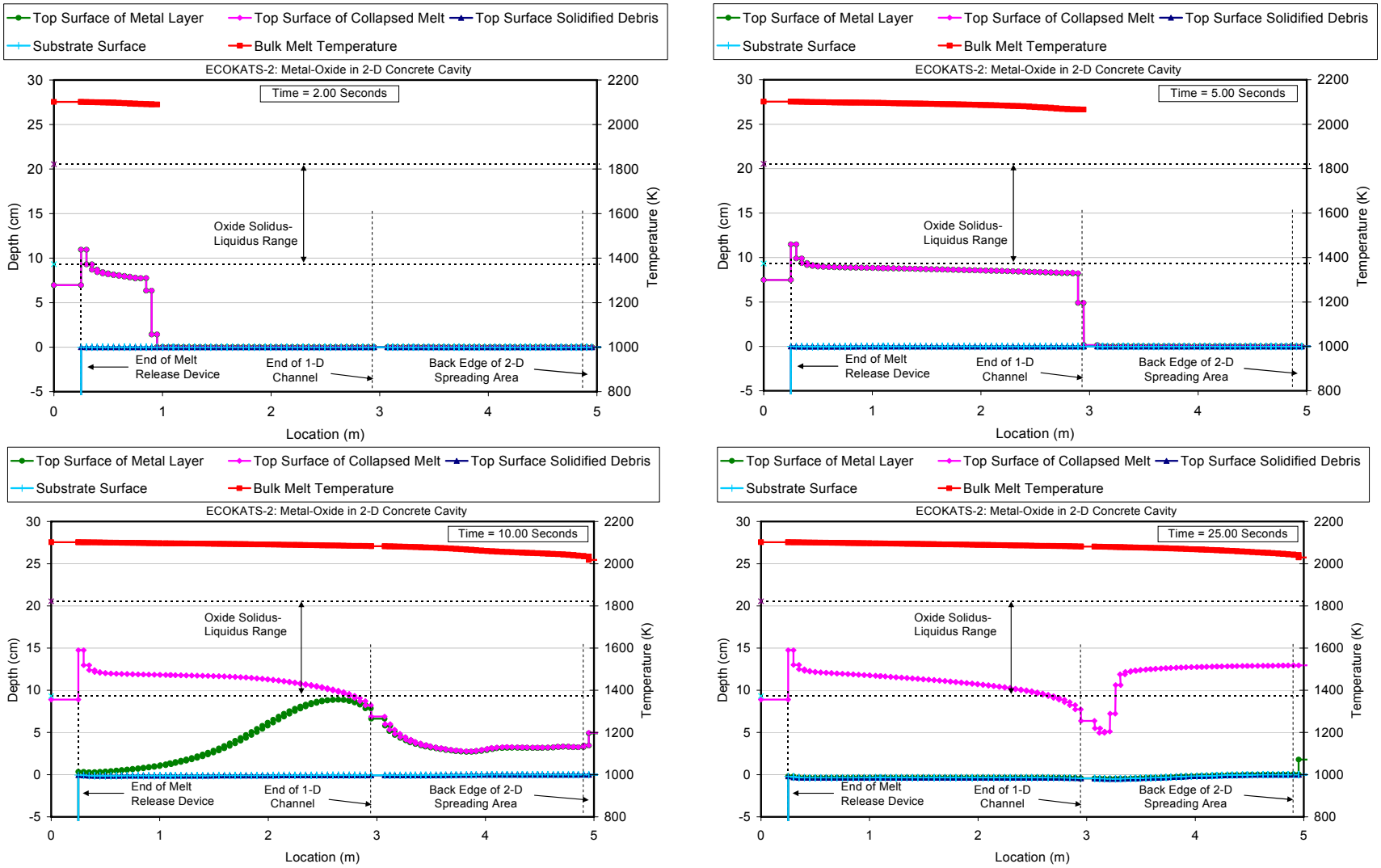

Figure A.42. Melt depth and temperature profiles at 2, 5, 10, and 25 seconds for the ECKOTAS-2 test.

transient when the stratified melt layers, behaving as two interacting gravity currents, would gradually relocate into a well defined oxide-over metal pool configuration. This is due to the fact that the two phases are assumed to be intermixed during spreading and so they relocate with the same velocity through the mesh. A more thorough analysis would treat the two distinct gravity currents with heat and mass transfer between them. However, this would be a major modeling change to the code which lies beyond the current scope of work.

A.2.3 RIT Calcia-Boria Simulant Spreading Tests

These tests[11,38] involved spreading of high temperature CaO-B_2O_3 melts that were produced in a resistance heated furnace and poured into instrumented test sections. A summary of the test matrix is provided in Table A.14. A total of six experiments were conducted; all tests were in a 1-D channel flow geometry. The first three tests were conducted under dry conditions and parameterized on substrate composition and initial melt temperature. One of the unique aspects of this program was that three of the tests were conducted under water. As is evident, the tests with water principally parameterized on the mass of melt spread in the experiment.

Table A.14. Summary of Test Parameters for RIT Spreading Tests.

Test	Substrate Material	Melt Temperature (K)	Pour Mass (kg)	Pour Rate (kg/sec)	Cavity Condition	Water Temperature (K)	Water Depth (cm)
3MDC-Ox-1	Concrete	1473	30.0	0.75	Dry	N/A	N/A
3MDS-Ox-1	Steel	″	″	″	″	N/A	N/A
3MDS-Ox-2	″	1373	″	″	″	N/A	N/A
2MWS-Ox-1	″	″	5.0	″	Wet	353	12
2MWS-Ox-2	″	″	12.5	″	″	358	12
2MWS-Ox-3	″	″	25.0	″	″	363	12

Test characteristics and the corresponding code input for the 3MDC-OX-1 test are summarized in Table A.15. As is evident, the melt thermal-physical property data recommended by the experimentalist's was used as part of the input, while the code default siliceous concrete composition was selected since the concrete property data was not provided.

The calculated leading edge penetration vs. time is compared to the test data in Figure A.43, while local melt substrate temperature and post-spreading material profile predictions are compared in Figures A.44-A.45 and A.46, respectively. For the melt penetration data, results for C_R and $C_R \pm 2\sigma_{C_R}$ (Table 2.4) are shown in the figure. The code underpredicts the spreading velocity early in the transient, but in general captures the overall characteristics. As is evident from Figure A.44 and A.45, the code seems to overpredict the heat transfer to the substrate, particularly at the 110 cm location. The information in Figure A.46 indicates that the code provides a reasonable estimate of the debris distribution following the spreading transient.

Table A.15. Input File Data Sheet for RIT Test 3MDC-Ox-1 with a Dry Concrete Channel.

Test parameter	Value
Test name	3MDC-Ox-1
Melt composition (wt %)	30 CaO, 70 B_2O_3
Melt delivery technique	Melt poured from a furnace through a 2.8 cm diameter nozzle at an average rate of 0.75 kg/sec into one end of a rectilinear spreading channel.
Melt temperature	1473 K
Total pour mass	30.0 kg
Substrate material	Siliceous concrete
Spreading geometry	1-D channel, 347.5 cm long by 20 cm wide
Code input parameter(s)	**Value(s)**
Melt composition	30 CaO, 70 B_2O_3
Melt pour temperature	1473 K
Melt oxide phase solidus – liquidus	1225 K – 1323 K
Melt metal phase solidus – liquidus	1810 – 1820 K
Melt pour rate and duration	0.75 kg/sec over 40.0 sec
Melt material property evaluation[a]	User-specified property data used: c_s = 1530 J/kg-K, c_l = 2200 J/kg-K, Δh_f= 460 kJ/kg, ρ_s = 3300 kg/m^3, ρ_l = 2500 kg/m^3, k_s = 2.0 W/m-K, k_l = 3.0 W/m-K, μ_o = 0.2 Pa-s, σ = 0.75 N-m, M = 65.1 g/mole, and ε = 0.3
Substrate composition	Default siliceous concrete
Substrate initial temperature	298 K
Substrate material properties evaluation	Code subroutines
Substrate solidus - liquidus temperatures	1403 – 1523 K (Code default values)
Substrate nodalization	At each substrate nodal location, first cell is 2.0 mm, second is 3.0 mm, and these are followed by ten 5.0 mm cells. All nodes cell-centered.
Spreading cavity nodalization	Accumulator: modeled as a single cell that is 40 cm wide, 25 cm long, and 5 cm deep. Channel: modeled using 120 cells; each is 40 cm wide and 5.33 cm long. All nodes cell-centered.
Cavity condition	Dry
Upper atmosphere temperature	300 K
Upper atmosphere emissivity	0.6
Ambient pressure	0.1 MPa
Melt/substrate heat transfer coefficient model	Locally, largest of Dittus – Boelter and Bradley slag film heat transfer coefficients
Melt/substrate interfacial heat transfer resistance	0
Best-fit constant in Ramacciotti correlation	5.03
Solid-fraction variation between liquidus/solidus	See Figure 2.3
Timestep	0.02 seconds

[a]Here, c denotes specific heat, Δh_f is latent heat of fusion, ρ is density, k is thermal conductivity, μ_o is viscosity at the liquidus, σ is surface tension, M is molecular weight, ε is emissivity, and subscripts s and l denote solid and liquid phases, respectively.

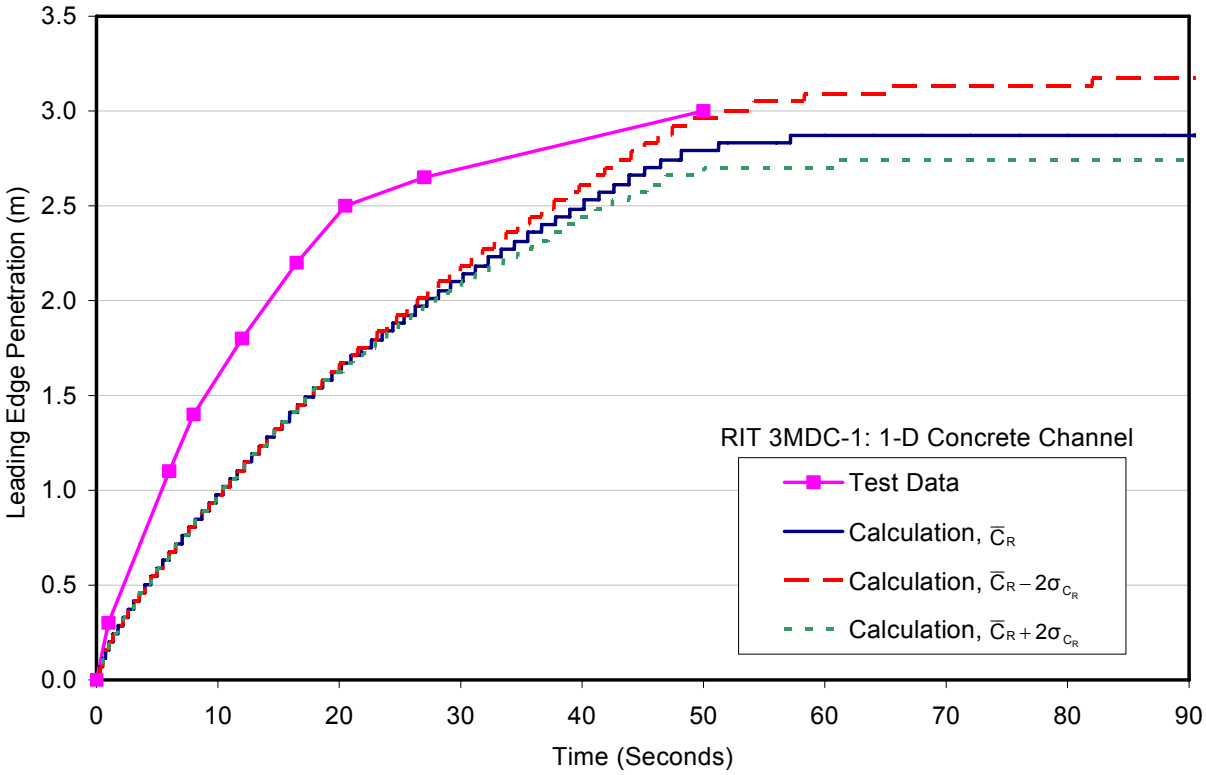

Figure A.43. Leading edge comparison for RIT 3MDC-Ox-1 spreading test.

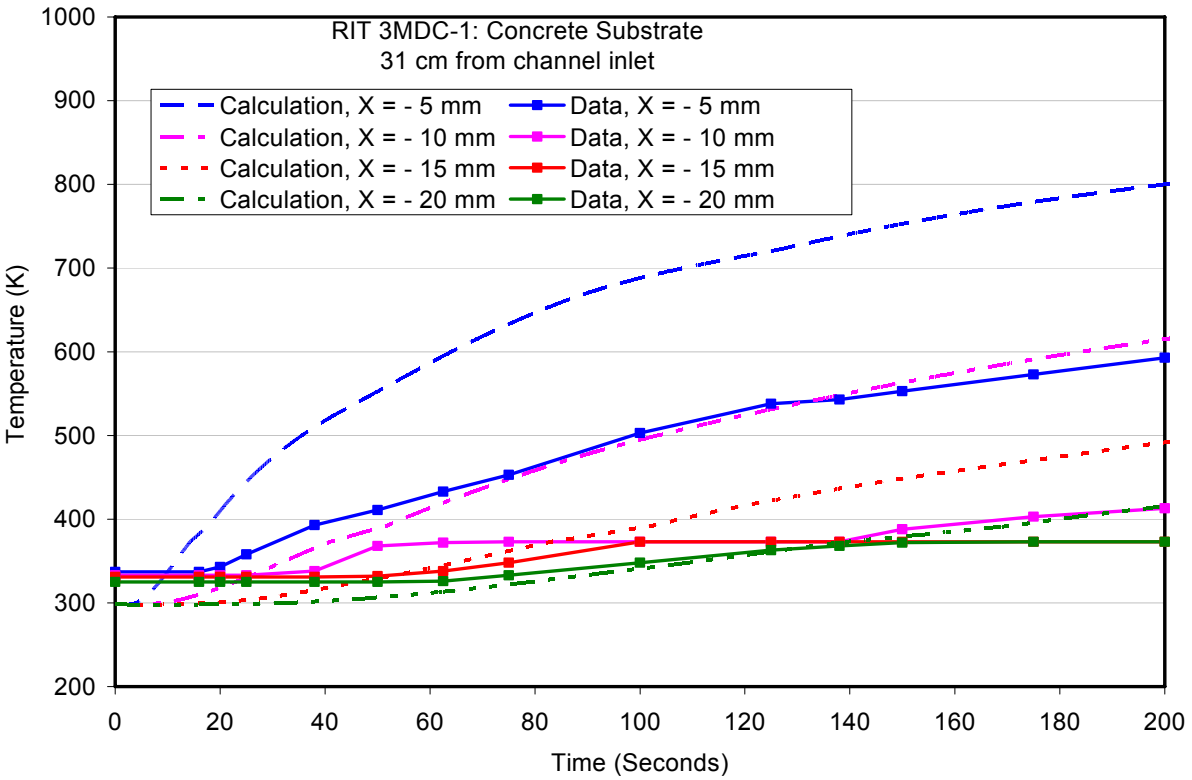

Figure A.44. Comparison of substrate thermal response predictions with RIT 3MDC-Ox-1 data 31 cm from channel inlet.

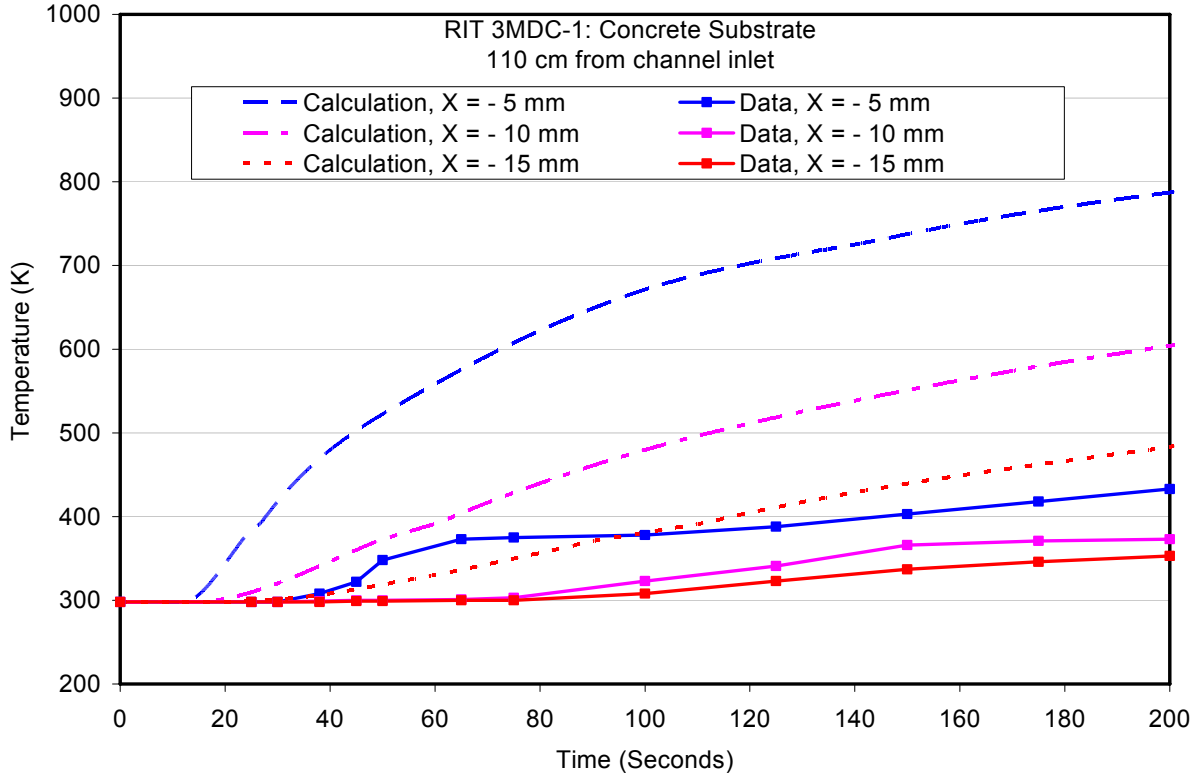

Figure A.45. Comparison of substrate thermal response predictions with RIT 3MDC-Ox-1 data 110 cm from channel inlet.

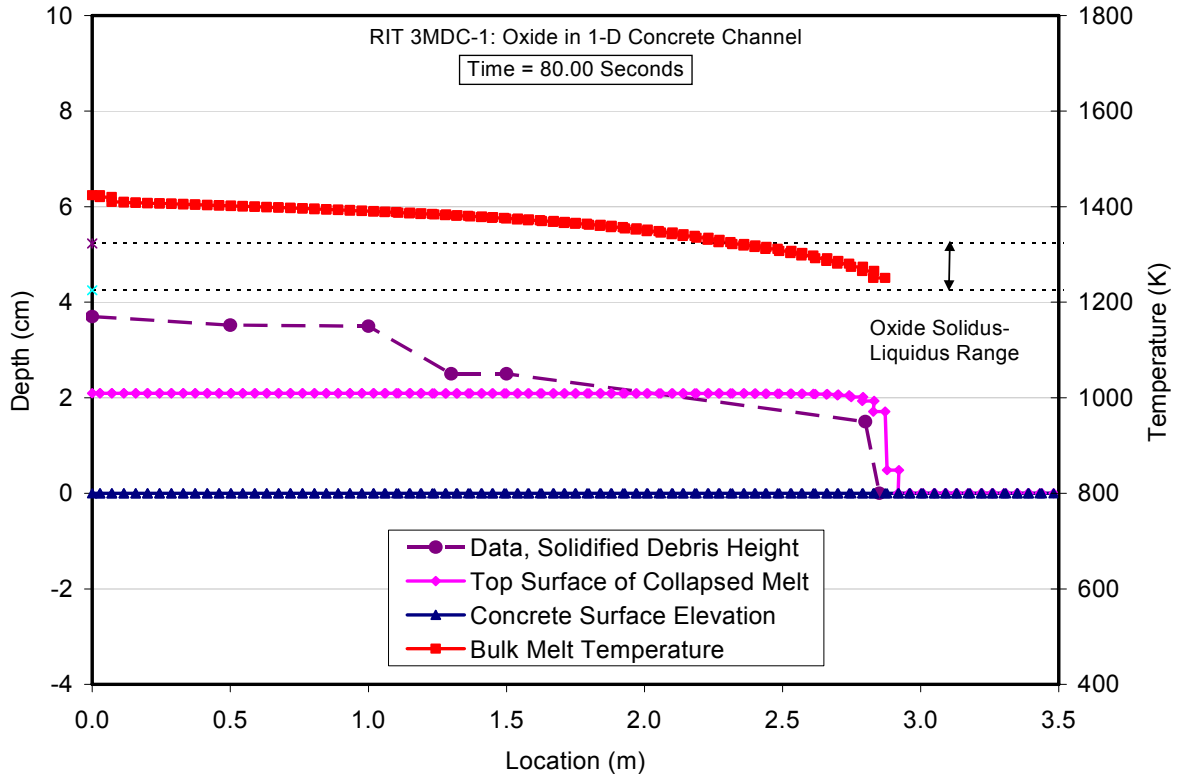

Figure A.46. Comparison of posttest debris profile prediction with RIT 3MDC-Ox-1 data.

Test characteristics and the corresponding code input for the 3MDS-OX-1 test are summarized in Table A.16. This was a counterpart test to 3MDC-OX-1 with the substrate material being the parametric variation (i.e. steel vs. concrete). The melt thermal-physical property data recommended by the experimenters was used as input, while the code default steel property data were utilized for the substrate.

The calculated leading edge penetration vs. time is compared to the test data in Figure A.47, while the post-spreading material profile prediction is compared in Figure A.48. As for the previous test with the concrete substrate, the code underpredicts the spreading velocity early in the sequence, but in general captures the overall characteristics. Data in Figure A.48 indicates that the code provides a reasonable estimate of the debris distribution following the spreading transient.

Test characteristics and the corresponding code input for the 3MDS-OX-2 test are summarized in Table A.17. This was a counterpart test to 3MDS-OX-1 with the initial melt temperature being the parametric variation (i.e. 1473 K vs. 1373 K).

Comparisons of leading edge penetration and material distribution following spreading with the test data are provided in Figures A.49 and A.50, respectively. In terms of melt penetration, the code seems to do a better job in predicting the leading edge penetration rate for this test compared to the other two dry experiments that had higher initial melt temperatures (see Table A.14). The information in Figure A.50 indicates that the code does a fair job in estimating the debris distribution following spreading.

The next three spreading tests in the RIT series all were conducted with a 12 cm water depth with a small amount of subcooling. These tests were more difficult to execute, and as a result, the only data that was reported was the maximum melt penetration distance. Thus, it was not possible to compare spreading velocities or posttest debris profiles with the test results. On this basis, the plots of spreading rate and debris distribution are provided for these three tests to be consistent with the material presented for the others.

The primary parametric variation in the wet spreading tests was the mass of the melt, which increased from 5 to 12.5 and then 25 kg for the three tests. The melt pour rate was the same as that used for the dry tests, the spreading surface was steel, and initial melt temperature was fixed at 1373 K.

The tables of test characteristics and modeling assumptions, leading edge penetration, and posttest material distribution for tests 2MWS-OX-1, -2, and -3 are provided in sequential order at the end of this subsection. Examination of this collection of information indicates that the code predictions and test data exhibit a systematic increase in ultimate melt penetration distance with pour mass when all other parameters are fixed. Unlike other experiments in this and other test series that were conducted under cavity dry conditions, the code predicts substantial debris solidification at the leading edge near the end of the spreading transient which is attributable to the increased heat transfer rate to overlying water. As shown, the code locally nodalizes the solidified debris into the basemat mesh so that the solidified material becomes a physical impediment that the melt must spread over to further propagate down the channel.

Table A.16. Input File Data Sheet for RIT Test 3MDS-Ox-1 with a Dry Steel Channel.

Test parameter	Value
Test name	3MDS-Ox-1
Melt composition (wt %)	30 CaO, 70 B_2O_3
Melt delivery technique	Melt poured from a furnace through a 2.8 cm diameter nozzle at an average rate of 0.75 kg/sec into one end of a rectilinear spreading channel.
Melt temperature	1473 K
Total pour mass	30.0 kg
Substrate material	Steel
Spreading geometry	1-D channel, 347.5 cm long by 20 cm wide
Code input parameter(s)	**Value(s)**
Melt composition	30 CaO, 70 B_2O_3
Melt pour temperature	1473 K
Melt oxide phase solidus – liquidus	1225 K – 1323 K
Melt metal phase solidus – liquidus	1810 K – 1820 K
Melt pour rate and duration	0.75 kg/sec over 40.0 sec
Melt material property evaluation[a]	User-specified property data used: c_s = 1530 J/kg-K, c_l = 2200 J/kg-K, Δh_f= 460 kJ/kg, ρ_s = 3300 kg/m^3, ρ_l = 2500 kg/m^3, k_s = 2.0 W/m-K, k_l = 3.0 W/m-K, μ_o = 0.2 Pa-s, σ = 0.75 N-m, M = 65.1 g/mole, and ε = 0.3
Substrate composition	Steel (code default composition)
Substrate initial temperature	298 K
Substrate material properties evaluation	Code subroutines
Substrate solidus - liquidus temperatures	1810 K – 1811 K (code default values)
Substrate nodalization	At each substrate nodal location, first cell is 2.0 mm, second is 3.0 mm, and these are followed by ten 5.0 mm cells. All nodes cell-centered.
Spreading cavity nodalization	Melt injection zone: modeled as a single cell that is 2.8 cm long, 20 cm wide, and flush with the spreading surface. Channel: modeled using 80 cells; each is 4.31 cm long and 20 cm wide. All nodes cell-centered.
Cavity condition	Dry
Upper atmosphere temperature	300 K
Upper atmosphere emissivity	0.6
Ambient pressure	0.1 MPa
Melt/substrate heat transfer coefficient model	Dittus – Boelter
Melt/substrate interfacial heat transfer resistance	0
Best-fit constant in Ramacciotti correlation	3.03
Solid-fraction variation between liquidus/solidus	See Figure 2.3
Timestep	0.02 seconds

[a]Here, c denotes specific heat, Δh_f is latent heat of fusion, ρ is density, k is thermal conductivity, μ_o is viscosity at the liquidus, σ is surface tension, M is molecular weight, ε is emissivity, and subscripts s and l denote solid and liquid phases, respectively.

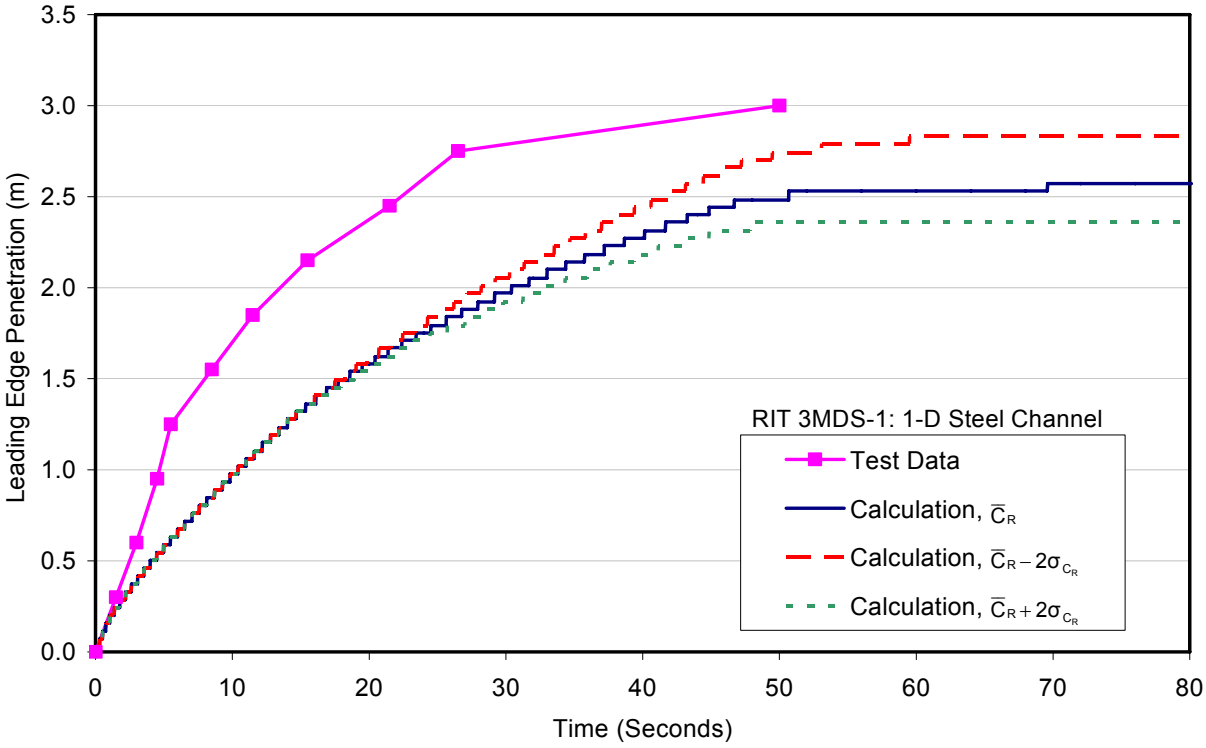

Figure A.47. Leading edge comparison for RIT 3MDS-Ox-1 spreading test.

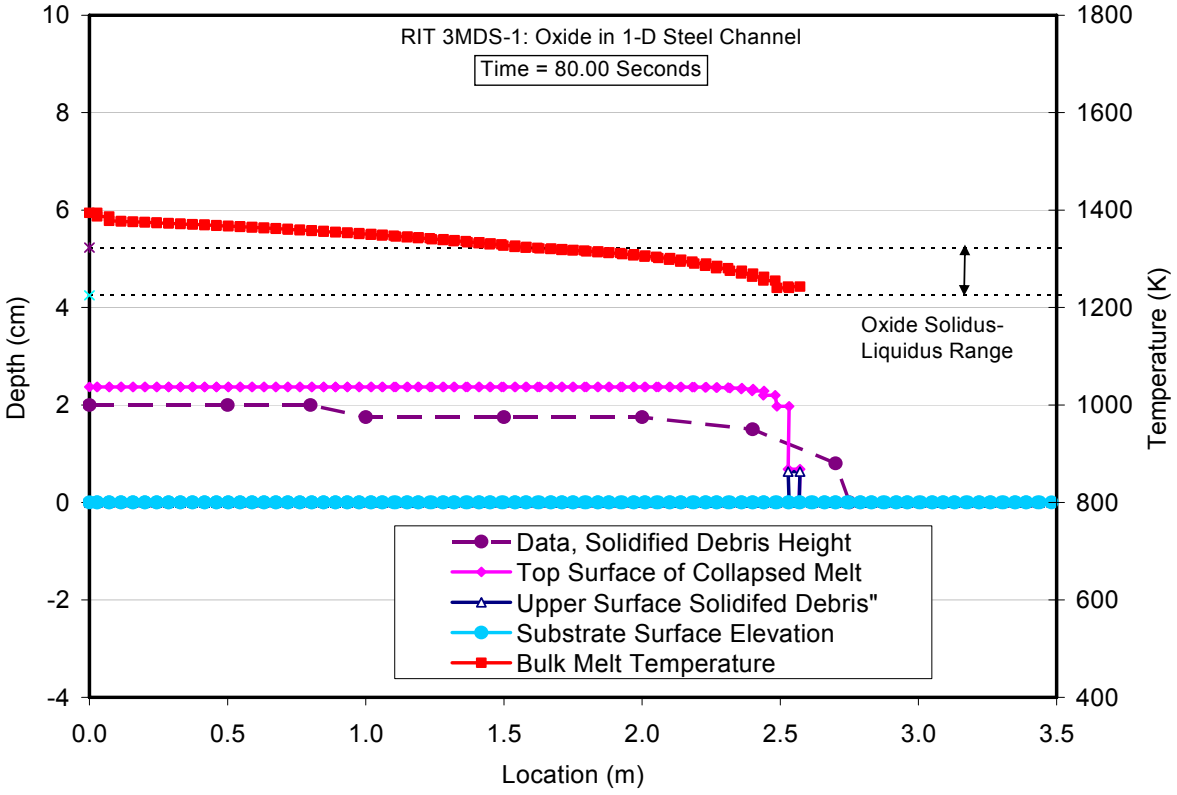

Figure A.48. Comparison of posttest debris profile prediction with RIT 3MDS-Ox-1 data.

Table A.17. Input File Data Sheet for RIT Test 3MDS-Ox-2 with a Dry Steel Channel.

Test parameter	Value
Test name	3MDS-Ox-2
Melt composition (wt %)	30 CaO, 70 B_2O_3
Melt delivery technique	Melt poured from a furnace through a 2.8 cm diameter nozzle at an average rate of 0.75 kg/sec into one end of a rectilinear spreading channel.
Melt temperature	1373 K
Total pour mass	30.0 kg
Substrate material	Steel
Spreading geometry	1-D channel, 347.5 cm long by 20 cm wide
Code input parameter(s)	**Value(s)**
Melt composition	30 CaO, 70 B_2O_3
Melt pour temperature	1373 K
Melt oxide phase solidus – liquidus	1225 K – 1323 K
Melt metal phase solidus – liquidus	1810 K – 1820 K
Melt pour rate and duration	0.75 kg/sec over 40.0 sec
Melt material property evaluation[a]	User-specified property data used: c_s = 1530 J/kg-K, c_l = 2200 J/kg-K, Δh_f= 460 kJ/kg, ρ_s = 3300 kg/m^3, ρ_l = 2500 kg/m^3, k_s = 2.0 W/m-K, k_l = 3.0 W/m-K, μ_o = 0.2 Pa-s, σ = 0.75 N-m, M = 65.1 g/mole, and ε = 0.3
Substrate composition	Steel (code default composition)
Substrate initial temperature	298 K
Substrate material properties evaluation	Code subroutines
Substrate solidus - liquidus temperatures	1810 K – 1811 K (code default values)
Substrate nodalization	At each substrate nodal location, first cell is 2.0 mm, second is 3.0 mm, and these are followed by ten 5.0 mm cells. All nodes cell-centered.
Spreading cavity nodalization	Melt injection zone: modeled as a single cell that is 2.8 cm long, 20 cm wide, and flush with the spreading surface. Channel: modeled using 80 cells; each is 4.31 cm long and 20 cm wide. All nodes cell-centered.
Cavity condition	Dry
Upper atmosphere temperature	300 K
Upper atmosphere emissivity	0.6
Ambient pressure	0.1 MPa
Melt/substrate heat transfer coefficient model	Dittus – Boelter
Melt/substrate interfacial heat transfer resistance	0
Best-fit constant in Ramacciotti correlation	6.55
Solid-fraction variation between liquidus/solidus	See Figure 2.3
Timestep	0.02 seconds

[a]Here, c denotes specific heat, Δh_f is latent heat of fusion, ρ is density, k is thermal conductivity, μ_o is viscosity at the liquidus, σ is surface tension, M is molecular weight, ε is emissivity, and subscripts s and l denote solid and liquid phases, respectively.

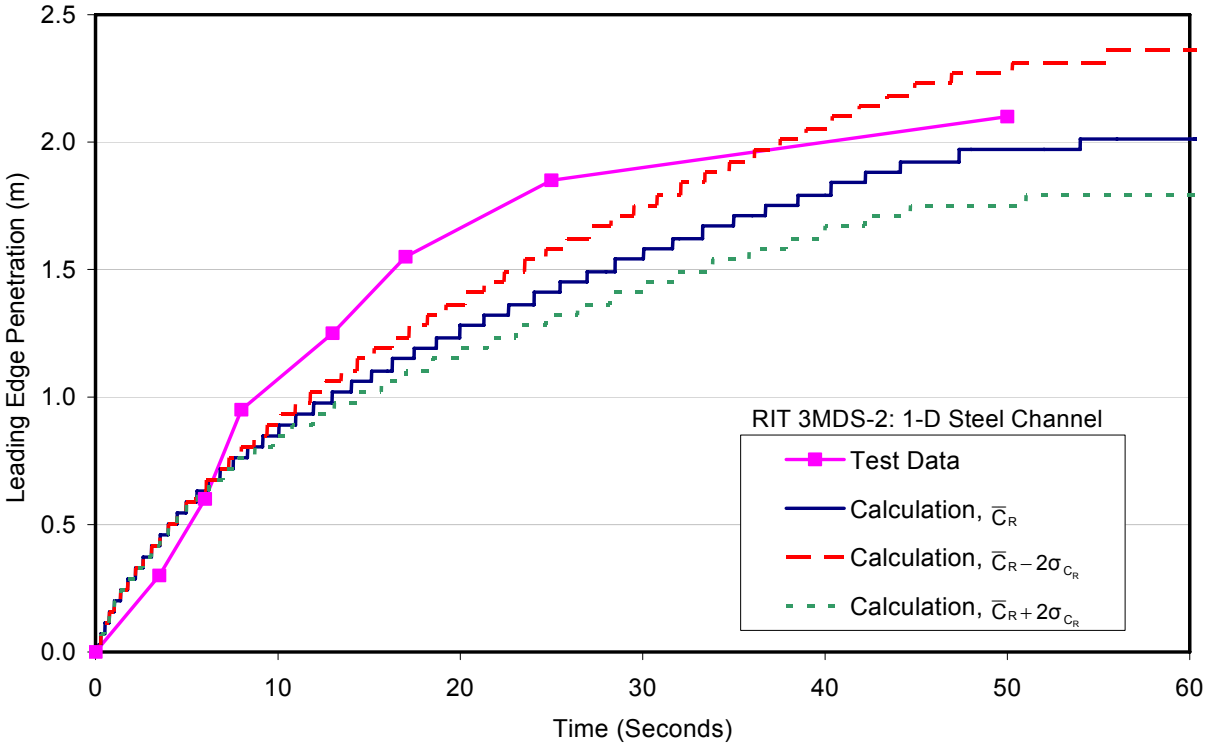

Figure A.49. Leading edge comparison for RIT 3MDS-Ox-2 spreading test.

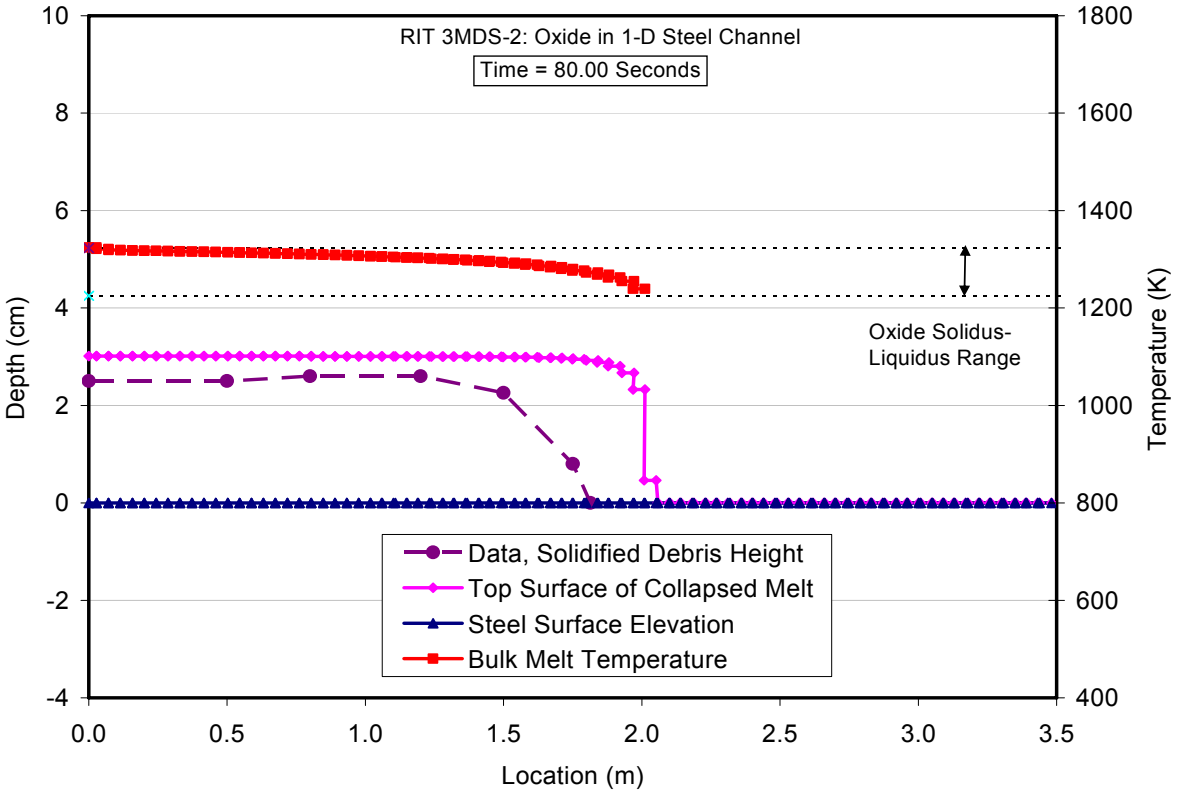

Figure A.50. Comparison of posttest debris profile prediction with RIT 3MDS-Ox-2 data.

Table A.18. Input File Data Sheet for RIT Test 2MWS-Ox-1 with a Wet Steel Channel.

Test parameter	Value
Test name	2MWS-Ox-1
Melt composition (wt %)	30 CaO, 70 B_2O_3
Melt delivery technique	Melt poured from a furnace through a 2.8 cm diameter nozzle at an average rate of 0.75 kg/sec into one end of a rectilinear spreading channel.
Melt temperature	1373 K
Total pour mass	5.0 kg
Substrate material	Steel
Spreading geometry	1-D channel, 200 cm long by 20 cm wide
Code input parameter(s)	**Value(s)**
Melt composition	30 CaO, 70 B_2O_3
Melt pour temperature	1373 K
Melt oxide phase solidus – liquidus	1225 K – 1323 K
Melt metal phase solidus – liquidus	1810 – 1820 K
Melt pour rate and duration	0.75 kg/sec over 6.66 sec
Melt material property evaluation[a]	User-specified property data used: c_s = 1530 J/kg-K, c_l = 2200 J/kg-K, Δh_f= 460 kJ/kg, ρ_s = 3300 kg/m^3, ρ_l = 2500 kg/m^3, k_s = 2.0 W/m-K, k_l = 3.0 W/m-K, μ_o = 0.2 Pa-s, σ = 0.75 N-m, M = 65.1 g/mole, and ε = 0.3
Substrate composition	Steel (code default composition)
Substrate initial temperature	298 K
Substrate material properties evaluation	Code subroutines
Substrate solidus - liquidus temperatures	1403 – 1523 K (Code default values)
Substrate nodalization	At each substrate nodal location, first cell is 2.0 mm, second is 3.0 mm, and these are followed by ten 5.0 mm cells. All nodes cell-centered.
Spreading cavity nodalization	Melt injection zone: modeled as a single cell that is 2.8 cm long, 20 cm wide, and flush with the spreading surface. Channel: modeled using 80 cells; each is 4.31 cm long and 20 cm wide. All nodes cell-centered.
Cavity condition	Wet
Water temperature (subcooling)	353 (20) K
Ambient pressure	0.1 MPa
Water depth	12 cm
Melt/substrate heat transfer coefficient model	Dittus – Boelter
Melt/substrate interfacial heat transfer resistance	0
Best-fit constant in Ramacciotti correlation	4.40
Solid-fraction variation between liquidus/solidus	See Figure 2.3
Timestep	0.02 seconds

[a]Here, c denotes specific heat, Δh_f is latent heat of fusion, ρ is density, k is thermal conductivity, μ_o is viscosity at the liquidus, σ is surface tension, M is molecular weight, ε is emissivity, and subscripts s and l denote solid and liquid phases, respectively.

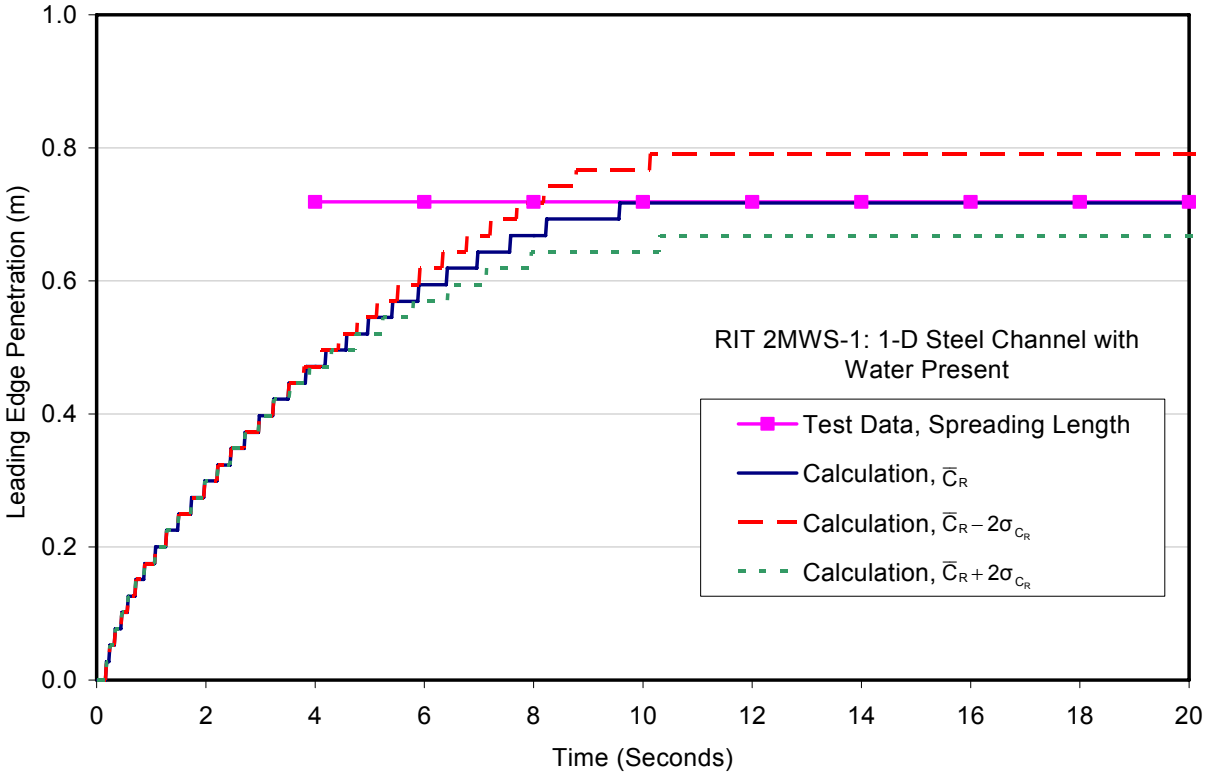

Figure A.51. Leading edge comparison for RIT 2MWS-Ox-1 spreading test.

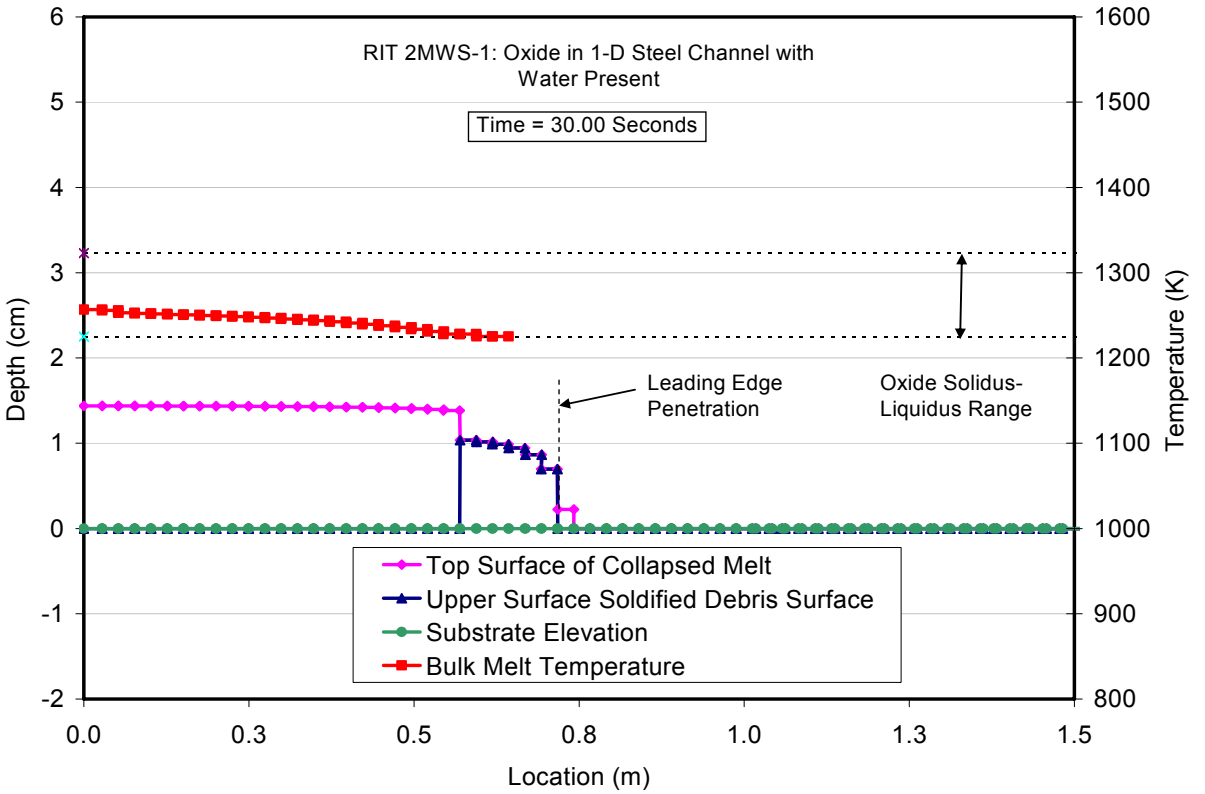

Figure A.52. Comparison of posttest debris profile prediction with RIT 2MWS-Ox-1 data.

Table A.19. Input File Data Sheet for RIT Test 2MWS-Ox-2 with a Wet Steel Channel.

Test parameter	Value
Test name	2MWS-Ox-2
Melt composition (wt %)	30 CaO, 70 B_2O_3
Melt delivery technique	Melt poured from a furnace through a 2.8 cm diameter nozzle at an average rate of 0.75 kg/sec into one end of a rectilinear spreading channel.
Melt temperature	1373 K
Total pour mass	12.5 kg
Substrate material	Steel
Spreading geometry	1-D channel, 200 cm long by 20 cm wide
Code input parameter(s)	**Value(s)**
Melt composition	30 CaO, 70 B_2O_3
Melt pour temperature	1373 K
Melt oxide phase solidus – liquidus	1225 K – 1323 K
Melt metal phase solidus – liquidus	1810 K – 1820 K
Melt pour rate and duration	0.75 kg/sec over 16.66 sec
Melt material property evaluation[a]	User-specified property data used: c_s = 1530 J/kg-K, c_l = 2200 J/kg-K, Δh_f= 460 kJ/kg, ρ_s = 3300 kg/m^3, ρ_l = 2500 kg/m^3, k_s = 2.0 W/m-K, k_l = 3.0 W/m-K, μ_o = 0.2 Pa-s, σ = 0.75 N-m, M = 65.1 g/mole, and ε = 0.3
Substrate composition	Steel (code default composition)
Substrate initial temperature	298 K
Substrate material properties evaluation	Code subroutines
Substrate solidus - liquidus temperatures	1810 K – 1811 K (code default values)
Substrate nodalization	At each substrate nodal location, first cell is 2.0 mm, second is 3.0 mm, and these are followed by ten 5.0 mm cells. All nodes cell-centered.
Spreading cavity nodalization	Melt injection zone: modeled as a single cell that is 2.8 cm long, 20 cm wide, and flush with the spreading surface. Channel: modeled using 80 cells; each is 2.46 cm long and 20 cm wide. All nodes cell-centered.
Cavity condition	Wet
Water temperature (subcooling)	358 (15) K
Ambient pressure	0.1 MPa
Water depth	12 cm
Melt/substrate heat transfer coefficient model	Dittus – Boelter
Melt/substrate interfacial heat transfer resistance	0
Best-fit constant in Ramacciotti correlation	4.80
Solid-fraction variation between liquidus/solidus	See Figure 2.3
Timestep	0.02 seconds

[a]Here, c denotes specific heat, Δh_f is latent heat of fusion, ρ is density, k is thermal conductivity, μ_o is viscosity at the liquidus, σ is surface tension, M is molecular weight, ε is emissivity, and subscripts s and l denote solid and liquid phases, respectively.

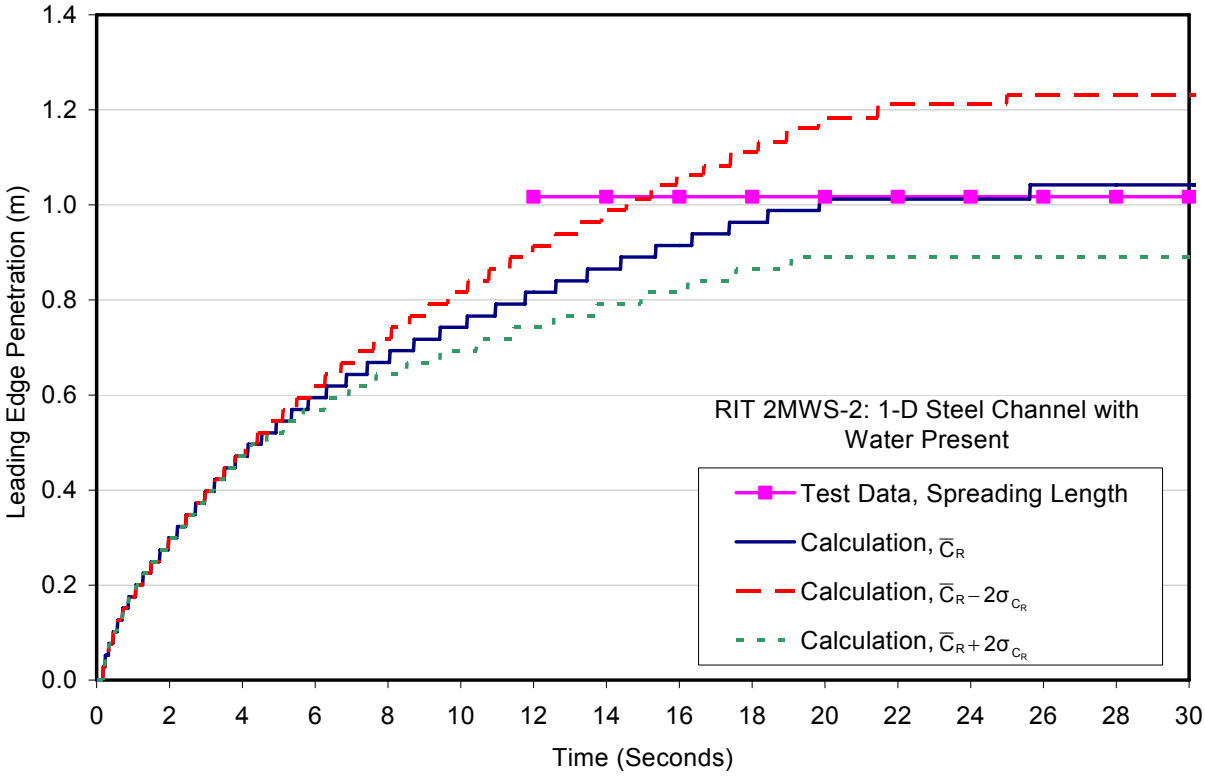

Figure A.53. Leading edge comparison for RIT 2MWS-Ox-2 spreading test.

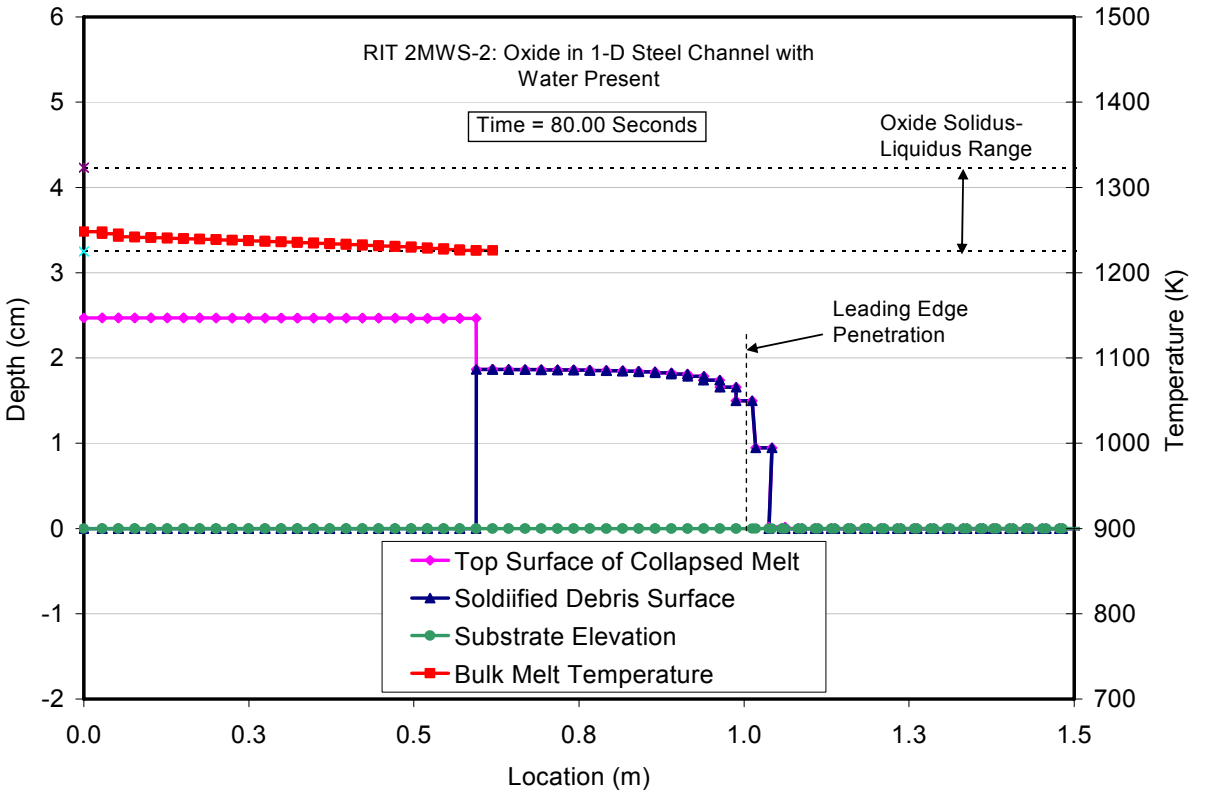

Figure A.54. Comparison of posttest debris profile prediction with RIT 2MWS-Ox-2 data.

Table A.20. Input File Data Sheet for RIT Test 2MWS-Ox-3 with a Wet Steel Channel.

Test parameter	Value
Test name	2MWS-Ox-3
Melt composition (wt %)	30 CaO, 70 B_2O_3
Melt delivery technique	Melt poured from a furnace through a 2.8 cm diameter nozzle at an average rate of 0.75 kg/sec into one end of a rectilinear spreading channel.
Melt temperature	1373 K
Total pour mass	25.0 kg
Substrate material	Steel
Spreading geometry	1-D channel, 200 cm long by 20 cm wide
Code input parameter(s)	**Value(s)**
Melt composition	30 CaO, 70 B_2O_3
Melt pour temperature	1373 K
Melt oxide phase solidus – liquidus	1225 K – 1323 K
Melt metal phase solidus – liquidus	1810 K – 1820 K
Melt pour rate and duration	0.75 kg/sec over 33.33 sec
Melt material property evaluation[a]	User-specified property data used: c_s = 1530 J/kg-K, c_l = 2200 J/kg-K, Δh_f= 460 kJ/kg, ρ_s = 3300 kg/m^3, ρ_l = 2500 kg/m^3, k_s = 2.0 W/m-K, k_l = 3.0 W/m-K, μ_o = 0.2 Pa-s, σ = 0.75 N-m, M = 65.1 g/mole, and ε = 0.3
Substrate composition	Steel (code default composition)
Substrate initial temperature	298 K
Substrate material properties evaluation	Code subroutines
Substrate solidus - liquidus temperatures	1810 K – 1811 K (code default values)
Substrate nodalization	At each substrate nodal location, first cell is 2.0 mm, second is 3.0 mm, and these are followed by ten 5.0 mm cells. All nodes cell-centered.
Spreading cavity nodalization	Melt injection zone: modeled as a single cell that is 2.8 cm long, 20 cm wide, and flush with the spreading surface. Channel: modeled using 80 cells; each is 2.46 cm long and 20 cm wide. All nodes cell-centered.
Cavity condition	Wet
Water temperature (subcooling)	363 (10) K
Ambient pressure	0.1 MPa
Water depth	12 cm
Melt/substrate heat transfer coefficient model	Dittus – Boelter
Melt/substrate interfacial heat transfer resistance	0
Best-fit constant in Ramacciotti correlation	4.66
Solid-fraction variation between liquidus/solidus	See Figure 2.3
Timestep	0.02 seconds

[a]Here, c denotes specific heat, Δh_f is latent heat of fusion, ρ is density, k is thermal conductivity, μ_o is viscosity at the liquidus, σ is surface tension, M is molecular weight, ε is emissivity, and subscripts s and l denote solid and liquid phases, respectively.

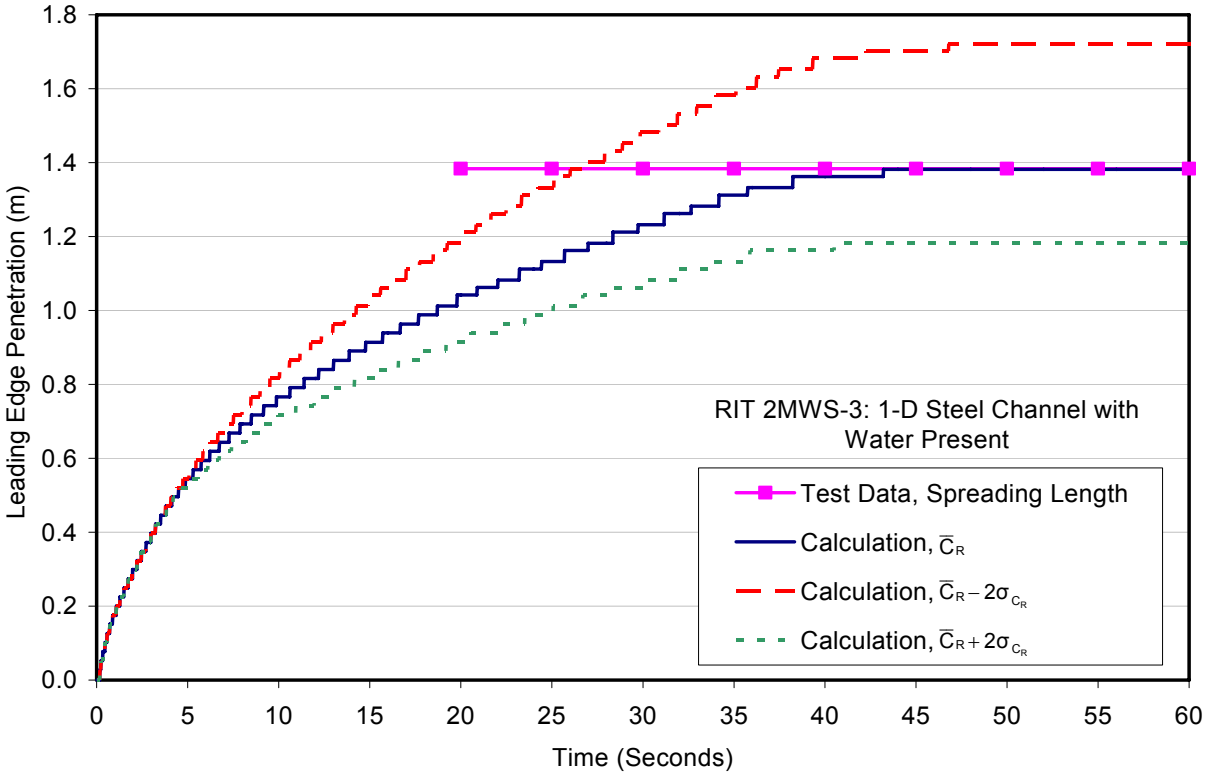

Figure A.55. Leading edge comparison for RIT 2MWS-Ox-3 spreading test.

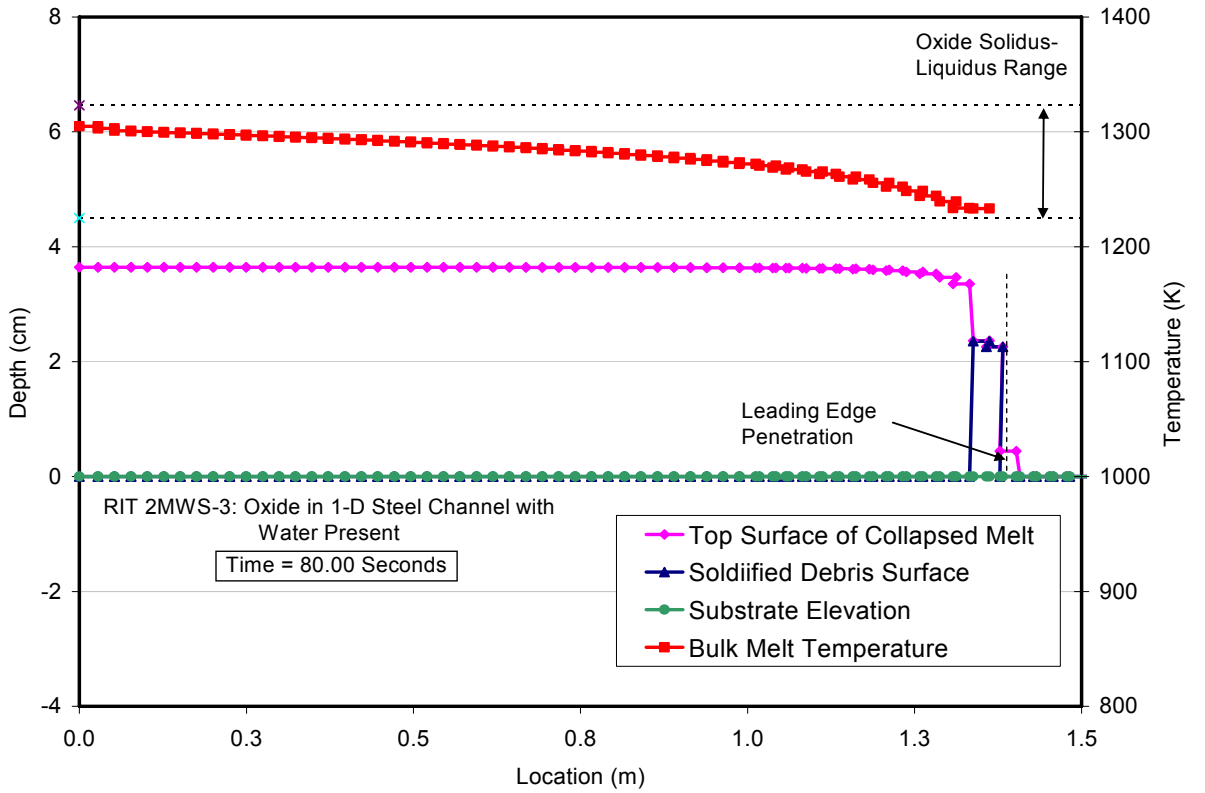

Figure A.56. Comparison of posttest debris profile prediction with RIT 2MWS-Ox-3 data.

A.3 Spreading Tests with Molten Steel

Following the benchmarking exercise against oxide simulant melt spreading tests, the code was further exercised against tests conducted with molten iron and stainless steel. Tests that fall into this category include those carried out by Eppinger et al.[13] in the KATS test facility, and the SPREAD tests conducted by Suzuki et al.[9] The code assessment against these tests is provided in this section.

A.3.1 KATS Iron Spreading Tests

As discussed in Section A.2, these tests involved spreading of high temperature oxide and iron melts that were generated by a modified iron-alumina thermite reaction. The previous subsection addressed spreading tests conducted with the oxide phase of that reaction, while the current discussion focuses on the spreading tests with the metal phase.

The KATS-12, -13, and -14 metal tests were selected for analysis (see Table 2.1). KATS-12 and -13 parameterized on substrate composition, with KATS-12 utilizing ceramic (Corderite), and KATS-13 utilizing concrete. KATS-14 was also conducted with a ceramic substrate, but the melt pour rate was reduced relative to KATS-12.

As noted in Section A.2, the accumulator design in these tests was somewhat novel, with a base that was elevated elevation slightly above that of the spreading surface. The general characteristics were shown previously in Figure A.21, while the corresponding dimensions for the metal tests are summarized in Table A.7. As is evident, a small incline connected the accumulator box to the spreading channel. An effort was made to mock up the details of the melt accumulator, gate, and incline leading to the spreading channel with the meshing scheme.

Test characteristics and the corresponding model input that was developed for the KATS-12 metal test are summarized in Table A.21. The ceramic substrate thermal-physical properties were input as user-defined quantities based on project documentation.[13] The iron melt properties were calculated using the code subroutines. As discussed in Section 2, the approach for the metal tests was to set the constant in the Ramacciotti viscosity correlation to the best-fit value for the oxide tests (i.e., C_R = 7.26), and then to develop statistical data on the melt-substrate interfacial heat transfer resistance, h_r, that best fit the collection of steel spreading test data. This information is shown in Table 2.6. The results shown in this section are calculated on the basis of this statistical information, unless otherwise noted.

The calculated leading edge penetration vs. time is compared to the test data in Figure A.57, while local melt temperature and post-spreading material profile predictions are compared with data in Figures A.58 and A.59, respectively. As for the counterpart KATS-12 oxide test, the pour rate was relatively high and so the spreading rate was initially dominated by inertial effects. As a result, viscous forces that retard spreading do not show up until late in the transient; see Figure A.57. Results for h_r and $h_r \pm 2\sigma_{h_r}$ (Table 2.6) are shown in this figure.

As is evident from Figure A.58, peak melt temperature is predicted quite well 1 m from the melt accumulator, but under-predicted by ~ 80 K 3.5 m from the accumulator. The debris

Table A.21. Input File Data Sheet for the KATS-12 Metal Melt Test with Ceramic Channel.

Test parameter	Value
Test name	KATS-12, metal, ceramic channel
Melt composition (wt %)	100 Fe
Melt delivery technique	Melt poured into an accumulator box that was 17.0 cm wide, 30.2 cm long, and 7.0 cm above the spreading surface. Pour initiated by opening a gate to the spreading channel.
Melt temperature	2170 K
Total pour mass	135 kg
Substrate material	Cordierite
Spreading geometry	1-D channel, 15 m long by 15 cm wide
Code input parameter(s)	**Value(s)**
Melt composition (wt %)	100 Fe
Melt pour temperature	2170 K
Melt oxide phase solidus – liquidus	1893 K – 1923 K
Melt metal phase solidus – liquidus	1806 K – 1816 K
Melt pour rate and duration	Linear decrease in pour rate from 40.3 kg/sec to zero over 6.7 second interval
Melt material property evaluation	Code subroutines
Substrate composition	Corderite (modeled using user-specified material input properties)
Substrate initial temperature	298 K
Substrate material properties evaluation[a]	$c_s = c_l = 840$ J/kg-K, $\Delta h_f = 1.0$ MJ/kg, $\rho_s = \rho_l = 2200$ kg/m^3, $k_s = k_l = 3.8$ W/m-K, and $\varepsilon = 0.3$
Substrate solidus - liquidus temperatures	1893 K – 1923 K
Substrate nodalization	At each substrate nodal location, twelve 6.0 mm cells are used; all nodes are cell-centered.
Spreading cavity nodalization	Accumulator: modeled as a single cell that is 17.0 cm wide, 30.2 cm long, and 7.0 cm above the channel surface. Gate: modeled as a single cell that is 8 cm wide, 4.3 cm long, and 7.0 cm above the channel. Incline down to channel: modeled as a single cell that is 10 cm long, 15 cm wide, and 3.5 cm above the channel. Channel: 12 m modeled using 120 cells; each is 15 cm wide and 10 cm long. All nodes cell-centered.
Cavity condition	Dry
Upper atmosphere temperature	300 K
Upper atmosphere emissivity	0.7
Ambient pressure	0.1 MPa
Melt/substrate heat transfer coefficient model	Dittus - Boelter
Best estimate melt/substrate interfacial heat transfer resistance	3470 W/m^2-K
Constant used in Ramacciotti correlation	7.26
Solid-fraction variation between liquidus/solidus	See Figure 2.3
Timestep	0.02 seconds

[a]As applicable, c denotes specific heat, Δh_f is latent heat of fusion, ρ is density, k is thermal conductivity, ε is emissivity, and subscripts s and l denote solid and liquid phases, respectively.

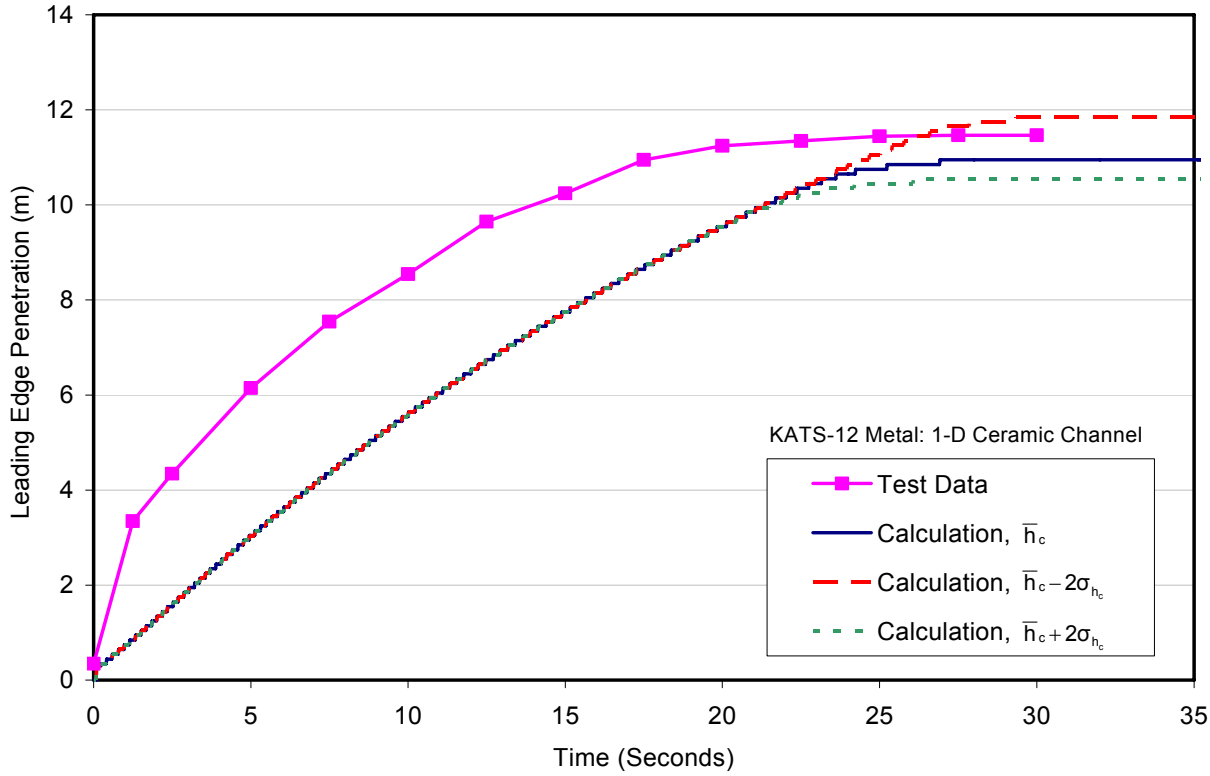

Figure A.57. Leading edge penetration comparison for the KATS-12 metal spreading test.

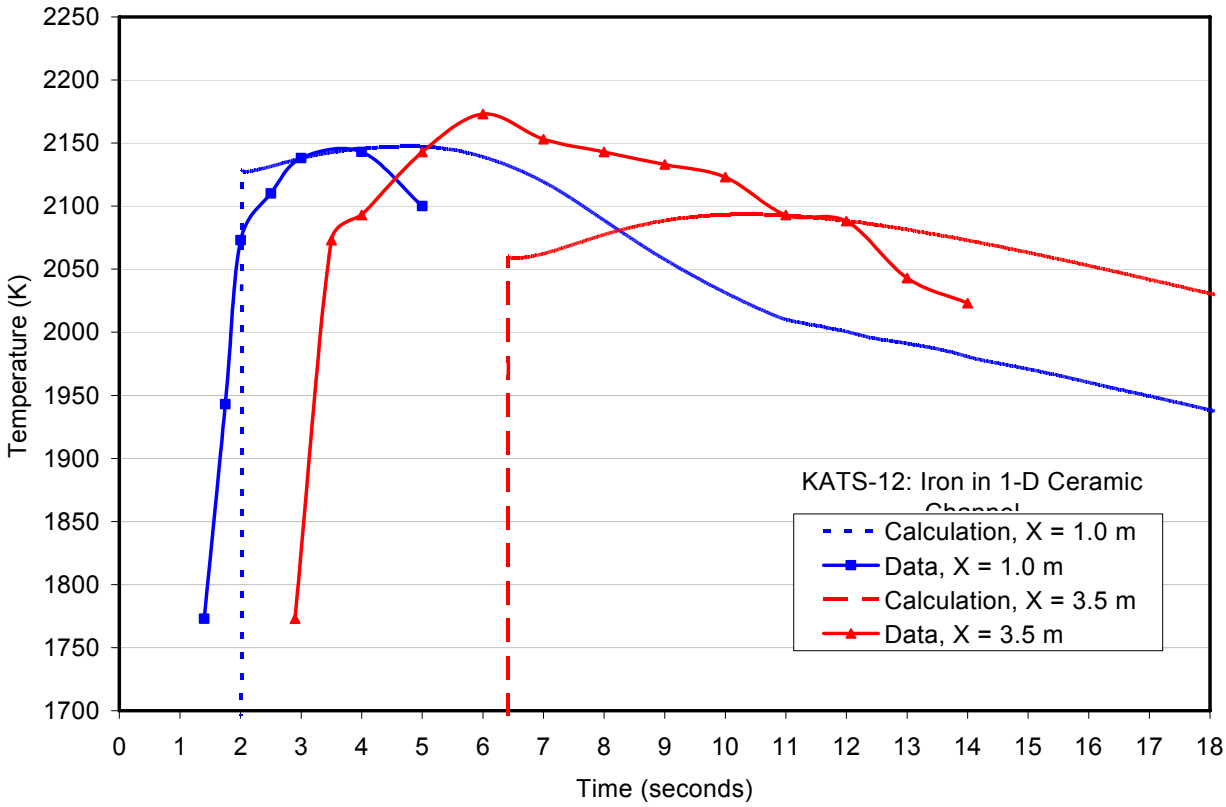

Figure A.58. Comparison of local melt temperature predictions with KATS-12 metal data.

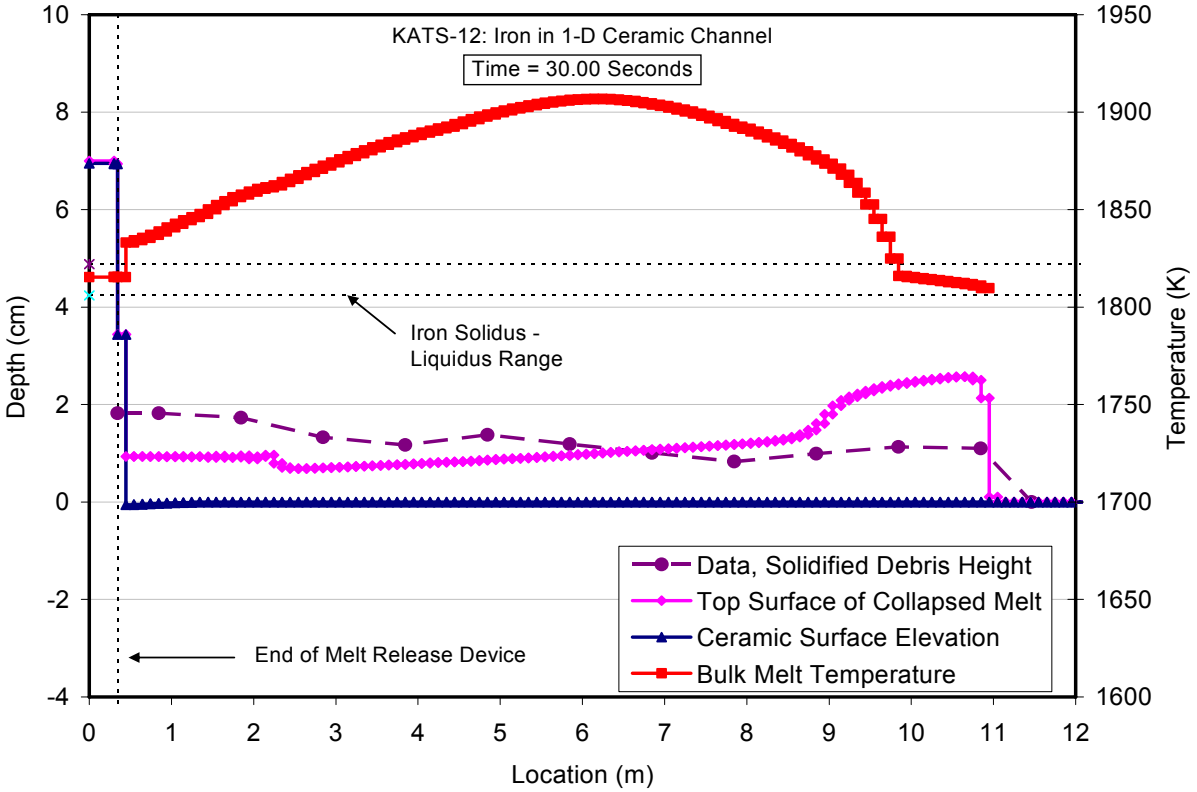

Figure A.59. Comparison of posttest debris profile prediction with KATS-12 metal data.

profile comparison in Figure A.59 shows some discrepancies between the calculation and the experiment (code data are for the average h_r case). The large accumulation that develops at the leading edge in the calculation is a byproduct of the melt flowrate function for the test, viz., initially large, and then a linear decline. The large structure to the left in Figure A.59 is the melt accumulator. As discussed earlier, this design may have caused overshoot of some (unknown) distance of the spreading surface and a corresponding initial spreading velocity that would exceed what the code would calculate based on gravity-driven spreading alone. This may explain at least part of the discrepancy in initial spreading rate seen early in Figure A.57 since the code assumes continuous flow through the mesh with no possibility of bypass.

Test characteristics and the corresponding modeling input data for the KATS-13 metal test are summarized in Table A.22. Code subroutines were used to evaluate melt properties, and the code default composition for siliceous concrete was assumed since the data report did not provide this information. As discussed in Section 2, this test was an outlier in terms of the interfacial heat transfer resistance that was required to match the spreading length observed in the experiment (see Table 2.6). On this basis, the calculated leading edge penetration vs. time is compared to the test data in Figure A.60 using only the best fit h_r value of 12,000 W/m^2-K. Local melt temperature and post-spreading material profile predictions, again based on the best-fit h_r, are compared with the data in Figures A.61 and A.62, respectively. As for KATS-12, this was a high flowrate test, and so the possibility exists that the melt overshot some distance of the spreading surface near the accumulator, leading to an apparent spreading velocity that was initially larger than the prediction.

Table A.22. Input File Data Sheet for the KATS-13 Metal Melt Test with Concrete Channel.

Test parameter	Value
Test name	KATS-13, metal, concrete channel
Melt composition (wt %)	100 Fe
Melt delivery technique	Melt poured into an accumulator box that was 17.0 cm wide, 30.2 cm long, and 9.0 cm above the spreading surface. Pour initiated by opening a gate to the spreading channel.
Melt temperature	2220 K
Total pour mass	135 kg
Substrate material	Siliceous concrete
Spreading geometry	1-D channel, 15 m long by 15 cm wide
Code input parameter(s)	**Value(s)**
Melt composition (wt %)	100 Fe
Melt pour temperature	2220 K
Melt oxide phase solidus – liquidus	1403 K – 1523 K
Melt metal phase solidus – liquidus	1806 K – 1816 K
Melt pour rate and duration	Linear decrease in pour rate from 40.3 kg/sec to zero over 6.7 second interval
Melt material property evaluation	Code subroutines
Substrate composition	Default siliceous concrete
Substrate initial temperature	298 K
Substrate material properties evaluation	Code subroutines
Substrate solidus - liquidus temperatures	1403 – 1523 K (Code default values)
Substrate nodalization	At each substrate nodal location, twelve 6.0 mm cells are used; all nodes cell-centered.
Spreading cavity nodalization	Accumulator: modeled as a single cell that is 17.0 cm wide, 30.2 cm long, and 9.0 cm above the channel surface. Gate: modeled as a single cell that is 8 cm wide, 4.3 cm long, and 9.0 cm above the channel. Incline down to channel: modeled as a single cell that is 10 cm long, 15 cm wide, and 4.5 cm above the channel. Channel: 12 m modeled using 120 cells; each is 15 cm wide and 10 cm long. All nodes cell-centered.
Cavity condition	Dry
Upper atmosphere temperature	300 K
Upper atmosphere emissivity	0.7
Ambient pressure	0.1 MPa
Melt/substrate heat transfer coefficient model	Locally, largest of Dittus – Boelter and Bradley slag film heat transfer coefficients
Best estimate melt/substrate interfacial heat transfer resistance	12,000 W/m^2-K
Constant used in Ramacciotti correlation	7.26
Solid-fraction variation between liquidus/solidus	See Figure 2.3
Timestep	0.01 seconds

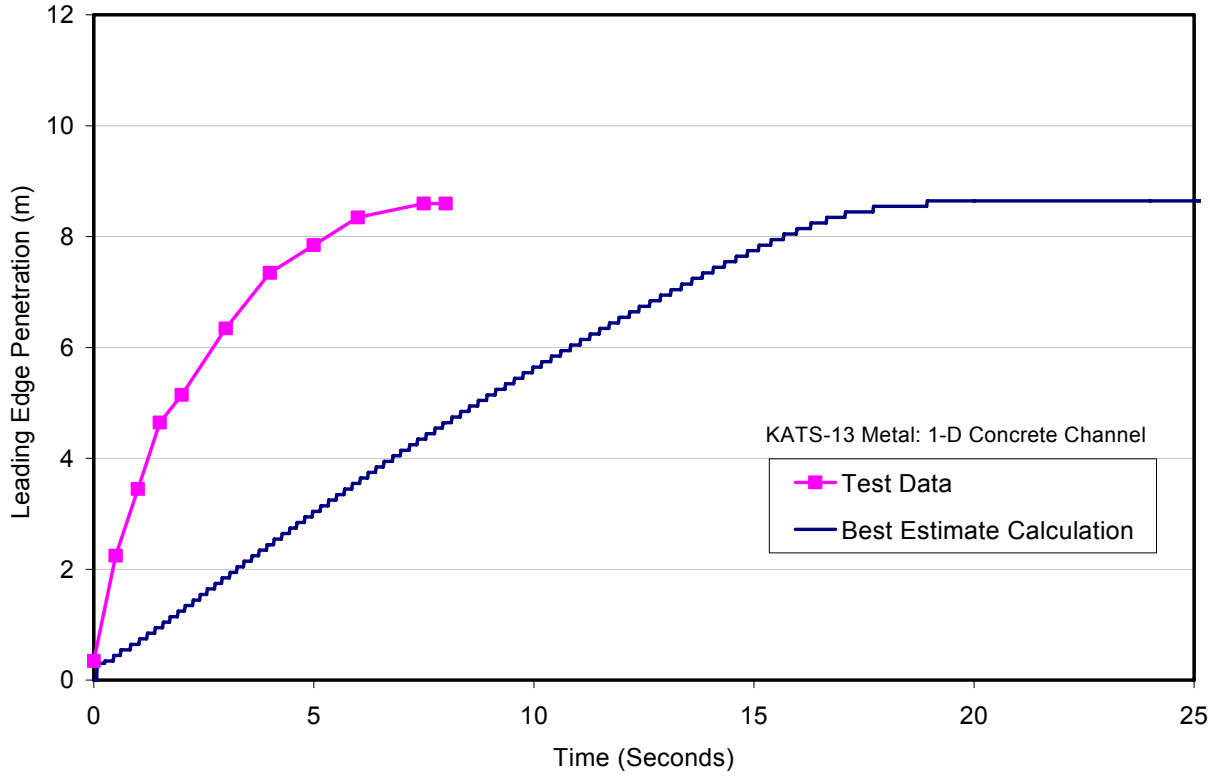

Figure A.60. Leading edge penetration comparison for the KATS-13 metal spreading test.

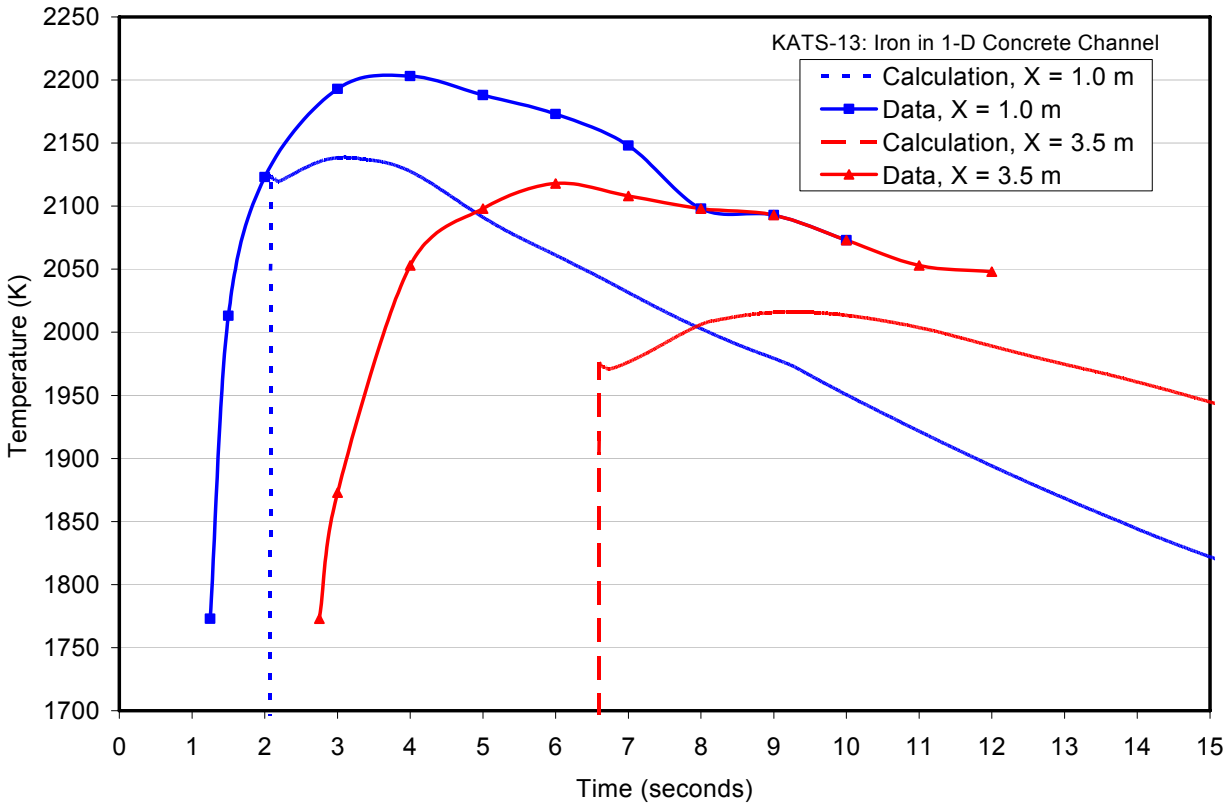

Figure A.61. Comparison of local melt temperature predictions with KATS-13 metal data.

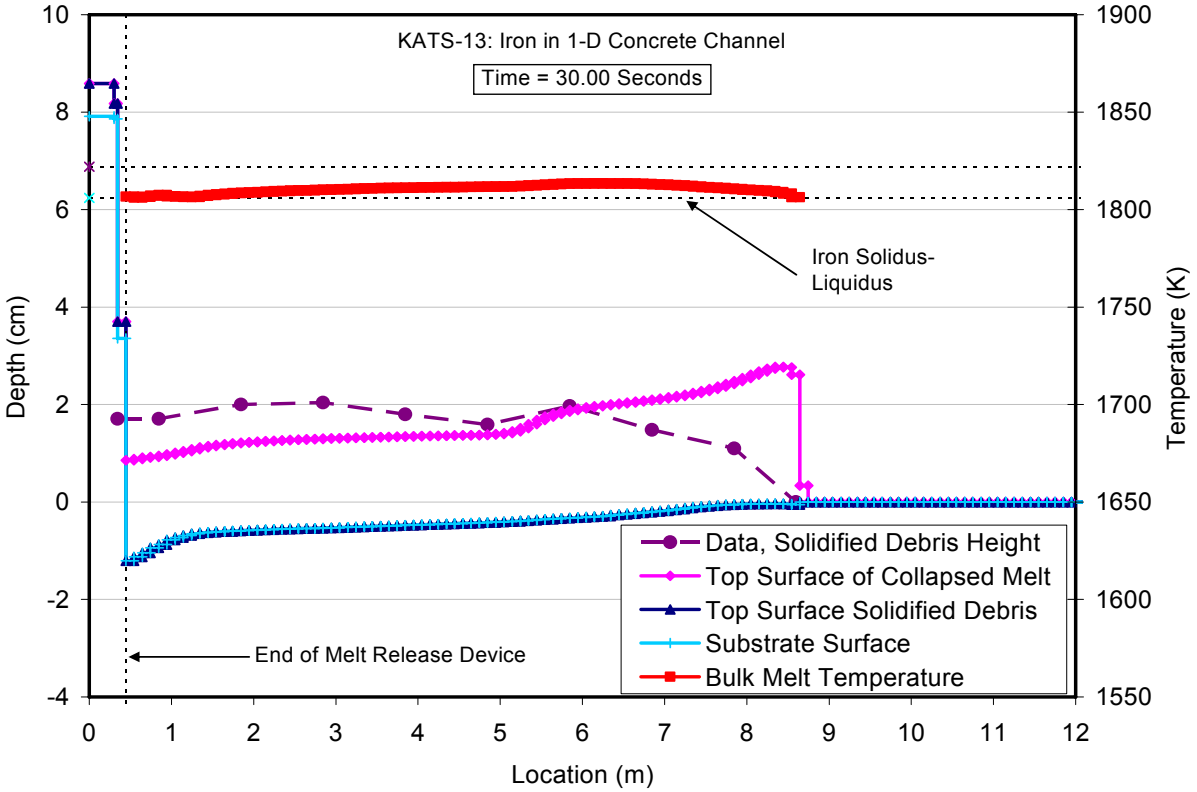

Figure A.62. Comparison of posttest debris profile prediction with KATS-13 metal data.

As is evident from Figure A.61, peak melt temperature 1 m from the gate was underpredicted by ~ 70 K, and the discrepancy grows to almost 100 K at the 3.5 m distance. There are also some discrepancies in the overall shape of the posttest debris distribution (Figure A.62). The code predicts up to 1 cm of basemat erosion, but data on basemat erosion was not collected as part of the posttest exams for this experiment.

Test characteristics and the corresponding code input for the KATS-14 metal test are summarized in Table A.23. As for KATS-12, the recommended substrate thermal-physical property data was used, but the melt properties were calculated using code subroutines. The calculated leading edge penetration versus time is compared to the test data in Figure A.63, while local melt temperature and post-spreading material profile predictions are compared with the data in Figures A.64 and A.65, respectively. The pour rate in this test was lower compared to the counterpart test KATS-12, and so the time interval over which the spreading characteristics were governed by inertial effects was larger. In general, the code does a much better job capturing the initial rate of melt spreading from the accumulator box in comparison to KATS-12.

Examination of the melt temperature data in Figure A.64 indicates that despite discrepancies in melt arrival times, peak melt temperatures are predicted to within ~ 40 K at the 1 meter location, ~ 100 K at the 4 m location, and ~ 50 K at the 7 m location. As shown in Figure A.65, there are again some discrepancies in the overall shape of the debris, but the code does a qood job of replicating the shape of the basemat erosion profile; for this experiment, that information was provided.

Table A.23. Input File Data Sheet for the KATS-14 Metal Melt Test with Ceramic Channel.

Test parameter	Value
Test name	KATS-14, metal, ceramic channel
Melt composition (wt %)	100 Fe
Melt delivery technique	Melt poured into an accumulator box that was 18.0 cm wide, 20.0 cm long, and 5.0 cm above the spreading surface. Pour initiated by opening a gate to the spreading channel.
Melt temperature	2440 K
Total pour mass	154 kg
Substrate material	Cordierite
Spreading geometry	1-D channel, 12 m long by 15 cm wide
Code input parameter(s)	**Value(s)**
Melt composition (wt %)	100 Fe
Melt pour temperature	2440 K
Melt oxide phase solidus – liquidus	1893 K – 1923 K
Melt metal phase solidus – liquidus	1806 K – 1816 K
Melt pour rate and duration	Linear increase in pour rate from 6.16 to 9.24 kg/sec over a 20 second interval
Melt material property evaluation	Code subroutines
Substrate composition	Corderite (modeled using user-specified material input properties)
Substrate initial temperature	298 K
Substrate material properties evaluation[a]	$c_s = c_l = 840$ J/kg-K, $\Delta h_f = 1.0$ MJ/kg, $\rho_s = \rho_l = 2200$ kg/m^3, $k_s = k_l = 3.8$ W/m-K, and $\varepsilon = 0.3$
Substrate solidus - liquidus temperatures	1893 K – 1923 K
Substrate nodalization	At each substrate nodal location, twelve 6.0 mm cells are used; all nodes are cell-centered.
Spreading cavity nodalization	Accumulator: modeled as a single cell that is 18.0 cm wide, 20.0 cm long, and 5.0 cm above the channel surface. Gate: modeled as a single cell that is 14.0 cm wide, 4.3 cm long, and 5.0 cm above the channel. Incline down to channel: modeled as a single cell that is 3.0 cm long, 15 cm wide, and 2.5 cm above the channel. Channel: 12 m modeled using 120 cells; each is 15 cm wide and 10 cm long. All nodes cell-centered.
Cavity condition	Dry
Upper atmosphere temperature	300 K
Upper atmosphere emissivity	0.7
Ambient pressure	0.1 MPa
Melt/substrate heat transfer coefficient model	Dittus - Boelter
Best estimate melt/substrate interfacial heat transfer resistance	5950 W/m^2-K
Constant used in Ramacciotti correlation	7.26
Solid-fraction variation between liquidus/solidus	See Figure 2.3
Timestep	0.02 seconds

[a]As applicable, c denotes specific heat, Δh_f is latent heat of fusion, ρ is density, k is thermal conductivity, ε is emissivity, and subscripts s and l denote solid and liquid phases, respectively.

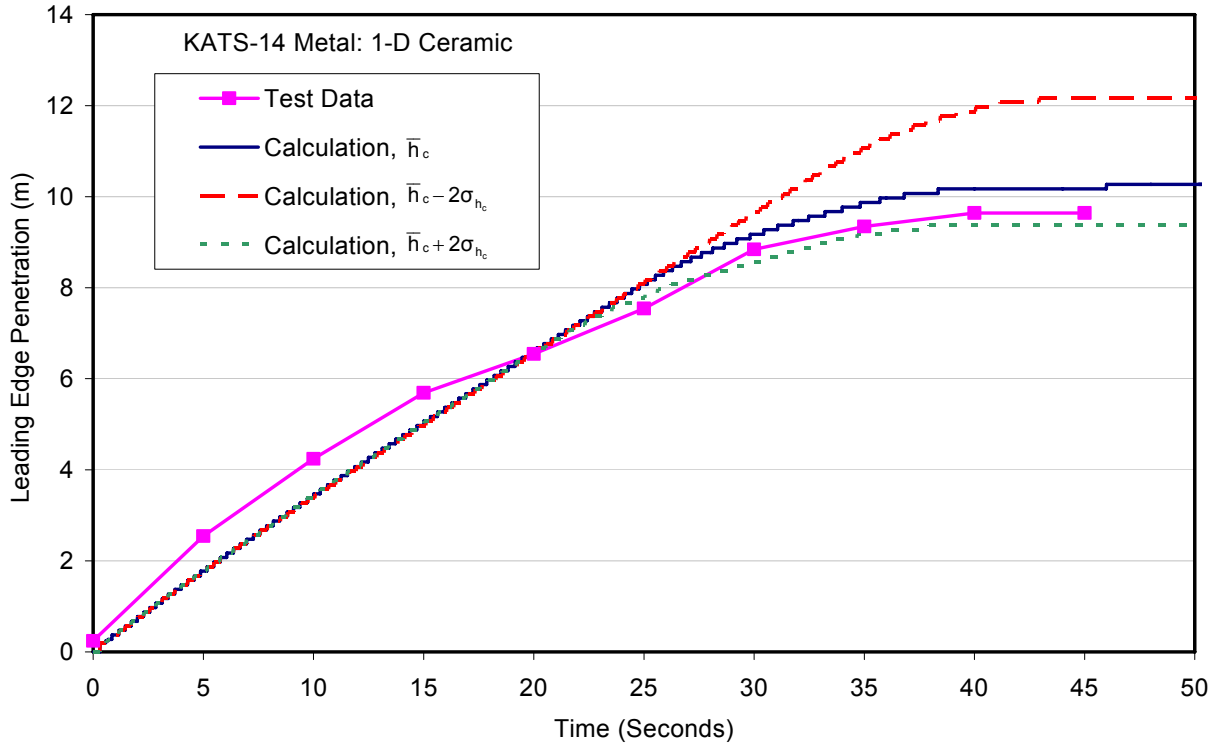

Figure A.63. Leading edge penetration comparison for the KATS-14 metal spreading test.

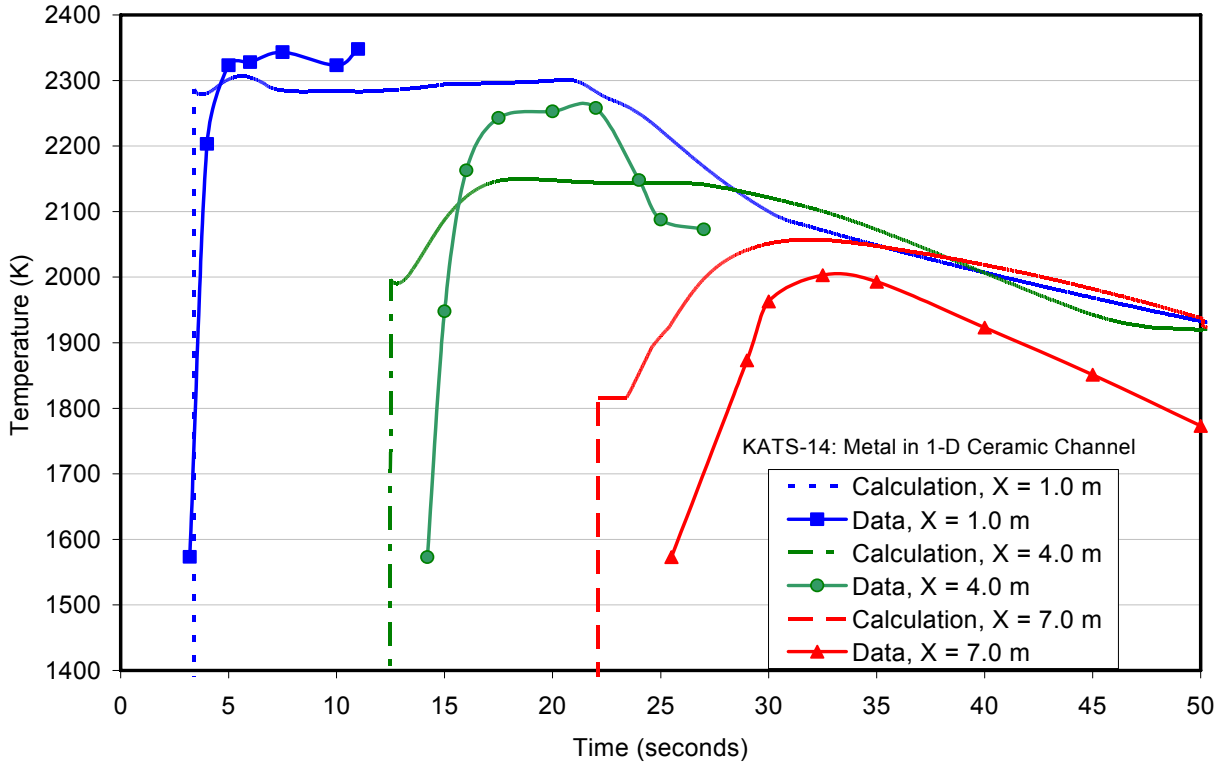

Figure A.64. Comparison of local melt temperature predictions with KATS-14 metal data.

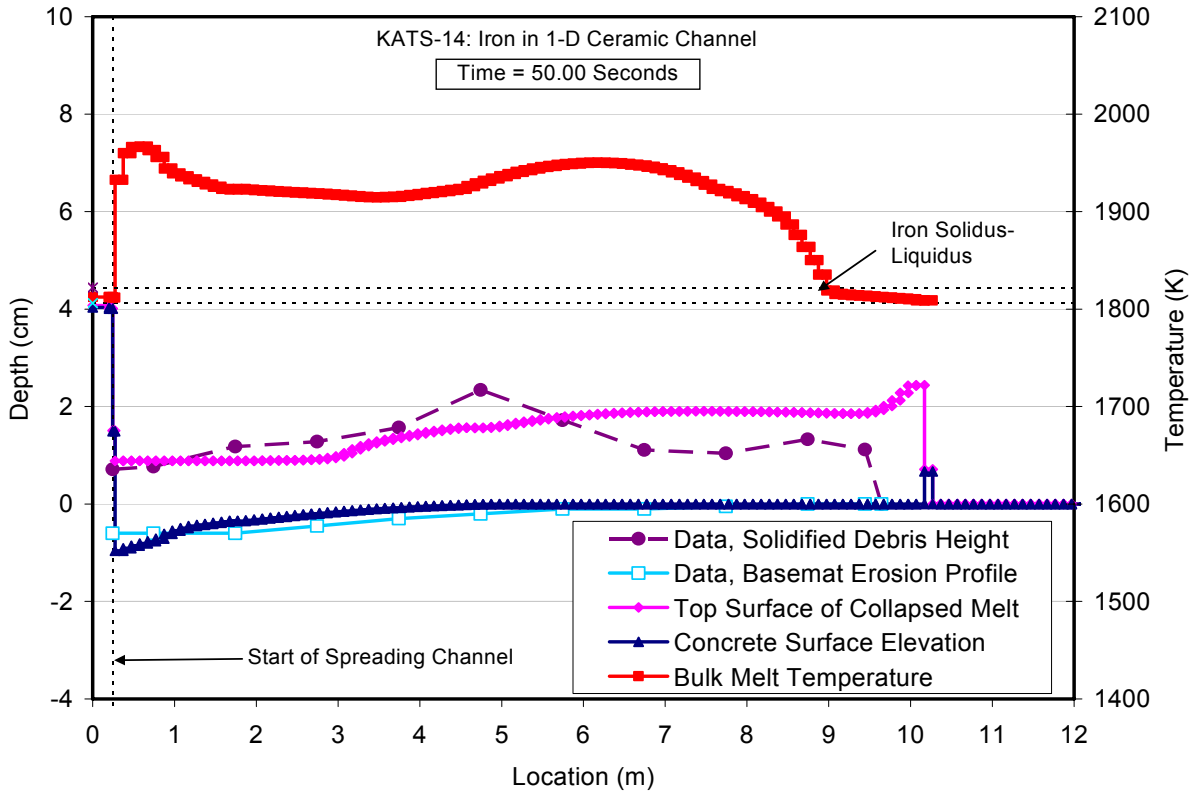

Figure A.65. Comparison of posttest debris profile prediction with KATS-14 metal data.

A.3.2 SPREAD Stainless Steel Spreading Tests

As discussed in Section 1, these tests involved spreading of stainless steel melts in test sections that mimicked the key features of the GE BWR Mark I containment. In particular, melt was poured into a cylindrical cavity that represented the reactor pedestal. The melt then spread into a large open region simulating the cavity annulus through a doorway. Although many spreading tests were conducted in this program, minimal data was reported in the open literature. Sufficient information was gathered to examine two tests: i) Test 15, which was a dry cavity experiment, and ii) Test 21, which was similar to Test 15 but had water present.

Test characteristics and code input for Test 15 are summarized in Table A.24, while comparisons with maximum melt penetration distance and the posttest debris profile are provided in Figures A.66 and A.67, respectively. The analogous set of information for Test 21 that was conducted with water present is provided in Table A.25 and Figures A.68 and A.69, respectively. Both tests used stainless steel melts with siliceous concrete substrates. MELTSPREAD was originally developed for Mark I containment applications, and on that basis the code has an automated meshing scheme for this geometry. This option was used to generate the nodalization schemes for these tests, with the melt spreading angle outside the pedestal doorway set to the experimentally observed value of 130º. Code subroutines were used to calculate the melt and substrate thermal-physical properties.

As is evident from the figures, the code calculates that melt spreading would be limited by solidification at the leading edge for both tests. In addition, a few millimeters of substrate

Table A.24. Input File Data Sheet for SPREAD Test 15 with Metal Melt in a Mockup of the Mark I Containment with Dry Concrete Floor.

Test parameter	Value
Test name	SPREAD Test 15
Melt composition (wt %)	70 Fe, 20 Cr, 10 Ni (stainless steel)
Melt delivery technique	Melt poured into a 17.5 cm radius cylindrical cavity that simulated the pedestal of a Mark I containment.
Melt temperature	1804 K
Total pour mass	63.6 kg
Substrate material	Siliceous concrete
Spreading geometry	Mockup of a Mark I containment: A 17.5 cm inner radius cylindrical cavity with a 5 cm wide doorway leading to an annular spreading region with a radius of 1.275 m. The wall thickness of the pedestal was 5 cm.
Code input parameter(s)	**Value(s)**
Melt composition (wt %)	70 Fe, 20 Cr, 10 Ni
Melt pour temperature	1804 K
Melt oxide phase solidus – liquidus	1403 K – 1523 K
Melt metal phase solidus – liquidus	1671 K – 1727 K
Melt pour rate and duration	Steady pour rate of 9.5 kg/sec over a 6.7 second interval
Melt material property evaluation	Code subroutines
Substrate composition	Default siliceous concrete
Substrate initial temperature	298 K
Substrate material properties evaluation	Code subroutines
Substrate solidus - liquidus temperatures	1403 – 1523 K (Code default values)
Substrate nodalization	At each substrate nodal location, six 5.0 mm cells followed by six 10 mm cells; all nodes cell-centered.
Spreading cavity nodalization	Automated Mark I shell meshing option used: melt assumed pour into the sump which was taken to have a radius of 10 cm and was flush with the concrete surface; balance of pedestal interior meshed with 3 nodes that were 2.5 cm wide. The 5 cm wide doorway was meshed with 2 cells that were 2.5 cm wide. As concluded by the experimenters, the melt was assumed to spread outside the doorway with a spreading angle of 130º. The distance from the doorway to the shell was meshed with 61 cells that were 2.17 cm wide. All nodes cell-centered.
Cavity condition	Dry
Upper atmosphere temperature	300 K
Upper atmosphere emissivity	0.6
Ambient pressure	0.1 MPa
Melt/substrate heat transfer coefficient model	Locally, largest of Dittus – Boelter and Bradley slag film heat transfer coefficients
Best estimate melt/substrate interfacial heat transfer resistance	4980 W/m^2-K
Constant used in Ramacciotti correlation	7.26
Solid-fraction variation between liquidus/solidus	See Figure 2.3
Timestep	0.02 seconds

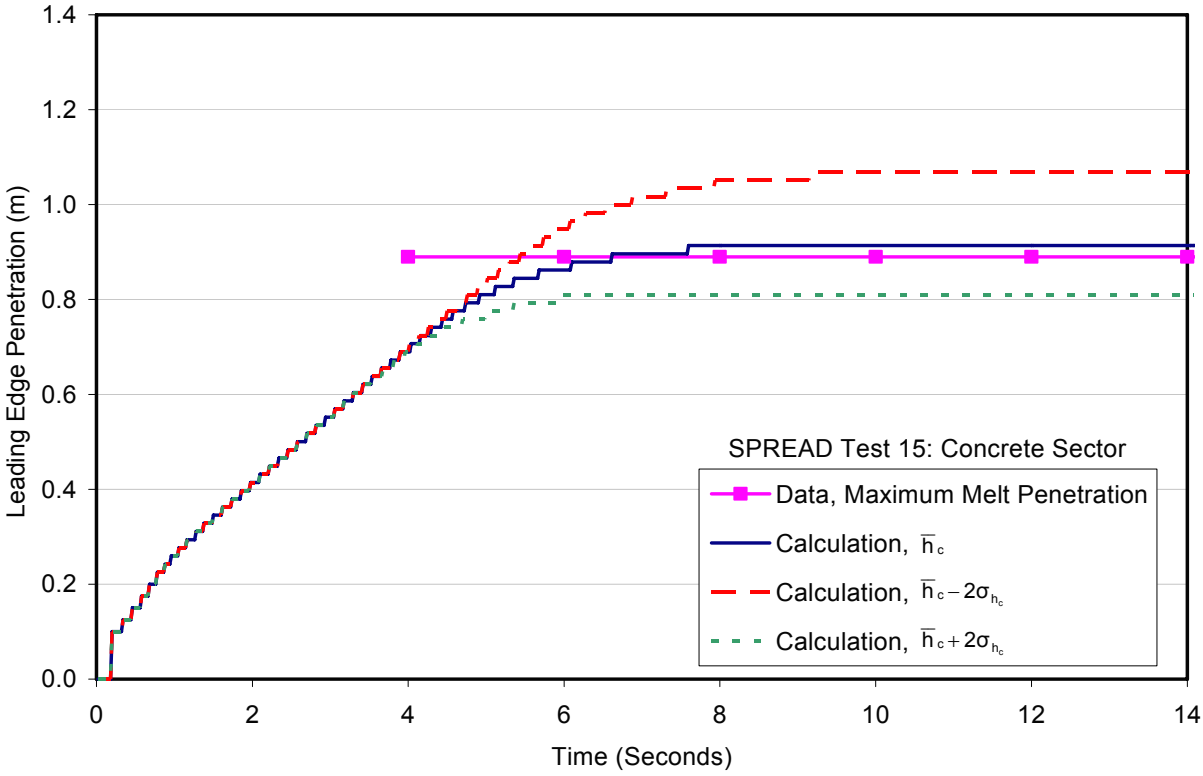

Figure A.66. Leading edge penetration comparison for the SPREAD Test 15 metal spreading test.

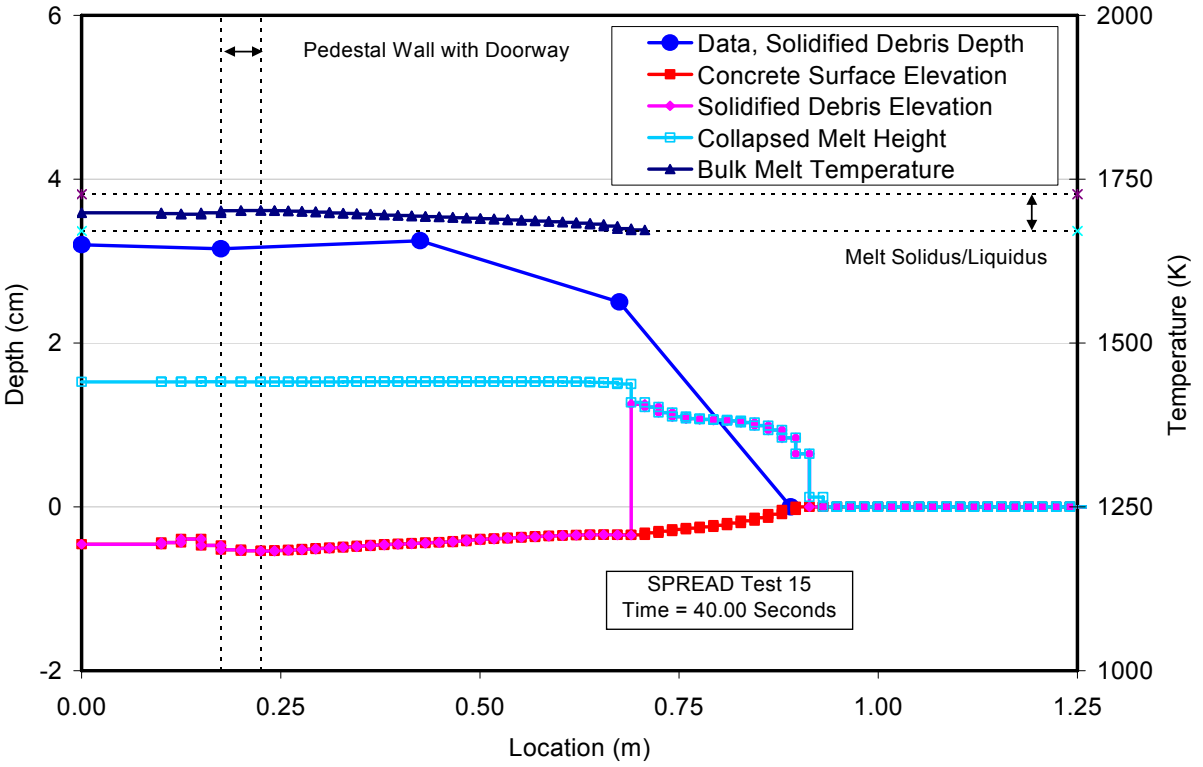

Figure A.67. Comparison of posttest debris profile prediction with SPREAD Test 15 data.

Table A.25. Input File Data Sheet for SPREAD Test 21 with Metal Melt in a Mockup of the Mark I Containment with Wet Concrete Floor.

Test parameter	Value
Test name	SPREAD Test 21
Melt composition (wt %)	70 Fe, 20 Cr, 10 Ni (stainless steel)
Melt delivery technique	Melt poured into a 17.5 cm radius cylindrical cavity that simulated the pedestal of a Mark I containment.
Melt temperature	1778 K
Total pour mass	69.2 kg
Substrate material	Siliceous concrete
Spreading geometry	Mockup of a Mark I containment: A 17.5 cm inner radius cylindrical cavity with a 5 cm wide doorway leading to an annular spreading region with a radius of 1.275 m. The wall thickness of the pedestal was 5 cm.
Code input parameter(s)	**Value(s)**
Melt composition (wt %)	70 Fe, 20 Cr, 10 Ni
Melt pour temperature	1778 K
Melt oxide phase solidus – liquidus	1403 K – 1523 K
Melt metal phase solidus – liquidus	1671 K – 1727 K
Melt pour rate and duration	Steady pour rate of 9.5 kg/sec over a 7.27 second interval
Melt material property evaluation	Code subroutines
Substrate composition	Default siliceous concrete
Substrate initial temperature	298 K
Substrate material properties evaluation	Code subroutines
Substrate solidus - liquidus temperatures	1403 – 1523 K (Code default values)
Substrate nodalization	At each substrate nodal location, six 5.0 mm cells followed by six 10 mm cells; all nodes cell-centered.
Spreading cavity nodalization	Automated Mark I shell meshing option used: melt assumed pour into the sump which was taken to have a radius of 10 cm and was flush with the concrete surface; balance of pedestal interior meshed with 3 nodes that were 2.5 cm wide. The 5 cm wide doorway was meshed with 2 cells that were 2.5 cm wide. As concluded by the experimenters, the melt was assumed to spread outside the doorway with a spreading angle of 130º. The distance from the doorway to the shell was meshed with 61 cells that were 2.17 cm wide. All nodes cell-centered.
Cavity condition	Wet
Water temperature (subcooling)	298 (75) K
Ambient pressure	0.1 MPa
Water depth	4.0 cm
Melt/substrate heat transfer coefficient model	Locally, largest of Dittus – Boelter and Bradley slag film heat transfer coefficients
Melt/substrate interfacial heat transfer resistance assumed in calculation	4980 W/m^2-K
Constant used in Ramacciotti correlation	7.26
Solid-fraction variation between liquidus/solidus	See Figure 2.3
Timestep	0.01 seconds

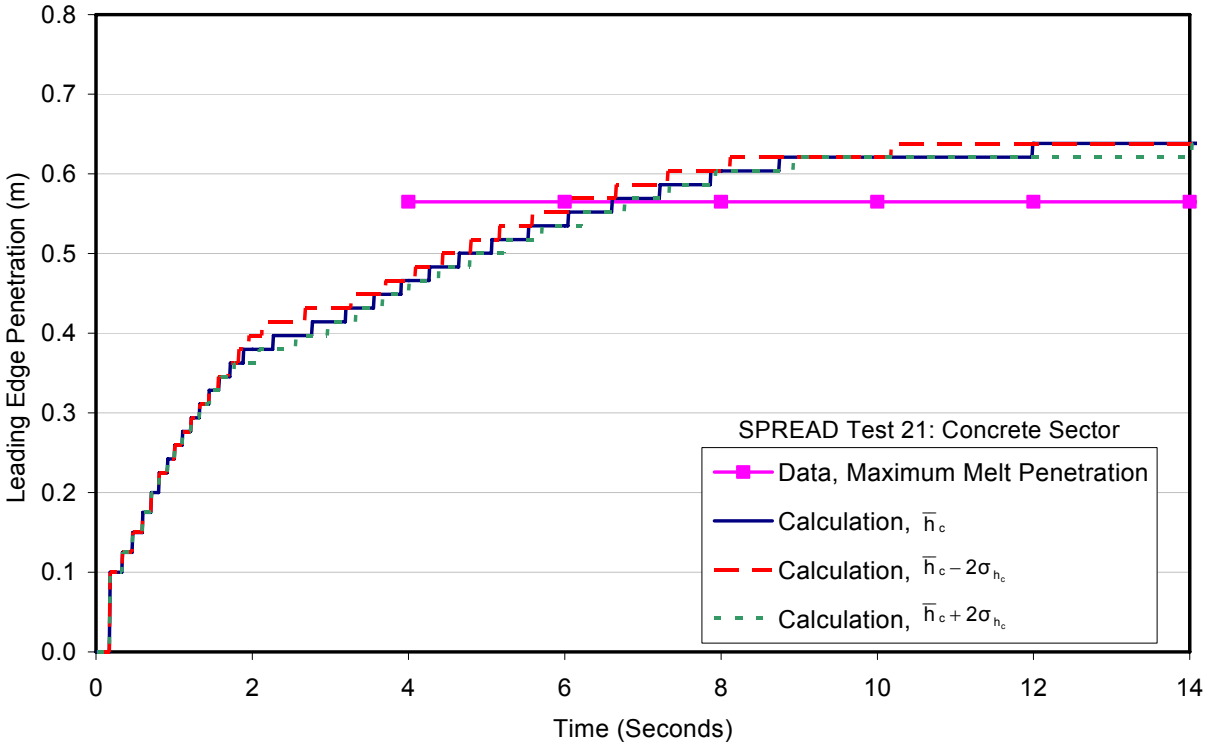

Figure A.68. Leading edge penetration comparison for the SPREAD Test 21 metal spreading test.

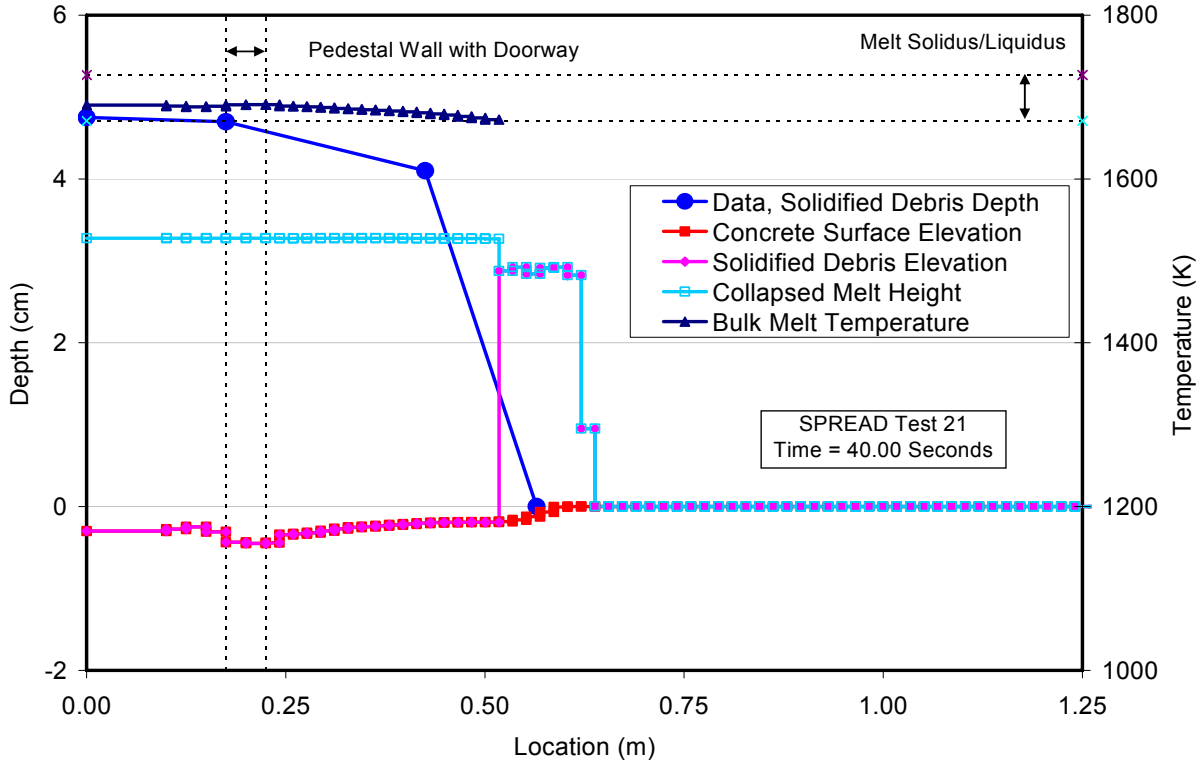

Figure A.69. Comparison of posttest debris profile prediction with SPREAD Test 21 data.

erosion are calculated for both tests, but this was not reported in the documentation.[9] The overall shape of the debris profiles following spreading are also similar to the data, but depth is consistently underpredicted. This is again due to the fact that the code does not account for porosity upon solidification, and since concrete decomposition gases would have been produced as a result of heat transfer to the substrate, porosity would have been present as the melt cooled and solidified.

A.4 Reactor Material Melt Spreading Tests

Following the benchmarking exercise against oxide simulant and metal melt spreading tests, the code was further exercised against tests conducted with reactor materials. As reported by Cognet et al.[16] and Journeau et al.,[17-18] several corium melt spreading tests were carried out at CEA with varying melt compositions and substrate materials in the VULCANO facility. Two corium tests were also conducted by Magallon and Tromm[19] as part of the FARO program, one of them under wet cavity conditions. Finally, several large scale spreading tests at up to 2 metric ton melt mass were conducted at Siempelkamp Nuklear in Germany on various types of surface materials (Sappok and Steinwarz[20] and Steinwarz et al.[21]). The code assessment against these tests is provided in this section.

A.4.1 Vulcano Spreading Tests

These tests[16-18] involved spreading of high temperature core oxide melts that were generated using a specially designed plasma arc furnace. Once the melts had reached the desired initial condition, the furnace was tilted and the melt was poured and spread within instrumented test sections. A total of 12 tests were conducted as part of this experiment program. The VULCANO VE-U7 test was selected from the matrix for analysis here because the experiment apparatus, operating conditions, and results have been very well documented in the open literature. For this test, a 40 kg core melt mass was generated and poured into an accumulator that fed two parallel spreading channels: one concrete, the other refractory ceramic. The overall spreading geometry was a 19º sector with a wall in the center dividing the two parallel channels. Thus, each channel was modeled as an isolated 9.5º sector.

Test characteristics and the corresponding code input that was used to model the concrete channel spreading test are summarized in Table A.26. As is evident, the code subroutines were used to calculate both the melt and substrate thermal-physical property data. Furthermore, as part of the specifications for the experiment, the concrete composition was provided and so this was also used as code input to improve the fidelity of the simulation. One of the modeling challenges for these tests was how to best define the melt pour rate into the two parallel channels given the fact that the code can only calculate one channel at a time. What is known regarding the test operations is the total pour mass into the accumulator, the pour duration, and the corium mass recovered from each channel. With this information, the pour rate into each channel was calculated by dividing the recovered mass by the overall pour duration.

The calculated leading edge penetration vs. time is compared to the concrete channel test data in Figure A.70, while substrate thermal response and post-spreading material profile predictions are compared with data in Figures A.71 and A.72, respectively.

Table A.26. Input File Data Sheet for the VULCANO VE-U7 Test with Concrete Channel.

Test parameter	Value
Test name	VULCANO VE-U7, concrete channel
Melt composition (wt %)	61 UO_2, 30 ZrO_2, 3 FeO, 2 $CaSiO_3$, 2 SiO_2, 0.6 CaO, 0.4 Al_2O_3, 1 Fe
Melt delivery technique	Melt poured into a common accumulator that fed both the concrete and ceramic channels of the apparatus. The accumulator had an average width of 20 cm, length of 15 cm, and was 0.5 cm deep relative to spreading surface. The total 40 kg melt mass was poured at an average rate of 3.0 kg/sec from a furnace into the accumulator.
Melt temperature	2450 K
Total pour mass	18.5 kg[a] for the concrete channel side
Substrate material	Siliceous concrete
Spreading geometry	9.5º sector with an opening width of 9.5 cm from the accumulator; overall channel length was 1.084 m.
Code input parameter(s)	**Value(s)**
Melt composition (wt %)	61 UO_2, 30 ZrO_2, 3 FeO,1, Fe, 5 slag (slag is 3 SiO_2, 1.6 CaO, 0.4 Al_2O_3)
Melt pour temperature	2450 K
Melt oxide phase solidus – liquidus	1270 K – 2640 K
Melt metal phase solidus – liquidus	1810 K – 1820 K
Melt pour rate and duration	Steady pour of 21.7 kg melt mass into the accumulator over a 13.3 second interval; average pour rate of 1.62 kg/sec.
Melt material property evaluation	Code subroutines
Substrate composition	4.2 CO_2, 3.7 H_2O, 1.4 K_2O, 0.7 Na_2O, 0.8 TiO_2, 69.8 SiO_2, 13.7 CaO, 0.7 MgO, 4.0 Al_2O_3, 1.0 Fe_2O_3
Substrate initial temperature	300 K
Substrate material properties evaluation	Code subroutines
Substrate solidus - liquidus temperatures	1390 K – 1960 K
Substrate nodalization	At each substrate nodal location, six 5.0 mm cells, followed by six 10 mm cells. All nodes cell-centered.
Spreading cavity nodalization	Accumulator: modeled as a single cell that is 10 cm wide, 15 cm long, and 0.5 cm deep. Spreading surface: modeled as 9.5º sector with 50 cells with a radial length of 2.17 cm. All nodes cell-centered.
Cavity condition	Dry
Upper atmosphere temperature	300 K
Upper atmosphere emissivity	1.0
Ambient pressure	0.1 MPa
Melt/substrate heat transfer coefficient model	Locally, larger of the Dittus – Boelter and Bradley slag film heat transfer coefficient models
Melt/substrate interfacial heat transfer resistance	0
Best-fit constant in Ramacciotti correlation	7.58
Solid-fraction variation between liquidus/solidus	See Figure 2.3
Timestep	0.02 seconds

[a]Estimate. Reported information: total pour mass was 40 kg, with 14 kg recovered from the ceramic channel and 12 kg from the concrete channel. The missing 12 kg was assumed to be retained in the accumulator, and was split between the concrete and ceramic channel sides according to the mass % recovered from each channel.

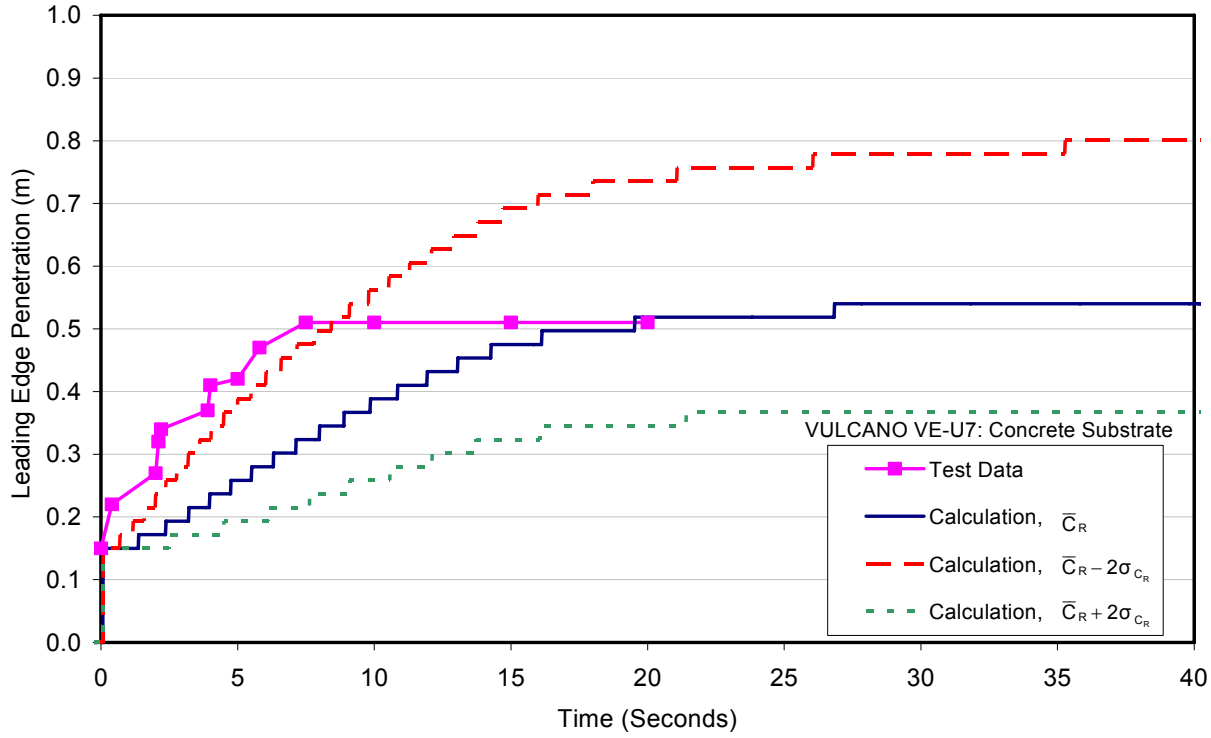

Figure A.70. Leading edge penetration comparison for the VULCANO VE-U7 core oxide spreading test over a concrete surface.

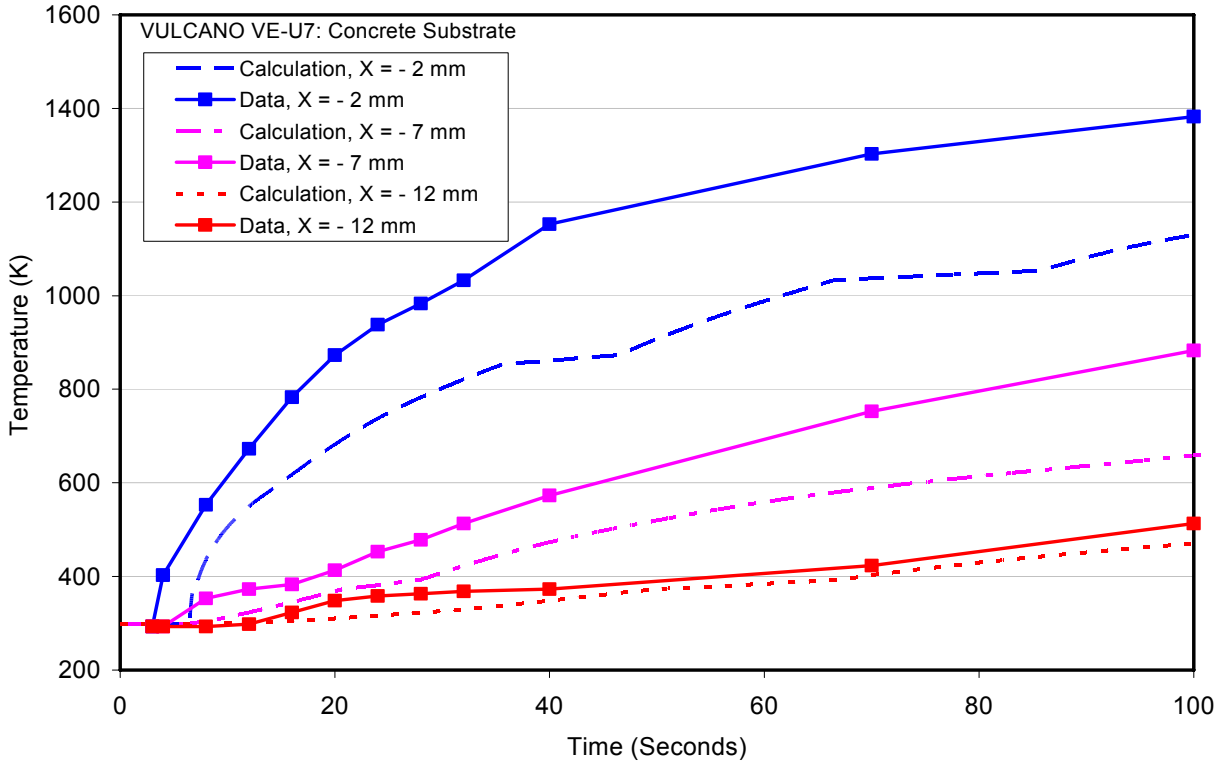

Figure A.71. Comparison of substrate thermal response predictions with VULCANO VE-U7 concrete channel data 12 cm from channel inlet.

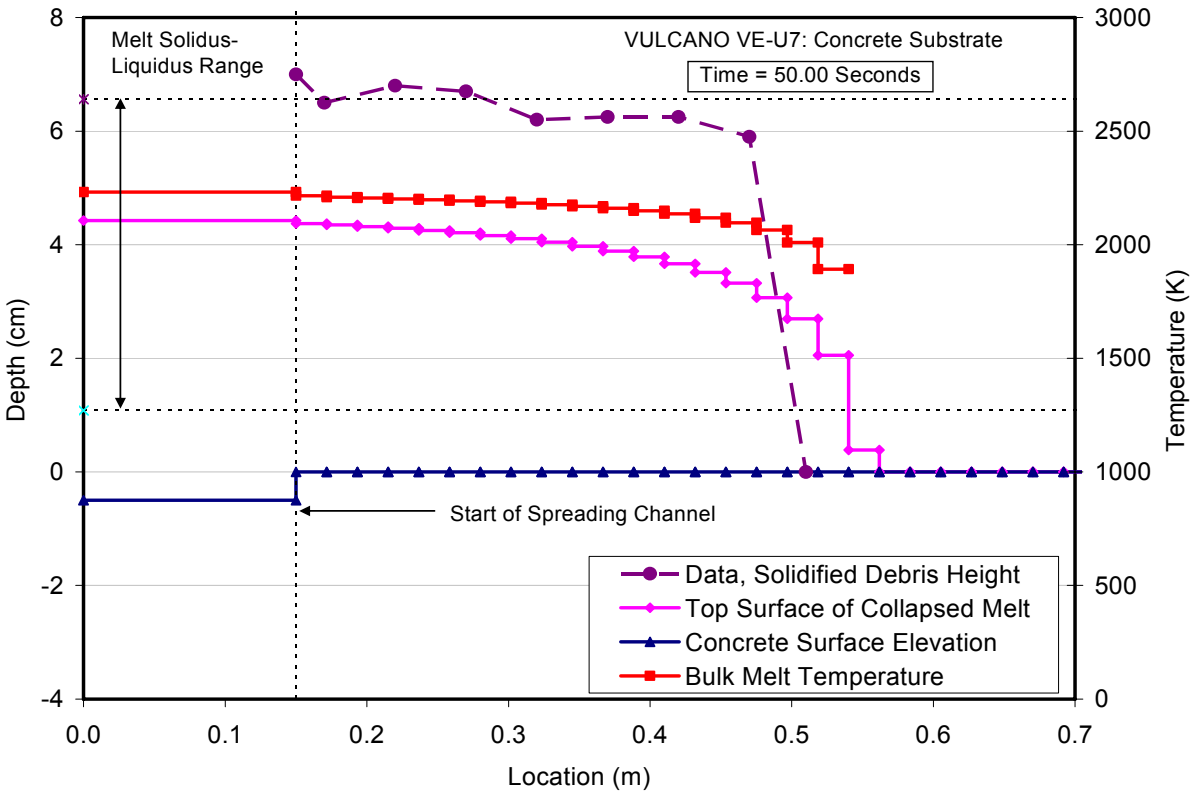

Figure A.72. Comparison of posttest debris profile prediction with VULCANO VE-U7 concrete channel data.

For the melt penetration data, results for C_R and $C_R \pm 2\sigma_{C_R}$ based on curve fits to the reactor material data (Table 2.5) are shown in the figure. The code slightly under predicts the velocity early in the transient, but the overall trend is reasonably reproduced. As is evident from Figure A.71, the code seems to underpredict heat transfer to the substrate for this test, with local temperatures falling ~ 200 K below those measured near the surface. Finally, the overall shape of the debris profile following spreading is similar to the data, but depth is consistently under-predicted. This again is due to the fact that the code does not account for porosity upon solidification, which would be present due to concrete decomposition gases.

The calculated leading edge penetration vs. time is compared to the ceramic channel test data in Figure A.73, while substrate thermal response and post-spreading material profile predictions are compared with data in Figures A.74 and A.75, respectively.

For this test, the code seems to do a reasonable job of predicting the leading edge propagation, including both the initial transient and longer term deceleration phases (Figure A.73). Moreover, the basemat thermal response is much better calculated for this test (Figure A.74); i.e., after the first few seconds of melt contact, the thermal response at the two recorded depths are reproduced to within ~ 50 K. Finally, the shape of the posttest debris distribution is reasonably replicated (Figure A.75), but depths are again slightly underpredicted since the code does not account for the presence of porosity during solidification.

Table A.27. Input File Data Sheet for the VULCANO VE-U7 Test with Ceramic Channel.

Test parameter	Value
Test name	VULCANO VE-U7, ceramic channel
Melt composition (wt %)	61 UO_2, 30 ZrO_2, 3 FeO, 2 $CaSiO_3$, 2 SiO_2, 0.6 CaO, 0.4 Al_2O_3, 1 Fe
Melt delivery technique	Melt poured into a common accumulator that fed both the concrete and ceramic channels of the apparatus. The accumulator had an average width of 20 cm, length of 15 cm, and was 0.5 cm deep relative to spreading surface. The total 40 kg melt mass was poured at an average rate of 3.0 kg/sec from a furnace into the accumulator.
Melt temperature	2450 K
Total pour mass	21.7 kg[a] for the ceramic channel side
Substrate material	zirconia
Spreading geometry	9.5º sector with an opening width of 9.5 cm from the accumulator; overall channel length was 1.084 m.
Code input parameter(s)	**Value(s)**
Melt composition (wt %)	61 UO_2, 30 ZrO_2, 3 FeO,1, Fe, 5 slag (slag is 3 SiO_2, 1.6 CaO, 0.4 Al_2O_3)
Melt pour temperature	2450 K
Melt oxide phase solidus – liquidus	1270 K – 2640 K
Melt metal phase solidus – liquidus	1810 K – 1820 K
Melt pour rate and duration	Steady pour of 21.7 kg melt mass into the accumulator over a 13.3 second interval; average pour rate of 1.62 kg/sec.
Melt material property evaluation	Code subroutines
Substrate composition	zirconia (modeled using user-specified material input properties)
Substrate initial temperature	300 K
Substrate material properties evaluation[b]	$c_s = c_l = 575$ J/kg-K, $\Delta h_f = 0.706$ MJ/kg, $\rho_s = \rho_l = 5300$ kg/m^3, $k_s = k_l = 4.7$ W/m-K, and $\varepsilon = 0.3$
Substrate solidus - liquidus temperatures	1780 K – 2900 K
Substrate nodalization	At each substrate nodal location, six 5.0 mm cells, followed by six 10 mm cells. All nodes cell-centered.
Spreading cavity nodalization	Accumulator: modeled as a single cell that is 10 cm wide, 15 cm long, and 0.5 cm deep. Spreading surface: modeled as 9.5º sector with 50 cells with a radial length of 2.17 cm. All nodes cell-centered.
Cavity condition	Dry
Upper atmosphere temperature	300 K
Upper atmosphere emissivity	1.0
Ambient pressure	0.1 MPa
Melt/substrate heat transfer coefficient model	Dittus - Boelter
Melt/substrate interfacial heat transfer resistance	0
Best-fit constant in Ramacciotti correlation	7.48
Solid-fraction variation between liquidus/solidus	See Figure 2.3
Timestep	0.02 seconds

[a]Estimate. Reported information: total pour mass was 40 kg, with 14 kg recovered from the ceramic channel and 12 kg from the concrete channel. The missing 12 kg was assumed to be retained in the accumulator, and was split between the concrete and ceramic channel sides according to the mass % recovered from each channel.

[b]Here, c denotes specific heat, Δh_f is latent heat of fusion, ρ is density, k is thermal conductivity, ε is emissivity, and subscripts s and l denote solid and liquid phases, respectively.

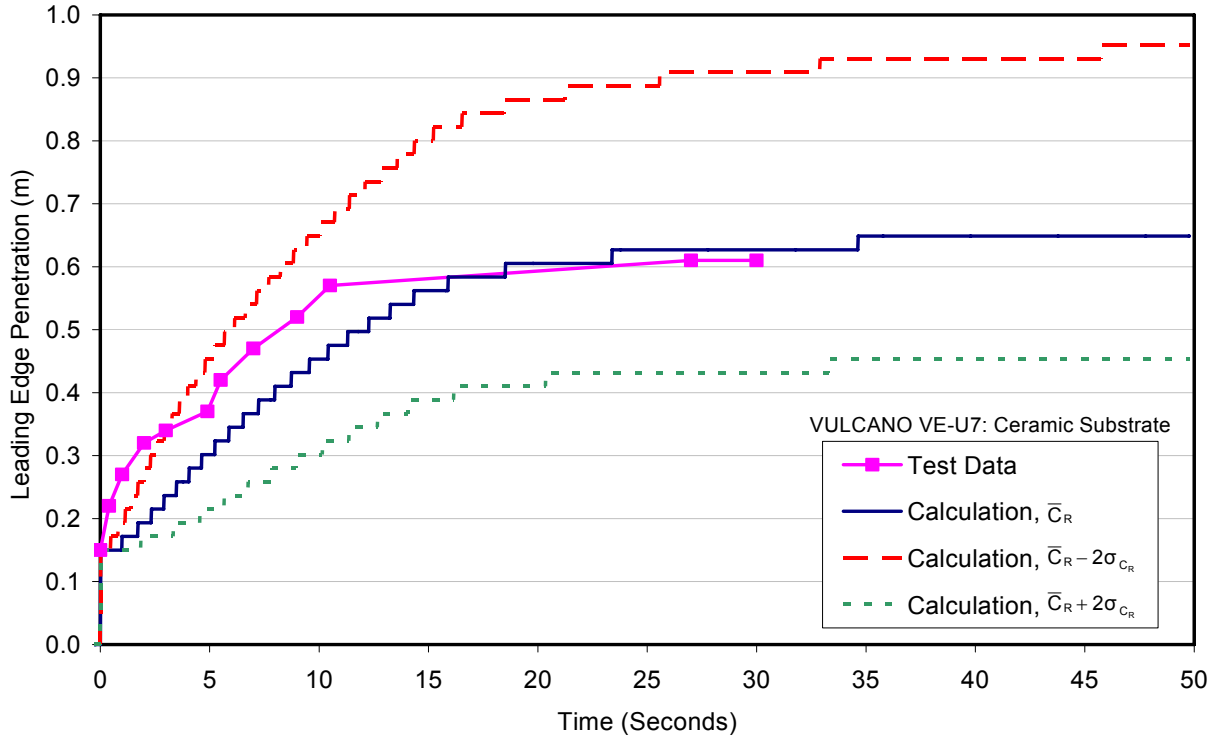

Figure A.73. Leading edge penetration comparison for the VULCANO VE-U7 core oxide spreading test over a ceramic surface.

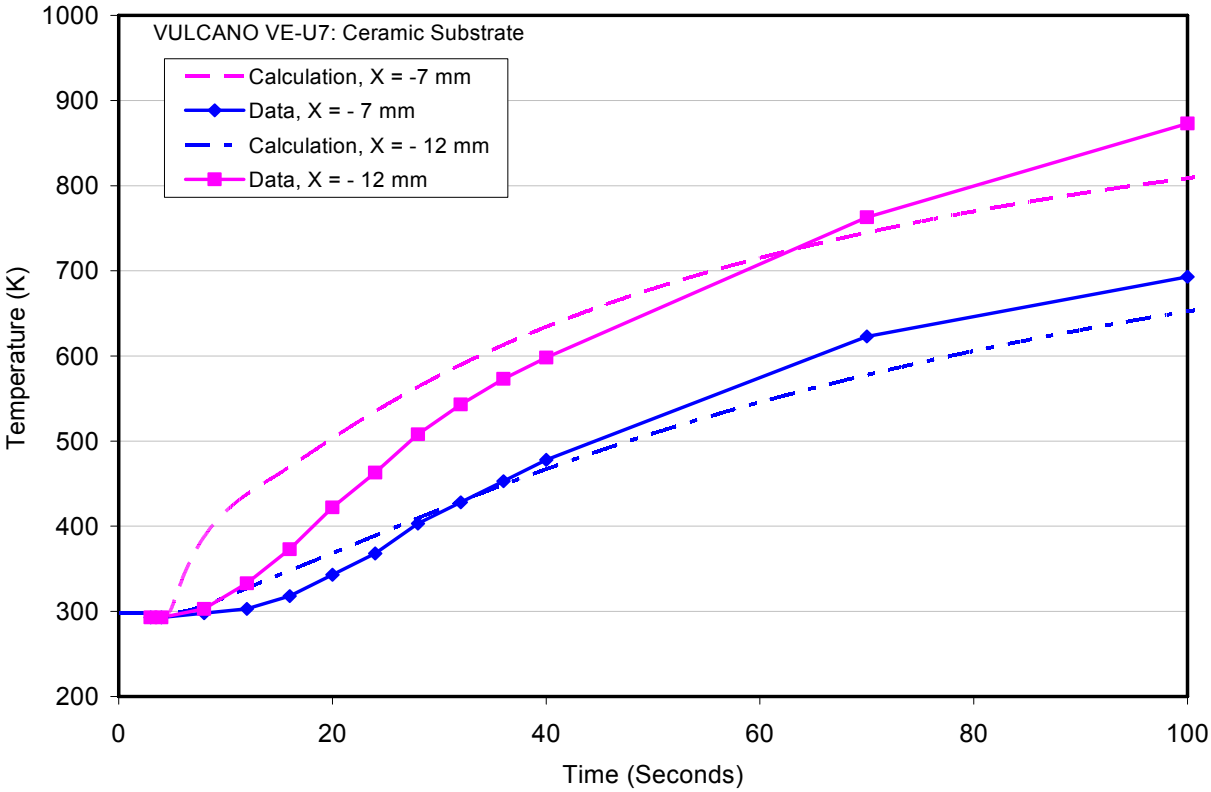

Figure A.74. Comparison of substrate thermal response predictions with VULCANO VE-U7 ceramic channel data 12 cm from channel inlet.

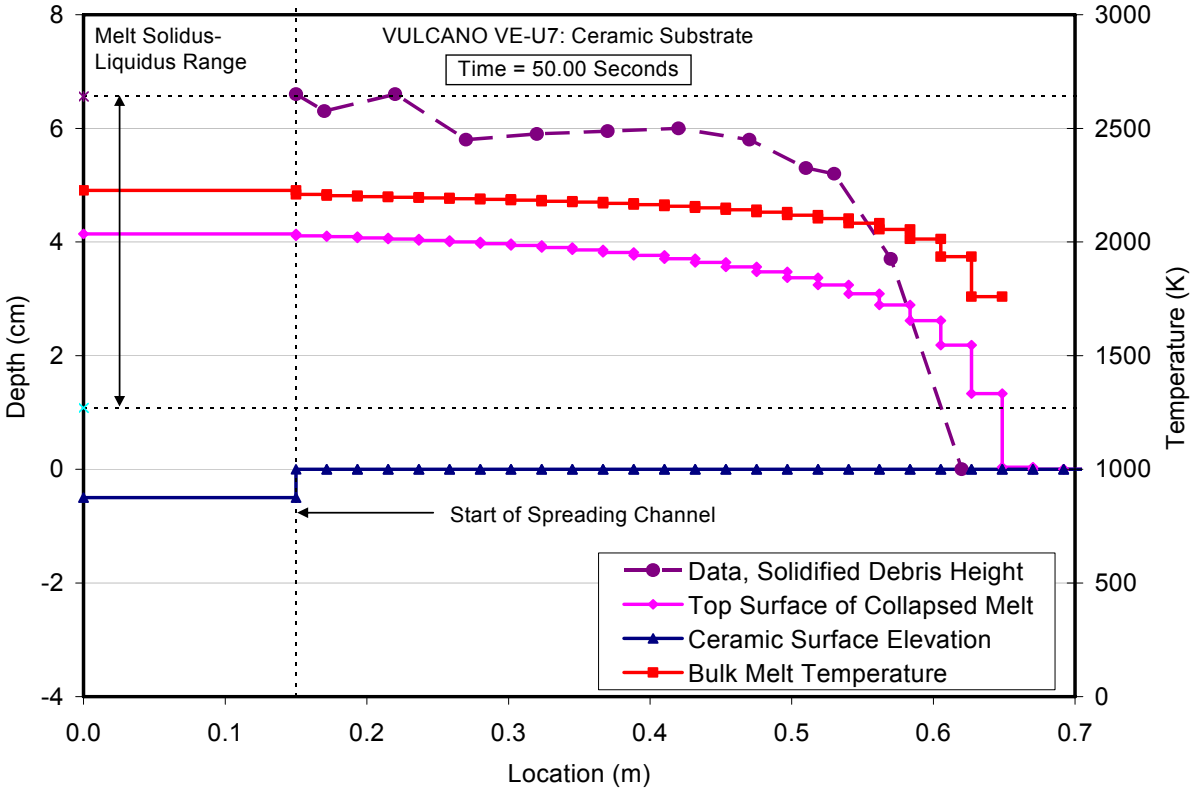

Figure A.75. Comparison of posttest debris profile prediction with VULCANO VE-U7 ceramic channel data.

A.4.2 Faro Spreading Tests

These tests[19] involved spreading of high temperature core oxide melts that were generated in a graphite resistance heating furnace. Once the melts had reached the desired initial condition, a plug was opened and the material was poured into a cylindrical accumulator that fed a spreading channel that was a 17º sector lined with steel. The accumulator included a 4 cm high weir that prevented splashing at pour inception. As shown in Table 2.1, two tests were conducted in this experiment series; the first with a dry surface (denoted L-26S), and the second with a thin (1 cm deep) water layer (denoted L-32S). For both tests, code subroutines were used to calculate the melt and substrate thermal-physical properties, and the 4 cm high weir was modeled as part of the nodalization scheme.

Test characteristics and the corresponding code input for L-26S are summarized in Table A.28, while the leading edge penetration and post-spreading material profile predictions are shown in Figures A.76 and A.77 respectively. For this test, the initial rate of spreading observed in the test was somewhat over-predicted by the model. The code predicts a thick accumulation of melt following spreading, which qualitatively agrees with the experiment results, but sufficient information was not provided in Reference 19 for a direct comparison here.

Experimental details and modeling input for L-32S are summarized in Table A.29, while the leading edge penetration and post-spreading material profile predictions are shown in Figures A.78 and A.79, respectively. The code also over-predicts the initial rate of spreading for this test,

Table A.28. Input File Data Sheet for the Faro L-26S Test with Dry Steel Channel.

Test parameter	Value
Test name	Faro L-26S, dry steel channel
Melt composition (wt %)	80 UO_2, 20 ZrO_2
Melt delivery technique	Melt poured into a circular accumulator with an ID of 10 cm and an elevation flush with the spreading surface. The accumulator was separated from the channel by a 3.2 cm thick, 4.0 cm high weir with a width of 15 cm leading to the channel. The total 160.4 kg melt mass was poured at an average rate of 16.54 kg/sec from a furnace into the accumulator.
Melt temperature	2950 K
Total pour mass	160.4 kg
Substrate material	steel
Spreading geometry	17º sector with an opening width of 15 cm from the accumulator; overall channel length was 2.0 m.
Code input parameter(s)	**Value(s)**
Melt composition (wt %)	80 UO_2, 20 ZrO_2
Melt pour temperature	2950 K
Melt oxide phase solidus – liquidus	2860 – 2910 K
Melt metal phase solidus – liquidus	1810 – 1820 K
Melt pour rate and duration	Steady pour of 160.4 kg melt mass into the accumulator over a 9.7 second interval; average pour rate of 16.54 kg/sec.
Melt material property evaluation	Code subroutines
Substrate composition	steel
Substrate initial temperature	296 K
Substrate material properties evaluation	Code subroutines
Substrate solidus - liquidus temperatures	1810 K – 1811 K (code default values)
Substrate nodalization	At each substrate nodal location, six 5.0 mm cells, followed by six 10 mm cells. All nodes cell-centered.
Spreading cavity nodalization	Accumulator: modeled as a single, cylindrical, 10 cm ID cell with an elevation flush with the spreading surface. Weir: modeled as a single 4 cm high, 15 cm wide 3.2 cm long cell Spreading surface: modeled as a 17º sector with 80 cells with a radial length of 2.5 cm. All nodes cell-centered.
Cavity condition	Dry
Upper atmosphere temperature	300 K
Upper atmosphere emissivity	1.0
Ambient pressure	0.1 MPa
Melt/substrate heat transfer coefficient model	Dittus - Boelter
Melt/substrate interfacial heat transfer resistance	0
Best-fit constant in Ramacciotti correlation	5.77
Solid-fraction variation between liquidus/solidus	See Figure 2.3
Timestep	0.01 seconds

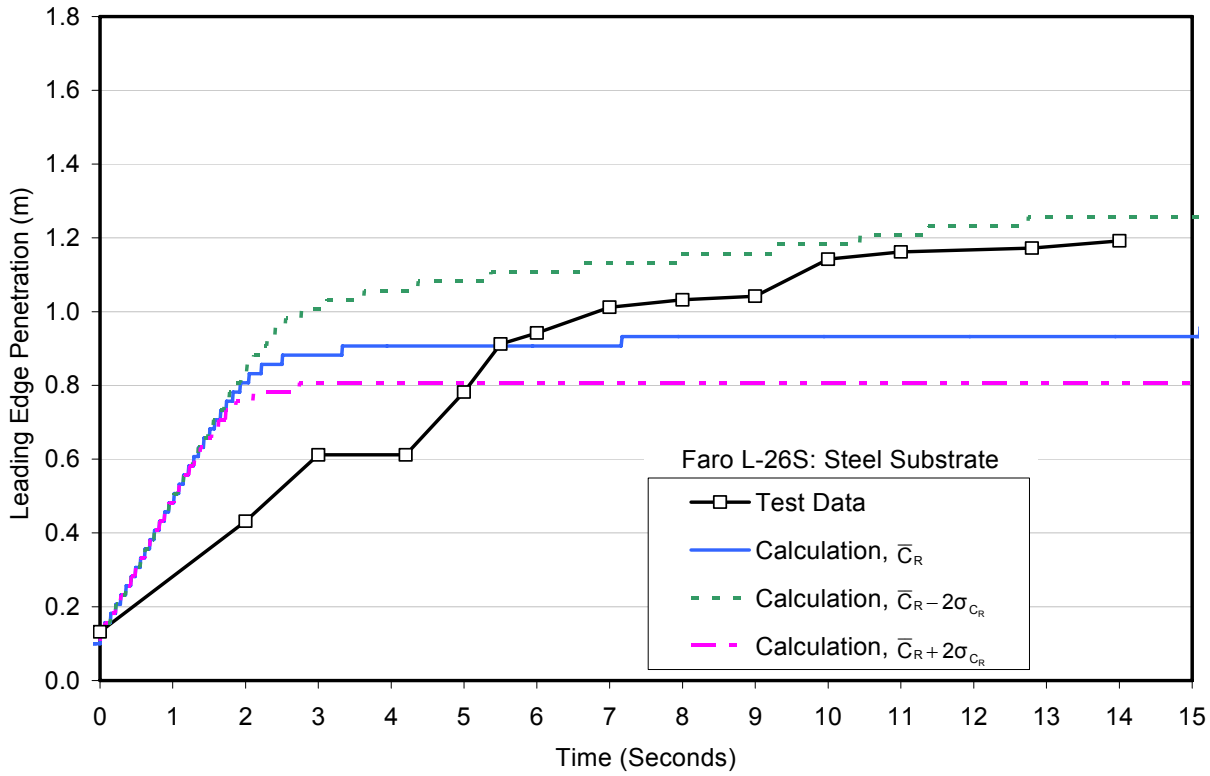

Figure A.76. Leading edge penetration comparison for FARO L-26S core oxide spreading test.

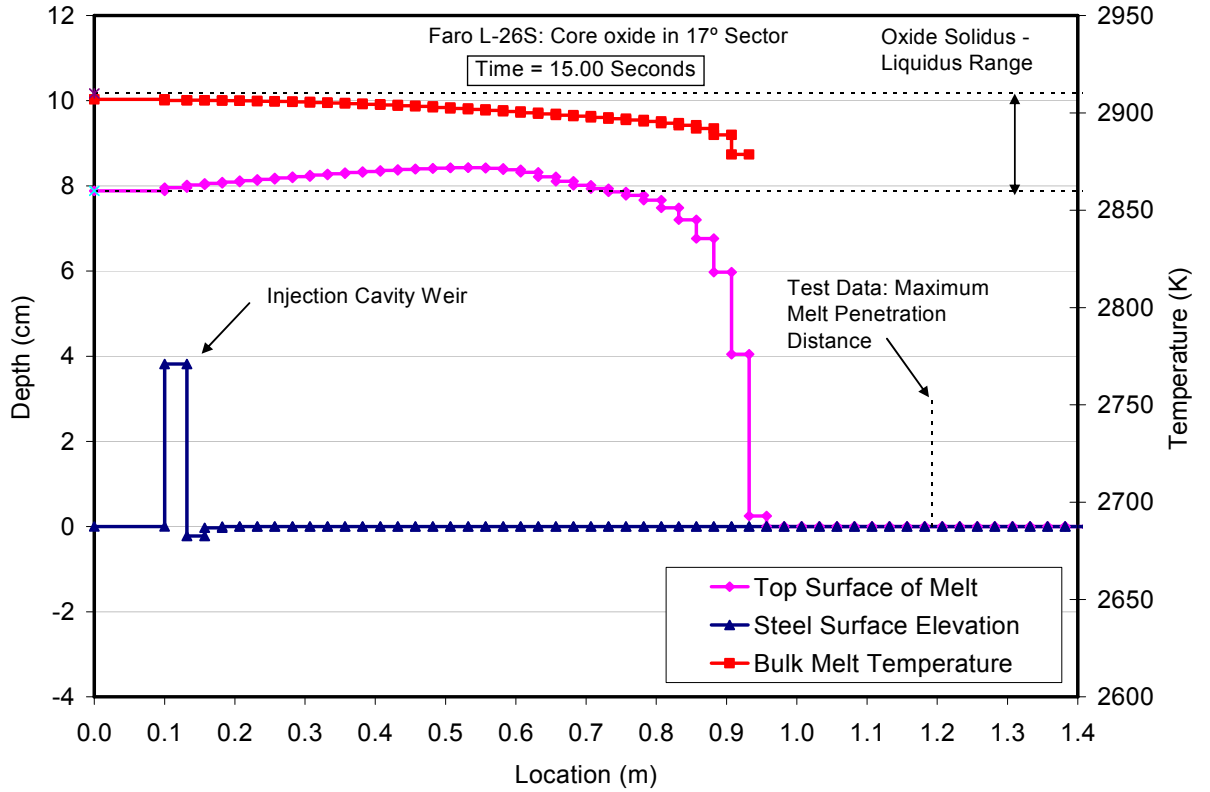

Figure A.77. Posttest debris profile prediction for the FARO L-26S core oxide spreading test.

Table A.29. Input File Data Sheet for the Faro L-32S Test with Wet Steel Channel.

Test parameter	Value
Test name	Faro L-32S, wet steel channel
Melt composition (wt %)	80 UO_2, 20 ZrO_2
Melt delivery technique	Melt poured into a circular accumulator with an ID of 10 cm and an elevation flush with the spreading surface. The accumulator was separated from the channel by a 3.2 cm thick, 4.0 cm high weir with a width of 15 cm leading to the channel. The total 128 kg melt mass was poured at an average rate of 18.55 kg/sec from a furnace into the accumulator.
Melt temperature	3000 K
Total pour mass	128 kg
Substrate material	steel
Spreading geometry	17º sector with an opening width of 15 cm from the accumulator; overall channel length was 2.0 m.
Code input parameter(s)	**Value(s)**
Melt composition (wt %)	80 UO_2, 20 ZrO_2
Melt pour temperature	3000 K
Melt oxide phase solidus – liquidus	2860 – 2910 K
Melt metal phase solidus – liquidus	1810 – 1820 K
Melt pour rate and duration	Steady pour of 128 kg melt mass into the accumulator over a 6.9 second interval; average pour rate of 18.55 kg/sec.
Melt material property evaluation	Code subroutines
Substrate composition	steel
Substrate initial temperature	300 K
Substrate material properties evaluation	Code subroutines
Substrate solidus - liquidus temperatures	1810 K – 1811 K (code default values)
Substrate nodalization	At each substrate nodal location, six 5.0 mm cells, followed by six 10 mm cells. All nodes cell-centered.
Spreading cavity nodalization	Accumulator: modeled as a single, cylindrical, 10 cm ID cell with an elevation flush with the spreading surface. Weir: modeled as a single 4 cm high, 15 cm wide 3.2 cm long cell Spreading surface: modeled as a 17º sector with 80 cells with a radial length of 2.5 cm. All nodes cell-centered.
Cavity condition	Wet
Water temperature (subcooling)	293 (80) K
Ambient pressure	0.1 MPa
Water depth	1.0 m
Melt/substrate heat transfer coefficient model	Dittus - Boelter
Melt/substrate interfacial heat transfer resistance	0
Best-fit constant in Ramacciotti correlation	10.08
Solid-fraction variation between liquidus/solidus	See Figure 2.3
Timestep	0.01 seconds

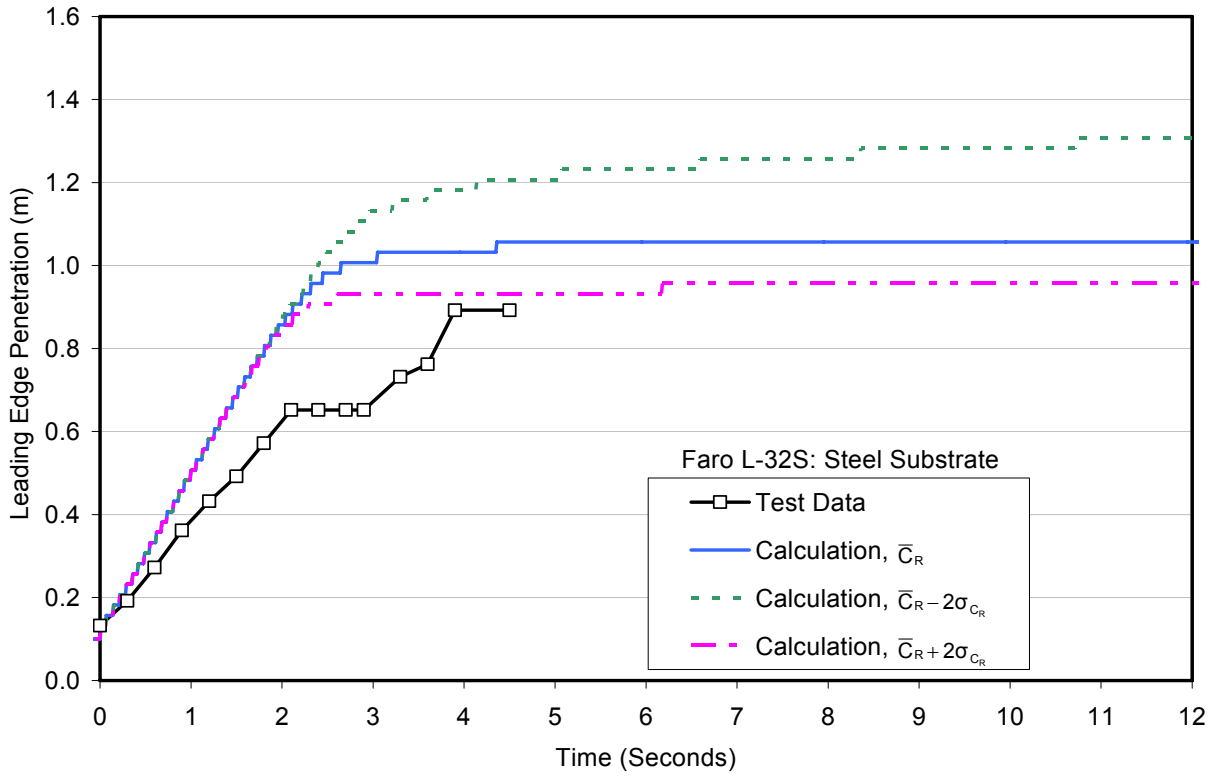

Figure A.78. Leading edge penetration comparison for FARO L-32S core oxide spreading test.

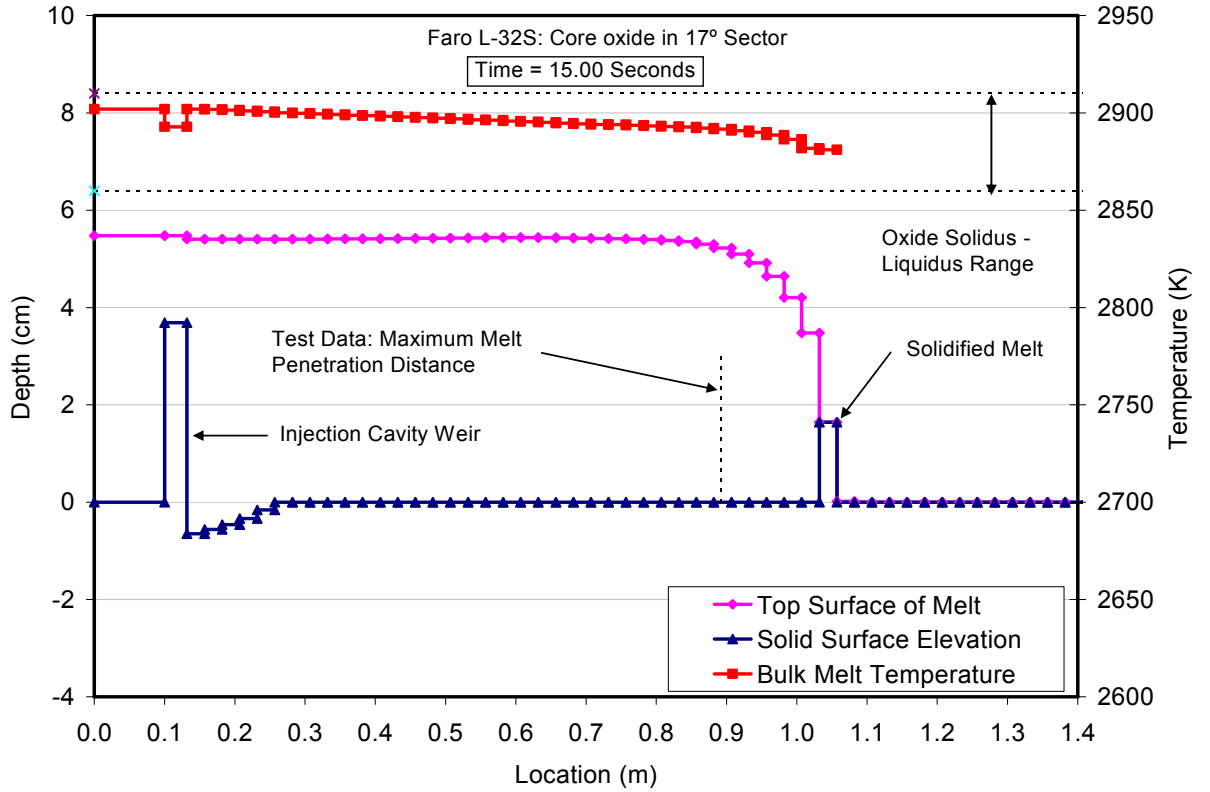

Figure A.79. Posttest debris profile prediction for the FARO L-32S core oxide spreading test.

but less so in comparison to L-26S. As for L-26S, a thick melt layer following spreading is predicted, which qualitatively agrees with the experiment results, but sufficient information was not provided for a direct comparison here.

A.4.3 COMAS Spreading Tests

These large scale tests[20-21] involved spreading of core melts that were produced by induction heating of the metallic (iron) component of a core oxide-metal mixture. Once the melt reached target temperature, the material was poured into an accumulator, and then a gate was opened to initiate the spreading transient. There were a variety of tests conducted as part of this program. Of this matrix, three specific tests have been selected for analysis (see Table 2.1):

1. Comas-5a, wherein a core oxide-metal mixture was poured into a common accumulator that fed three parallel channels with different substrates (i.e., ceramic, concrete, and steel),
2. Comas EU-2b, which was essentially the same as Comas-5a with the exception that the metal phase was separated from the oxide before the oxide phase was spread, and
3. Comas EU4, which was a large scale (2000 kg) demonstration test in which a metal-oxide mixture was spread on a steel surface in a geometry similar to the EPR core catcher.

This matrix embodies seven individual tests that cover spreading on ceramic, concrete, and steel surfaces with different melt compositions and flow geometries. Although the nature and extent of these tests was significant, it should be pointed out that the open literature publications did not provide a few key pieces of information that were required to construct detailed models, the most notable of which was the geometry of the accumulator and gate plug assembly. The models utilized here were developed from several different sources of information in an attempt to assemble as accurate a representation as possible.

The Comas-5a experiment was a combined metal-oxide spreading test, and no mention was made in the literature regarding a stratified melt injection configuration. Thus, the metal and oxide phases in the spread melt were assumed to be well-mixed. The code subroutines were used to calculate the melt properties for all tests. The ceramic substrate was assumed to be composed of Cordierite, and the same material properties used for the KATS tests[13] were used. The total pour mass of 1000 kg was assumed to be equally spread between the three channels. Computationally, the melt was dropped into the accumulator over a time interval of 0.1 seconds to rapidly accumulate the material and thereby simulate a dam break type spreading event, as intended with the gate plug design. Finally, the geometry of the accumulator for each ‘channel’ was assumed to be a 40 cm wide (same as channel width), 25 cm long rectilinear box with a surface elevation that was 5 cm below that of the channel.

Test characteristics and the corresponding code input for the COMAS 5a ceramic channel test are summarized in Table A.30, while the calculated leading edge penetration and ultimate melt penetration predictions are compared to the data in Figures A.80 and A.81. Table A.31 and Figures A.82-A.83 provide the same information for the concrete channel test. Finally, Table A.32 summarizes characteristics and input for the steel channel test, while Figures A.84-A.85 provide plots of leading edge penetration, substrate thermal response, and ultimate melt penetration distance, respectively.

Table A.30. Input File Data Sheet for the Comas 5a Test with Ceramic Channel.

Test parameter	Value
Test name	Comas 5a, ceramic channel
Melt composition (wt %)	29 UO_2, 12 ZrO_2 18 FeO, 2 Cr_2O_3, 39 Fe
Melt delivery technique	Melt poured into an accumulator box that was 40 cm wide (per channel), 25 cm long, and 5 cm deep relative to spreading surface. Pour initiated by opening a plug device at the bottom of the accumulator.
Melt temperature	2173 K
Total pour mass	333.3 kg (assumes 1000 kg pour uniformly distributed between the 3 channels)
Substrate material	Unspecified ceramic; assumed to be Cordierite
Spreading geometry	1-D channel, 6.4 m long by 40 cm wide
Code input parameter(s)	**Value(s)**
Melt composition (wt %)	29 UO_2, 12 ZrO_2 18 FeO, 2 Cr_2O_3, 39 Fe
Melt pour temperature	2173 K
Melt oxide phase solidus – liquidus	1598 K – 2223 K
Melt metal phase solidus – liquidus	1810 K – 1820 K
Melt pour rate and duration	3333.3 kg/sec over a 0.1 sec (simulating instantaneous deposition in the accumulator, followed by initiation of spreading)
Melt material property evaluation	Code subroutines
Substrate composition	Corderite (modeled using user-specified material input properties)
Substrate initial temperature	300 K
Substrate material properties evaluation[a]	$c_s = c_l = 840$ J/kg-K, $\Delta h_f = 1.0$ MJ/kg, $\rho_s = \rho_l = 2200$ kg/m^3, $k_s = k_l = 3.8$ W/m-K, and $\varepsilon = 0.3$
Substrate solidus - liquidus temperatures	1893 K – 1923 K
Substrate nodalization	At each substrate nodal location, six 5.0 mm cells, followed by six 10 mm cells. All nodes cell-centered.
Spreading cavity nodalization	Accumulator: modeled as a single cell that is 40 cm wide, 25 cm long, and 5 cm deep. Channel: modeled using 120 cells; each is 40 cm wide and 5.33 cm long. All nodes cell-centered.
Cavity condition	Dry
Upper atmosphere temperature	300 K
Upper atmosphere emissivity	1.0
Ambient pressure	0.1 MPa
Melt/substrate heat transfer coefficient model	Dittus - Boelter
Melt/substrate interfacial heat transfer resistance	0
Best-fit constant in Ramacciotti correlation	7.23
Solid-fraction variation between liquidus/solidus	See Figure 2.3
Timestep	0.025 seconds

[a]Here, c denotes specific heat, Δh_f is latent heat of fusion, ρ is density, k is thermal conductivity, ε is emissivity, and subscripts s and l denote solid and liquid phases, respectively.

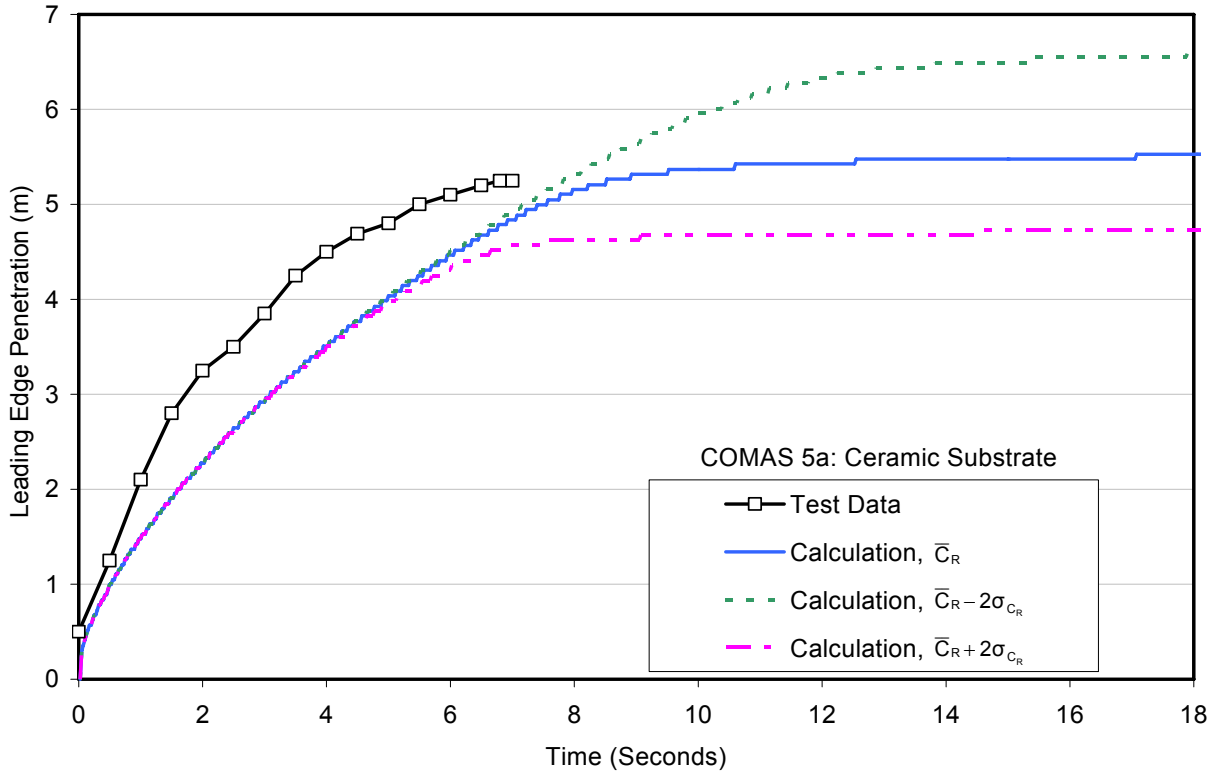

Figure A.80 Leading edge penetration comparison for COMAS-5a core oxide spreading test with ceramic channel.

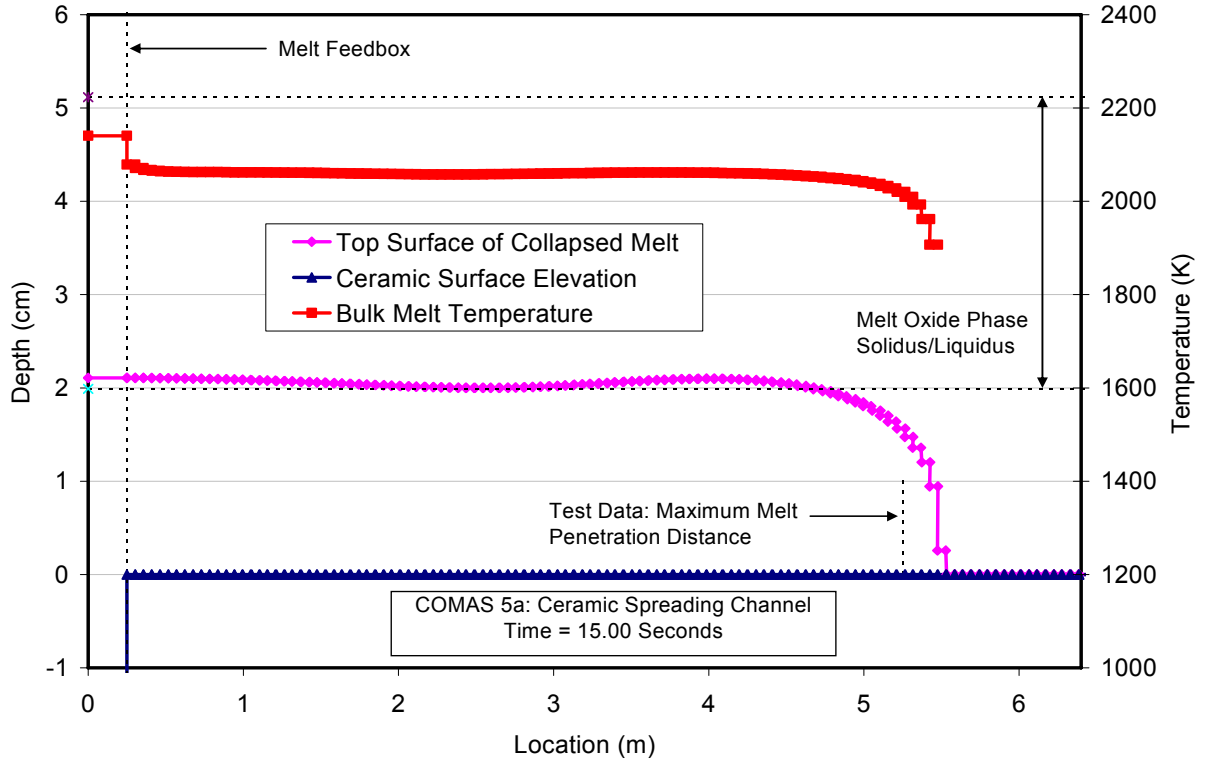

Figure A.81. Posttest debris profile prediction for the COMAS 5a core oxide spreading test with ceramic channel.

Table A.31. Input File Data Sheet for the Comas 5a Test with Concrete Channel.

Test parameter	Value
Test name	Comas 5a, concrete channel
Melt composition (wt %)	29 UO_2, 12 ZrO_2 18 FeO, 2 Cr_2O_3, 39 Fe
Melt delivery technique	Melt poured into an accumulator box that was 40 cm wide (per channel), 25 cm long, and 5 cm deep relative to spreading surface. Pour initiated by opening a plug device at the bottom of the accumulator.
Melt temperature	2173 K
Total pour mass	333.3 kg (assumes 1000 kg pour uniformly distributed between the 3 channels)
Substrate material	Siliceous concrete
Spreading geometry	1-D channel, 6.4 m long by 40 cm wide
Code input parameter(s)	**Value(s)**
Melt composition (wt %)	29 UO_2, 12 ZrO_2 18 FeO, 2 Cr_2O_3, 39 Fe
Melt pour temperature	2173 K
Melt oxide phase solidus – liquidus	1598 K – 2223 K
Melt metal phase solidus – liquidus	1810 K – 1820 K
Melt pour rate and duration	3333.3 kg/sec over a 0.1 sec (simulating instantaneous deposition in the accumulator, followed by initiation of spreading)
Melt material property evaluation	Code subroutines
Substrate composition (wt %)	4.2 CO_2, 3.7 H_2O, 1.4 K_2O, 0.7 Na_2O, 0.8 TiO_2, 69.8 SiO_2, 13.7 CaO, 0.7 MgO, 4.0 Al_2O_3, 1.0 Fe_2O_3
Substrate initial temperature	300 K
Substrate material properties evaluation	Code subroutines
Substrate solidus - liquidus temperatures	1390 K – 1960 K
Substrate nodalization	At each substrate nodal location, six 5.0 mm cells, followed by six 10 mm cells. All nodes cell-centered.
Spreading cavity nodalization	Accumulator: modeled as a single cell that is 40 cm wide, 25 cm long, and 5 cm deep. Channel: modeled using 120 cells; each is 40 cm wide and 5.33 cm long. All nodes cell-centered.
Cavity condition	Dry
Upper atmosphere temperature	300 K
Upper atmosphere emissivity	1.0
Ambient pressure	0.1 MPa
Melt/substrate heat transfer coefficient model	Locally, largest of Dittus – Boelter and Bradley slag film heat transfer coefficients
Melt/substrate interfacial heat transfer resistance	0
Best-fit constant in Ramacciotti correlation	7.23
Solid-fraction variation between liquidus/solidus	See Figure 2.3
Timestep	0.025 seconds

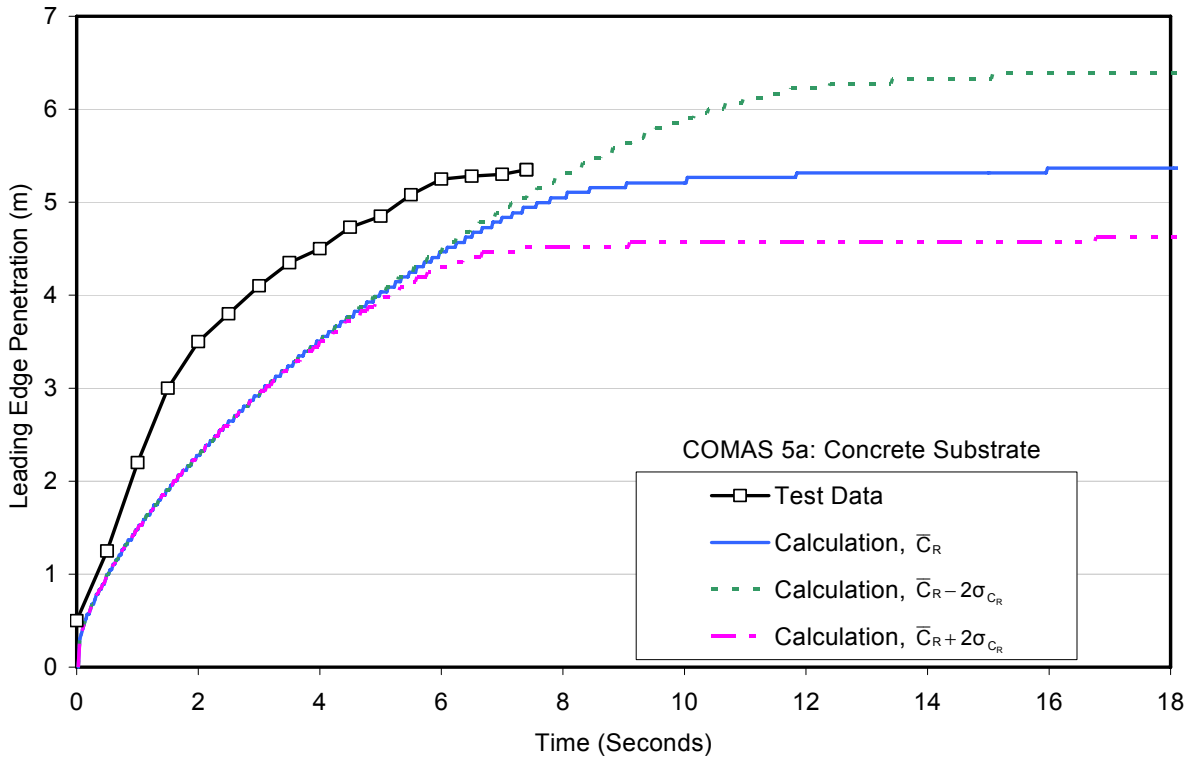

Figure A.82. Leading edge penetration comparison for COMAS-5a core oxide spreading test with concrete channel.

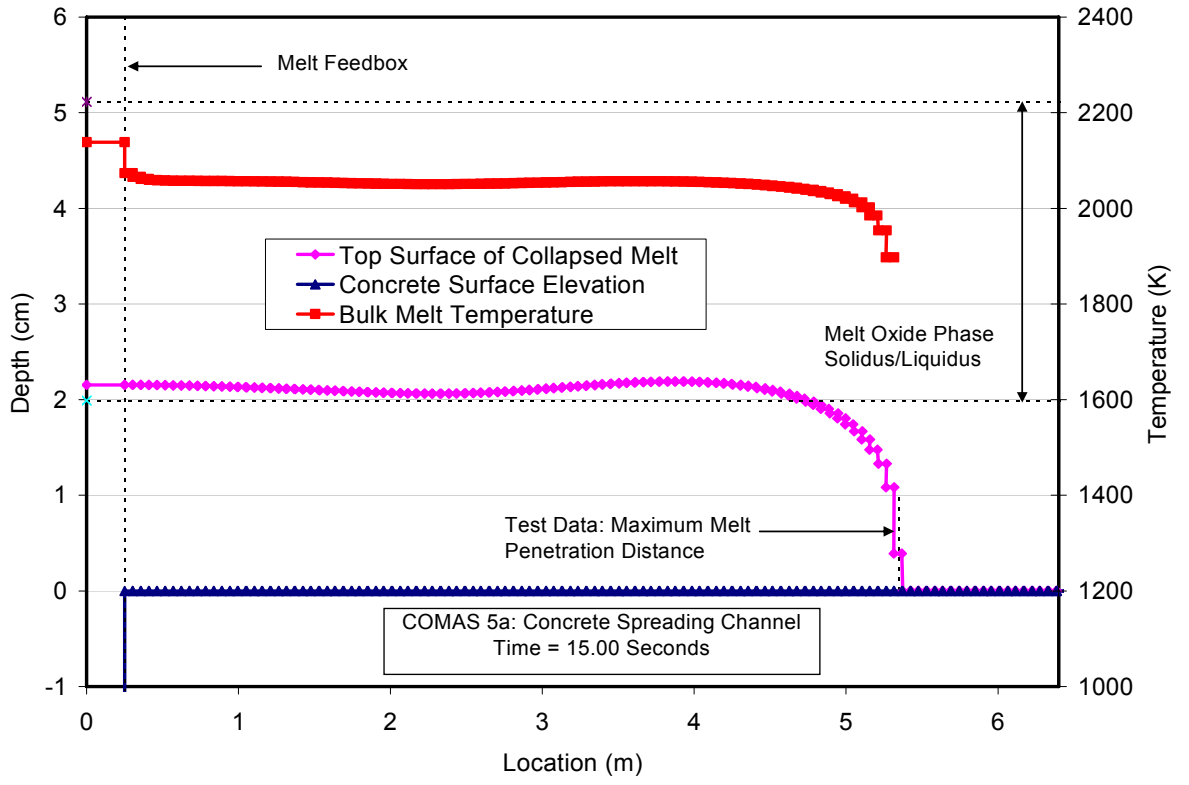

Figure A.83. Posttest debris profile prediction for the COMAS 5a core oxide spreading test with concrete channel.

Table A.32. Input File Data Sheet for the Comas 5a Test with Steel Channel.

Test parameter	Value
Test name	Comas 5a, steel channel
Melt composition (wt %)	29 UO_2, 12 ZrO_2 18 FeO, 2 Cr_2O_3, 39 Fe
Melt delivery technique	Melt poured into an accumulator box that was 40 cm wide (per channel), 25 cm long, and 5 cm deep relative to spreading surface. Pour initiated by opening a plug device at the bottom of the accumulator.
Melt temperature	2173 K
Total pour mass	333.3 kg (assumes 1000 kg pour uniformly distributed between the 3 channels)
Substrate material	Steel
Spreading geometry	1-D channel, 6.4 m long by 40 cm wide
Code input parameter(s)	**Value(s)**
Melt composition (wt %)	29 UO_2, 12 ZrO_2 18 FeO, 2 Cr_2O_3, 39 Fe
Melt pour temperature	2173 K
Melt oxide phase solidus – liquidus	1598 K – 2223 K
Melt metal phase solidus – liquidus	1810 K – 1820 K
Melt pour rate and duration	3333.3 kg/sec over a 0.1 sec (simulating instantaneous deposition in the accumulator, followed by initiation of spreading)
Melt material property evaluation	Code subroutines
Substrate composition	Steel (code default composition)
Substrate initial temperature	300 K
Substrate material properties evaluation	Code subroutines
Substrate solidus - liquidus temperatures	1810 K – 1811 K (code default values)
Substrate nodalization	At each substrate nodal location, six 5.0 mm cells, followed by six 10 mm cells. All nodes cell-centered.
Spreading cavity nodalization	Accumulator: modeled as a single cell that is 40 cm wide, 25 cm long, and 5 cm deep. Channel: modeled using 120 cells; each is 40 cm wide and 5.33 cm long. All nodes cell-centered.
Cavity condition	Dry
Upper atmosphere temperature	300 K
Upper atmosphere emissivity	1.0
Ambient pressure	0.1 MPa
Melt/substrate heat transfer coefficient model	Dittus – Boelter
Melt/substrate interfacial heat transfer resistance	0
Best-fit constant in Ramacciotti correlation	7.93
Solid-fraction variation between liquidus/solidus	See Figure 2.3
Timestep	0.025 seconds

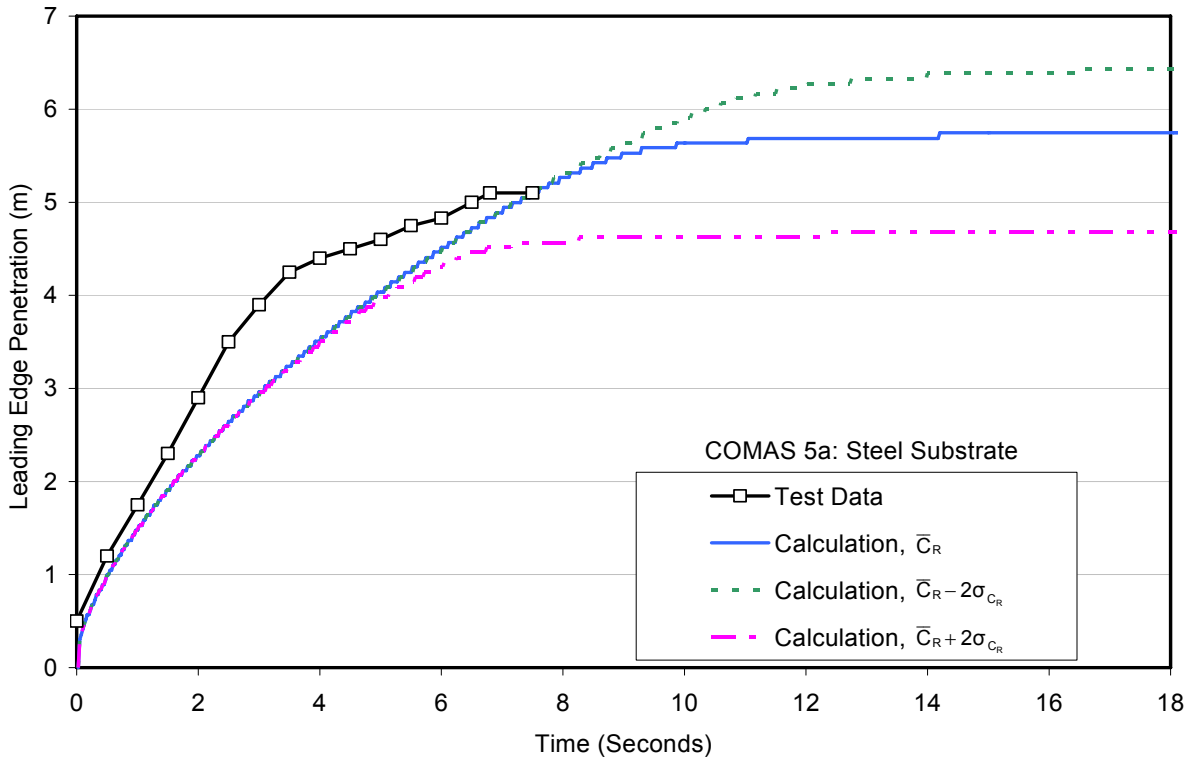

Figure A.84. Leading edge penetration comparison for COMAS-5a core oxide spreading test with steel channel.

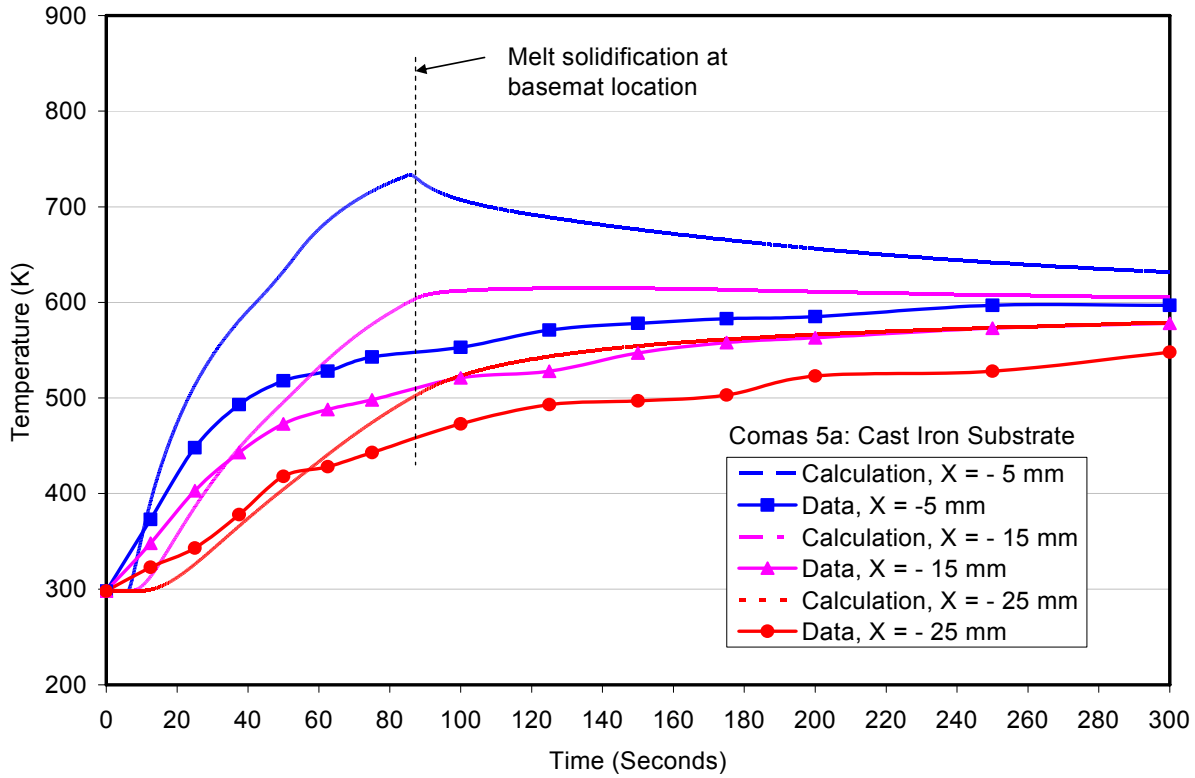

Figure A.85. Comparison of substrate thermal response predictions with COMAS 5a steel channel data 4 m from channel inlet.

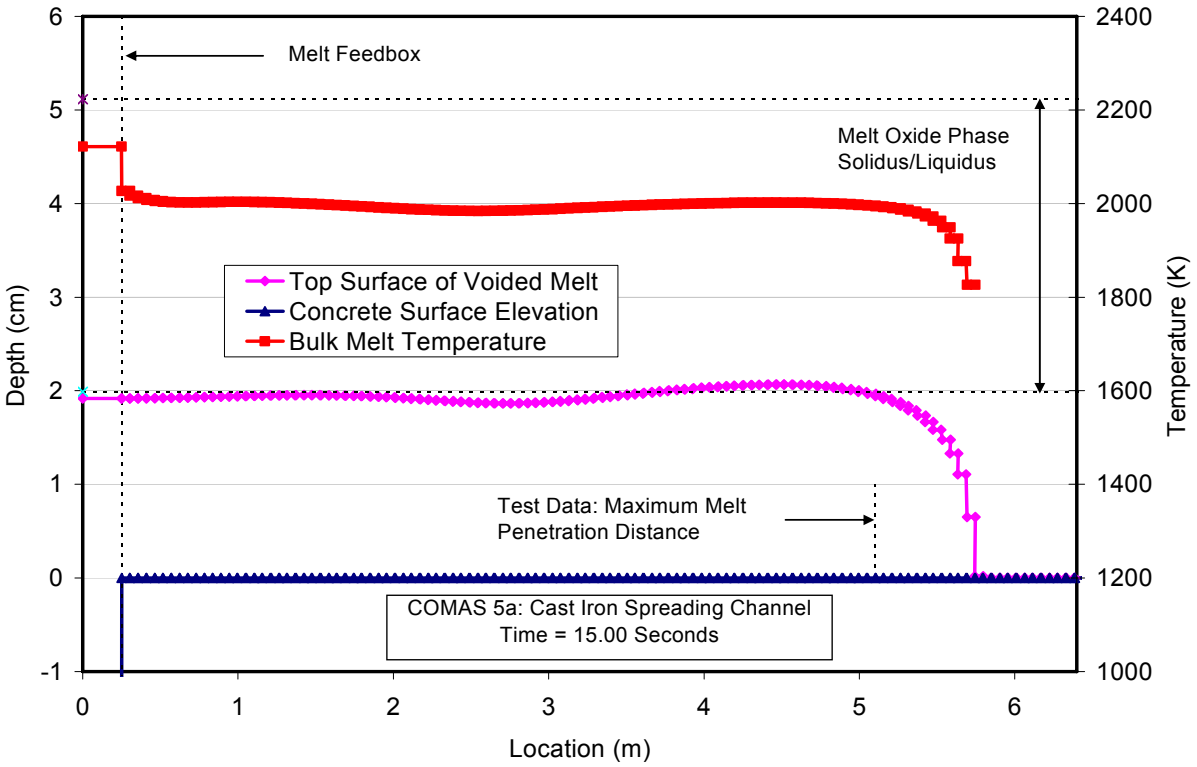

Figure A.86. Posttest debris profile prediction for the COMAS 5a core oxide spreading test with steel channel.

In general, the code somewhat under-predicts spreading velocity early in the transient for all three tests, but the overall agreement is favorable. As shown in Figure A.85, the heatup in the steel substrate is overpredicted by ~ 150 K during the first 85 seconds of the transient. Afterwards, melt solidification occurs at the measurement location, and the temperature predictions approach the measurements.

The Comas EU2b test was very similar to Comas 5a, with the exception that the oxide phase was slightly modified by the addition of SiO_2, and the metal phase was decanted so that only the oxide phase was spread. Test characteristics and the corresponding code input for the ceramic channel test are summarized in Table A.33, while the calculated leading edge penetration and ultimate melt penetration predictions are compared to the test data in Figures A.87 and A.88. Table A.34 and Figures A.89-A.90 provide the analogous comparisons for the concrete channel test, while Table A.35 and Figures A.91-A.92 provide the comparisons for the steel channel test. As for Comas 5a, the initial spreading velocity is under-predicted for all three cases, but the overall agreement is reasonable.

Finally, Table A.36 summarizes characteristics and model input for the COMAS EU4 2-D steel channel test, while Figures A.93-A.94 provide comparisons of the leading edge penetration and ultimate melt penetration distance, respectively. This was a combined metal-oxide spreading test, and no mention of a stratified pour condition was made.[20-21] Thus, the metal and oxide were assumed to spread in a well-mixed configuration. Examination of Figure A.93 indicates that the code does an excellent job in predicting spreading velocity for this experiment.

Table A.33. Input File Data Sheet for the Comas EU2b Test with Ceramic Channel.

Test parameter	Value
Test name	Comas EU2b, ceramic channel
Melt composition (wt %)	42.8 UO_2, 17.7 ZrO_2, 26.5 FeO, 3.0 Cr_2O_3, 10.0 SiO_2
Melt delivery technique	Melt poured into an accumulator box that was 40 cm wide (per channel), 25 cm long, and 5 cm deep relative to spreading surface. Pour initiated by opening a plug device at the bottom of the accumulator.
Melt temperature	2343 K
Total pour mass	210 kg (assumes 630 kg pour uniformly distributed between the 3 channels)
Substrate material	Unspecified ceramic; assumed to be Cordierite
Spreading geometry	1-D channel, 6.4 m long by 40 cm wide
Code input parameter(s)	**Value(s)**
Melt composition (wt %)	42.8 UO_2, 17.7 ZrO_2, 26.5 FeO, 3.0 Cr_2O_3, 10.0 SiO_2
Melt pour temperature	2343 K
Melt oxide phase solidus – liquidus	1443 K – 2173 K
Melt metal phase solidus – liquidus	1810 K – 1820 K
Melt pour rate and duration	2100 kg/sec over a 0.1 sec (simulating instantaneous deposition in the accumulator, followed by initiation of spreading)
Melt material property evaluation	Code subroutines
Substrate composition	Corderite (modeled using user-specified material input properties)
Substrate initial temperature	300 K
Substrate material properties evaluation[a]	$c_s = c_l = 840$ J/kg-K, $\Delta h_f = 1.0$ MJ/kg, $\rho_s = \rho_l = 2200$ kg/m^3, $k_s = k_l = 3.8$ W/m-K, and $\varepsilon = 0.3$
Substrate solidus - liquidus temperatures	1893 K – 1923 K
Substrate nodalization	At each substrate nodal location, six 5.0 mm cells, followed by six 10 mm cells. All nodes cell-centered.
Spreading cavity nodalization	Accumulator: modeled as a single cell that is 40 cm wide, 25 cm long, and 5 cm deep. Channel: modeled using 120 cells; each is 40 cm wide and 5.33 cm long. All nodes cell-centered.
Cavity condition	Dry
Upper atmosphere temperature	300 K
Upper atmosphere emissivity	1.0
Ambient pressure	0.1 MPa
Melt/substrate heat transfer coefficient model	Dittus - Boelter
Melt/substrate interfacial heat transfer resistance	0
Best-fit constant in Ramacciotti correlation	8.40
Solid-fraction variation between liquidus/solidus	See Figure 2.3
Timestep	0.025 seconds

[a]Here, c denotes specific heat, Δh_f is latent heat of fusion, ρ is density, k is thermal conductivity, ε is emissivity, and subscripts s and l denote solid and liquid phases, respectively.

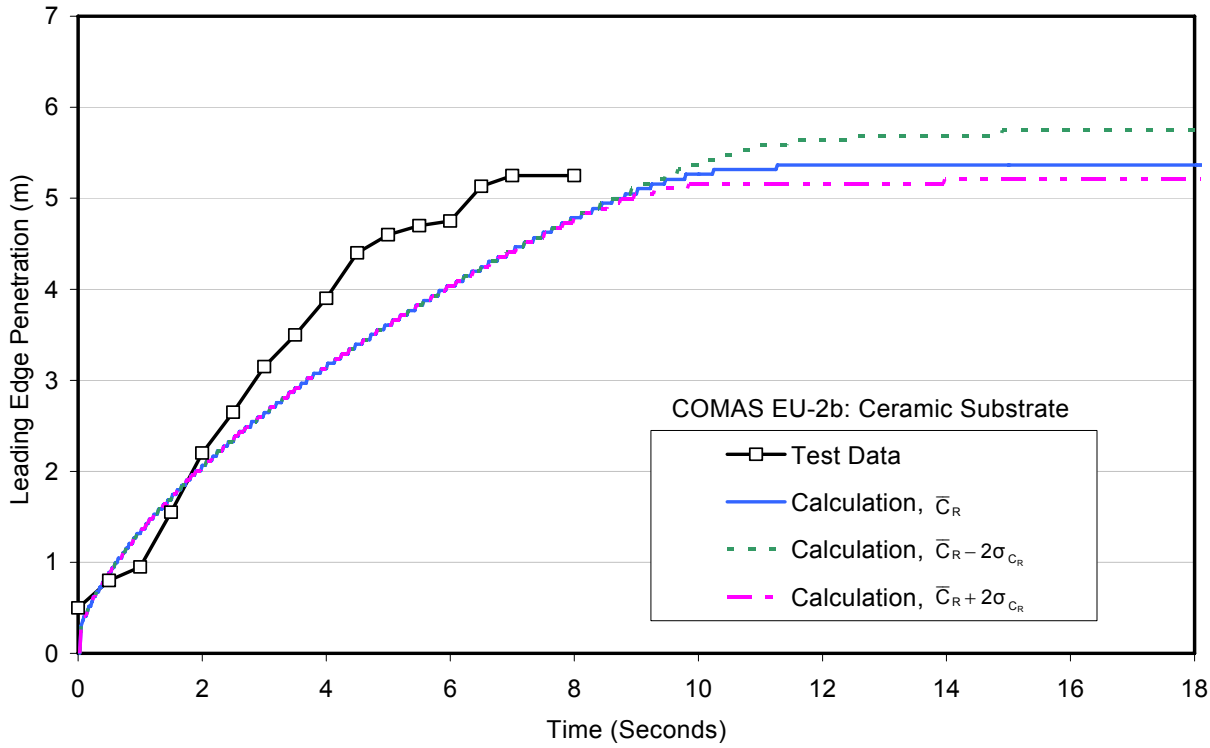

Figure A.87. Leading edge penetration comparison for COMAS-EU2b core oxide spreading test with ceramic channel.

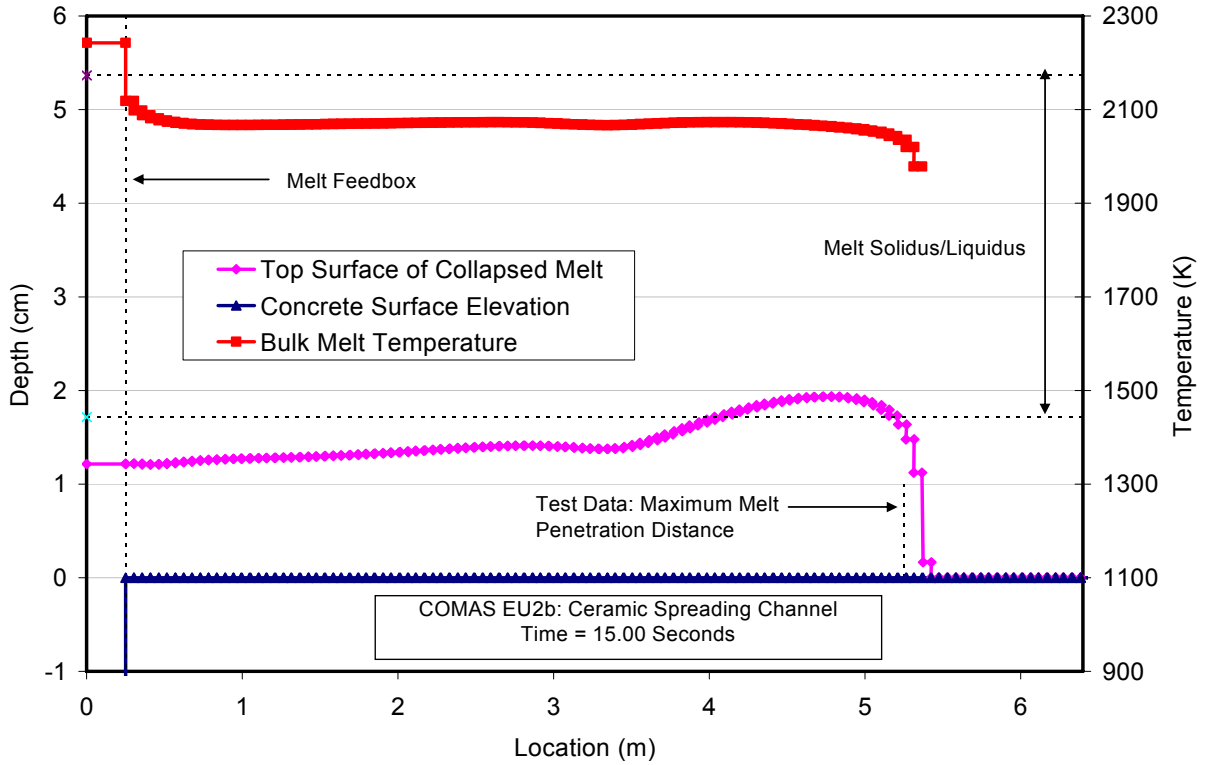

Figure A.88. Posttest debris profile prediction for the COMAS EU2b core oxide spreading test with ceramic channel.

Table A.34. Input File Data Sheet for the Comas EU2b Test with Concrete Channel.

Test parameter	Value
Test name	Comas EU2b, concrete channel
Melt composition (wt %)	42.8 UO_2, 17.7 ZrO_2, 26.5 FeO, 3.0 Cr_2O_3, 10.0 SiO_2
Melt delivery technique	Melt poured into an accumulator box that was 40 cm wide (per channel), 25 cm long, and 5 cm deep relative to spreading surface. Pour initiated by opening a plug device at the bottom of the accumulator.
Melt temperature	2343 K
Total pour mass	210 kg (assumes 630 kg pour uniformly distributed between the 3 channels)
Substrate material	Siliceous concrete
Spreading geometry	1-D channel, 6.4 m long by 40 cm wide
Code input parameter(s)	**Value(s)**
Melt composition (wt %)	42.8 UO_2, 17.7 ZrO_2, 26.5 FeO, 3.0 Cr_2O_3, 10.0 SiO_2
Melt pour temperature	2343 K
Melt oxide phase solidus – liquidus	1443 K – 2173 K
Melt metal phase solidus – liquidus	1810 K – 1820 K
Melt pour rate and duration	2100 kg/sec over a 0.1 sec (simulating instantaneous deposition in the accumulator, followed by initiation of spreading)
Melt material property evaluation	Code subroutines
Substrate composition	4.2 CO_2, 3.7 H_2O, 1.4 K_2O, 0.7 Na_2O, 0.8 TiO_2, 69.8 SiO_2, 13.7 CaO, 0.7 MgO, 4.0 Al_2O_3, 1.0 Fe_2O_3
Substrate initial temperature	300 K
Substrate material properties evaluation	Code subroutines
Substrate solidus - liquidus temperatures	1390 K – 1960 K
Substrate nodalization	At each substrate nodal location, six 5.0 mm cells, followed by six 10 mm cells. All nodes cell-centered.
Spreading cavity nodalization	Accumulator: modeled as a single cell that is 40 cm wide, 25 cm long, and 5 cm deep. Channel: modeled using 120 cells; each is 40 cm wide and 5.33 cm long. All nodes cell-centered.
Cavity condition	Dry
Upper atmosphere temperature	300 K
Upper atmosphere emissivity	1.0
Ambient pressure	0.1 MPa
Melt/substrate heat transfer coefficient model	Locally, larger of the Dittus – Boelter and Bradley slag film heat transfer coefficient models
Melt/substrate interfacial heat transfer resistance	0
Best-fit constant in Ramacciotti correlation	5.33
Solid-fraction variation between liquidus/solidus	See Figure 2.3
Timestep	0.025 seconds

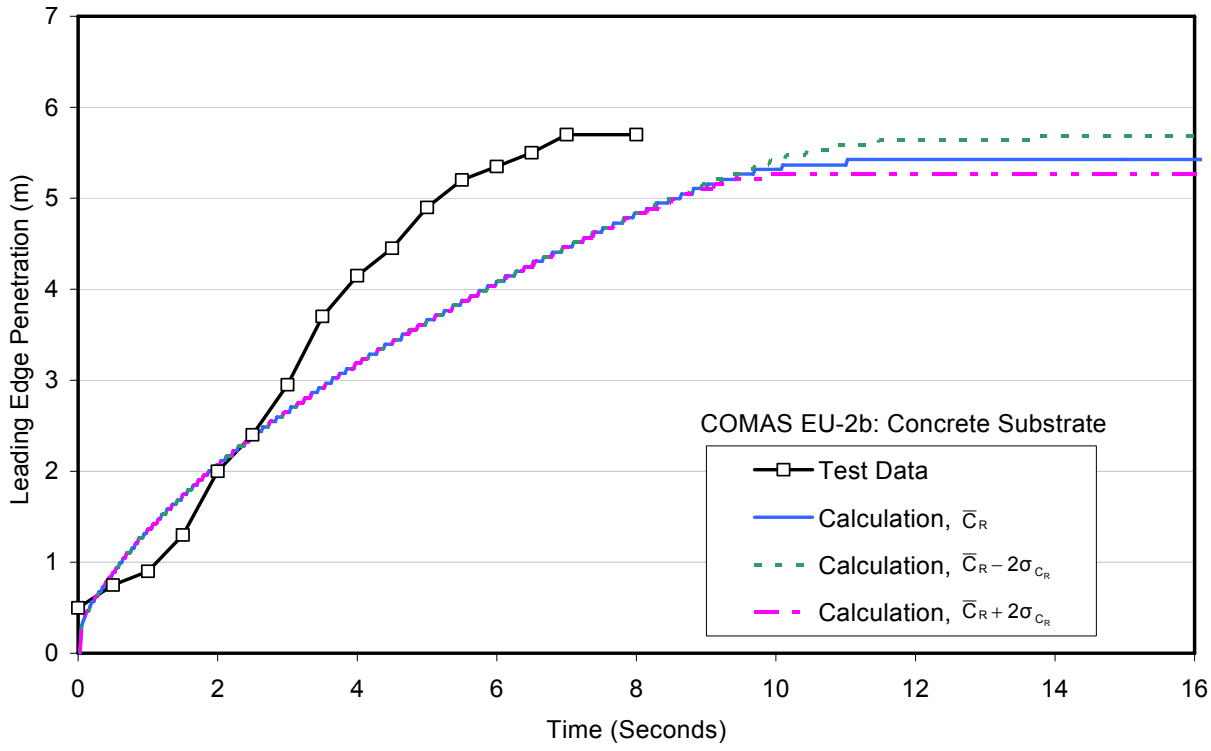

Figure A.89. Leading edge penetration comparison for COMAS-EU2b core oxide spreading test with concrete channel.

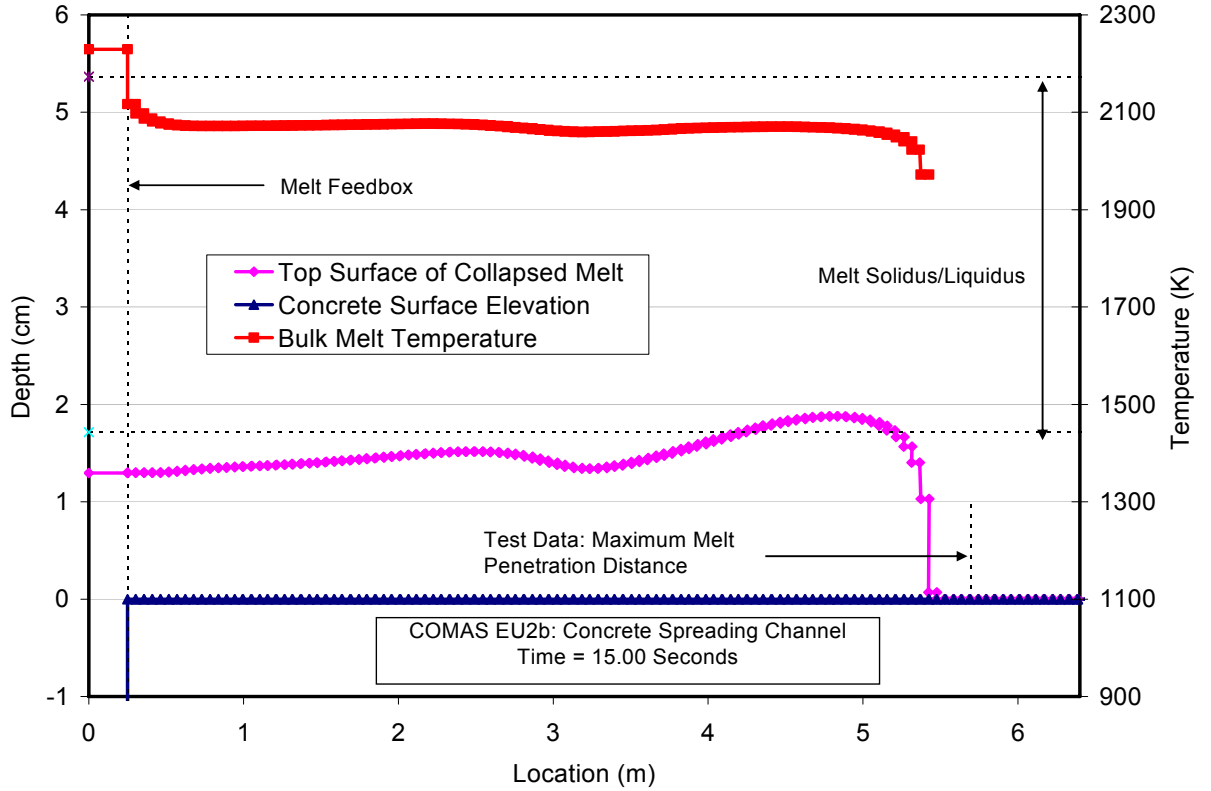

Figure A.90. Posttest debris profile prediction for the COMAS EU2b core oxide spreading test with concrete channel.

Table A.35. Input File Data Sheet for the Comas EU2b Test with Steel Channel.

Test parameter	Value
Test name	Comas EU2b, steel channel
Melt composition (wt %)	42.8 UO_2, 17.7 ZrO_2, 26.5 FeO, 3.0 Cr_2O_3, 10.0 SiO_2
Melt delivery technique	Melt poured into an accumulator box that was 40 cm wide (per channel), 25 cm long, and 5 cm deep relative to spreading surface. Pour initiated by opening a plug device at the bottom of the accumulator.
Melt temperature	2343 K
Total pour mass	210 kg (assumes 630 kg pour uniformly distributed between the 3 channels)
Substrate material	Steel
Spreading geometry	1-D channel, 6.4 m long by 40 cm wide
Code input parameter(s)	**Value(s)**
Melt composition (wt %)	42.8 UO_2, 17.7 ZrO_2, 26.5 FeO, 3.0 Cr_2O_3, 10.0 SiO_2
Melt pour temperature	2343 K
Melt oxide phase solidus – liquidus	1443 K – 2173 K
Melt metal phase solidus – liquidus	1810 K – 1820 K
Melt pour rate and duration	2100 kg/sec over a 0.1 sec (simulating instantaneous deposition in the accumulator, followed by initiation of spreading)
Melt material property evaluation	Code subroutines
Substrate composition	Steel (code default composition)
Substrate initial temperature	300 K
Substrate material properties evaluation	Code subroutines
Substrate solidus - liquidus temperatures	1810 K – 1811 K (code default values)
Substrate nodalization	At each substrate nodal location, six 5.0 mm cells, followed by six 10 mm cells. All nodes cell-centered.
Spreading cavity nodalization	Accumulator: modeled as a single cell that is 40 cm wide, 25 cm long, and 5 cm deep. Channel: modeled using 120 cells; each is 40 cm wide and 5.33 cm long. All nodes cell-centered.
Cavity condition	Dry
Upper atmosphere temperature	300 K
Upper atmosphere emissivity	1.0
Ambient pressure	0.1 MPa
Melt/substrate heat transfer coefficient model	Dittus – Boelter
Melt/substrate interfacial heat transfer resistance	0
Best-fit constant in Ramacciotti correlation	5.77
Solid-fraction variation between liquidus/solidus	See Figure 2.3
Timestep	0.025 seconds

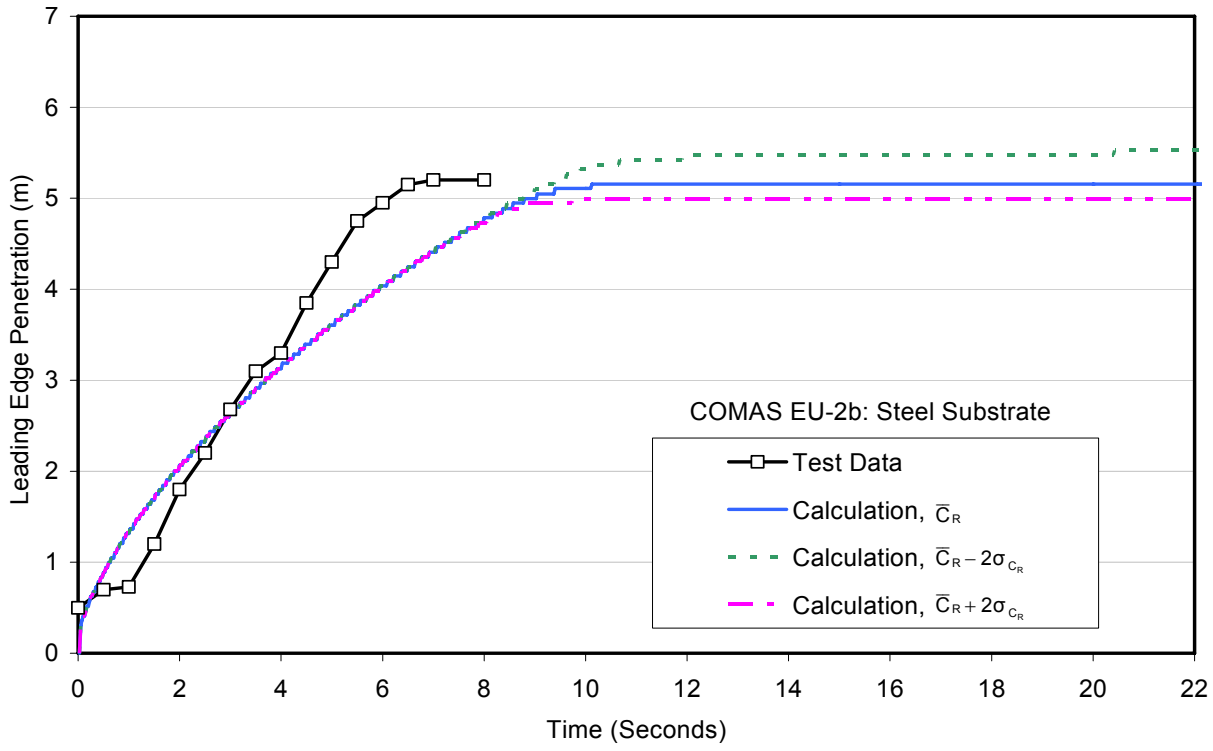

Figure A.91. Leading edge penetration comparison for COMAS-EU2b core oxide spreading test with steel channel.

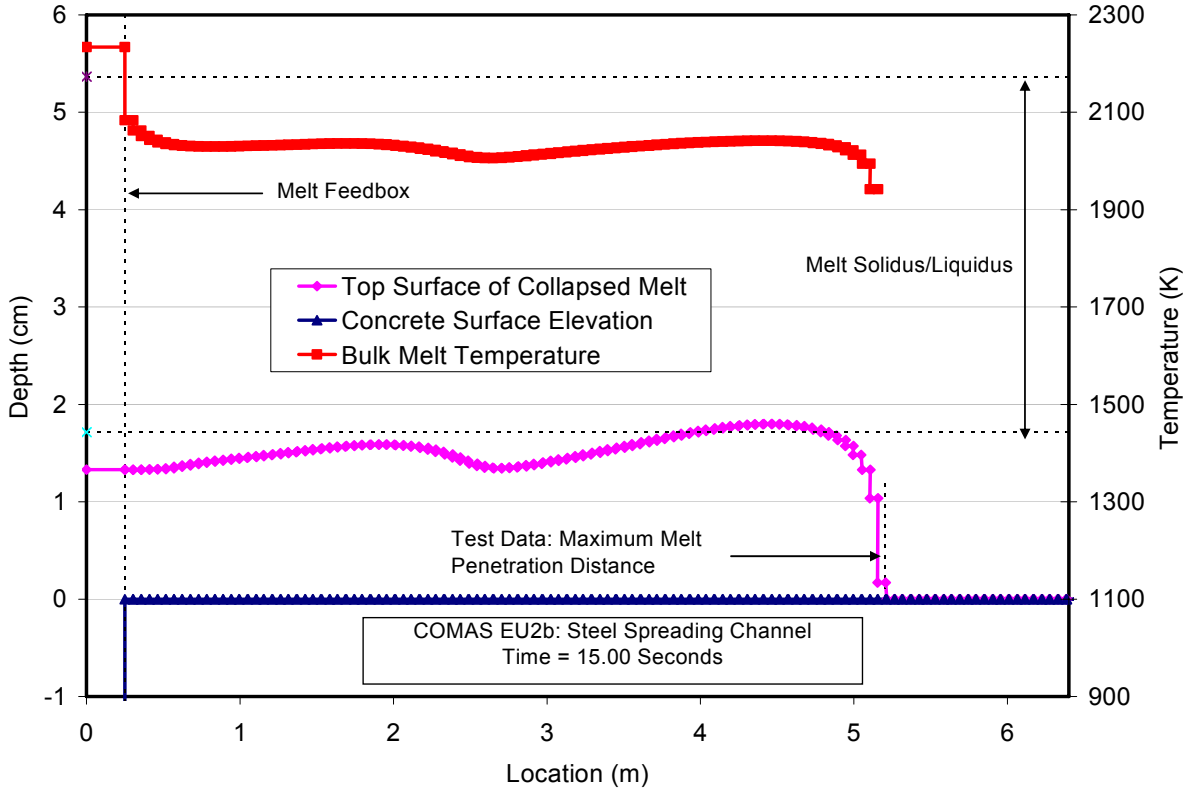

Figure A.92. Posttest debris profile prediction for the COMAS EU2b core oxide spreading test with steel channel.

Table A.36. Input File Data Sheet for the Comas EU-4 Test with Steel Substrate.

Test parameter	Value
Test name	Comas EU-4
Melt composition (wt %)	29 UO_2, 12 ZrO_2 18 FeO, 2 Cr_2O_3, 39 Fe
Melt delivery technique	Melt poured into an accumulator box that was 40 cm wide (per channel), 25 cm long, and 5 cm deep relative to spreading surface. Pour initiated by opening a plug device at the bottom of the accumulator.
Melt temperature	2323 K
Total pour mass	2000 kg
Substrate material	Steel
Spreading geometry	1-D channel, 2.5 m long, followed by a 45º sector with an effective radius of 6.0 m.
Code input parameter(s)	**Value(s)**
Melt composition (wt %)	29 UO_2, 12 ZrO_2 18 FeO, 2 Cr_2O_3, 39 Fe
Melt pour temperature	2323 K
Melt oxide phase solidus – liquidus	1598 K – 2233 K
Melt metal phase solidus – liquidus	1810 K – 1820 K
Melt pour rate and duration	$2.0 \cdot 10^4$ kg/sec over a 0.1 sec (simulating instantaneous deposition in the accumulator, followed by initiation of spreading)
Melt material property evaluation	Code subroutines
Substrate composition	Steel (code default composition)
Substrate initial temperature	300 K
Substrate material properties evaluation	Code subroutines
Substrate solidus - liquidus temperatures	1810 K – 1811 K (code default values)
Substrate nodalization	At each substrate nodal location, six 5.0 mm cells, followed by six 10 mm cells. All nodes cell-centered.
Spreading cavity nodalization	Accumulator: modeled as single 40 cm wide, 25 cm long, and 5 cm deep cell. Channel: modeled with 50 cells that are 40 cm wide and 5.33 cm long. 2-D spreading area: modeled as 45º sector with 110 cells with a radial length of 5.33 cm. All nodes cell-centered.
Cavity condition	Dry
Upper atmosphere temperature	300 K
Upper atmosphere emissivity	1.0
Ambient pressure	0.1 MPa
Melt/substrate heat transfer coefficient model	Dittus – Boelter
Melt/substrate interfacial heat transfer resistance	0
Best-fit constant in Ramacciotti correlation	8.17
Solid-fraction variation between liquidus/solidus	See Figure 2.3
Timestep	0.025 seconds

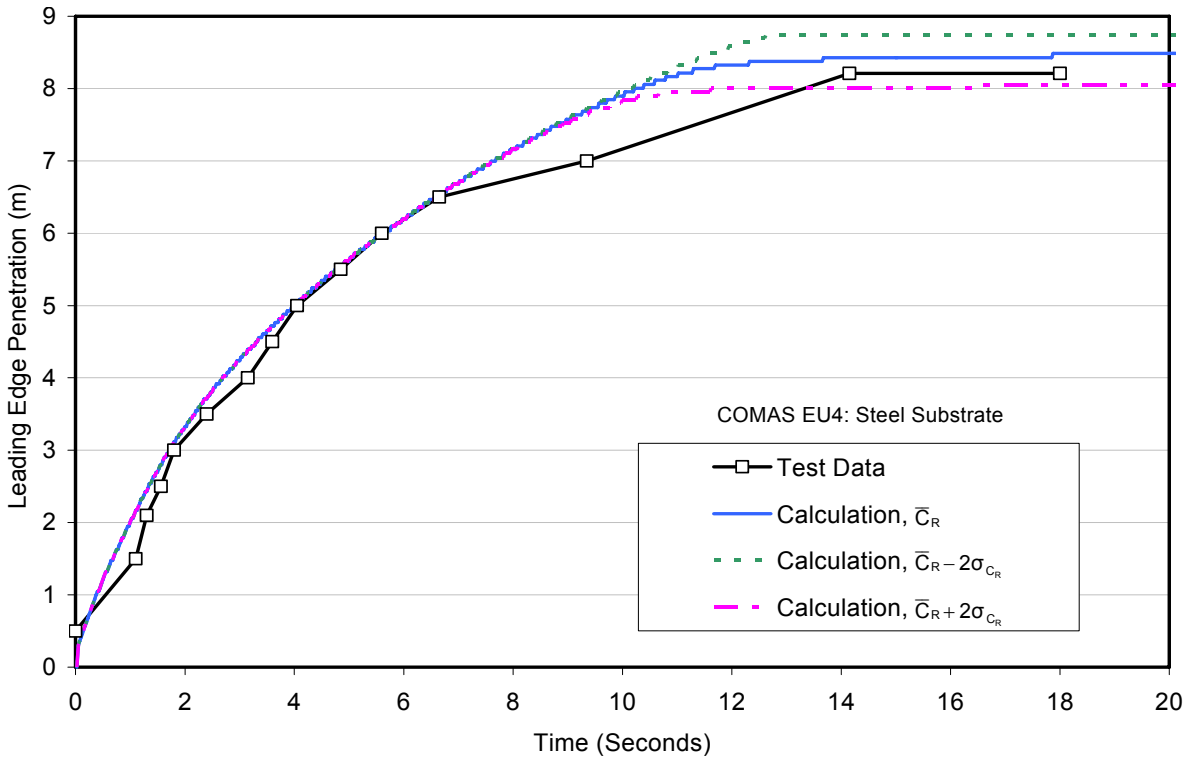

Figure A.93. Leading edge penetration comparison for COMAS-EU4 core oxide spreading test in 2-D geometry with steel channel.

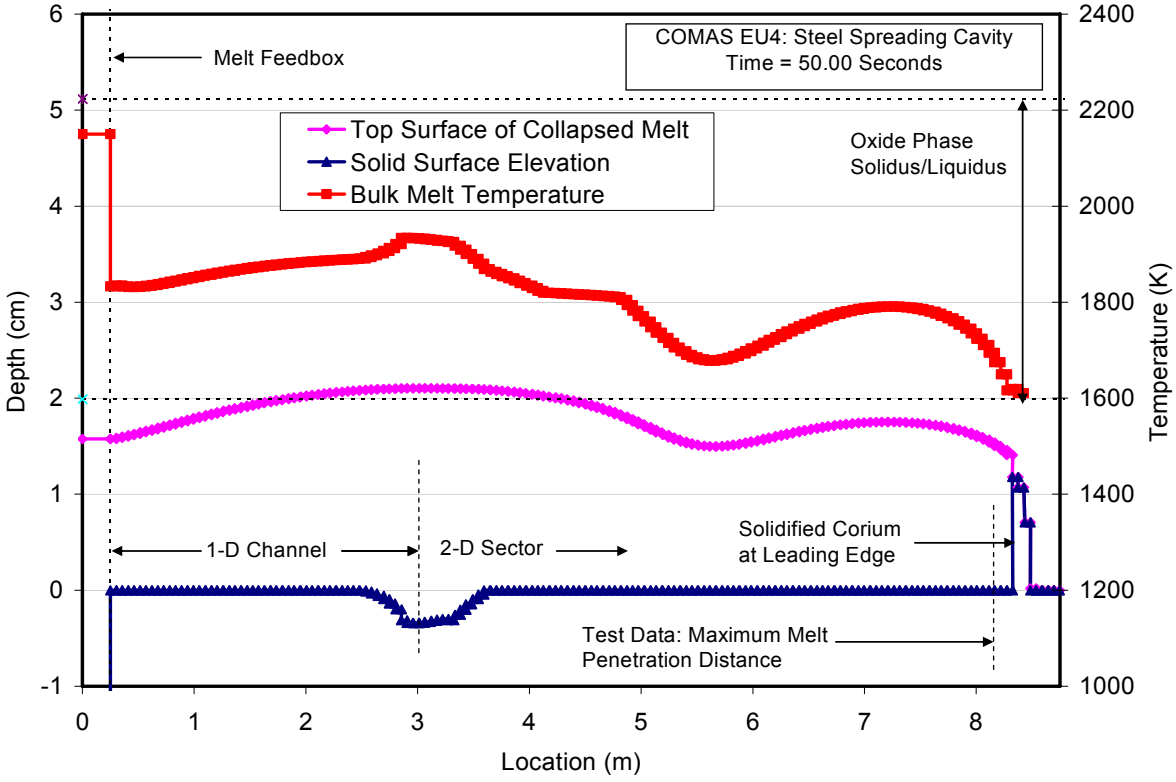

Figure A.94. Posttest debris profile prediction for the COMAS EU4 core oxide spreading test in 2-D geometry with steel channel.

APPENDIX B
Verification Studies

Aside from the code validation calculations that were summarized in Section 2 and detailed in Appendix A, an equally important task of the current workscope was to perform a set of verification calculations to ensure that the code was producing numerically correct solutions. The results of these various verification exercises are summarized in this appendix.

Table B.1 provides a summary of all cases that were calculated as part of the code verification activity. This matrix examines: 1) the ability of the code to reproduce an analytical solution for the 1-D dam break problem, and 2) numerical sensitivities to mesh size and time step for reactor material core melt, oxide simulant, and metal melt spreading tests on concrete, steel, and ceramic spreading surfaces. These test cases were selected to span the types of melt compositions and spreading surface materials that were addressed as part of the code validation exercise (see Appendix B). The results provide an indication of the types of time steps and mesh sizes that are required to obtain converged solutions using the code. Note that a verification exercise was also carried out for the model that was constructed for the EPR core melt spreading analysis, but those results are presented in the main body of the report (i.e., see Figure 3.1).

The results of the verification calculations are described below in the order they are described in Table B.1.

Table B.1. Summary of MELTSPREAD Verification Exercises.

Verification Case or Exercise	Objective(s)
1-D Dam Break Problem[8]	1) verify that the code could reproduce the analytical solution for leading edge velocity and depth, and 2) examine solution sensitivity to mesh size.
Corine HEC Spreading Test[9]	For a viscous isothermal spreading test, examine solution sensitivities to: 1) mesh size, and 2) timestep.
COMAS EU-2b Spreading Test[20-21]	For a core oxide material spreading test, examine solution sensitivity to mesh size for 1) concrete, 2) ceramic, and 3) steel spreading surfaces.
KATS-12 Simulant Oxide Melt Spreading Test[13]	Examine solution sensitivity to mesh size for a simulant oxide melt composition.
KATS-13 Metal Melt Spreading Test[13]	Examine solution sensitivity to mesh size for a metal melt composition.

B.1 1-D Dam Break Problem

As a starting point for the verification of the hydrodynamics modeling, the code was compared with the analytical solution for the one-dimensional dam break problem.[8] The input file that was assembled for this case is shown in Table B.2. Since this problem contains no heat transfer effects, the code was executed using the 'adiabatic' spreading option. Further, the analytical solution is based on inviscid flow theory, and so the 'inviscid flow' modeling option was also selected in which the friction shear stress term in the momentum equation is set to zero.

The particular case that is modeled assumes a 20 m long, 15 cm wide channel that is initially filled with a 10 cm water depth over ½ the channel length. At time t = 0, the 'dam' barrier is removed and the water is allowed to relocate under the influence of gravity. Computationally, this situation is modeled by pouring the water at a high flowrate into the nodes that cover the first half of the spreading channel to rapidly accumulating the 10 cm water depth.

According to simple gravity current theory,[8] after short term transient effects have died away, the advancing front will achieve a depth equal to ½ the initial fluid depth, and (in an Eulerian coordinate system) the advancing and receding fronts will achieve a constant velocity that is given through the equation,

$$U = \frac{\sqrt{gd}}{2} \quad , \tag{B.1}$$

where U is the front velocity, g is gravitational acceleration, and d is the initial fluid depth in the channel (10 cm). Thus, for the particular example under consideration, the advancing front should eventually achieve a constant velocity of 0.5 m/sec.

The calculated height distributions at various times are shown in Figure B.1, while leading edge spreading velocity is shown in Figure B.2. As is evident from Figure B.1, the model slightly under-predicts (by ~ 10 %) the theoretical advancing front depth of 5 cm throughout the calculated time domain. In addition, examination of Figure B.2 indicates that after transient effects have died away, the model slightly over-predicts leading edge spreading velocity by ~ 4 %. Thus, the results of this comparison indicate that the fluid mechanics algorithm in MELTSPREAD reproduces a simple analytical solution for the dam break problem to within a tolerance of 10 %.

Table B.2. Input File Data Sheet for 1-D Dam Break Problem.

Test parameter	**Value**
Test name	1-D Dam Break Problem
Fluid composition (wt %)	100 H_2O
Fluid delivery technique	Water assumed to be poured rapidly into the first 10 m of the spreading channel to establish a uniform water depth of 10 cm over the first 10 meters
Total pour mass	150 kg
Spreading geometry	20 m long channel with a uniform width of 15 cm
Code input parameter(s)	**Value(s)**
Fluid composition (wt %)	100 H_2O
Fluid pour rate and duration	Uniform injection water at a flowrate of 300 kg/sec over a time interval of 0.5 seconds; injection flow spread uniformly over ½ of the spreading channel to establish the initial 10 cm fluid depth.
Fluid material property evaluation[a]	User-specified property data used: $\rho = 1000$ kg/m^3 and $\sigma = 0.073$ N-m
Heat transfer modeling assumption	Flow is "adiabatic"
Fluid mechanics modeling assumption	Flow is "inviscid"
Spreading cavity nodalization	20 m cavity length subdivided into 200 cells each with a width of 15 cm and a length of 10 cm. All nodes cell-centered.
Timestep	0.05 seconds

[a]As applicable, ρ is density and σ is surface tension.

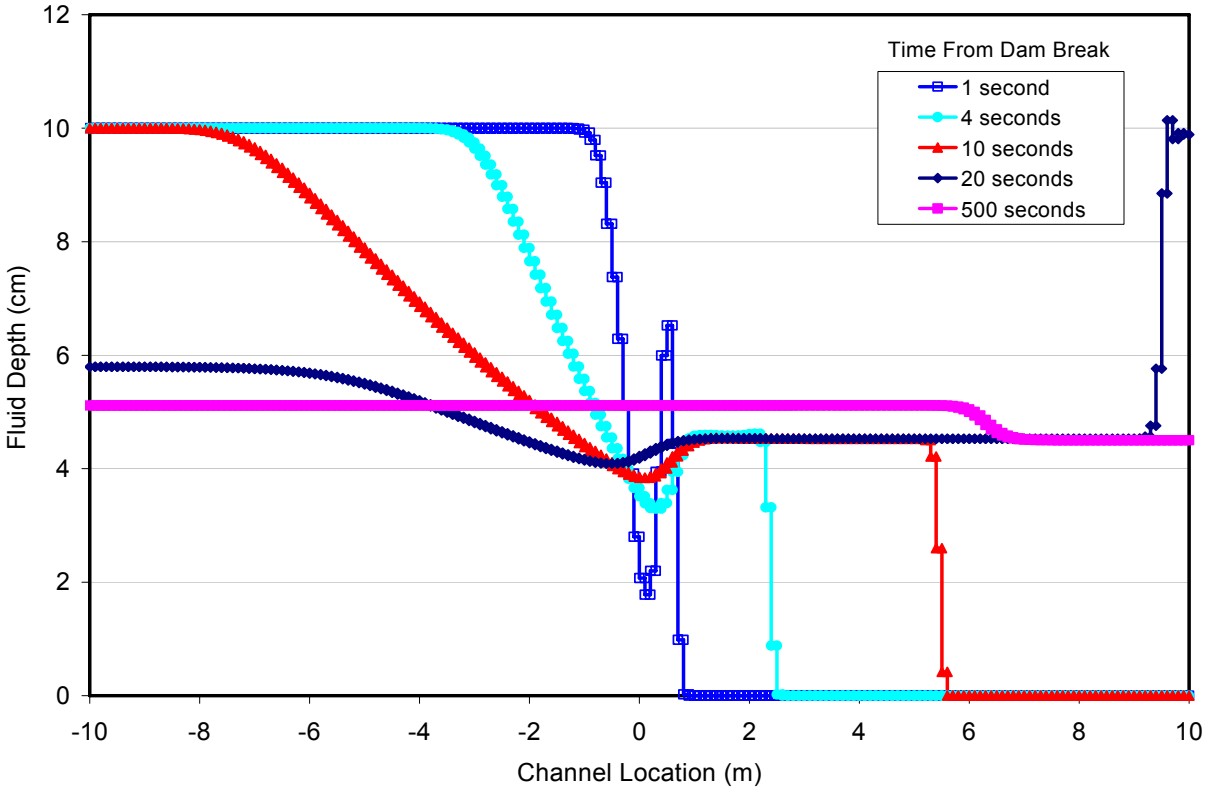

Figure B.1. Depth profiles at various times for the 1-D dam break problem.

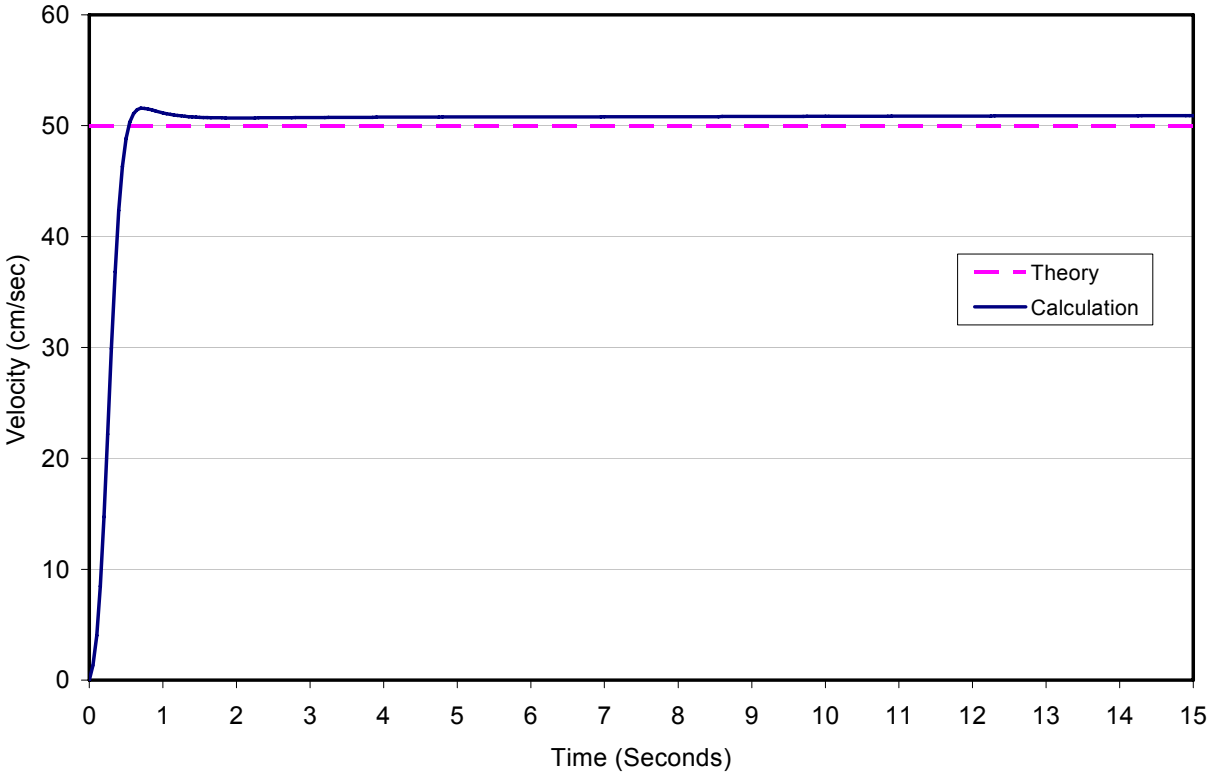

Figure B.2. Leading edge spreading velocity for the 1-D dam break problem compared with the analytical solution.

To evaluate the effect of mesh size on the numerical accuracy of the calculated results for the dam break problem, a range of cases were calculated with node sizes ranging from 40 cm down to 10 cm (case reported above). The leading edge penetration distance vs. time is shown in Figure B.3 for these various cases. As is evident, the fidelity of the calculation decreases with increasing node size, but the overall numerical accuracy of the solution remains the same for this particular case involving invisicid, isothermal spreading in a 1-D channel.

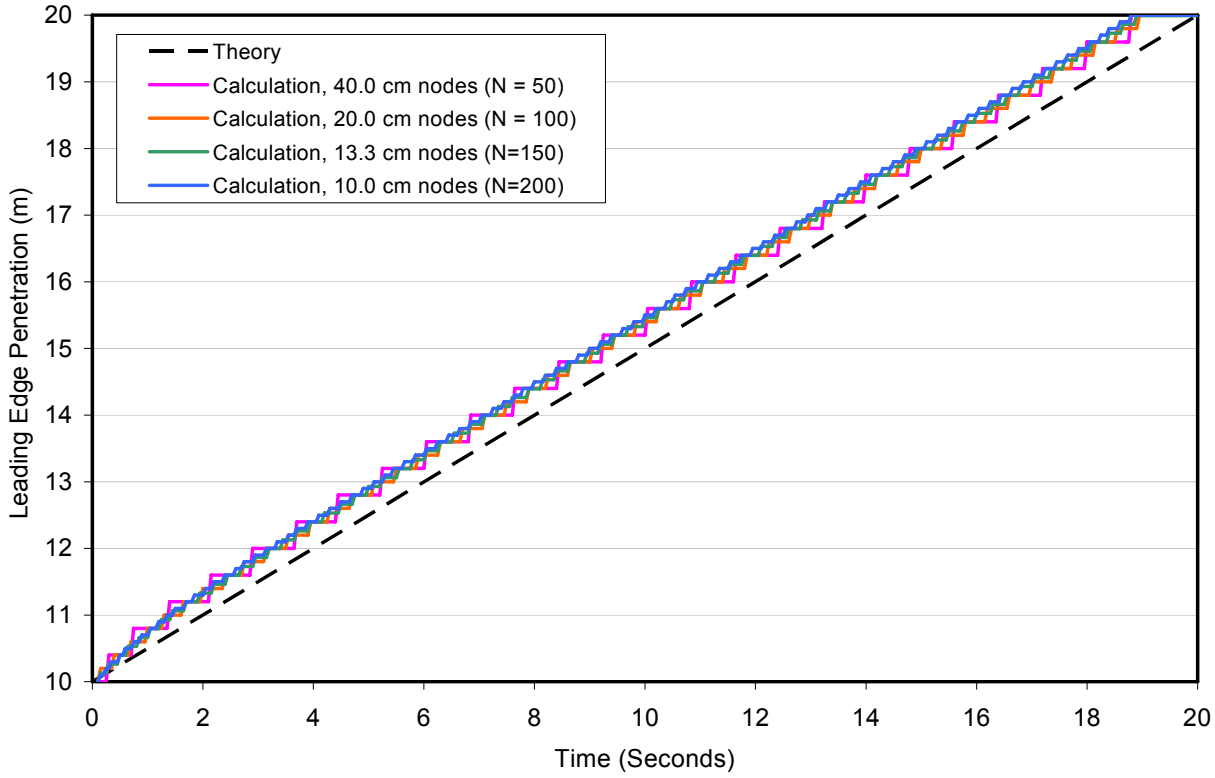

Figure B.3. The effect of mesh size on leading edge penetration for the 1-D dam break problem.

B.2 Corine HEC Spreading Test

The second case considered as part of the verification exercise is the isothermal spreading of a viscous fluid. As discussed in Section 2 and Appendix A, the large scale Corine spreading tests[9] were used as a database for code validation in this work, and one of the HEC (glycerol) spreading experiments was selected from that matrix (i.e., HEC_3_G0_2) to examine the sensitivity of the numerical solutions to the choices of mesh size and timestep. Test characteristics and principal modeling assumptions for this example can be found in Table A.6.

The first case considers the effect of mesh size on the numerical accuracy of the solution. A range of cases were run with node sizes ranging from 13 down to 3.3 cm (case reported above). The results for leading edge penetration are shown in Figure B.4. Again, the fidelity of the simulation is noted to degrade with increasing node size, but numerical accuracy does not. The second case investigates the influence of timestep on the accuracy of the solution; the results are shown in Figure B.5. Here, an influence is found; i.e., the results for the 25 and 50 ms timestep cases agree to within the resolution of the mesh, but when the timestep is increased to 200 ms, the solution is off by 2.7 % after 500 seconds.

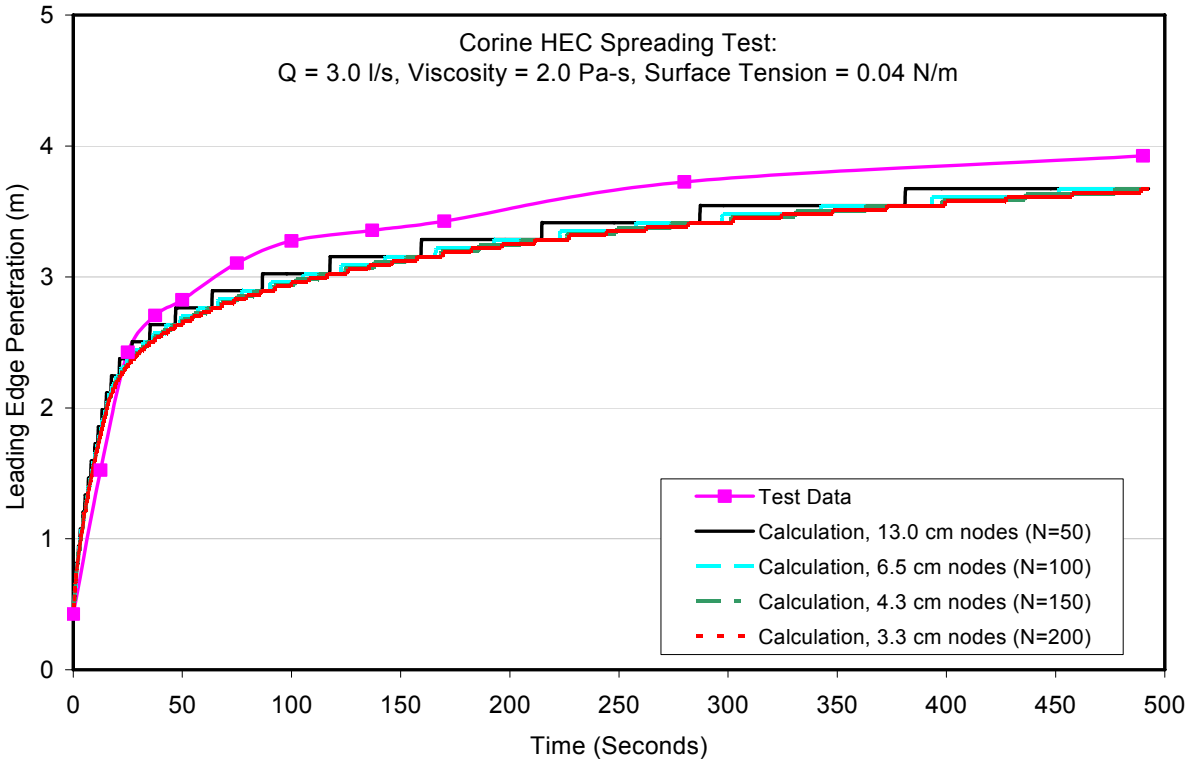

Figure B.4. The effect of mesh size on leading edge penetration rate for Corine HEC test HEC_3_G0_2.

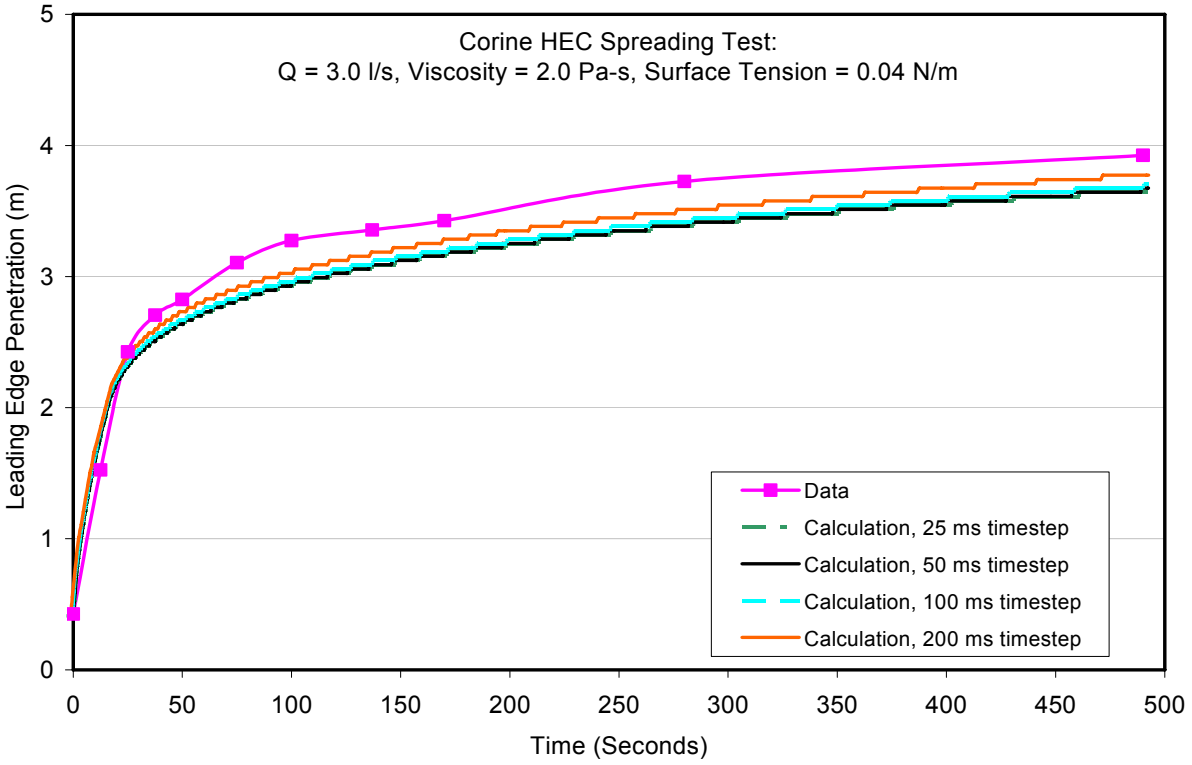

Figure B.5. The effect of timestep on leading edge penetration rate for Corine HEC test HEC_3_G0_2.

B.3 COMAS EU-2b Spreading Test

The focus of the third verification exercise was to examine the numerical sensitivity of the solutions to mesh size for the case of a core oxide melt spreading over ceramic, concrete, and steel surfaces. As discussed in Section 2 and Appendix A, the results of the large scale COMAS EU-2b experiment[20-21] were used as a database for code validation in this work, and this test was selected to examine the sensitivity of the numerical solutions to the choice of mesh size on these various spreading surfaces. These tests are much more challenging to calculate since they involve heat transfer and freezing effects. Test characteristics and principal modeling assumptions for the ceramic, concrete, and steel surface tests can be found in Tables A.33, A.34, and A.35, respectively.

The effect of mesh size on the numerical accuracy of the solutions for the ceramic, steel, and concrete surface tests are shown in Figures B.6, B.7, and B.8, respectively. All cases were run with node sizes ranging from 16 down to 4.0 cm. Unlike the isothermal tests described above, mesh size is found to have an influence on the results if the mesh is too course. For the steel and ceramic surfaces, the solutions have converged to with ~ 0.4 % for node sizes in the range of 4 to 5.3 cm. However, for the concrete test that involves mesh sizes in this same range, the solution varies by ~ 0.8% as the mesh size is reduced. This is due to the fact that the concrete case involves coupled heatup and decomposition of the underlying substrate; the corresponding gas release affects both the fluid mechanics (through void formation) and heat transfer (through the melt-substrate interfacial heat transfer coefficient). However, given all the other uncertainties involved in these types of analyses, this level of sensitivity to mesh size is deemed to be acceptable.

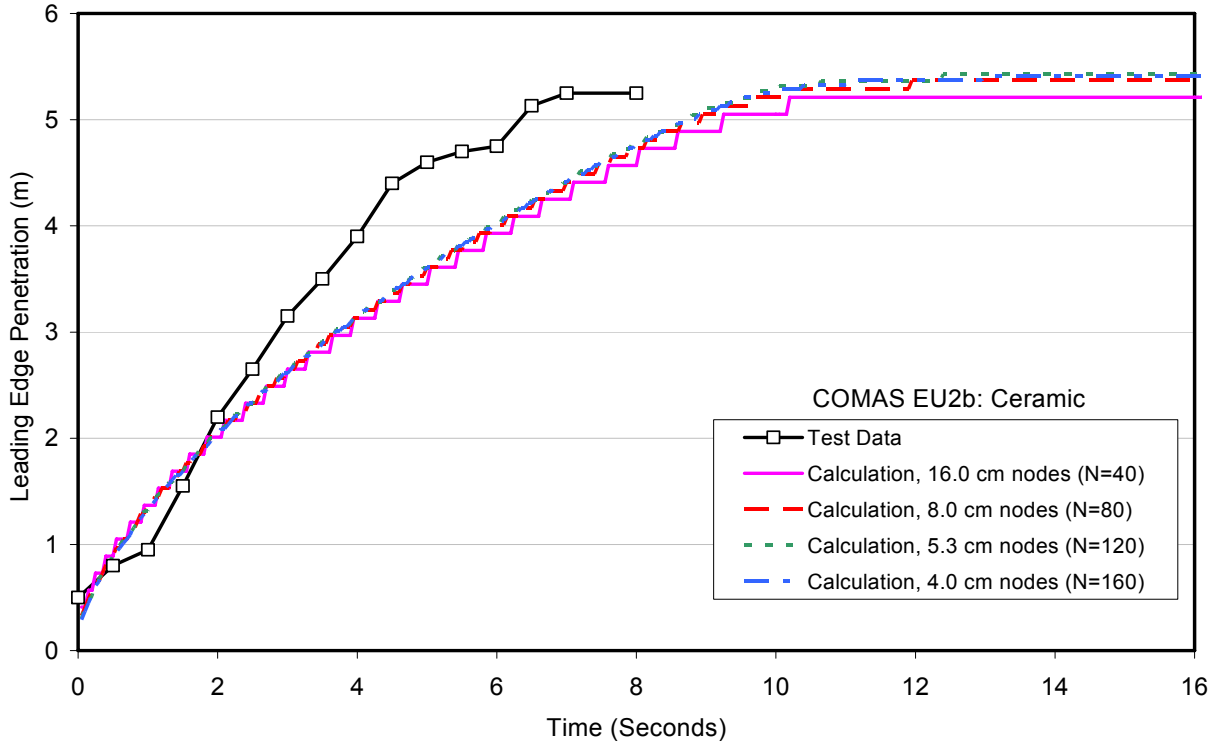

Figure B.6. The effect of mesh size on leading edge penetration rate for COMAS EU-2b ceramic substrate spreading test.

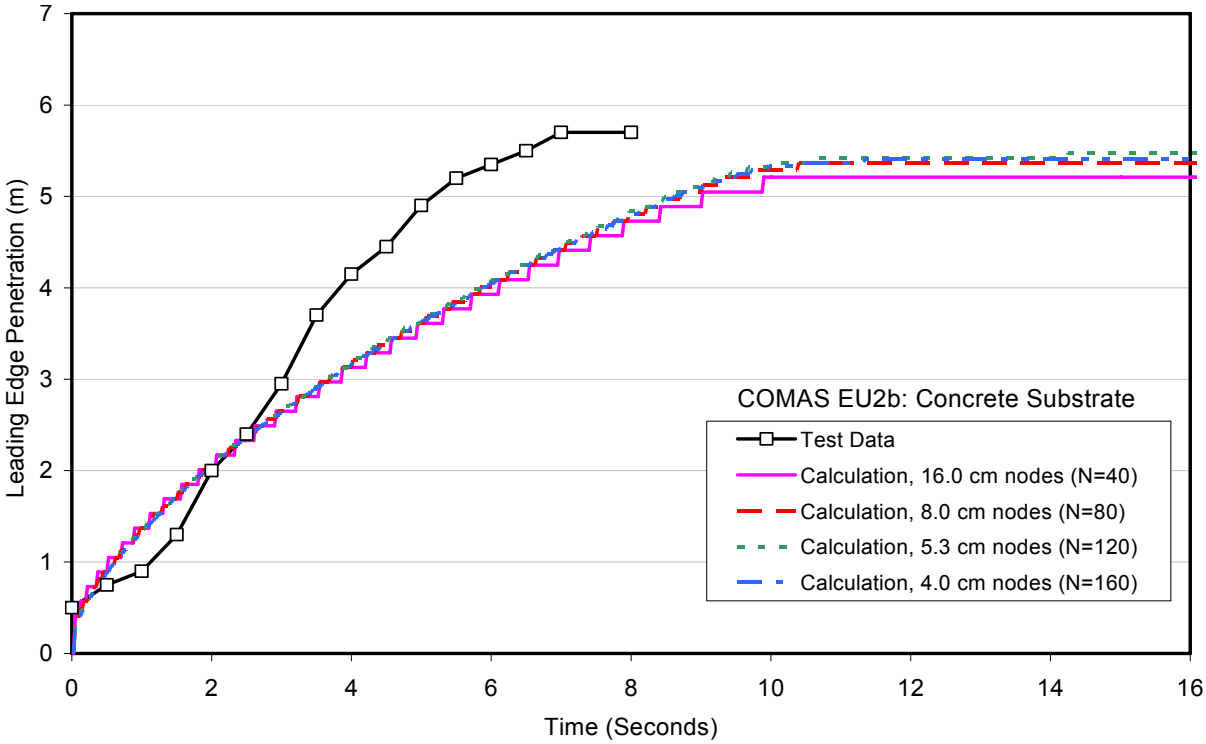

Figure B.7. The effect of mesh size on leading edge penetration rate for COMAS EU-2b concrete substrate spreading test.

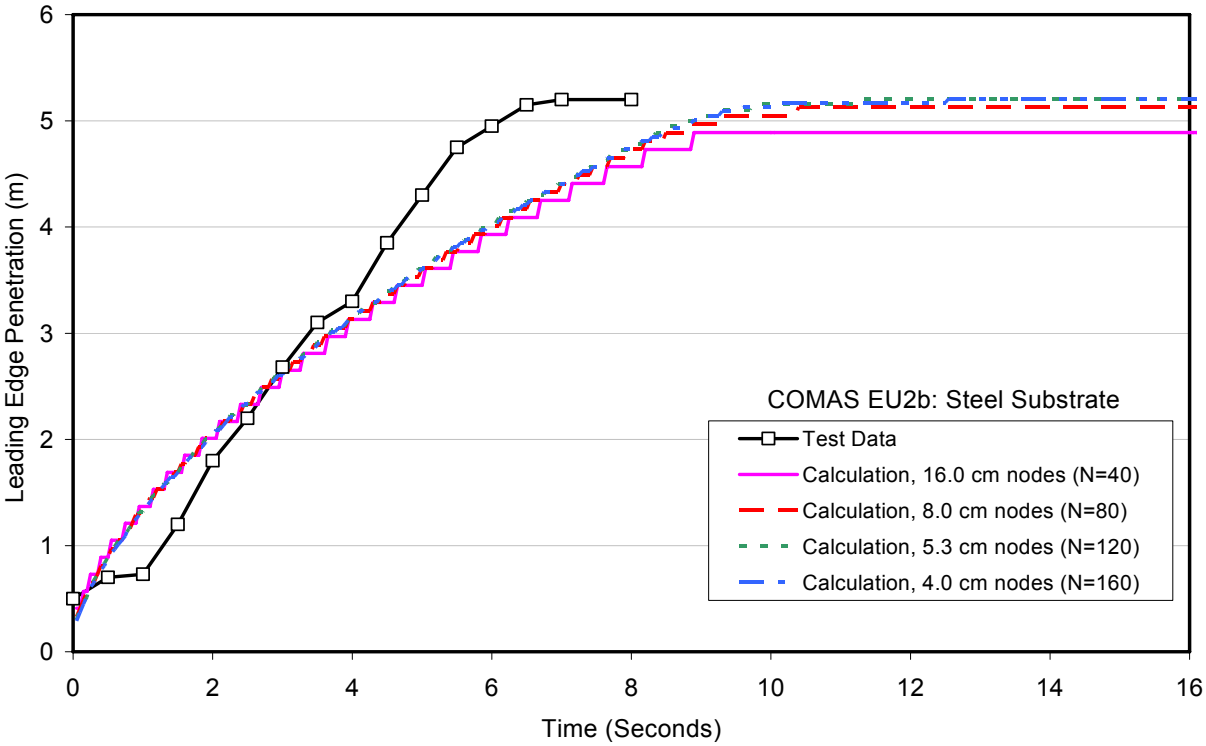

Figure B.8. The effect of mesh size on leading edge penetration rate for COMAS EU-2b steel substrate spreading test.

B.4 KATS-12 Simulant Oxide Melt Spreading Test

As discussed in Section 2, the ability to model simulant oxide melt material, as well as spreading on surfaces other than steel or concrete, were added as user options as part of this work. The objective of this fourth verification exercise was thus to examine solution sensitivity to mesh size for a test that invoked both of these new modeling options. The KATS-12 test was selected for this purpose; experiment details and modeling assumptions can be found in Table A.8.

The effect of mesh size on solution convergence for node sizes ranging from 40 cm down to 8 cm is shown in Figure B.9. As for the previously described tests involving heat transfer and freezing effects, mesh size is found to have an influence of the computed results if the mesh is too course. For this case, the solution has fully converged for node sizes of 10 cm or less.

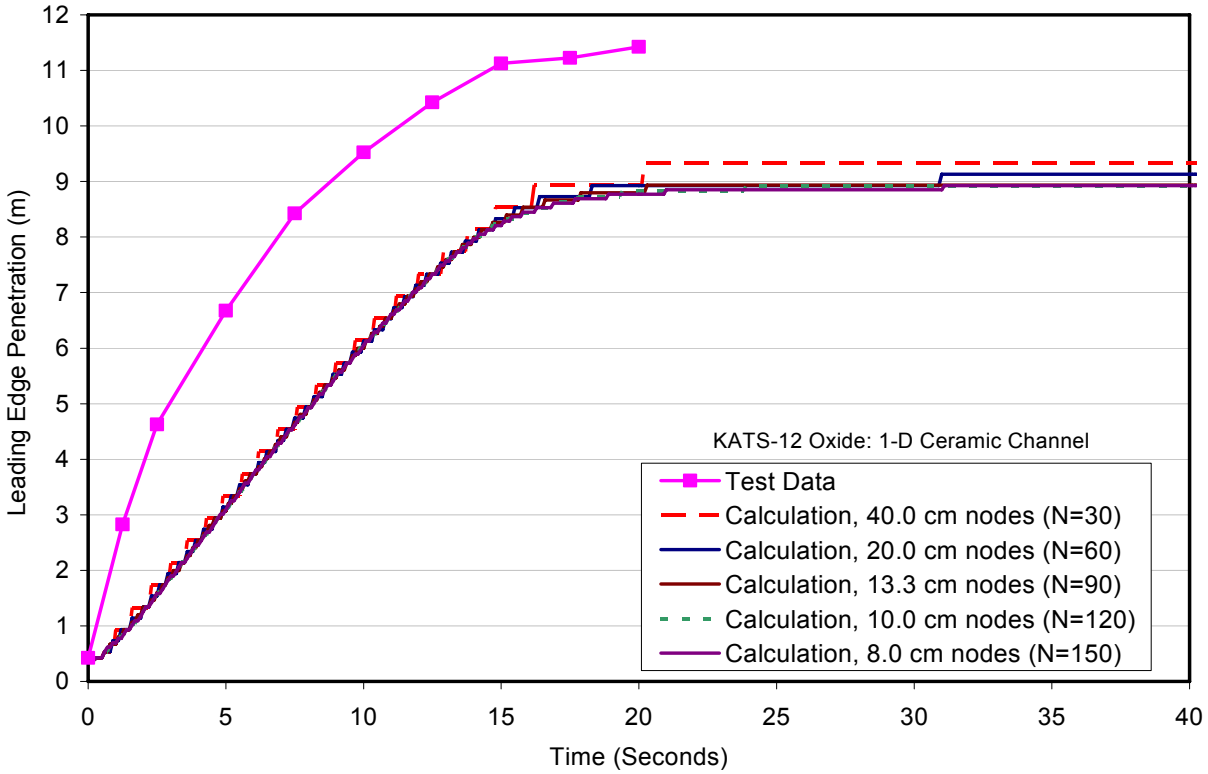

Figure B.9. The effect of mesh size on leading edge penetration rate for KATS-12 oxide spreading test in a ceramic channel.

B.5 KATS-13 Metal Melt Spreading Test

As discussed in Section 2, the code was also validated against the existing steel melt spreading database since this is a common structural material in LWRs. The objective of this fifth and final verification exercise was thus to examine the sensitivity of the solutions to mesh size for a test that involved steel melt. KATS-13 was selected since this test featured spreading on concrete, and previous work (see Section B.3) had shown that concrete decomposition with concurrent gas release offers the most challenging test of the numerical algorithms due to the coupling of the gas release with the fluid mechanics and heat transfer. Test characteristics and principal modeling assumptions for KATS-13 are provided in Table A.22.

The effect of mesh size on solution convergence for node sizes ranging from 40 cm down to 8 cm is shown in Figure B.10. As for the previous cases involving heat transfer, mesh size is found to have an influence of the computed results when the mesh is course. Examination of the data in Figure B.10 indicates that the solution has converged to within ~0.8 % for node sizes in the range of 8-10 cm. Given all the other uncertainties involved in these types of analyses, this level of sensitivity to mesh size is deemed to be acceptable.

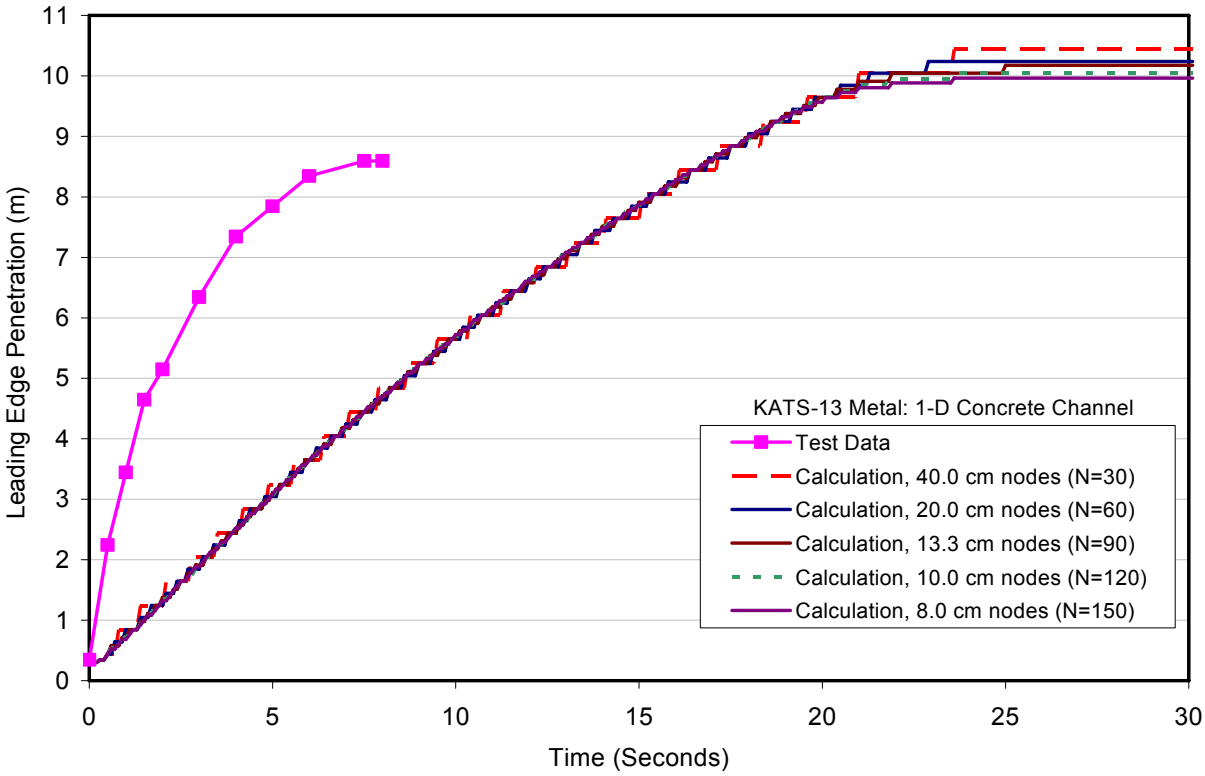

Figure B10. The effect of mesh size on leading edge penetration rate for KATS-13 metal spreading test in a concrete channel.

Nuclear Engineering Division
Argonne National Laboratory
9700 South Cass Avenue, Bldg. 208
Argonne, IL 60439-4842

www.anl.gov

UChicago ▶ Argonne LLC

A U.S. Department of Energy laboratory
managed by UChicago Argonne, LLC